

Jordan Journal of P H Y S I C S

An International Peer-Reviewed Research Journal

Volume 12, No. 2, August 2019, Muharram 1441 H

Jordan Journal of Physics (JJP): An International Peer-Reviewed Research Journal funded by the Scientific Research Support Fund, Jordan, and published biannually by the Deanship of Research and Graduate Studies, Yarmouk University, Irbid, Jordan.

EDITOR-IN-CHIEF:

Ibrahim O. Abu Al-Jarayesh

Department of Physics, Yarmouk University, Irbid, Jordan.

ijaraysh@yu.edu.jo

EDITORIAL BOARD:	ASSOCIATE EDITORIAL BOARD
<p>Prof. Nabil Y. Ayoub <i>President, American University of Madaba, Madaba, Jordan.</i> nabil.ayoub@gnu.edu.jo</p> <p>Prof. Jamil M. Khalifeh <i>Department of Physics, University of Jordan, Amman, Jordan.</i> jkalifa@ju.edu.jo</p> <p>Prof. Sami H. Mahmood <i>Department of Physics, University of Jordan, Amman, Jordan.</i> s.mahmood@ju.edu.jo</p> <p>Prof. Marwan S. Mousa <i>Department of Physics, Mu'tah University, Al-Karak, Jordan.</i> mmousa@mutah.edu.jo</p> <p>Prof. Mohammad Al-Sugheir <i>Department of Physics, The Hashemite University, Zarqa, Jordan.</i> msugh@hu.edu.jo</p> <p>Prof. Abdalmajeid M. Alyassin <i>Department of Physics, Yarmouk University, Irbid, Jordan.</i> alyassin@yu.edu.jo</p> <p>Prof. M-Ali H. Al-Akhras (AL-Omari) <i>Department of Physics, Jordan University of Science & Technology, Irbid, Jordan.</i> alakhmoh@just.edu.jo</p> <p>Prof. Ibrahim A. Bsoul <i>Department of Physics, Al al-Bayt University, Mafraq, Jordan.</i> Ibrahimbsoul@yahoo.com</p>	<p>Prof. Mark Haggmann <i>Desert Electronics Research Corporation, 762 Lacey Way, North Salt Lake 84064, Utah, U. S. A.</i> MHaggmann@NewPathResearch.Com</p> <p>Dr. Richard G. Forbes <i>Dept. of Electrical and Electronic Engineering, University of Surrey, Advanced Technology Institute and Guildford, Surrey GU2 7XH, UK.</i> r.forbes@surrey.ac.uk</p> <p>Prof. Roy Chantrell <i>Physics Department, The University of York, York, YO10 5DD, UK.</i> roy.chantrell@york.ac.uk</p> <p>Prof. Susamu Taketomi <i>2-35-8 Higashisakamoto, Kagoshima City, 892-0861, Japan.</i> staketomi@hotmail.com</p>

Editorial Secretary: Majdi Al-Shannaq.

Languages Editor: Haider Al-Momani

Manuscripts should be submitted to:

Prof. Ibrahim O. Abu Al-Jarayesh
Editor-in-Chief, Jordan Journal of Physics
Deanship of Research and Graduate Studies
Yarmouk University-Irbid-Jordan
Tel. 00 962 2 7211111 Ext. 2075
E-mail: jjp@yu.edu.jo
Website: <http://Journals.yu.edu.jo/jjp>

Jordan Journal of PHYSICS

An International Peer-Reviewed Research Journal

Volume 12, No. 2, August 2019, Muharram 1441 H

INTERNATIONAL ADVISORY BOARD

Prof. Dr. Ahmad Saleh

Department of Physics, Yarmouk University, Irbid, Jordan.
salema@yu.edu.jo

Prof. Dr. Aurore Savoy-Navarro

LPNHE Université de Paris 6/IN2P3-CNRS, Tour 33, RdC 4,
Place Jussieu, F 75252, Paris Cedex 05, France.
auore@lphnep.in2p3.fr

Prof. Dr. Bernard Barbara

Laboratoire Louis Neel, Salle/Room: D 108, 25, Avenue des
Martyrs BP 166, 38042-Grenoble Cedex 9, France.
Barbara@grenoble.cnrs.fr

Prof. Dr. Bruno Guiderdoni

Observatoire Astronomique de Lyon, g, avenue Ch. Antre-F-69561,
Saint Genis Laval Cedex, France.
Bruno.guiderdoni@olos.univ-lyon1.fr

Prof. Dr. Buford Price

Physics Department, University of California, Berkeley, CA 94720,
U. S. A.
bprice@berkeley.edu

Prof. Dr. Colin Cough

School of Physics and Astronomy, University of Birmingham, B15
2TT, U. K.
c.gough@bham.ac.uk

Prof. Dr. Desmond Cook

Department of Physics, Condensed Matter and Materials Physics
Research Group, Old Dominion University, Norfolk, Virginia
23529, U. S. A.
Dcook@physics.odu.edu

Prof. Dr. Evgeny Sheshin

MIPT, Institutskij per. 9, Dogoprudnyi 141700, Russia.
sheshin@lafeet.mipt.ru

Prof. Dr. Hans Ott

Laboratorium fuer Festkorperphysik, ETH Honggerberg, CH-
8093 Zurich, Switzerland.
ott@solid.phys.ethz.ch

Prof. Dr. Herwig Schopper

President SESAME Council, Chairman Scientific Board UNESCO
IBSP Programme, CERN, 1211 Geneva, Switzerland.
Herwig.Schopper@cern.ch

Prof. Dr. Humam Ghassib

Department of Physics, The University of Jordan, Amman 11942,
Jordan.
humamg@ju.edu.jo

Prof. Dr. Khalid Tougan

Chairman of Jordan Atomic Energy Commission, Amman, Jordan.

Prof. Dr. Nasr Zubeidey

President: Al-Zaytoonah University of Jordan, Amman, Jordan.
President@alzaytoonah.edu.jo

Prof. Dr. Patrick Roudeau

Laboratoire de l'Accelérateur, Lineaire (LAL), Université Paris-
Sud 11, Batiment 200, 91898 Orsay Cedex, France.
roudeau@mail.cern.ch

Prof. Dr. Paul Chu

Department of Physics, University of Houston, Houston, Texas
77204-5005, U. S. A.
Ching-Wu.Chu@mail.uh.edu

Prof. Dr. Peter Dowben

Nebraska Center for Materials and Nanoscience, Department of
Physics and Astronomy, 255 Behlen Laboratory (10th and R
Streets), 116 Brace Lab., P. O. Box 880111, Lincoln, NE 68588-
0111, U. S. A.
pdowben@unl.edu

Prof. Dr. Peter Mulser

Institute fuer Physik, T.U. Darmstadt, Hochschulstr. 4a, 64289
Darmstadt, Germany.
Peter.mulser@physik.tu-darmstadt.de

Prof. Dr. Rasheed Azzam

Department of Electrical Engineering, University of New Orleans
New Orleans, Louisiana 70148, U. S. A.
razzam@uno.edu

Prof. Dr. Shawqi Al-Dallal

Department of Physics, Faculty of Science, University of Bahrain,
Manamah, Kingdom of Bahrain.

Prof. Dr. Wolfgang Nolting

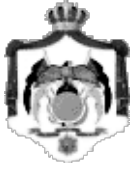
Institute of Physics / Chair: Solid State Theory, Humboldt-
University at Berlin, Newtonstr. 15 D-12489 Berlin, Germany
Wolfgang.nolting@physik.hu-berlin.de

Prof. Dr. Ingo Hofmann

GSI Darmstadt, Planckstr. 1, 64291, Darmstadt, Germany.
i.hofmann@gsi.de

Prof. Dr. Jozef Lipka

Department of Nuclear Physics and Technology, Slovak University
of Technology, Bratislava, Ilkovicova 3, 812 19 Bratislava,
Slovakia.
Lipka@elf.stuba.sk



The Hashemite Kingdom of Jordan



Yarmouk University

Jordan Journal of
PHYSICS

An International Peer-Reviewed Research Journal
Funded by the Scientific Research Support Fund

Volume 12, No. 2, August 2019, Muharram 1441 H

Instructions to Authors

Instructions to authors concerning manuscript organization and format apply to hardcopy submission by mail, and also to electronic online submission via the Journal homepage website (<http://jjp.yu.edu.jo>).

Manuscript Submission

1- **E-mail to** : jjp@yu.edu.jo

2- **Online**: Follow the instructions at the journal homepage website.

Original *Research Articles*, *Communications* and *Technical Notes* are subject to critical review by minimum of two competent referees. Authors are encouraged to suggest names of competent reviewers. *Feature Articles* in active Physics research fields, in which the author's own contribution and its relationship to other work in the field constitute the main body of the article, appear as a result of an invitation from the Editorial Board, and will be so designated. The author of a *Feature Article* will be asked to provide a clear, concise and critical status report of the field as an introduction to the article. *Review Articles* on active and rapidly changing Physics research fields will also be published. Authors of *Review Articles* are encouraged to submit two-page proposals to the Editor-in-Chief for approval. Manuscripts submitted in *Arabic* should be accompanied by an Abstract and Keywords in English.

Organization of the Manuscript

Manuscripts should be typed double spaced on one side of A4 sheets (21.6 x 27.9 cm) with 3.71 cm margins, using Microsoft Word 2000 or a later version thereof. The author should adhere to the following order of presentation: Article Title, Author(s), Full Address and E-mail, Abstract, PACS and Keywords, Main Text, Acknowledgment. Only the first letters of words in the Title, Headings and Subheadings are capitalized. Headings should be in **bold** while subheadings in *italic* fonts.

Title Page: Includes the title of the article, authors' first names, middle initials and surnames and affiliations. The affiliation should comprise the department, institution (university or company), city, zip code and state and should be typed as a footnote to the author's name. The name and complete mailing address, telephone and fax numbers, and e-mail address of the author responsible for correspondence (designated with an asterisk) should also be included for official use. The title should be carefully, concisely and clearly constructed to highlight the emphasis and content of the manuscript, which is very important for information retrieval.

Abstract: A one paragraph abstract not exceeding 200 words is required, which should be arranged to highlight the purpose, methods used, results and major findings.

Keywords: A list of 4-6 keywords, which expresses the precise content of the manuscript for indexing purposes, should follow the abstract.

PACS: Authors should supply one or more relevant PACS-2006 classification codes, (available at <http://www.aip.org/pacs/pacs06/pacs06-toc.html>)

Introduction: Should present the purpose of the submitted work and its relationship to earlier work in the field, but it should not be an extensive review of the literature (e.g., should not exceed 1 ½ typed pages).

Experimental Methods: Should be sufficiently informative to allow competent reproduction of the experimental procedures presented; yet concise enough not to be repetitive of earlier published procedures.

Results: should present the results clearly and concisely.

Discussion: Should be concise and focus on the interpretation of the results.

Conclusion: Should be a brief account of the major findings of the study not exceeding one typed page.

Acknowledgments: Including those for grant and financial support if any, should be typed in one paragraph directly preceding the References.

References: References should be typed double spaced and numbered sequentially in the order in which they are cited in the text. References should be cited in the text by the appropriate Arabic numerals, enclosed in square brackets. Titles of journals are abbreviated according to list of scientific periodicals. The style and punctuation should conform to the following examples:

1. Journal Article:

- a) Heisenberg, W., Z. Phys. 49 (1928) 619.
- b) Bednorz, J. G. and Müller, K. A., Z. Phys. B64 (1986) 189
- c) Bardeen, J., Cooper, L.N. and Schrieffer, J. R., Phys. Rev. 106 (1957) 162.
- d) Asad, J. H., Hijjawi, R. S., Sakaji, A. and Khalifeh, J. M., Int. J. Theor. Phys. 44(4) (2005), 3977.

2. Books with Authors, but no Editors:

- a) Kittel, C., "Introduction to Solid State Physics", 8th Ed. (John Wiley and Sons, New York, 2005), chapter 16.
- b) Chikazumi, S., C. D. Graham, JR, "Physics of Ferromagnetism", 2nd Ed. (Oxford University Press, Oxford, 1997).

3. Books with Authors and Editors:

- a) Allen, P. B. "Dynamical Properties of Solids", Ed. (1), G. K. Horton and A. A. Maradudin (North-Holland, Amsterdam, 1980), p137.
- b) Chantrell, R. W. and O'Grady, K., "Magnetic Properties of Fine Particles" Eds. J. L. Dormann and D. Fiorani (North-Holland, Amsterdam, 1992), p103.

4. Technical Report:

Purcell, J. "The Superconducting Magnet System for the 12-Foot Bubble Chamber", report ANL/HEP6813, Argonne Natl. Lab., Argonne, III, (1968).

5. Patent:

Bigham, C. B., Schneider, H. R., US patent 3 925 676 (1975).

6. Thesis:

Mahmood, S. H., Ph.D. Thesis, Michigan State University, (1986), USA (Unpublished).

7. Conference or Symposium Proceedings:

Blandin, A. and Lederer, P. Proc. Intern. Conf. on Magnetism, Nottingham (1964), P.71.

8. Internet Source:

Should include authors' names (if any), title, internet website, URL, and date of access.

9. Prepublication online articles (already accepted for publication):

Should include authors' names (if any), title of digital database, database website, URL, and date of access.

For other types of referenced works, provide sufficient information to enable readers to access them.

Tables: Tables should be numbered with Arabic numerals and referred to by number in the Text (e.g., Table 1). Each table should be typed on a separate page with the legend above the table, while explanatory footnotes, which are indicated by superscript lowercase letters, should be typed below the table.

Illustrations: Figures, drawings, diagrams, charts and photographs are to be numbered in a consecutive series of Arabic numerals in the order in which they are cited in the text. Computer-generated illustrations and good-quality digital photographic prints are accepted. They should be black and white originals (not photocopies) provided on separate pages and identified with their corresponding numbers. Actual size graphics should be provided, which need no further manipulation, with lettering (Arial or Helvetica) not smaller than 8 points, lines no thinner than 0.5 point, and each of uniform density. All colors should be removed from graphics except for those graphics to be considered for publication in color. If graphics are to be submitted digitally, they should conform to the following minimum resolution requirements: 1200 dpi for black and white line art, 600 dpi for grayscale art, and 300 dpi for color art. All graphic files must be saved as TIFF images, and all illustrations must be submitted in the actual size at which they should appear in the journal. Note that good quality hardcopy original illustrations are required for both online and mail submissions of manuscripts.

Text Footnotes: The use of text footnotes is to be avoided. When their use is absolutely necessary, they should be typed at the bottom of the page to which they refer, and should be cited in the text by a superscript asterisk or multiples thereof. Place a line above the footnote, so that it is set off from the text.

Supplementary Material: Authors are encouraged to provide all supplementary materials that may facilitate the review process, including any detailed mathematical derivations that may not appear in whole in the manuscript.

Revised Manuscript and Computer Disks

Following the acceptance of a manuscript for publication and the incorporation of all required revisions, authors should submit an original and one more copy of the final disk containing the complete manuscript typed double spaced in Microsoft Word for Windows 2000 or a later version thereof. All graphic files must be saved as PDF, JPG, or TIFF images.

Allen, P.B., “.....”, in: Horton, G.K., and Muradudin, A. A., (eds.), “Dynamical.....”, (North.....), pp....

Reprints

Twenty (20) reprints free of charge are provided to the corresponding author. For orders of more reprints, a reprint order form and prices will be sent with the article proofs, which should be returned directly to the Editor for processing.

Copyright

Submission is an admission by the authors that the manuscript has neither been previously published nor is being considered for publication elsewhere. A statement transferring copyright from the authors to Yarmouk University is required before the manuscript can be accepted for publication. The necessary form for such transfer is supplied by the Editor-in-Chief. Reproduction of any part of the contents of a published work is forbidden without a written permission by the Editor-in-Chief.

Disclaimer

Opinions expressed in this Journal are those of the authors and neither necessarily reflects the opinions of the Editorial Board or the University, nor the policy of the Higher Scientific Research Committee or the Ministry of Higher Education and Scientific Research. The publisher shoulders no responsibility or liability whatsoever for the use or misuse of the information published by JJP.

Indexing

JJP is currently indexing in:

	Emerging Sources Citation Index (ESCI)	 ULRICHSWEB™ GLOBAL SERIALS DIRECTORY
---	---	--

Jordan Journal of
P H Y S I C S

An International Peer-Reviewed Research Journal

Volume 12, No. 2, August 2019, Muharram 1441 H

Table of Contents:

English Articles	Pages
Comparison between Viscosity and Surface Tension of Polyvinylpyrrolidone/ Silver Nanoparticle (PVP/ AgNP) Solutions and Polyethylene Glycol/ Silver Nanoparticle (PEG/ AgNP) Solutions	97-102
Najla Ali Elgheryani	
Solutions of the Dirac Equation for the Quadratic Exponential-Manning-Rosen Potential plus Yukawa Potential within the Yukawa-like Tensor Interaction using the Framework of Nikiforov-Uvarov Formalism	103-112
Hitler Louis, Ita I. Benedict, Nzeata I. Nelson, and Ike V. Chidinma	
Basic Concepts and Development of Dry Deposition Modelling	113-132
Tareq Hussein, Safa' Ibrahim and Sawsan Malek	
Structural, Spectroscopic and Magnetic Characterization of $\text{Bi}_{0.9}\text{X}_{0.1}\text{Fe}_{0.98}\text{Mg}_{0.02}\text{O}_3$ (X = Gd, Sm, Ba) Multiferroic Compounds	133-140
Mansour M. Al-Haj	
Structural and Magnetic Properties of $\text{La}_{2/3}\text{D}_{1/3}\text{MnO}_3$ (D = Ca, Sr, Ba) Manganites Prepared By Ball Milling	141-152
Sami Mahmood, Haneen Badran, Eman Al-Hwaitat, Ibrahim Bsoul and Rola Bqaen	
Investigation of Radioactivity Levels and Radiation Hazards in Soil Samples Collected from Different Sites in Tafila Governorate, Jordan	153-161
Ahmad M. Al-Qarah, Abdallah H. Almahasneh, Derar Altarawneh and Alaa Jaffal	
Classification of LRS Bianchi Type I Spacetime through Its Conformal Killing Vector Fields	163-170
Suhail Khan, Syed Zaheer Ullah, M. Ramzan and Muhammad Ayaz	
Wireless Electricity Transmission by Coupled Magnetic Resonances	171-181
DaifAoulah Nassor, Ali Daroesho and Abdalrahman H. Alhashim	
Radiological Characterization of Settled Dust during a Severe Dust Episode in Jordan	183-189
Manal J. Abdallah, Molham M. Eyadeh, Hamed H. Hamadneh, Abdulrahman N. Akour, Mustafa M. Hawamdeh and Ibtisam F. Almaaitah	

Comparison between Viscosity and Surface Tension of Polyvinylpyrrolidone/ Silver Nanoparticle (PVP/ AgNP) Solutions and Polyethylene Glycol/ Silver Nanoparticle (PEG/ AgNP) Solutions

Najla Ali Elgheryani

Physics Department, Faculty of Education, University of Benghazi, Benghazi, Libya.

Received on: 18/5/2018;

Accepted on: 24/9/2018

Abstract: In the present study, viscosity and surface tension of Polyvinylpyrrolidone (PVP) solutions and Polyethylene glycol (PEG) solutions in water and nitric acid with different concentrations (0.0, 0.2, 0.4, 0.6, 0.8 and 1.0 %) of silver nanoparticles have been measured. However, the relative viscosity of PVP/ AgNP solutions increased from 2.245 to 2.585 and the relative viscosity of PEG / AgNP solutions increased from 1.150 to 1.204. Viscosity is a significant parameter during the electrospinning process. While the surface tension of the PVP/ AgNP solutions has changed from 0.052 Nm^{-1} to 1.46 Nm^{-1} , it has changed from 0.063 Nm^{-1} to 0.160 Nm^{-1} for PEG / AgNP solutions. In this paper, attempts were made to obtain improvements to the properties of samples by comparing them with the pure samples of polymers. I think that there are personal errors in the measurements. These results can be used in medical, industrial applications and in scientific studies.

Keywords: Polyvinylpyrrolidone (PVP), Polyethylene glycol (PEG), Silver nanoparticles (AgNPs), Viscosity (η), Surface tension (γ).

1. Introduction

Silver nanoparticles (AgNPs) have received enormous attention of researchers due to their extraordinary defense against a wide range of microorganisms and due to their drug resistance against commonly used antibiotics [1]. Silver nanoparticles might exhibit additional antimicrobial capabilities not exerted by ionic silver, because of their small size and large surface to volume ratio, which lead to both chemical and physical differences in their properties compared with their bulk counterparts. AgNPs can be produced with various sizes and shapes depending on the fabrication method, among which the most widely used is the method of chemical reduction [2].

Polyvinylpyrrolidone (PVP) is a completely nontoxic polymer and has a long polyvinyl backbone [3]. It serves as an excellent capping

agent, especially for noble metal particles. It is soluble in water as well as in physiological solutions [3]. Several studies have used Polyvinylpyrrolidone (PVP) as the carrier medium in various fields of application that include the formation of nanoparticles or nanofibers [4]. Noting that PVP has been recognized by FDA (Food and Drug Administration), USA, it is widely used as a drug carrier to increase drug solubility [4].

Polyethylene glycol (PEG) is a linear polyether of ethylene glycol [3]. PEG molecules are synthetic, highly water soluble, inert polymers that are produced in a wide range of molecular weights [5]. PEGs of various molecular weights have been widely used in consumer care products, such as laxatives, toothpaste and hair shampoos [5]. Polymer blends can be defined as physical mixtures of two or more homo-polymer or copolymers,

which interact with secondary forces such as hydrogen bonding with no covalent bonding. Polymer blends are prepared by many methods. Among them, solution blending is very simple and brisk [6]. The polymer blends include both crystalline and amorphous polymers and the mixing of two chemically dissimilar polymers is miscible or independent on the thermodynamics of mixing [6]. The precise definition of viscosity is based on laminar, or nonturbulent, flow. Laminar flow is characterized by the smooth flow of the fluid in layers that do not mix. Turbulent flow, or turbulence, is characterized by eddies and swirls that mix layers of fluid together. Viscosity is, essentially, fluid friction. Like friction between moving solids, viscosity transforms kinetic energy of (macroscopic) motion into heat energy. Viscosity is a fundamental characteristic property of all liquids. Viscosity is a measure of internal resistance presence in each real fluid causing the fluid to oppose the dynamic variation of its motion and therefore restricting its tendency to flow. Dynamic viscosity is defined as the ratio of shear stress (force over cross sectional area) to the rate of deformation [7].

Liquids possess some properties, like density, viscosity, surface tension ...etc. Also, the shape of drops is governed by the property of surface tension [8]. Surface tension is the property of the liquid that shows the strong cohesiveness of the liquid molecules, indicating the dissimilarity of the phases at the interface [9]. Surface tension, which is strongly influenced by the nature of the solvent from the polymer solution, is a very important factor in electrospinning. This is why the correct selection of the solvent is critical, not only to obtain a homogeneous solution of the polymer, but also to obtain the right surface tension [9].

2. Experimental

2.1 Samples

PVP, PEG and Ag nanoparticles used in the present work were supplied by Sigma-Aldrich, GmbH. The two types of polymer solutions (PVP solutions and PEG solutions) with different concentrations (0.0, 0.2, 0.4, 0.6, 0.8 and 1.0 %) of silver nanoparticles were prepared by dissolving a polymer in twice-distilled water at room temperature [10] and the different concentrations of silver nanoparticles were

dissolved in the same amount of nitric acid, then mixed with polymer solutions [10].

2.2 Measurements

2.2.1 Viscosity Measurements

In determining the efflux time of the solutions, the methodology stated by ASTM (1989) was used. The efflux time for solvents and polymers/ silver nanoparticle solutions was measured by glass capillary viscometer. The measured values have been expressed in terms of relative (η_r), specific (η_{sp}) and intrinsic ($[\eta]$) as follows [11]:

$$\eta_r = \frac{t_{solution}}{t_{solvent}} \quad (1)$$

$$\eta_{sp} = \eta_r - 1 \quad (2)$$

$$[\eta] = \lim_{c \rightarrow \infty} \frac{\eta_{sp}}{c} \quad (3)$$

where C is the mass concentration of Ag nanoparticles in nitric acid [11].

2.2.2 Surface Tension Measurement

Using the drop- weight method, a counted number of drops were collected and the average mass of a drop found. The mean radius of the orifice was determined, then the surface tension against air was expressed by the measured values as follows [12]:

$$\gamma = \frac{mg}{2\pi r} \quad (4)$$

where m = average mass of a drop, g = acceleration of gravity and r = internal radius of the tube used (4mm). All measurements have been conducted at a temperature of 25 (\pm 0.1) °C.

Surface tension force (F) and surface tension energy (E) can be calculated by Eq. (5) and Eq. (6), respectively [13].

$$F = 4 \pi r \gamma \quad (5)$$

$$E = \gamma A \quad (6)$$

where A is the surface area of the drop.

3. Results and Discussion

3.1 Viscosity

Fig. 1 shows a plot of PVP and PEG relative viscosity values against mass concentration of silver nanoparticles. This plot demonstrates that viscosity increases monotonically with the increase of concentration. Furthermore, the plot indicates that the viscosity values of PEG

solutions are less than the viscosity values of PVP solutions. Thus, it is clear that silver nanoparticle concentrations produce changes in the viscosity of all solutions. Viscosity is a significant parameter during the electrospinning process [14]. When viscosity is increased, which means that there will be a higher amount of polymer chain entanglement in the solution, the charges on the electrospinning jet will be able to

fully stretch the solution with the solvent molecules distributed among the polymer chains [15]. This is probably due to the greater resistance of the solution to be stretched by the charges on the jet [15].

The plots in Fig. 2 agree with Schulz-Blaschke equation for PVP solutions and PEG solutions.

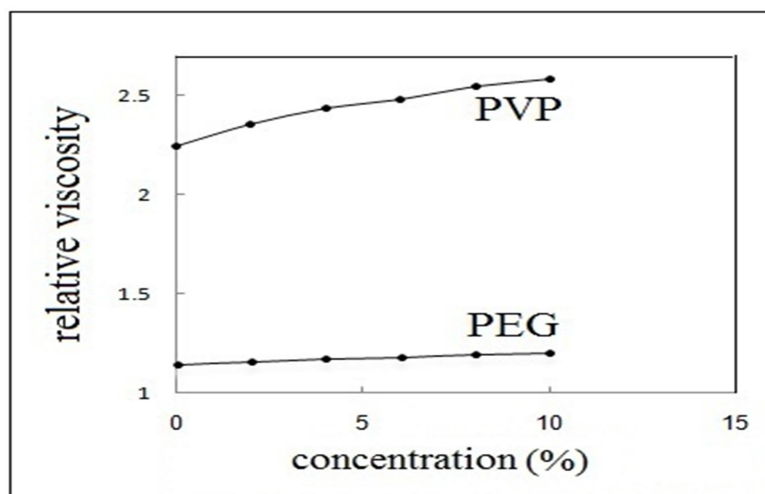


FIG. 1. Relative viscosity vs. concentration of Ag nanoparticles for PVP solutions and PEG solutions at 25°C.

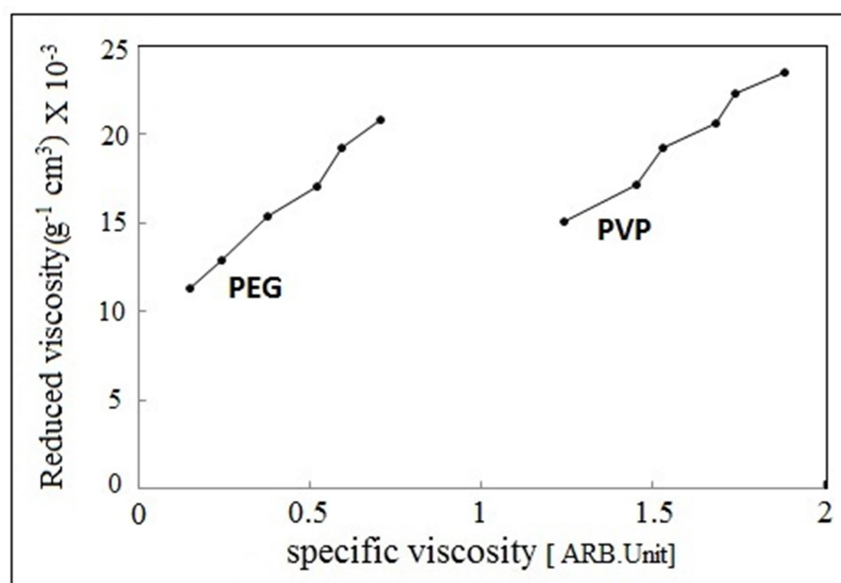


FIG. 2. Reduced viscosity vs. specific viscosity for PVP solutions and PEG solutions at 25°C.

$$\eta_{red} = [\eta] + K_{sb} [\eta] \eta_{sp} \quad (7)$$

where η_{red} = reduced viscosity, $[\eta]$ = intrinsic viscosity and K_{sb} = Schulz-Blaschke constant [11]. Fig. 3 shows a plot of Schulz-Blaschke constant k_{sb} values against flow time. It reflects

how far the values of Schulz-Blaschke constant of the solutions increase with increasing the flow time. This could be attributed to scission on the polymer chains [11].

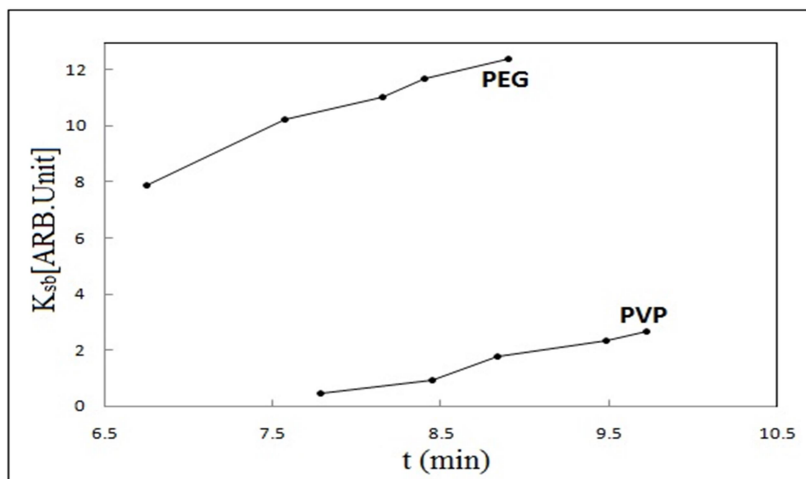


FIG. 3. Schulz-Blaschke constant vs. flow times of solutions.

3.2 Surface Tension

In Fig. 4, there are plots showing the surface tension of PVP/ AgNP solutions and PEG/ AgNP solutions against mass concentration of silver nanoparticles, where the solution surface

tension increases with increasing the concentration of silver nanoparticles, but the surface tension values of PEG solutions are greater than the surface tension values of PVP solutions [16, 17].

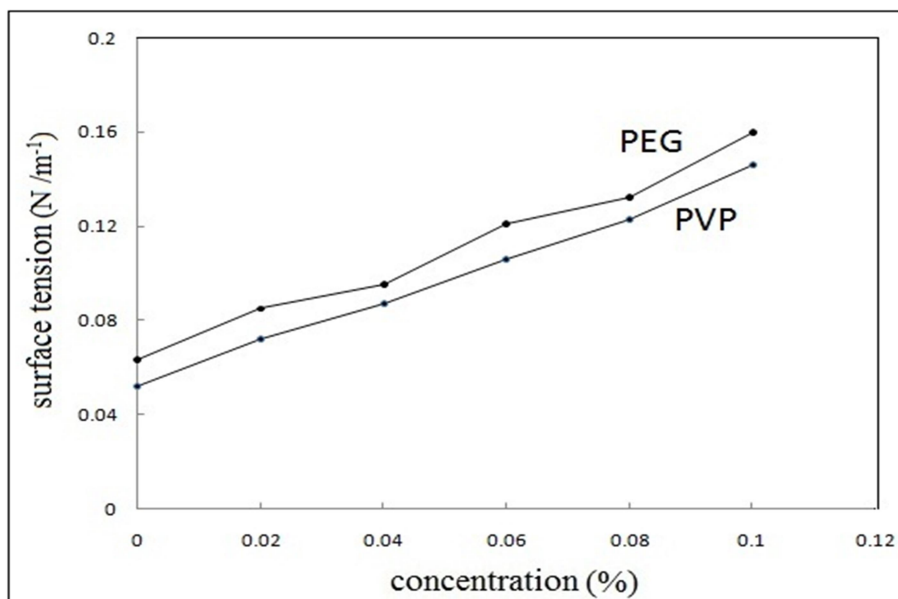


FIG. 4. Surface tension vs. concentration of Ag nanoparticles for PVP solutions and PEG solutions at 25°C.

Since the surface tension of the solutions increases with increasing the concentration of silver nanoparticles as shown in Fig. 4, the surface tension force and surface tension energy increase as shown in Fig. 5 and Fig. 6, respectively. As a result, a strong, cohesive force is exerted between the molecules, resulting in a

higher surface tension of the solution [18]. When the concentration increases, the mean spacing between the molecules and the nanoparticles reduces [18]. Hence, an attractive van der Waals force is employed over the electrostatic repulsion force between the molecules, which increases the surface tension of the solution [18].

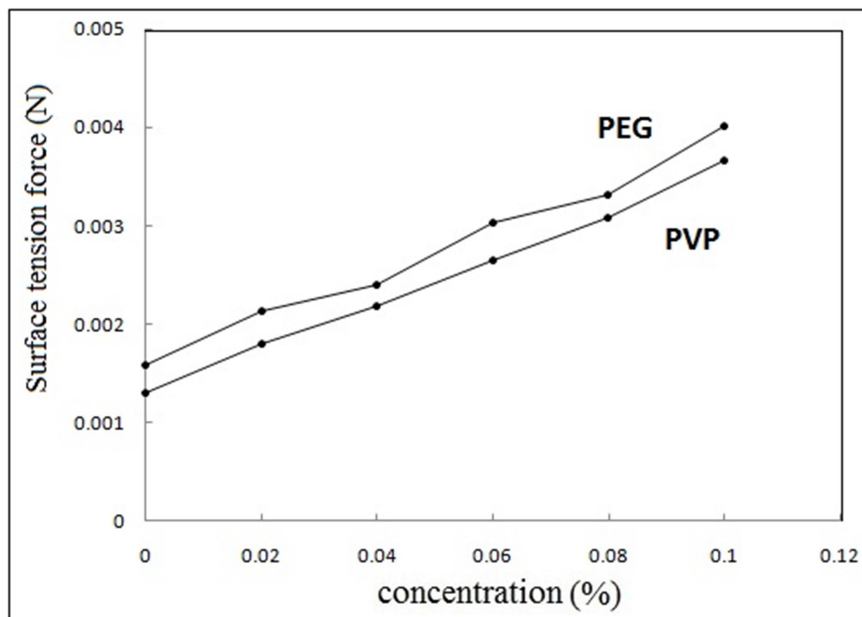


FIG. 5. Surface tension force vs. concentration of Ag nanoparticles for PVP solutions and PEG solutions at 25°C.

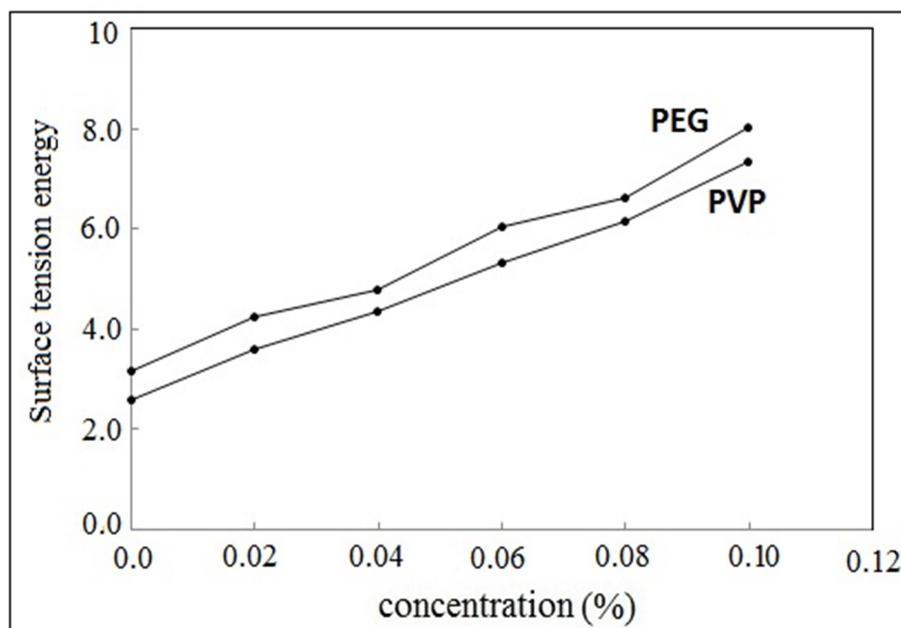


Fig. 6. Surface tension energy vs. concentration of Ag nanoparticles for PVP solutions and PEG solutions at 25°C.

4. Conclusion

The graphics of the viscosity of solutions indicate increased viscosity with increased concentration, but PVP/ AgNP solutions have viscosities higher than those of PEG / AgNP solutions, noting that viscosity is a significant parameter during the electrospinning process.

While the surface tension of PEG/AgNP solutions is greater than the surface tension of PVP/AgNP solutions, as the surface tension increases by increasing the concentration, van der Waals forces are exerted, which increases the surface free energy and results in the enhancement of surface tension. These properties can be used in medical, industrial applications and scientific studies.

References

- [1] Srirangam, G.M. and Parameswara Rao, K., *Rasayan J. Chem.*, 10 (1) (2017) 46.
- [2] Campillo, G.E., *IOP Conf. Series: Journal of Physics*, 850 (2017) 012023.
- [3] Tulika, D., Vidyalatha, K., Srijeeb, K. and Nandini, S., *Biomedicines*, 5(2) (2017) 19.
- [4] Kamaruddin et al., *IOP Conf. Series: Materials Science and Engineering*, 202 (2017) 012043.
- [5] Peter, L., Turecek, M., Bossard, J., Freddy, S. and Inge, A.I., *Journal of Pharmaceutical Sciences*, 105 (2016) 460.
- [6] Adel, H., Omran, A., Ali, H. and Al-Zahraa, A., *IOSR Journal of Applied Physics*, 8 (1) (I) (2016) 11.
- [7] Eman, A.A., MA Thesis, An-Najah National University, (2015), Nablus, Palestine.
- [8] Shinde, U.P., Chougule, S.S., Dighavkar, C.G., Jagadale, B.S. and Halwar, D.K. *International Journal of Chemical and Physical Sciences*, 4 (3) (2015) 1.
- [9] Amarieil, N. et al., *IOP Conf. Series: Materials Science and Engineering*, 209 (2017) 012092.
- [10] Nagla, A.G., *Scientific Journal of the Faculty of Education, Benghazi*, 1 (2015) 196.
- [11] El-Ashhab, F., Sheha, L., Abdalkhalek, M. and Hussein, A.K., *Journal of the Association of Arab Universities for Basic and Applied Sciences*, 14 (2013) 46.
- [12] Ulhas, B.H. and Asavari, S.H., *Indian Journal of Pharmaceutical Education and Research*, 49 (2) (2015) 134.
- [13] Gouiller, C., Guittonneau, A. and Jacquot, L., *Emergent Scientist*, 1 (2017) 1.
- [14] Zhao, Y., Wu, X., Wang, L., Xua, L. and Weib, S., *Applied Surface Science*, 258 (2012) 8867.
- [15] Hosnie, B. and Seyed, H.B., *Journal of Textiles and Polymers*, 3 (2) (2015) 64.
- [16] Tomer, M., David, A. and Rudi, P., *J. Chem. Phys.*, 142 (2015) 044702.
- [17] Zia, U., Noor, R., Farman, A., Nasir, M.K. and Hidayat, U., *Journal of Materials and Environmental Sciences*, 8 (3) (2017) 1029.
- [18] Bhuiyan, M.H.U., Saidur, R., Amalina, M.A., Mostafizur, R.M. and Islam, A., *Procedia-Engineering*, 105 (2015) 431.

Solutions of the Dirac Equation for the Quadratic Exponential-Manning-Rosen Potential plus Yukawa Potential within the Yukawa-like Tensor Interaction using the Framework of Nikiforov-Uvarov Formalism

Hitler Louis^a, Ita I. Benedict^{a*}, Nzeata I. Nelson^a, and Ike V. Chidinma^b

^aPhysical/Theoretical Chemistry Research Group, Department of Pure and Applied Chemistry, Faculty of Physical Sciences, University of Calabar, Calabar, CRS, Nigeria.

^bDepartment of Chemistry, Faculty of Physical Sciences, Nnamdi Azikiwe University, Awka, Anambra State, Nigeria.

Received on: 23/5/2018;

Accepted on: 25/9/2018

Abstract: Here, we solve the Dirac equation for the quadratic exponential-type potential plus Manning-Rosen potential including a Yukawa-like tensor potential with arbitrary spin-orbit coupling quantum number κ . In the framework of the spin and pseudo-spin (pspin) symmetry, we obtain the energy eigenvalue equation and the corresponding eigenfunctions in closed form by using the Nikiforov-Uvarov method. Also, special cases of the potential have been considered and their energy eigenvalues as well as their corresponding eigenfunctions were obtained for both relativistic and non-relativistic scope.

Keywords: Dirac equation, Quadratic exponential-type potential, Manning-Rosen potential, Spin and pseudospin symmetry, Nikiforov-Uvarov method.

Introduction

It has been scientifically established that the exact analytical eigenstate solution plays a significant role in quantum theory. It is generally and well known that the Dirac equation which describes the motion of a spin-1/2 particle has been extensively used in the study of precisely solvable problems in quantum mechanics. Over the past decade, spin and pseudo-spin symmetric solutions of the Dirac equation have been of great interest [1–3]. Dirac equation is the well-known equation that describes spin half particles in relativistic quantum mechanics [4]. The Dirac equation with vector $V(r)$ and scalar $S(r)$ potentials possesses pseudo-spin (pspin) symmetry when the difference ($[V(r) - S(r)] = 0$) and the sum $[V(r) + S(r)] = 0$ of the

potentials is constant, which means that $\frac{d}{dr} [V(r) - S(r)] = 0$ or $\frac{d}{dr} [V(r) + S(r)] = 0$ [4]. The specific investigation which attracted many authors to dedicate more attention to the solutions of the Dirac equation having spin and pseudo-spin symmetry such as Morse, Eckart, the modified Pöschl-Teller, the Manning-Rosen potentials and the symmetrical well potential [5–12] is the fact that in a relativistic domain, symmetries were utilized in the concept of deformation and superdeformation in nuclei, magnetic moment interpretation, as well as identical bonds.

Furthermore, in the non-relativistic domain, carrying out a helical unitary transformation to a single particle Hamiltonian maps the normal

state onto the pseudo state [13, 4]. In addition to the spin symmetry, the Dirac Hamiltonian also has a pseudo- $U(3)$ symmetry with vector and scalar harmonic oscillator potentials [14, 15].

Recently, we have studied the bound state solutions of Klein-Gordon, Dirac and Schrödinger equations using combined or mixed interacting potentials, some of which include Woods-Saxon plus Attractive Inversely Quadratic Potential (WSAIQP) [16], Manning-Rosen plus a class of Yukawa potential (MRCYP) [17], generalised Wood-Saxon plus Mie-type Potential (GWSMP) [18] and the Kratzer plus Reduced Pseudo-harmonic Oscillator Potential (KRPPOP) [19]. In this present work, we aim to solve the Dirac equation for Quadratic Exponential-type potential plus Manning-Rosen (QEMR) potential in the presence of spin and pseudo-spin symmetries and by including a Yukawa-like tensor potential [20-22].

The QEMR potential takes the following form:

$$V(r) = D \left[\frac{ae^{2\alpha r} + be^{\alpha r} + c}{(e^{\alpha r} - 1)^2} \right] - \left[\frac{Ae^{-\alpha r} + Be^{-2\alpha r}}{(1 - e^{-\alpha r})^2} \right] \quad (1a)$$

Thus, Eq. (1a) can be further expressed as:

$$V(r) = D \left[\frac{a + be^{-\alpha r} + ce^{-2\alpha r}}{(1 - e^{-\alpha r})^2} \right] - \left[\frac{Ae^{-\alpha r} + Be^{-2\alpha r}}{(1 - e^{-\alpha r})^2} \right] \quad (1b)$$

where α is the range of the potential, D , A and B are potential depths and a , b and c are adjustable parameters. This potential is known as an analytical potential model and is used for the vibrational energy of diatomic molecules.

The Yukawa potential, also known as the screened Coulomb potential in atomic physics and as the Debye-Huckel potential in plasma physics, is of vital importance in many areas of quantum mechanics. Initially, it was applied for modeling strong nucleon-nucleon interactions as a result of meson exchange in nuclear physics by Yukawa [23, 24]. It is also used to represent a screened Coulomb potential due to the cloud of electronic charges around the nucleus in atomic physics or to account for the shielding by outer charges of the Coulomb field experienced by an atomic electron in hydrogen plasma. The generic form of this potential is given by:

$$U(r) = -\frac{g}{r} V(r) \quad (1c)$$

where g is the strength of the potential and

$$V(r) = e^{-kr} \quad (1d)$$

This paper is organized as follows: In section 2, we briefly introduce the Dirac equation with scalar and vector potentials with arbitrary spin-orbit coupling quantum number κ including tensor interaction under spin and pspin symmetry limits. The Nikiforov-Uvarov (NU) method is presented in section 3. The energy eigenvalue equations and corresponding Eigenfunctions are obtained in section 4. In section 5, we discussed some individual cases of the potential. Finally, our conclusion is given in section 6.

2. The Dirac Equation with Tensor Coupling Potential

The Dirac equation for fermionic massive spin-1/2 particles moving in the field of an attractive scalar potential $S(r)$, a repulsive vector potential $V(r)$ and a tensor potential $U(r)$ (in units $\hbar = c = 1$) is:

$$[\vec{\alpha} \cdot \vec{p} + \beta(M + S(r)) - i\beta\vec{\alpha} \cdot \vec{r}U(r)]\psi(\vec{r}) = [E - V(r)]\psi(\vec{r}) \quad (2)$$

where E is the relativistic binding energy of the system, $\vec{p} = -i\vec{\nabla}$ is the three-dimensional momentum operator and M is the mass of the fermionic particle. $\vec{\alpha}$ and β are the 4×4 usual Dirac matrices given by:

$$\vec{\alpha} = \begin{pmatrix} 0 & \vec{\sigma} \\ \vec{\sigma} & 0 \end{pmatrix}, \quad \beta = \begin{pmatrix} I & 0 \\ 0 & -I \end{pmatrix}, \quad (3)$$

where I is the 2×2 unitary matrix and $\vec{\sigma}$ represents three vector spin matrices:

$$\sigma_1 = \begin{pmatrix} 0 & 1 \\ 1 & 0 \end{pmatrix}, \quad \sigma_2 = \begin{pmatrix} 0 & -i \\ i & 0 \end{pmatrix}, \quad \sigma_3 = \begin{pmatrix} 1 & 0 \\ 0 & -1 \end{pmatrix} \quad (4)$$

The eigenvalues of the spin-orbit coupling operator are $\kappa = \left(j + \frac{1}{2}\right) > 0$ and $\kappa = -\left(j + \frac{1}{2}\right) < 0$ for unaligned spin $j = l - \frac{1}{2}$ and aligned spin $j = l + \frac{1}{2}$, respectively. The set (H^2, K, J^2, J_z) can be taken as the complete set of conservative quantities with \vec{J} being the total angular momentum operator and $K = (\vec{\sigma} \cdot \vec{L} + 1)$ is the spin-orbit, where \vec{L} is the orbital angular momentum of the spherical nucleons that commutes with the Dirac Hamiltonian. Thus, the spinor wave functions can be classified according to their angular momentum j , the spin-orbit quantum number κ and the radial quantum number n . Hence, they can be written as follows:

$$\psi_{n,\kappa}(\vec{r}) = \begin{pmatrix} f_{n,\kappa}(\vec{r}) \\ g_{n,\kappa}(\vec{r}) \end{pmatrix} = \frac{1}{r} \begin{pmatrix} F_{n,\kappa}(r) & Y_{jm}^l(\theta, \varphi) \\ iG_{n,\kappa}(r) & Y_{jm}^{\hat{l}}(\theta, \varphi) \end{pmatrix}, \quad (5)$$

where $f_{n,\kappa}(\vec{r})$ is the upper (large) component and $g_{n,\kappa}(\vec{r})$ is the lower (small) component of the Dirac spinors. $Y_{jm}^l(\theta, \varphi)$ and $Y_{jm}^{\hat{l}}(\theta, \varphi)$ are spin and pspin spherical harmonics, respectively and m is the projection of the angular momentum on the z -axis. Substituting Eq. (5) into Eq. (2) and making use of the following relations:

$$(\vec{\sigma} \cdot \vec{A})(\vec{\sigma} \cdot \vec{B}) = \vec{A} \cdot \vec{B} + i\vec{\sigma} \cdot (\vec{A} \times \vec{B}), \quad (6a)$$

$$(\vec{\sigma} \cdot \vec{P}) = \vec{\sigma} \cdot \hat{r} \left(\hat{r} \cdot \vec{P} + i\frac{\vec{\sigma} \cdot \vec{L}}{r} \right), \quad (6b)$$

together with the properties:

$$(\vec{\sigma} \cdot \vec{L})Y_{jm}^{\hat{l}}(\theta, \varphi) = (\kappa - 1)Y_{jm}^{\hat{l}}(\theta, \varphi),$$

$$(\vec{\sigma} \cdot \vec{L})Y_{jm}^l(\theta, \varphi) = -(\kappa - 1)Y_{jm}^l(\theta, \varphi), \quad (7)$$

$$(\vec{\sigma} \cdot \hat{r})Y_{jm}^{\hat{l}}(\theta, \varphi) = -Y_{jm}^l(\theta, \varphi),$$

$$(\vec{\sigma} \cdot \hat{r})Y_{jm}^l(\theta, \varphi) = -Y_{jm}^{\hat{l}}(\theta, \varphi),$$

one obtains two coupled differential equations whose solutions are the upper and lower radial wave functions $F_{n,\kappa}(r)$ and $G_{n,\kappa}(r)$ as:

$$\left(\frac{d}{dr} + \frac{\kappa}{r} - U(r) \right) F_{n,\kappa}(r) = (M + E_{n\kappa} - \Delta(r))G_{n,\kappa}(r), \quad (8a)$$

$$\left(\frac{d}{dr} - \frac{\kappa}{r} + U(r) \right) G_{n,\kappa}(r) = (M - E_{n\kappa} + \Sigma(r))F_{n,\kappa}(r), \quad (8b)$$

where

$$\Delta(r) = V(r) - S(r), \quad (9a)$$

$$\Sigma(r) = V(r) + S(r). \quad (9b)$$

After eliminating $F_{n,\kappa}(r)$ and $G_{n,\kappa}(r)$ in Eq. (8), we obtain the following two Schrödinger-like differential equations for the upper and lower radial spinor components:

$$\left[\frac{d^2}{dr^2} - \frac{\kappa(\kappa+1)}{r^2} + \frac{2\kappa}{r}U(r) - \frac{dU(r)}{dr} - U^2(r) \right] F_{n,\kappa}(r) + \frac{\frac{d\Delta(r)}{dr}}{M+E_{n\kappa}-\Delta(r)} \left(\frac{d}{dr} + \frac{\kappa}{r} - U(r) \right) F_{n,\kappa}(r) = [(M + E_{n\kappa} - \Delta(r))(M - E_{n\kappa} + \Sigma(r))]F_{n,\kappa}(r) \quad (10)$$

$$\left[\frac{d^2}{dr^2} - \frac{\kappa(\kappa-1)}{r^2} + \frac{2\kappa}{r}U(r) + \frac{dU(r)}{dr} - U^2(r) \right] G_{n,\kappa}(r) + \frac{\frac{d\Sigma(r)}{dr}}{M-E_{n\kappa}+\Sigma(r)} \left(\frac{d}{dr} - \frac{\kappa}{r} + U(r) \right) G_{n,\kappa}(r) = [(M + E_{n\kappa} - \Delta(r))(M - E_{n\kappa} + \Sigma(r))]G_{n,\kappa}(r), \quad (11)$$

respectively, where $\kappa(\kappa - 1) = \hat{l}(\hat{l} + 1)$ and $\kappa(\kappa + 1) = l(l + 1)$.

The quantum number κ is related to the quantum numbers for spin symmetry l and pspin symmetry \hat{l} as:

$$\kappa = \begin{cases} -(l+1) = -(j + \frac{1}{2})(s_{1/2}, p_{3/2}, etc) \\ j = l + \frac{1}{2}, \text{aligned spin } (\kappa < 0), \\ +l = +(j + \frac{1}{2})(p_{1/2}, d_{3/2}, etc) \\ j = l - \frac{1}{2}, \text{unaligned spin } (\kappa > 0) \end{cases} \quad (12)$$

and the quasi-degenerate doublet structure can be expressed regarding a pseudo-spin angular momentum $\hat{s} = 1/2$ and pseudo-orbital angular momentum \hat{l} , which is defined as:

$$\kappa = \begin{cases} -\hat{l} = -(j + \frac{1}{2})(s_{1/2}, p_{3/2}, etc) \\ j = \hat{l} - \frac{1}{2}, \text{aligned spin } (\kappa < 0), \\ +(\hat{l} + 1) = +(j + \frac{1}{2})(d_{3/2}, f_{5/2}, etc) \\ j = \hat{l} + \frac{1}{2}, \text{unaligned spin } (\kappa > 0), \end{cases} \quad (13)$$

where $\kappa = \pm 1, \pm 2, \dots$. For example, $(1s_{1/2}, 0d_{3/2})$ and $(0p_{3/2}, 0f_{5/2})$ can be considered as pspin doublets.

2.1 Spin Symmetry Limit

In the spin symmetry limit, $\frac{d\Delta(r)}{dr} = 0$ or $\Delta(r) = C_s = \text{constant}$, with $\Sigma(r)$ taken as the QEMR potential Eq. (1b) and the Yukawa-like tensor potential; i.e.,

$$\Sigma(r) = V(r) = D \left[\frac{a+be^{-\alpha r}+ce^{-2\alpha r}}{(1-e^{-\alpha r})^2} \right] - \left[\frac{Ae^{-\alpha r}+Be^{-2\alpha r}}{(1-e^{-\alpha r})^2} \right], \quad (14)$$

$$U(r) = -\frac{H}{r}e^{-\alpha r} \quad (15)$$

Under this symmetry, Eq. (10) is recast in the simple form:

$$\left[\frac{d^2}{dr^2} - \frac{\kappa(\kappa+1)}{r^2} - \frac{2\kappa H}{r^2} - \frac{H}{r^2} - \frac{H^2}{r^2} \right] F_{n,\kappa}(r) = \left[\gamma \left(D \left[\frac{a+be^{-\alpha r} + ce^{-2\alpha r}}{(1-e^{-\alpha r})^2} \right] - \left[\frac{Ae^{-\alpha r} + Be^{-2\alpha r}}{(1-e^{-\alpha r})^2} \right] \right) + \beta^2 \right] F_{n,\kappa}(r) \quad (16a)$$

where $\kappa = l$ and $\kappa = -l - 1$ for $\kappa < 0$ and $\kappa > 0$, respectively. Also, $\gamma = (M + E_{n\kappa} - C_s)$ and $\beta^2 = (M - E_{n\kappa})(M + E_{n\kappa} - C_s)$. (16b)

2.2 Pseudo-Spin Symmetry Limit

Ginocchio [25] showed that there is a connection between pseudo-spin symmetry and near equality of the time component of the vector potential and the scalar potential, $V(r) \approx -S(r)$. After that, [26, 27] derived that if $\frac{d\Sigma(r)}{dr} = 0$ or $\Sigma(r) = C_{ps} = \text{constant}$, then pspin symmetry is exact in the Dirac equation. Here, we are taking $\Delta(r)$ as the QEMR potential Eq. (1) and the tensor potential as the Yukawa-like potential. Thus, Eq. (11) is recast in the simple form:

$$\left[\frac{d^2}{dr^2} - \frac{\kappa(\kappa-1)}{r^2} - \frac{2\kappa H}{r^2} + \frac{H}{r^2} - \frac{H^2}{r^2} \right] G_{n,\kappa}(r) = \left[\tilde{\gamma} \left(D \left[\frac{a+be^{-\alpha r} + ce^{-2\alpha r}}{(1-e^{-\alpha r})^2} \right] - \left[\frac{Ae^{-\alpha r} + Be^{-2\alpha r}}{(1-e^{-\alpha r})^2} \right] \right) + \tilde{\beta}^2 \right] G_{n,\kappa}(r) \quad (17a)$$

where $\kappa = -\tilde{l}$ and $\kappa = \tilde{l} + 1$ for $\kappa < 0$ and $\kappa > 0$, respectively. Also, $\tilde{\gamma} = (E_{n\kappa} - M - C_{ps})$ and $\tilde{\beta}^2 = (M + E_{n\kappa})(M - E_{n\kappa} + C_{ps})$. (17b)

In order to obtain the analytic solution, we use an approximation for the centrifugal term as [20]:

$$\frac{1}{r^2} = \frac{\alpha^2}{(1-e^{-\alpha r})^2} \quad (18)$$

Finally, for the solutions of Eq. (16) and Eq. (17) with the above approximation, we will employ the NU method, which is briefly introduced in the next section.

3. The Nikiforov–Uvarov Method

The NU method is based on the solutions of a generalized second-order linear differential equation with special orthogonal functions. The hyper-geometric NU method has shown its power in calculating the exact energy levels of all bound states for some solvable quantum systems [21-22].

$$\Psi_n''(s) + \frac{\tilde{\tau}(s)}{\sigma(s)} \Psi_n'(s) + \frac{\bar{\sigma}(s)}{\sigma^2(s)} \Psi_n(s) = 0 \quad (19)$$

where $\sigma(s)$ and $\bar{\sigma}(s)$ are polynomials at most second degree and $\tilde{\tau}(s)$ represents first-degree polynomials. The parametric generalization of the (NU) method is given by the generalized hyper-geometric-type equation:

$$\Psi_n''(s) + \frac{c_1 - c_2 s}{s(1 - c_3 s)} \Psi_n'(s) + \frac{1}{s^2(1 - c_3 s)^2} [-\epsilon_1 s^2 + \epsilon_2 s - \epsilon_3] \Psi_n(s) = 0. \quad (20)$$

Thus, Eq. (2) can be solved by comparing it with Eq. (3) and the following polynomials are obtained:

$$\begin{aligned} \tilde{\tau}(s) &= (c_1 - c_2 s), & \sigma(s) &= s(1 - c_3 s), \\ \bar{\sigma}(s) &= -\epsilon_1 s^2 + \epsilon_2 s - \epsilon_3. \end{aligned} \quad (21)$$

The parameters obtainable from Eq. (4) serve as essential tools for finding the energy eigenvalue and eigen functions. They satisfy the following sets of equations, respectively:

$$c_2 n - (2n + 1)c_5 + (2n + 1)(\sqrt{c_9} + c_3 \sqrt{c_8}) + n(n - 1)c_3 + c_7 + 2c_3 c_8 + 2\sqrt{c_8 c_9} = 0 \quad (22)$$

$$\begin{aligned} (c_2 - c_3)n + c_3 n^2 - (2n + 1)c_5 + \\ (2n + 1)(\sqrt{c_9} + c_3 \sqrt{c_8}) + c_7 + 2c_3 c_8 + \\ 2\sqrt{c_8 c_9} = 0 \end{aligned} \quad (23)$$

while the wave function is given as:

$$\begin{aligned} \Psi_n(s) = \\ N_{n,l} S^{c_{12}} (1 - c_3 s)^{-c_{12} - \frac{c_{13}}{c_3}} P_n(c_{10} - 1, \frac{c_{11}}{c_3} - c_{10} - 1) (1 - 2c_3 s) \end{aligned} \quad (24)$$

where

$$\begin{aligned} c_4 &= \frac{1}{2}(1 - c_1), \quad c_5 = \frac{1}{2}(c_2 - 2c_3), \quad c_6 = c_5^2 + \epsilon_1, \\ c_7 &= 2c_4 c_5 - \epsilon_2, \quad c_8 = c_4^2 + \epsilon_3, \\ c_9 &= c_3 c_7 + c_3^2 c_8 + c_6, \quad c_{10} = c_1 + 2c_4 + 2\sqrt{c_8}, \\ c_{11} &= c_2 - 2c_5 + 2(\sqrt{c_9} + c_3 \sqrt{c_8}) \\ c_{12} &= c_4 + \sqrt{c_8}, \quad c_{13} = c_5 - (\sqrt{c_9} + c_3 \sqrt{c_8}) \end{aligned} \quad (25)$$

and P_n represents the orthogonal polynomials.

4. Solutions to the Dirac Equation

We will now solve the Dirac equation with the QEPE potential and tensor potential by using the NU method.

4.1 The Symmetric Spin Case

To obtain the solution to Eq. (16), we employ the use of the transformation $s = e^{-\alpha r}$. Hence, we rewrite it as follows:

$$\frac{d^2 F_{n,\kappa}(s)}{ds^2} + \frac{(1-s)}{s(1-s)} \frac{dF_{n,\kappa}(s)}{ds} + \frac{1}{s^2(1-s)^2} \left[-\kappa(\kappa+1) - 2\kappa Hs - 2Hs + Hs^2 - H^2 s^2 - \frac{\gamma}{\alpha^2} (Da + Dbs + Dcs^2 + As + Bs^2) - \frac{\beta^2}{\alpha^2} (1-s)^2 \right] F_{n,\kappa}(s) = 0, \quad (26)$$

Eq. (26) is further simplified as:

$$\frac{d^2 F_{n,\kappa}(s)}{ds^2} + \frac{(1-s)}{s(1-s)} \frac{dF_{n,\kappa}(s)}{ds} + \frac{1}{s^2(1-s)^2} \left[-\left(\frac{\beta^2}{\alpha^2} + \frac{\gamma}{\alpha^2} Dc - \frac{\gamma}{\alpha^2} B + H^2 - H\right) s^2 + \left(\frac{2\beta^2}{\alpha^2} + \frac{\gamma}{\alpha^2} A - \frac{\gamma}{\alpha^2} Db - 2\kappa H - 2H\right) s - \left(\frac{\beta^2}{\alpha^2} + \frac{\gamma}{\alpha^2} Da + \kappa(\kappa+1)\right) \right] F_{n,\kappa}(s) = 0, \quad (27)$$

Comparing Eq. (27) with Eq. (20), we obtain:

$$c_1 = 1, \epsilon_1 = \frac{\beta^2}{\alpha^2} + \frac{\gamma}{\alpha^2} Dc - \frac{\gamma}{\alpha^2} B + H^2 - H$$

$$c_2 = 1, \epsilon_2 = \frac{2\beta^2}{\alpha^2} + \frac{\gamma}{\alpha^2} A - \frac{\gamma}{\alpha^2} Db - 2\kappa H - 2H \quad (28)$$

$$c_3 = 1, \epsilon_3 = \frac{\beta^2}{\alpha^2} + \frac{\gamma}{\alpha^2} Da + \kappa(\kappa+1)$$

and from Eq. (25), we further obtain:

$$c_4 = 0, c_5 = -\frac{1}{2},$$

$$c_6 = \frac{1}{4} + \frac{\beta^2}{\alpha^2} + \frac{\gamma}{\alpha^2} Dc - \frac{\gamma}{\alpha^2} B + H^2 - H, c_7 = -\left(\frac{2\beta^2}{\alpha^2} + \frac{\gamma}{\alpha^2} A - \frac{\gamma}{\alpha^2} Db - 2\kappa H - 2H\right),$$

$$c_8 = \frac{\beta^2}{\alpha^2} + \frac{\gamma}{\alpha^2} Da + \kappa(\kappa+1), c_9 = \left(\eta_\kappa - \frac{1}{2}\right)^2 + \frac{\gamma}{\alpha^2} D(a+b+c) - \frac{\gamma}{\alpha^2} (A+B), \text{ where } \eta_\kappa = \kappa + H + 1,$$

$$c_{10} = 1 + 2\sqrt{\frac{\beta^2}{\alpha^2} + \frac{\gamma}{\alpha^2} Da + \kappa(\kappa+1)},$$

$$c_{11} = 2 + 2\left(\sqrt{\left(\eta_\kappa - \frac{1}{2}\right)^2 + \frac{\gamma}{\alpha^2} D(a+b+c) - \frac{\gamma}{\alpha^2} (A+B)} + \sqrt{\frac{\beta^2}{\alpha^2} + \frac{\gamma}{\alpha^2} Da + \kappa(\kappa+1)}\right), \quad (29)$$

$$c_{12} = \sqrt{\frac{\beta^2}{\alpha^2} + \frac{\gamma}{\alpha^2} Da + \kappa(\kappa+1)},$$

$$c_{13} = -\frac{1}{2} \sqrt{\left(\sqrt{\left(\eta_\kappa - \frac{1}{2}\right)^2 + \frac{\gamma}{\alpha^2} D(a+b+c) - \frac{\gamma}{\alpha^2} (A+B)} + \sqrt{\frac{\beta^2}{\alpha^2} + \frac{\gamma}{\alpha^2} Da + \kappa(\kappa+1)}\right)}$$

Also, the energy eigenvalue equation can be obtained by using Eq. (23) as follows:

$$\left(n + \frac{1}{2} + \sqrt{\left(\eta_\kappa - \frac{1}{2}\right)^2 + \frac{\gamma}{\alpha^2} D(a+b+c) - \frac{\gamma}{\alpha^2} (A+B)} + \sqrt{\frac{\beta^2}{\alpha^2} + \frac{\gamma}{\alpha^2} Da + \kappa(\kappa+1)}\right)^2 = \frac{\beta^2}{\alpha^2} + \frac{\gamma}{\alpha^2} Dc - \frac{\gamma}{\alpha^2} B + H^2 - H. \quad (30)$$

By substituting the explicit forms of γ and β^2 after Eq. (16) into Eq. (30), one can readily obtain the closed form for the energy formula as:

$$\left(n + \frac{1}{2} + \sqrt{\left(\eta_\kappa - \frac{1}{2}\right)^2 + \frac{D(a+b+c)}{\alpha^2} (M + E_{n\kappa} - C_s) - \frac{(A+B)}{\alpha^2} (M + E_{n\kappa} - C_s)} + \sqrt{\frac{1}{\alpha^2} ((M - E_{n\kappa})(M + E_{n\kappa} - C_s)) + \frac{Da}{\alpha^2} (M + E_{n\kappa} - C_s) + \kappa(\kappa+1)}\right)^2 = \frac{1}{\alpha^2} ((M - E_{n\kappa})(M + E_{n\kappa} - C_s)) + \frac{Dc}{\alpha^2} (M + E_{n\kappa} - C_s) - \frac{B}{\alpha^2} (M + E_{n\kappa} - C_s) + H^2 - H. \quad (31)$$

On the other hand, to find the corresponding wave functions, referring to Eq. (29) and Eq. (24), we obtain the upper component of the Dirac spinor from Eq. (24) as:

$$F_{n,\kappa}(s) = B_{n,\kappa} S \sqrt{\frac{\beta^2}{\alpha^2} + \frac{\gamma}{\alpha^2} Da + \kappa(\kappa+1)} \left(1 - s\right)^{\frac{1}{2} + \sqrt{\left(\eta_\kappa - \frac{1}{2}\right)^2 + \frac{\gamma}{\alpha^2} D(a+b+c) - \frac{\gamma}{\alpha^2} (A+B)}} \left(\frac{2\sqrt{\frac{\beta^2}{\alpha^2} + \frac{\gamma}{\alpha^2} Da + \kappa(\kappa+1)}}{\sqrt{\left(\eta_\kappa - \frac{1}{2}\right)^2 + \frac{\gamma}{\alpha^2} D(a+b+c) - \frac{\gamma}{\alpha^2} (A+B)}}\right) P_n \left(\frac{\sqrt{\left(\eta_\kappa - \frac{1}{2}\right)^2 + \frac{\gamma}{\alpha^2} D(a+b+c) - \frac{\gamma}{\alpha^2} (A+B)}}{\sqrt{\frac{\beta^2}{\alpha^2} + \frac{\gamma}{\alpha^2} Da + \kappa(\kappa+1)}}\right) (1 - 2s) \quad (32)$$

where $B_{n,\kappa}$ is the normalization constant. The lower component of the Dirac spinor can be calculated from Eq. (8a):

$$G_{n,\kappa}(r) = \frac{1}{(M+E_{n\kappa}-C_s)} \left(\frac{d}{dr} + \frac{\kappa}{r} - U(r) \right) F_{n,\kappa}(r) \quad (33)$$

where $E_{n\kappa} \neq -M + C_s$.

4.2 The Pseudo-Spin Symmetric Case

To avoid repetition in the solution of Eq. (17), we follow the same procedure explained in section 4.1 and hence obtain the following energy eigenvalue equation:

$$\left(n + \frac{1}{2} + \sqrt{\left(\Lambda_\kappa - \frac{1}{2} \right)^2 + \frac{\tilde{\gamma}}{\alpha^2} D(a+b+c) - \frac{\tilde{\gamma}}{\alpha^2} (A+B) + \frac{\tilde{\beta}^2}{\alpha^2} + \frac{\tilde{\gamma}}{\alpha^2} Da + \kappa(\kappa-1)} \right)^2 = \frac{\tilde{\beta}^2}{\alpha^2} + \frac{\tilde{\gamma}}{\alpha^2} Dc + \frac{\tilde{\gamma}}{\alpha^2} A + H^2 + H. \quad (34)$$

By substituting the explicit forms of $\tilde{\gamma}$ and $\tilde{\beta}^2$ after Eq. (17b) into Eq. (34), one can readily obtain the closed form for the energy formula as:

$$\left(n + \frac{1}{2} + \sqrt{\left(\Lambda_\kappa - \frac{1}{2} \right)^2 + \frac{D(a+b+c)}{\alpha^2} (E_{n\kappa} - M - C_{ps}) + \frac{B}{\alpha^2} (E_{n\kappa} - M - C_{ps})} \right)^2 = \frac{1}{\alpha^2} \left((M + E_{n\kappa})(M - E_{n\kappa} + C_{ps}) \right) + \frac{Da}{\alpha^2} (E_{n\kappa} - M - C_{ps}) + \kappa(\kappa-1) = \frac{1}{\alpha^2} \left((M + E_{n\kappa})(M - E_{n\kappa} + C_{ps}) \right) + \frac{Dc}{\alpha^2} (E_{n\kappa} - M - C_{ps}) - \frac{B}{\alpha^2} (E_{n\kappa} - M - C_{ps}) + H^2 + H \quad (35)$$

and the corresponding wave functions for the upper Dirac spinor as:

$$G_{n,\kappa}(r) = \tilde{B}_{n,\kappa} S \sqrt{\frac{\tilde{\beta}^2}{\alpha^2} + \frac{\tilde{\gamma}}{\alpha^2} Da + \kappa(\kappa-1)} \left(1 - S \right)^{\frac{1}{2}} \sqrt{\left(\Lambda_\kappa - \frac{1}{2} \right)^2 + \frac{\tilde{\gamma}}{\alpha^2} D(a+b+c) - \frac{\tilde{\gamma}}{\alpha^2} (A+B)} \left(\frac{2\sqrt{\frac{\tilde{\beta}^2}{\alpha^2} + \frac{\tilde{\gamma}}{\alpha^2} Da + \kappa(\kappa-1)}}{\sqrt{\left(\Lambda_\kappa - \frac{1}{2} \right)^2 + \frac{\tilde{\gamma}}{\alpha^2} D(a+b+c) - \frac{\tilde{\gamma}}{\alpha^2} (A+B)}} \right) \left(1 - 2S \right) \quad (36)$$

where $\Lambda_\kappa = \kappa + H$ and $\tilde{B}_{n,\kappa}$ is the normalization constant. Finally, the upper-spinor component of

the Dirac equation can be obtained *via* Eq. (8b) as:

$$F_{n,\kappa}(r) = \frac{1}{(M-E_{n\kappa}+C_{ps})} \left(\frac{d}{dr} - \frac{\kappa}{r} + U(r) \right) G_{n,\kappa}(r) \quad (37)$$

where $E_{n\kappa} \neq M + C_{ps}$.

5. Discussion

In this section, we are going to study some individual cases of the energy eigenvalues given by Eq. (31) and Eq. (35) for the spin and pseudo-spin symmetries, respectively.

Case 1: If one set $C_s = 0, C_{ps} = 0, A = B = 0$ in Eq. (31) and Eq. (35), we obtain the energy equation of quadratic exponential-type potential for spin and pseudo-spin symmetric Dirac theory, respectively as:

$$\left(n + \frac{1}{2} + \sqrt{\left(\eta_\kappa - \frac{1}{2} \right)^2 + \frac{D(a+b+c)}{\alpha^2} (M + E_{n\kappa})} \right)^2 = \frac{1}{\alpha^2} \left((M - E_{n\kappa})(M + E_{n\kappa}) \right) + \frac{Da}{\alpha^2} (M + E_{n\kappa}) + \kappa(\kappa+1) = \frac{1}{\alpha^2} \left((M - E_{n\kappa})(M + E_{n\kappa}) \right) + \frac{Dc}{\alpha^2} (M + E_{n\kappa}) + H^2 - H \quad (38)$$

and

$$\left(n + \frac{1}{2} + \sqrt{\left(\Lambda_\kappa - \frac{1}{2} \right)^2 + \frac{D(a+b+c)}{\alpha^2} (E_{n\kappa} - M)} \right)^2 = \frac{1}{\alpha^2} \left((M + E_{n\kappa})(M - E_{n\kappa}) \right) + \frac{Da}{\alpha^2} (E_{n\kappa} - M) + \kappa(\kappa-1) = \frac{1}{\alpha^2} \left((M + E_{n\kappa})(M - E_{n\kappa}) \right) + \frac{Dc}{\alpha^2} (E_{n\kappa} - M) + H^2 + H. \quad (39)$$

Eq. (38) and Eq. (39) are parallel to Eq. (45) of ref. [31]

Case 2: If one set $C_s = 0, C_{ps} = 0, D = 0$ in Eq. (31) and Eq. (35), we obtain the energy equation of Manning-Rosen potential for spin and pseudo-spin symmetric Dirac theory, respectively as:

$$\left(n + \frac{1}{2} + \sqrt{\left(\eta_\kappa - \frac{1}{2} \right)^2 - \frac{A}{\alpha^2} (M + E_{n\kappa}) - \frac{B}{\alpha^2} (M + E_{n\kappa}) + \frac{1}{\alpha^2} \left((M - E_{n\kappa})(M + E_{n\kappa}) \right) + \kappa(\kappa + 1)} \right)^2 = \frac{1}{\alpha^2} \left((M - E_{n\kappa})(M + E_{n\kappa}) \right) - \frac{B}{\alpha^2} (M + E_{n\kappa}) + H^2 - H \quad (40)$$

and

$$\left(n + \frac{1}{2} + \sqrt{\left(\Lambda_\kappa - \frac{1}{2} \right)^2 - \frac{A}{\alpha^2} (E_{n\kappa} - M) - \frac{B}{\alpha^2} (E_{n\kappa} - M) + \frac{1}{\alpha^2} \left((M + E_{n\kappa})(M - E_{n\kappa}) \right) + \kappa(\kappa - 1)} \right)^2 = \frac{1}{\alpha^2} (M + E_{n\kappa})(M - E_{n\kappa}) - \frac{B}{\alpha^2} (E_{n\kappa} - M) + H^2 + H. \quad (41)$$

Case 3: If one set $C_s = 0, C_{ps} = 0, A = B = 0, b = 1, c = -1$ and $D = -D$, Eq. (1b) reduces to the Hulthen potential:

$$V(r) = -D \frac{e^{-\alpha r}}{1 - e^{-\alpha r}}. \quad (42)$$

From Eq. (31) and Eq. (35), if $C_s = 0, C_{ps} = 0$, we obtain the energy equation of Hulthen potential for spin and pseudo-spin symmetric Dirac theory, respectively as:

$$\left(n + \eta_\kappa + \sqrt{\frac{1}{\alpha^2} \left((M - E_{n\kappa})(M + E_{n\kappa}) \right) + \kappa(\kappa + 1)} \right)^2 = \frac{1}{\alpha^2} \left((M - E_{n\kappa})(M + E_{n\kappa}) \right) + \frac{D}{\alpha^2} (M + E_{n\kappa}) + H^2 - H \quad (43)$$

and

$$\left(n + \Lambda_\kappa + \sqrt{\frac{1}{\alpha^2} \left((M + E_{n\kappa})(M - E_{n\kappa}) \right) + \kappa(\kappa - 1)} \right)^2 = \frac{1}{\alpha^2} \left((M + E_{n\kappa})(M - E_{n\kappa}) \right) + \frac{D}{\alpha^2} (E_{n\kappa} - M) + H^2 + H. \quad (44)$$

Eq. (43) and Eq. (44) are similar to the energy eigenvalue Eq. (26) of ref. [32] which represents the pseudo-spin and spin symmetry solutions

obtained for the Hulthen potential within a Yukawa-type tensor interaction.

Case 4: If $A = B = 0, a = 1, b = -2(1 + \delta), c = (1 + \delta)^2$ and $\delta = e^{\alpha r} - 1$, Eq. (1b) reduces to the generalized Morse potential:

$$V(r) = D \left[\frac{1 - 2(1 + \delta)e^{-\alpha r} + e^{-2\alpha r}}{(1 - e^{-\alpha r})^2} \right] \quad (45)$$

From Eq. (31) and Eq. (35), if $C_s = 0, C_{ps} = 0$, we obtain the energy equation generalized Morse potential for spin and pseudo-spin symmetric Dirac theory, respectively as:

$$\left(n + \frac{1}{2} + \sqrt{\left(\eta_\kappa - \frac{1}{2} \right)^2 + \frac{D\delta^2}{\alpha^2} (M + E_{n\kappa}) + \frac{1}{\alpha^2} \left((M - E_{n\kappa})(M + E_{n\kappa}) \right) + \frac{D}{\alpha^2} (M + E_{n\kappa}) + \kappa(\kappa + 1)} \right)^2 = \frac{1}{\alpha^2} \left((M - E_{n\kappa})(M + E_{n\kappa}) \right) + \frac{D(1 + \delta)^2}{\alpha^2} (M + E_{n\kappa}) + H^2 + H \quad (46)$$

and

$$\left(n + \frac{1}{2} + \sqrt{\left(\Lambda_\kappa - \frac{1}{2} \right)^2 + \frac{D\delta^2}{\alpha^2} (E_{n\kappa} - M) + \frac{1}{\alpha^2} \left((M + E_{n\kappa})(M - E_{n\kappa}) \right) + \frac{D}{\alpha^2} (E_{n\kappa} - M) + \kappa(\kappa - 1)} \right)^2 = \frac{1}{\alpha^2} \left((M + E_{n\kappa})(M - E_{n\kappa}) \right) + \frac{D(1 + \delta)^2}{\alpha^2} (E_{n\kappa} - M) + H^2 - H. \quad (47)$$

In the same manner, Eq. (46) and Eq. (47) are comparable to Eq. (31) of ref. [33] on the bound-state solutions for the Morse potential.

Case 5: Let us now discuss the relativistic limit of the energy eigenvalues and wave functions of our solutions. If we take $C_s = 0, H = 0, \kappa \rightarrow l$ and put $S(r) = V(r) = \Sigma(r)$, the non-relativistic limit of energy Eq. (31) and wave function (32) under the following appropriate transformations $M + E_{n\kappa} \rightarrow \frac{2\mu}{\hbar^2}$, and $M - E_{n\kappa} \rightarrow -E_{nl}$ become:

$$E_{nl} = -\frac{\alpha^2 \hbar^2}{2\mu} \left\{ \left[\frac{2l(l+1) + \frac{2\mu D}{\alpha^2 \hbar^2}(2a+b) - \frac{2\mu}{\alpha^2 \hbar^2} + (n^2 + n + \frac{1}{2}) + (2n+1)\sqrt{(l+\frac{1}{2})^2 + \frac{2\mu}{\alpha^2 \hbar^2}(a+b+c) - \frac{2\mu}{\alpha^2 \hbar^2}(A+B)}}{(2n+1)+2\sqrt{(l+\frac{1}{2})^2 + \frac{2\mu D}{\alpha^2 \hbar^2}(a+b+c) - \frac{2\mu}{\alpha^2 \hbar^2}(A+B)}} \right]^2 - \frac{2\mu Da}{\alpha^2 \hbar^2} - l(l+1) \right\} \quad (48)$$

and the associated wave functions $F_{n\kappa}(s) \rightarrow R_{n,l}(s)$ are:

$$R_{n,l}(s) = N_{n,l} s^{U/2} (1-s)^{(V-1)/2} P_n^{(U,V)}(1-2s), \quad (49)$$

where $U = 2\sqrt{\frac{2\mu E_{nl}}{\alpha^2 \hbar^2} + \frac{2\mu Da}{\alpha^2 \hbar^2} + l(l+1)}$ and

$$V = 2\sqrt{\left(l + \frac{1}{2}\right)^2 + \frac{2\mu D}{\alpha^2 \hbar^2}(a+b+c) - \frac{2\mu}{\alpha^2 \hbar^2}(A+B)} \quad (50)$$

Case 6: If one $A = B = 0$ in Eq. (48), we obtain the energy equation of quadratic exponential-type potential in the non-relativistic limit as:

$$E_{nl} = -\frac{\alpha^2 \hbar^2}{2\mu} \left\{ \left[\frac{2l(l+1) + \frac{2\mu D}{\alpha^2 \hbar^2}(2a+b) + (n^2 + n + \frac{1}{2}) + (2n+1)\sqrt{(l+\frac{1}{2})^2 + \frac{2\mu D}{\alpha^2 \hbar^2}(a+b+c)}}{(2n+1)+2\sqrt{(l+\frac{1}{2})^2 + \frac{2\mu D}{\alpha^2 \hbar^2}(a+b+c)}} \right]^2 - \frac{2\mu Da}{\alpha^2 \hbar^2} - l(l+1) \right\}. \quad (51)$$

Case 7: If $D = 0$ in Eq. (48), we obtain the energy equation of the Manning-Rosen potential in the non-relativistic limit as:

$$E_{nl} = -\frac{\alpha^2 \hbar^2}{2\mu} \left\{ \left[\frac{2l(l+1) - \frac{2\mu A}{\alpha^2 \hbar^2} + (n^2 + n + \frac{1}{2}) + (2n+1)\sqrt{(l+\frac{1}{2})^2 - \frac{2\mu}{\alpha^2 \hbar^2}(A+B)}}{(2n+1)+2\sqrt{(l+\frac{1}{2})^2 - \frac{2\mu}{\alpha^2 \hbar^2}(A+B)}} \right]^2 - l(l+1) \right\}. \quad (52)$$

Case 8: If $A = B = 0, a = 0, b = 1, c = -1$ and $D = -D$, Eq. (1b) reduces to the Hulthen potential:

$$V(r) = -D \frac{e^{-\alpha r}}{1 - e^{-\alpha r}}. \quad (53)$$

From Eq. (48), we obtain the energy equation of Hulthen potential for a spin and pseudo-spin symmetric Dirac theory, respectively as:

$$E_{nl} = -\frac{\alpha^2 \hbar^2}{2\mu} \left\{ \left[\frac{2l(l+1) - \frac{2\mu D}{\alpha^2 \hbar^2} + (n^2 + n + \frac{1}{2}) + (2n+1)\sqrt{(l+\frac{1}{2})^2}}{(2n+1)+2\sqrt{(l+\frac{1}{2})^2}} \right]^2 - l(l+1) \right\}. \quad (54)$$

Case 9: If $A = B = 0, a = 1, b = -2(1 + \delta), c = (1 + \delta)^2$ and $\delta = e^{\alpha r_e} - 1$, Eq. (1b) reduces to the generalized Morse potential:

$$V(r) = D \left[\frac{1 - 2(1 + \delta)e^{-\alpha r} + e^{-2\alpha r}}{(1 - e^{-\alpha r})^2} \right]. \quad (55)$$

From Eq. (48), we obtain the energy equation of generalized Morse potential as:

$$E_{nl} = -\frac{\alpha^2 \hbar^2}{2\mu} \left\{ \left[\frac{2l(l+1) - \frac{2\mu D \delta}{\alpha^2 \hbar^2} + (n^2 + n + \frac{1}{2}) + (2n+1)\sqrt{(l+\frac{1}{2})^2 + \frac{2\mu D \delta^2}{\alpha^2 \hbar^2}}}{(2n+1)+2\sqrt{(l+\frac{1}{2})^2 + \frac{2\mu D \delta^2}{\alpha^2 \hbar^2}}} \right]^2 - \frac{2\mu D}{\alpha^2 \hbar^2} - l(l+1) \right\}. \quad (56)$$

6. Conclusion

We solve the Dirac equation for the quadratic exponential-type potential plus Manning-Rosen potential including a Yukawa-like tensor potential with arbitrary spin-orbit coupling quantum number κ using the Nikiforov-Uvarov (NU) method. The energy spectrum of the Manning-Rosen potential obtained in Eq. (52) is parallel to the eigenstate solution obtained in Eq. (45) of ref. [34] and both describe the potential

in the non-relativistic limit. Similarly, the energy equation of Hulthen potential for a spin and pseudo-spin symmetric Dirac theory obtained in Eq. (54) is comparable to the Dirac solutions evaluated in Eq. (48) of ref. [20]. The various eigenstate energy solutions obtained are in concordance order and hence can find a useful application in atomic spectroscopy and astrophysical sciences [35].

References

- [1] Hecht, K.T. and Adler, A., Nucl. Phys. A, 137 (1969) 129.
- [2] Arima, A., Harvey, M. and Shimizu, K., Phys. Lett. B, 30 (8) (1969) 517.
- [3] Ginocchio, J.N., Phys. Rev. Lett., 78 (1997) 436.
- [4] Arda, A. and Sever, R., Z. Naturforsch., 69a (2014) 163.
- [5] Zhang, L.H., Li, X.P. and Jia, C.S., Phys. Scr., 80 (2009) 35003.
- [6] Wei, G.F. and Dong, S.H., Phys. Lett. A, 373 (2009) 2428.
- [7] Wei, G.F. and Dong, S.H., Phys. Scr., 81 (2010) 35009.
- [8] Wei, G.F. and Dong, S.H., Phys. Lett. A, 373 (2008) 49.
- [9] Wei, G.F. and Dong, S.H., Phys. Lett. B, 686 (2010) 288.
- [10] Wei, G.F. and Dong, S.H., EPL, 87 (2009) 40004.
- [11] Zhang, L.H., Li, X.P. and Jia, C.S., Phys. Lett. A, 372 (2008) 2201.
- [12] Xu, Y., He, S. and Jia, C.S., J. Phys. A, 41 (2008) 255302.
- [13] Blokhin, A.L., Bahri, C. and Draayer, J.P., Phys. Rev. Lett., 74 (1995) 4149.
- [14] Jia, C.S., Guo, P. and Peng, X.L., J. Phys. A, 39 (2006) 7737.
- [15] Xu, Y. and Zhu, S.J., Nucl. Phys. A, 768 (2006) 161.
- [16] Ita, B.I., Louis, H., Magu, T.O. and Nzeata-Ibe, N.A., World Scientific News, 74 (2017) 280.
- [17] Ita, B.I., Louis, H., Magu, T.O. and Nzeata-Ibe, N.A., World Scientific News, 70 (2017) 312.
- [18] Ita, B.I., Louis, H., Magu, T.O. and Nzeata-Ibe, N.A., J. Chem. Soc. Nigeria, 41 (2) (2017) 21.
- [19] Ita, B.I., Louis, H., Magu, T.O. and Nzeata-Ibe, N.A., Journal of Nigerian Association of Mathematical Physics, 36 (2) (2016) 199.
- [20] Louis, H., Ita, B.I., Amos, P.I., Akakuru, O.U., Orosun, M.M., Nzeata-Ibe, N.A. and Philip, M., IJCPS, 7 (1) (2018) 33.
- [21] Ita, B.I., Louis, H., Akakuru, O.U., Magu, T.O., Joseph, I., Tchoua, P., Amos, P.I., Effiong, I. and Nzeata, N.A., Journal of Quantum Information Science, 8 (2018) 24.
- [22] Tezcan, C. and Sever, R., Int. J. Theor. Phys., 48 (2009) 337.
- [23] Yukawa, H., Proceedings of the Physico-Mathematical Society of Japan, 17 (1935) 48.
- [24] Yukawa, H., Proceedings of the Physico-Mathematical Society of Japan, 19 (1937) 1084.
- [25] Ginocchio, J.N., Phys. Rev. Lett., 78 (1997) 436.
- [26] Ginocchio, J.N., Nucl. Phys. A, 654 (1999) 663c.
- [27] Ginocchio, J.N., Phys. Rep., 315 (1999) 231.
- [28] Onate, C.A. and Ojonubah, J.O., J. Theor. Appl. Phys., 10 (1) (2015) 21.
- [29] Hamzavi, M., Ikhdair, S.M. and Ita, B.I., Physica Scripta, 85 (4) (2012) 7.

- [30] Ma, Z.Q., Gonzalez-Cisneros, A., Xu, B.W. and Dong, S.H., *Phys. Lett. A*, 371 (2007) 180.
- [31] Peña, J.J., Morales, J. and García-Ravelo, J., *Journal of Mathematical Physics*, 58 (4) (2017) 043501.
- [32] Aydoğdu, O., Maghsoodi, E. and Hassanabadi, H., *Chinese Physics B*, 22 (1) (2013) 010302.
- [33] Zhang, P., Long, H.-C. and Jia, C.-S., *The European Physical Journal Plus*, 131 (4) (2016) 117.
- [34] Louis, H., Iserom, I.B., Odey, M.T., Ozioma, A.U., Nelson, N.-I., Alexander, I.I. and Okon, E.C., *International Journal of Chemistry*, 10 (3) (2018) 99.
- [35] Oyewumi, K.J. and Sen, K.D., *Journal of Mathematical Chemistry*, 50 (5) (2012) 1039.

Basic Concepts and Development of Dry Deposition Modelling

Tareq Hussein, Safa' Ibrahim and Sawsan Malek

Department of Physics, The University of Jordan, Amman 11942, Jordan.

Received on: 31/1/2018;

Accepted on: 3/10/2018

Abstract: Dry deposition is the primary mechanism by which suspended particles are transported from gas onto surfaces. Prediction of this transport rate represented by the dry deposition velocity (V_d) is needed in a vast range of applications, such as atmospheric climate and air quality models, industrial processes, nanomaterials, clean rooms, building engineering, particle losses inside sampling lines, health effect of atmospheric particles and pharmaceuticals. The particle transport rate towards the surface depends on many factors: above-surface air flow and fluid characteristics, physical characteristics of the particles and surface properties. Although dry deposition models have been improved significantly, they still need to be further developed to improve the model accuracy and include weak mechanisms of particle transport. In general, a dry deposition model incorporates Fickian diffusion (Brownian and Eddy) and gravitational settling. Turbophoresis was introduced to compensate for the enhancement in V_d as a result of inhomogeneous turbulent mixing. In real-life conditions, electrophoresis and thermophoresis are not strong enough mechanisms to be included in model calculations, but for some applications (such as air purifiers), these transport mechanisms are very important to be considered in model formulation. Magnetophoresis, which is a very weak mechanism in real-life conditions, can be enhanced for certain industrial applications. In general, deposition surfaces are rarely smooth and researchers have put great efforts to describe surface roughness in dry deposition models. After all, a unified dry deposition formulation is needed to be developed/ improved in the future to make dry deposition prediction and calculations easier and more accurate. In this paper, we present the basic concepts that have been developed and implemented in dry deposition models and illustrate the effect of different processes on the transport rate of suspended particles in the fluids towards surfaces. As a benchmark for the accuracy of the current dry deposition modelling, we present a comparison between model calculations and experimental data-bases found in the literature.

Keywords: Fickian diffusion, Gravitational settling, Turbophoresis, Electrophoresis, Thermophoresis, Magnetophoresis.

1. Introduction

Particle deposition onto surfaces is an important phenomenon from many aspects. It has a wide of range applications, such as environmental, industrial, medical, ... etc. The effectiveness of the deposition mechanism is usually represented by the dry deposition velocity (V_d), which is derived from the particle flux towards the surface across the so-called concentration boundary layer [1–4]. Above any type of surface, V_d depends on the physical

properties of the deposited particle (such as particle size, shape, density, ... etc.), fluid and air flow characteristics inside the concentration boundary layer and surface properties [5–14]. Detailed calculation of these features is not possible in practical applications, which calls for simple mathematical formulae for V_d [2].

The main challenge in calculating V_d , especially deriving a simple and accurate formula, is to find appropriate values for the

boundary-layer parameters (y_0 and y_{cbl}), which are depicted in Fig. 1. For a smooth surface, there is a well-known dependence of V_d on the particle size [2, 3, 14–20]. Above a rough surface, y_0 and y_{cbl} are shifted away from the

surface, so that V_d is different from that above a smooth surface (Fig. 2). Accounting for surface roughness in model calculations is complicated, but it is extremely important.

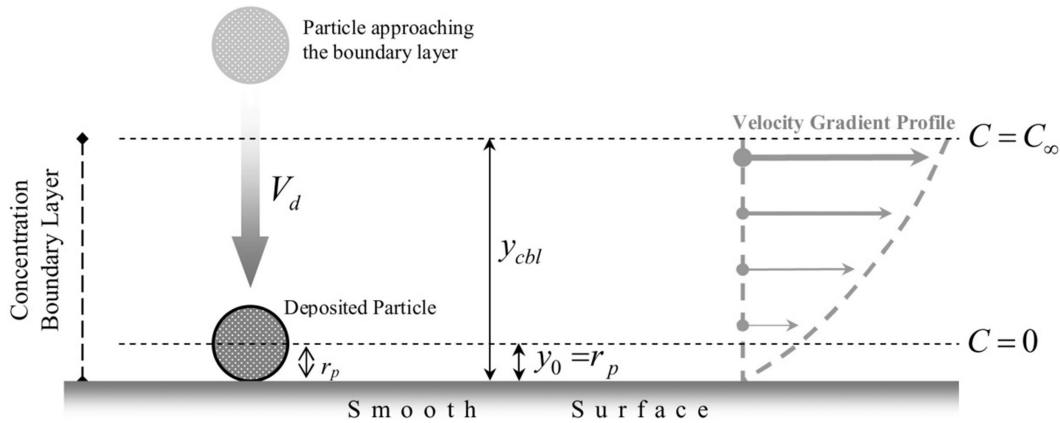


FIG. 1. Schematic illustration for the dry deposition of a particle (radius r_p) onto a smooth surface. The particle number concentration within the boundary layer is zero ($C = 0$) at y_0 and $C = C_\infty$ at y_{cbl} . Figure was adopted from Hussein et al. [12].

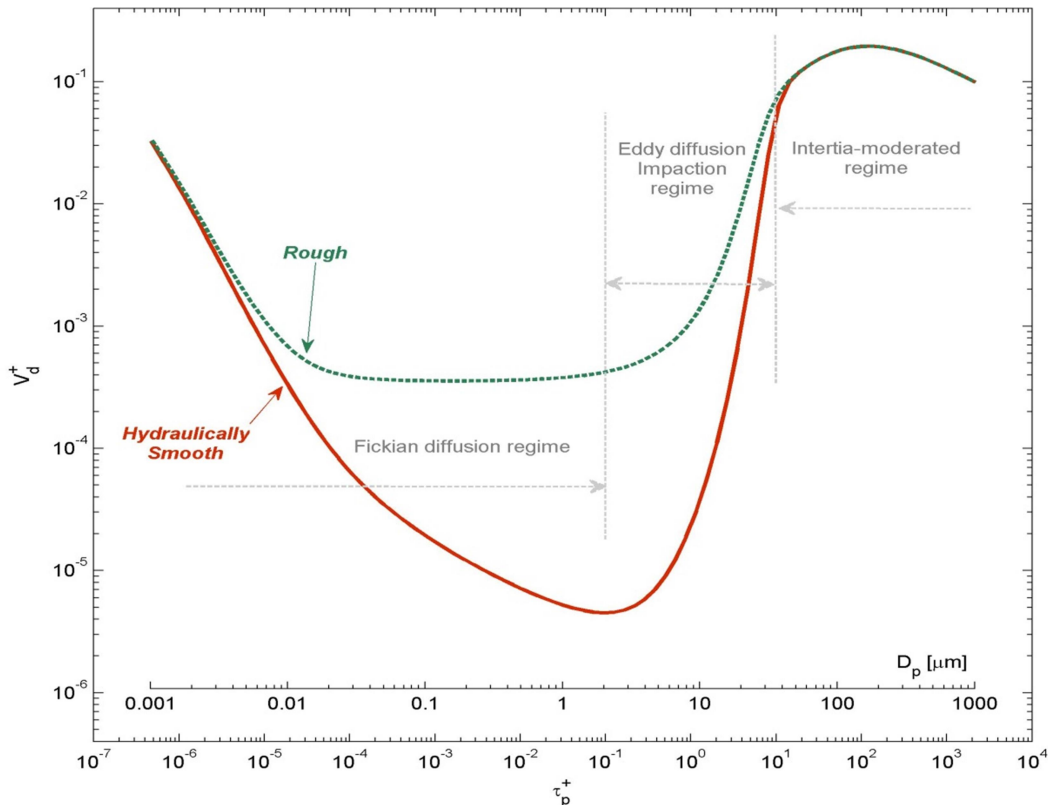


FIG. 2. Universal curve of dimensionless dry deposition velocity (V_d^+) versus particle diameter (D_p) or dimensionless particle relaxation time (τ_p^+). This curve represents deposition onto vertical surfaces. Figure was adopted from Hussein et al. [12].

Dry deposition mechanism onto a surface is believed to occur through two main stages: First, advection and turbulent mixing that transport suspended particles towards the deposition surface. Second, the particles are transported *via* several mechanisms across the boundary layer, which is a thin layer above the surface. It is believed that the second stage is the one that controls the deposition mechanism when the gas is turbulently well mixed. Guha [2] identified the most important transport mechanisms across the boundary layer as Fickian diffusion, thermophoresis, turbophoresis, electrophoresis and gravitational settling. Saffman lift force, pressure diffusion, stressphoresis and diffusio-phoresis are often ignored due to their very small effects compared to other mechanisms, lack of understanding and complications to incorporate them in deposition models. Nowadays, magnetophoresis can have important applications, because it enables to produce magnetic fields higher than before.

As mentioned above, particle size is one of the important parameters needed for calculating V_d . In general, there is a well-known universal dependence of the dimensionless dry deposition velocity (V_d^+) and the dimensionless particle relaxation time (τ_p^+), spanning over 6 orders of magnitude of particle diameter (D_p) and about 9 orders of magnitude of V_d (Fig. 2). Dry deposition is usually considered according to three regimes for V_d curve onto vertical *smooth* surfaces [2, 7, 15, 17, 20]: (1) Turbulent particle diffusion regime ($\tau_p^+ < 1$), (2) Eddy diffusion-impaction regime ($\tau_p^+ 0.1-10$) and (3) Particle inertia-moderated regime ($\tau^+ > 10$). In the first regime, deposition is affected by a combination of Brownian and Eddy diffusion, where V_d is proportional to $Sc^{-2/3}$ and increases with increasing turbulent intensity. The second regime is characterized by a sharp increase of V_d^+ with τ_p^+ , where Friedlander and Johnstone [2] and Davis [16] proposed that particles acquire velocities towards the wall due to the turbulent eddies in the turbulent core and buffer layer and then coast across the viscous sublayer because of their inertia. In the third regime, V_d^+ is saturated with τ_p^+ and eventually decreases with increasing τ_p^+ [18, 19].

In this paper, we present a review about the three-layer deposition model with respect to the types of mechanisms and processes and illustrate

that with numerical model simulations compared to some empirical observations.

2. Model Development and Description

2.1 Particle Flux across the Boundary Layer

Dry deposition of particles onto surfaces has been of great interest for more than 80 years [1, 21, 22]. There are two main approaches for calculating V_d [2]: Eulerian and Lagrangian. The three-layer deposition model follows an Eulerian approach [3, 4, 11]. The name “three-layer” comes from the fact that in this model, the viscous boundary layer is considered as three sub-layers. Many models have been developed based on three main particle transport mechanisms: Brownian diffusion, turbulent diffusion and gravitational settling. Additionally, some models incorporate other mechanisms, such as thermophoresis, electrostatic drifting, turbophoresis, ... etc. [2, 4, 8, 9, 11, 23].

The three-layer dry deposition model is based on the understanding that there is a very thin particle concentration boundary layer within the turbulent boundary layer above a surface. The particle flux, J [m^2s^{-1}], across the concentration boundary layer is written in the general form

$$J = J_{Fickian} + J_{Grav} + J_{Turbo} + J_{Ther} + J_{Elec} + J_{Mag} + \sum_n J_n \quad (1)$$

where the terms on the right-hand side respectively represent the particle flux due to Fickian diffusion (Brownian and Eddy), gravitation settling, turbophoresis, thermophoresis, electrophoresis, magnetophoresis and the sum of other weak mechanisms, which can be included in the model formulation if needed. The validity of Eq. (1) has the following assumptions [3]: (a) steady-state particle flux across the boundary layer, one-dimensional and perpendicular to the surface, (b) the particle concentration gradient exists only very close to the deposition surface, (c) there are no sources or sinks of particles within the boundary layer and (d) the surface is a perfect sink for particles.

As illustrated in Fig. 1, the particle reaches a smooth surface – or in other words: hydraulically smooth surface – and gets deposited on it when its center is at height y_0 from the deposition surface. Basically, for spherical particles, this is the radius of the particle (i.e., $y_0 = r_p$). At this height, the particle concentration is zero in the

fluid right above the surface. The concentration boundary layer is assumed to have an upper limit above which particle concentration becomes homogeneous (i.e., $dC/dy = 0$) as a result of the turbulent air mixing [24]. This implies that at the top of the concentration boundary layer (i.e., y_{cbl}) is set at the maximum concentration (i.e., C_∞).

In the case of a rough surface – or in other words: hydraulically rough surface – the concentration boundary layer is shifted away from the surface (i.e., $y_0 = r_p + F$), where F is a function of surface roughness characteristics [12]. It has been confirmed that surface roughness enhances V_d in the particle diffusion regime and the diffusion-impaction regime. In general, topography of a rough surface distorts the air flow characteristics above the surface and the boundary layer itself resulting in a shorter stopping distance of migrated particles towards the surface [2, 3, 13, 14, 25–27]. Many studies relied on the surface roughness formulation based on a single surface property, which is the surface roughness height [5, 7, 11, 28]. However, with this assumption, such dry deposition formulae fail in predicting V_d . Recently, a new approach was provided by Hussein et al. [12] to account for surface roughness based on hybrid parameter (F), which is a combination of surface roughness height (K) and peak-to-peak distance (L) between the roughness elements. In essence, F represents an effective surface roughness length that is used in the assumption for the shift in the concentration boundary layer.

Mathematically, the boundary conditions to solve the particle flux equation are:

$$C|_{y=r_p+F} = 0 \quad \text{and} \quad C|_{y=y_{cbl}} = 1. \quad (2)$$

Finally, the overall V_d due to all mechanisms included in the particle flux Eq. (1) is simply calculated according to the first assumption at the top of the concentration boundary layer:

$$V_d = \frac{|J|}{C_\infty}. \quad (3)$$

Usually, the particle flux equation is converted into a dimensionless form and then solved. Table 1 lists the nomenclature of each parameter and its conversion into dimensionless form.

Fickian Diffusion

The term ‘‘Fickian diffusion’’ refers to both Brownian diffusion and Eddy diffusion and the particle flux is written as a modified form of Fick’s first law [2]:

$$J_{Fickian} = -(\varepsilon_p + D) \frac{dC}{dy} \quad (4)$$

where D [$\text{m}^2 \text{s}^{-1}$] is Brownian diffusivity and ε_p [$\text{m}^2 \text{s}^{-1}$] is Eddy diffusivity of the particle. Contrary to Brownian diffusivity (D), Eddy diffusivity (ε_p) within the boundary layer increases with distance from the surface ($\varepsilon_p = 0$ at the surface) due to the physical constraints imposed by the surface. Therefore, ε_p is a function of the distance from the surface in dimensionless form (y^+) and the air turbulent viscosity (ν_t); see for example Table 2. Typically, the concentration boundary layer is treated as three sublayers when defining the dependence of ε_p on ν_t . This brought the name ‘‘three-layer’’ to the Eulerian approach of the deposition model.

Gravitational Settling

While diffusion is the dominant mechanism for small particles, gravitational settling is the dominant mechanism for big particles. The gravitational settling velocity (V_s) of a particle is the terminal velocity towards the surface [29, 30]:

$$V_s = \left[\frac{4}{3} \frac{g D_p (\rho_p - \rho)}{\rho C_D} C_c \right]^{\frac{1}{2}} \quad (5)$$

where g [m s^{-2}] is the gravitational acceleration, D_p [m] is the particle diameter, ρ_p [kg m^{-3}] is the particle density, ρ [kg m^{-3}] is the gas density, C_D [–] is the drag coefficient and C_c [–] is the Cunningham slip correction coefficient.

The particle flux due to gravitational settling is simply written as:

$$J_{Grav} = -i V_s C. \quad (6)$$

The deposition surface orientation as vertical, horizontal facing up (floor) or horizontal facing down (ceiling) is presented in the term i as 0, 1 or -1, respectively.

TABLE 1. List of important variables that appeared in the text.

B	Tesla	magnetic field nearby a surface
C	m^{-3}	particle concentration within the boundary layer, in dimensionless form $C^+ = C/C_\infty$
C_∞	m^{-3}	particle concentration above the boundary layer or far away from the surface
C_c	--	Cunningham slip correction coefficient
C_D	--	drag coefficient
C_p	$J\ kg^{-1}\ K^{-1}$	specific heat capacity of air
D	$m^2\ s^{-1}$	Brownian diffusivity of the particle, $D = k_B T C_c / 3\pi\mu D_p$ $D^+ = (\varepsilon_p + D)/\nu$
D_p	m	particle diameter, in dimensionless form $D_p^+ = D_p u^*/\nu$
E	N/C	electric field due to charge accumulation on a surface
e	C	elementary charge of the electron, $e = 1.6 \times 10^{-19}\ C$
g	$m\ s^{-2}$	acceleration of gravity
H_{Ther}	--	thermophoretic coefficient by Talbot et al. [33]
J	$m^{-2}\ s^{-1}$	total particle flux across the concentration boundary layer towards the surface
J_{Elec}	$m^{-2}\ s^{-1}$	particle flux due to electrophoresis, which is caused by electrostatic interaction between the deposited particle and the deposition surface
$J_{Fickian}$	$m^{-2}\ s^{-1}$	particle flux due to Brownian and Eddy diffusions
J_{Grav}	$m^{-2}\ s^{-1}$	particle flux to gravitational settling
J_{Mag}	$m^{-2}\ s^{-1}$	particle flux due to electrophoresis, which is caused by magnetic force exerted on the deposited particle
J_{Ther}	$m^{-2}\ s^{-1}$	particle flux due to thermophoresis, which is caused by nearby surface temperature gradients
J_{Turbo}	$m^{-2}\ s^{-1}$	particle flux due to turbophoresis, which is caused by inhomogeneous mixing
J_n	$m^{-2}\ s^{-1}$	particle flux across the concentration boundary layer due to other mechanisms to be included in the model in the future
K	m	roughness height, in dimensionless form $K^+ = Ku^*/\nu$
K	--	von Karman's constant
K_a	$W\ m^{-2}\ K^{-1}$	thermal conductivity of air
K_p	$W\ m^{-2}\ K^{-1}$	thermal conductivity of the particle
k_B	Joul/K	Boltzmann constant
Kn	--	Knudsen number, $Kn = 2\lambda/D_p$
Sc	--	Schmidt number $Sc = \nu/\rho$
L	m	peak-to-peak distance between roughness elements, in dimensionless form $L^+ = Lu^*/\nu$
m_p	kg	particle mass
n	--	number of elementary charges carried by the particle
Pr	--	Prandtl number of air
Re	--	Reynolds number, $Re = VD_p/\nu$
r_p	m	particle radius, in dimensionless form $r_p^+ = r_p u^*/\nu$
T	K	absolute temperature
ΔT	K	temperature difference, $T_{air} - T_{surface}$
u^*	$m\ s^{-1}$	friction velocity
V_d	$m\ s^{-1}$	deposition velocity onto a surface, in dimensionless form $V_d^+ = V_d/u^*$
V_{Elec}	$m\ s^{-1}$	migration velocity due to electrophoresis, $V_{Elec}^+ = V_{Elec}/u^*$
V_{Mag}	$m\ s^{-1}$	migration velocity due to magnetophoresis, $V_{Mag}^+ = V_{Mag}/u^*$
V_s	$m\ s^{-1}$	gravitational settling velocity, in dimensionless form $V_s^+ = V_s/u^*$
V_t	$m\ s^{-1}$	migration velocity towards a surface due to turbophoresis, $V_t^+ = V_t/u^*$
V_{Ther}	$m\ s^{-1}$	migration velocity due to thermophoresis, $V_{Ther}^+ = V_{Ther}/u^*$

$\langle V_y^2 \rangle$	$\text{m}^2 \text{s}^{-2}$	air wall normal fluctuating velocity intensity, in dimensionless form by Guha [2] after Kallio and Reeks [19]: $\langle V_y^2 \rangle^+ = \frac{\langle V_y^2 \rangle}{(u^*)^2} = \left[\frac{0.005(y^+)^2}{1 + 0.002923(y^+)^{2.128}} \right]^2$
$\langle V_{py}^2 \rangle$	$\text{m}^2 \text{s}^{-2}$	particle wall normal fluctuating velocity intensity by Johansen [32] (*): $\langle V_{py}^2 \rangle = \langle V_y^2 \rangle \left[1 + \frac{\tau_p}{\tau_L} \right]^{-1}$ and in dimensionless form $\langle V_{py}^2 \rangle^+ = \langle V_y^2 \rangle^+ / (u^*)^2$
y	m	vertical distance from the surface, in dimensionless form $y^+ = yu^*/\nu$
y_0	m	distance from the surface at which the particle with a radius r_p is deposited, in dimensionless form $y_0^+ = y_0u^*/\nu$
y_{cbl}	m	depth of the concentration boundary layer above which $dC/dy = 0$ in dimensionless form $y_{cbl}^+ = y_{cbl}u^*/\nu$
ε_p	$\text{m}^2 \text{s}^{-1}$	Eddy diffusivity of the particle, see also Table 2
λ	m	mean free path of air molecules
μ	$\text{kg m}^{-1} \text{s}^{-1}$	dynamic viscosity of the fluid
ν	$\text{m}^2 \text{s}^{-1}$	kinematic viscosity of the fluid, $\nu = \mu/\rho$
ν_t	$\text{m}^2 \text{s}^{-1}$	air turbulent viscosity, see also Table 2
ρ	kg m^{-3}	fluid density
ρ_p	kg m^{-3}	particle density
σ_t	--	turbulent Schmidt number
τ_L	s	Lagrangian time-scale of the fluid by Johansen [7]: $\tau_L = \nu_t / \langle V_y^2 \rangle$ and in dimensionless form $\tau_L^+ = \tau_L (u^*)^2 / \nu$
τ_p	s	particle relaxation time, $\tau_p = m_p C_c / 3\pi\mu D_p$, in dimensionless form $\tau_p^+ = \tau_p (u^*)^2 / \nu$

(*) The validity of this expression is limited for $\tau_p^+ < 138$. Most small particles meet this criterion because their $\tau_p^+ < 10$; and thus, this formula is reasonable [4].

Turbophoresis

Turbophoresis is a phenomenon that leads to the net migration of particles from regions of high Eddy diffusivity to regions of low Eddy diffusivity [2, 31]. This phenomenon is significant for particles with high inertia suspended in inhomogeneous turbulent fluid. In case of low air speed and small particles, particle momentum is small enough, so that turbophoresis can be neglected.

The particle flux due to this mechanism is written as:

$$J_{Turbo} = V_t C \quad (7)$$

where (V_t) is the deposition velocity due to this mechanism:

$$V_t = -\tau_p \frac{d}{dy} \langle V_{py}^2 \rangle. \quad (8)$$

Here, τ_p [s] is the particle relaxation time:

$$\tau_p = \frac{m_p C_c}{3\pi\mu D_p} \quad (9)$$

where m_p [kg] is the particle mass, C_c [--] is the Cunningham slip correction coefficient, μ [$\text{kg m}^{-1} \text{s}^{-1}$] is the fluid kinematic viscosity and D_p [m] is the particle diameter. $\langle V_{py}^2 \rangle$ is the particle wall normal fluctuating velocity intensity [32]:

$$\langle V_{py}^2 \rangle = \langle V_y^2 \rangle \left[1 + \frac{\tau_p}{\tau_L} \right]^{-1} \quad (10)$$

with $\tau_L = \nu_t / \langle V_y^2 \rangle$ as the fluid relaxation time and $\langle V_y^2 \rangle$ is the air wall normal fluctuating velocity intensity, which is adopted in dimensionless form after Kallio and Reeks [19].

TABLE 2. The dependence of the particle Eddy diffusivity (ε_p) on y^+ and ν_t and the dependence of the air turbulent viscosity on (ν_t) on y^+ .

$\frac{\varepsilon_p}{\nu} = (y^+)^4 (y^+)^{0.08} \left[\frac{2.5 \times 10^7}{\text{Re}} \right]^{\frac{-y^+}{400+y^+}} \times 10^{-3}$	universal expression	Guha [2] after Davies [16]
$\varepsilon_p = \nu_t$	relatively small particles and homogeneous isotropic turbulence	Lai and Nazaroff [3]
$\varepsilon_p = \left[1 + \frac{\tau_p}{\tau_L} \right]^{-1} \nu_t$	valid for any particle size ^(*)	Zhao and Wu [4] after Hinze [44]
$\frac{\nu_t}{\nu} = \begin{cases} \left(\frac{y^+}{14.5} \right)^3, & 0 \leq y^+ \leq 5 \\ 0.2y^+ + 0.959, & 0 \leq y^+ \leq 5 \end{cases}$	smooth surfaces	Wood [7] after Lin et al. [45]
$\frac{\nu_t}{\nu} = \begin{cases} 7.67 \times 10^{-4} (y^+)^3, & 0 \leq y^+ \leq 4.3 \\ 10^{-3} (y^+)^{2.8214}, & 4.3 \leq y^+ \leq 12.5 \\ 1.07 \times 10^{-2} (y^+)^{1.8895}, & 12.5 \leq y^+ \leq 30 \end{cases}$	smooth surfaces ^(**)	Lai and Nazaroff [3] after DNS simulation results by Kim et al. [46]
$\frac{\nu_t}{\nu} = \begin{cases} \left(\frac{y^+}{11.15} \right)^3, & 0 \leq y^+ \leq 3 \\ \left(\frac{y^+}{11.4} \right)^3 - 0.049774, & 3 \leq y^+ \leq 52.108 \\ 0.4y^+, & 52.108 \leq y^+ \end{cases}$	rough surface ^(***)	Zhao and Wu [11] after parameterization by Johansen [32]

^(*) While the Eddy diffusivity is valid for homogeneous turbulent mixing, the expression proposed by Hinze [44] is also valid for inhomogeneous turbulent mixing. This is because the rate-limiting transport mechanisms for particle deposition occur inside the viscous sublayer, which is known to be anisotropic [20], and particles might retain their earlier motion because of inertia into a region that has different turbulence properties.

^(**) Lai and Nazaroff [3] also justified that due to the low Brownian diffusivity of particles, the particle concentration boundary layer is generally contained within the viscous sublayer and therefore, the functional dependence of ν_t is most important in the region $0 \leq y^+ \leq 4.3$. They additionally emphasized that the cube power relationship for this region was observed in simulations and experiments [47–49]. Lai and Nazaroff [3] used the DNS simulation results of Kim et al. [46] and distinguished three sublayers for ν_t/ν .

^(***) In general, the above mentioned approaches by Lai and Nazaroff [3] and Zhao and Wu [4] are very similar for $y^+ < 30$ and the only difference is the extension beyond $y^+ = 52.108$ in the Zhao and Wu [4] approach to justify the conditions above a rough surface.

Thermophoresis

Thermophoresis is a phenomenon, where suspended particles in a gas experience a force in the direction opposite to the temperature gradient (∇T) in the fluid nearby a surface [33]. Thermophoresis is of practical importance in many industrial applications (e.g. thermal precipitators). The particle flux due to this mechanism is:

$$J_{\text{Ther}} = V_{\text{Ther}} C. \quad (11)$$

Here, the thermophoretic velocity is:

$$V_{\text{Ther}} = -\frac{C_c \nu H_{\text{Ther}}}{T} \frac{dT}{dy} \quad (12)$$

where C_c [--] is the Cunningham slip correction coefficient, ν [$\text{m}^2 \text{s}^{-1}$] is the fluid kinematic viscosity, T [K] is the gas temperature,

dT/dy [K m^{-1}] is the temperature gradient above the surface and H_{Ther} is the thermophoretic coefficient:

$$H_{Ther} = \left(\frac{2.34}{1 + 3.42Kn} \right) \left(\frac{\frac{k_a}{k_p} + 2.18Kn}{1 + 4.36Kn + 2\frac{k_a}{k_p}} \right) \quad (13)$$

with k_a and k_p [$\text{W m}^{-1} \text{K}^{-1}$] are the thermal conductivities of the air and the particle, respectively. Kn is the Knudsen number.

As suggested by Othmane et al. [34], who used the temperature gradient according to Nerisson [35],

$$\frac{dT}{dy} = \frac{1}{k_a} \frac{\rho C_p u^*}{y_0^+ \text{Pr} + \frac{\sigma_t}{\kappa} \ln\left(\frac{y^+}{y_0^+}\right)} \Delta T \quad (14)$$

where $\text{Pr} = 0.7$ is the Prandtl number of air, $\sigma_t = 1$ is the turbulent Schmidt number, $\kappa = 0.41$ is the von Karman's constant, $C_p = 1004$ [$\text{J kg}^{-1} \text{K}^{-1}$] is the specific heat capacity of air and ΔT (K) is the temperature difference between the top of the boundary layer and the deposition surface. Here, Othmane et al. [34] used $y^+ = 500$.

Electrophoresis

Electrophoresis is a mechanism, where particles migrate towards a surface due to two mechanisms: (1) electrostatic image forces and (2) electrostatic field due to charge accumulation on the surface [8]. Usually, the effect of charge accumulation (i.e., electrostatic field) is stronger than the effect of image forces. The migration velocity (V_{Elec}) due to the existence of a charged particle in an electric field E [N/C] generated by surface charge accumulation is:

$$V_{Elec} = \frac{neC_c E}{3\pi\mu D_p} \quad (15)$$

where n is the number of elementary charges carried by the particle, e [1.6×10^{-19} C] is the elementary charge of the electron, C_c [--] is the Cunningham slip correction coefficient, μ [$\text{kg m}^{-1} \text{s}^{-1}$] is the fluid kinematic viscosity and D_p [m] is the particle diameter.

Magnetophoresis

When a charged particle moves in a magnetic field, it experiences a magnetic force that is proportional to its velocity V [m s^{-1}] and the

magnitude of the magnetic field B [Tesla], bearing in mind that the direction of the particle velocity is not parallel (or anti-parallel) to the direction of the magnetic field. The migration velocity (V_{Mag}) due to this mechanism is:

$$V_{Mag} = \frac{neC_c}{3\pi\mu D_p} \vec{V} \times \vec{B} \quad (16)$$

where n is the number of elementary charges carried by the particle, e [1.6×10^{-19} C] is the elementary charge of the electron, C_c [--] is the Cunningham slip correction coefficient, μ [$\text{kg m}^{-1} \text{s}^{-1}$] is the fluid kinematic viscosity and D_p [m] is the particle diameter.

2.2 Numerical Solution for the Particle Flux Equation

More conveniently, the deposition velocity is derived in dimensionless formulation for Eq. (1):

$$\frac{dC^+}{dy^+} + \frac{1}{D^+} \left[V_{Mag}^+ + V_{Elec}^+ + V_{Ther}^+ + iV_s^+ + \tau_p^+ \frac{d}{dy^+} \langle V_{py}^2 \rangle^+ \right] C^+ = \frac{V_d^+}{D^+} \quad (17)$$

and here, the + superscript denotes that the variable is in dimensionless form (Table 1).

The general solution for C^+ as a function of y^+ is [36]:

$$C^+ = \frac{1}{F(y^+)} \int_{y_0^+}^{y^+} \frac{V_d^+}{D^+} F(x) \cdot dx \quad (18)$$

where

$$F(x) = \exp \left(\int_{y_0^+}^x p(y^+) \cdot dy^+ \right) \quad (19)$$

$$p(y^+) = \frac{1}{D^+} \left[V_{Mag}^+ + V_{Elec}^+ + V_{Ther}^+ + iV_s^+ + \tau_p^+ \frac{d}{dy^+} \langle V_{py}^2 \rangle^+ \right] \quad (20)$$

and the integrations are evaluated across the concentration boundary layer. In other words, the boundary conditions for this first-order differential Eq. (18) are:

$$C^+ \Big|_{y^+ = y_0^+ = r_p^+ + F^+} = 0 \quad \text{and} \quad C^+ \Big|_{y^+ = y_{cb}^+} = 1. \quad (21)$$

Substituting the first boundary condition into the general solution, Eq. (19) is already satisfied, because the particle concentration at the surface is null. The second boundary condition yields the deposition velocity:

$$\frac{1}{V_d^+} = \frac{1}{F(y_{cbl}^+)} \int_{y_0^+}^{y_{cbl}^+} \frac{1}{D^+} F(x) \cdot dx \quad (22)$$

3. Model Simulations

3.1 Smooth Surface

In this section, several model simulations were made to illustrate the effect of different dry deposition mechanisms. In the first place, the model simulation was made for the diffusion mechanisms and then gravitational settling was included after showing the effect of turbophoresis. Then, three weak mechanisms were considered: thermophoresis, electrophoresis and magnetophoresis. All model simulations were made to calculate the dry deposition velocity towards smooth surfaces. For universality, all model simulations are presented in dimensionless form; i.e., dimensionless dry deposition velocity (V_d^+) and dimensionless particle relaxation time (τ_p^+).

Brownian and Eddy Diffusion (Fickian Diffusion)

Initially, the effect of Brownian diffusion was assessed by assuming three heights ($y_{cbl}^+ = 30, 100$ and 300) for the concentration boundary layer (Fig. 3). In general, the height of the concentration boundary layer defines the concentration gradient, because the particle

concentration in the fluid right above the surface (i.e., $C = 0$ at $y^+ = r_p^+$) is assumed to be null, but it increases to reach a steady-state value (C_∞ at y_{cbl}^+) at the top of the concentration boundary layer. Therefore, the higher the concentration boundary layer is, the less is the concentration gradient. As can be seen from the model simulation (Fig. 3), V_d^+ increases with increasing the concentration gradient (i.e., with decreasing the height of the concentration boundary layer). It is also higher for smaller particles (i.e., shorter relaxation time of the particle τ_p^+). In other words, V_d^+ is enhanced by one order of magnitude when the concentration boundary layer height is decreased by one order of magnitude. It is also enhanced by five orders of magnitude when τ_p^+ is decreased by three orders of magnitude.

The Brownian diffusion occurs regardless of the fluid turbulence state. Once the fluid is stirred (i.e., turbulent fluid), the effect of Eddy diffusion starts to happen. This effect is illustrated in Fig. 3 by assuming a friction velocity $u^* = 0.1$ m/s. The higher the u^* is, the higher is the turbulence in the fluid. The enhancement in V_d^+ is seen for all particles. The overall effect of the Brownian and Eddy diffusion (i.e., Fickian diffusion) is summarized with famous U-shape of the dependence of V_d^+ on τ_p^+ .

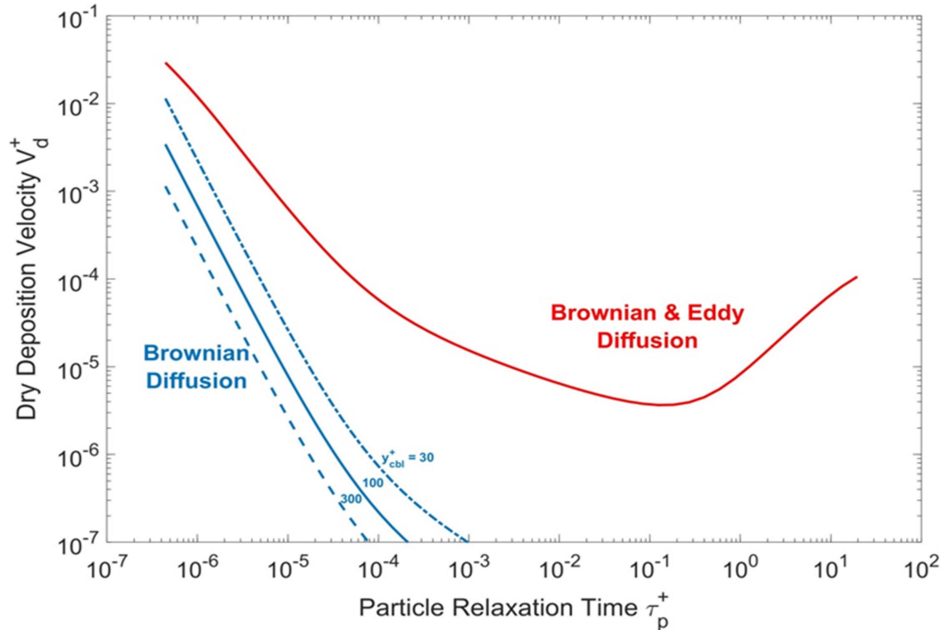


FIG. 3. Dimensionless dry deposition velocity (V_d^+) versus dimensionless particle relaxation time (τ_p^+) illustrating the effect of Brownian diffusion (three depths of the concentration boundary layer) compared to the model calculations by including Eddy diffusion. The model calculations were made for a vertical surface at standard air conditions ($T = 21^\circ\text{C}$ and $P = 1$ atm), friction velocity $u^* = 0.1$ m/s and spherical particles with unit density (i.e., $\rho_p = 1$ g/cc).

Turbophoresis

In practice, fluid turbulence can be inhomogeneous. As postulated in the “model development and description”, turbophoresis becomes significant for large particles in the conditions of inhomogeneous turbulence missing in the fluid. This is illustrated in Fig. 4, where four model simulations were made. The first model simulation was made for Fickian diffusion at $u^* = 0.1$ m/s without turbophoresis effect included (back curve in Fig. 4). That was

compared to three model simulations by including the effect of turbophoresis with three values of $u^* = 0.01, 0.1$ and 1 m/s (red curves in Fig. 4). As clearly seen, the U-shape of V_d^+ versus τ_p^+ is more pronounced, now enhancing V_d^+ with a couple of orders of magnitude for large particles (i.e., long relaxation time of the particle τ_p^+). For small particles (i.e., short relaxation time of the particle τ_p^+), V_d^+ is also enhanced by several orders of magnitude when u^* is increased by one order of magnitude.

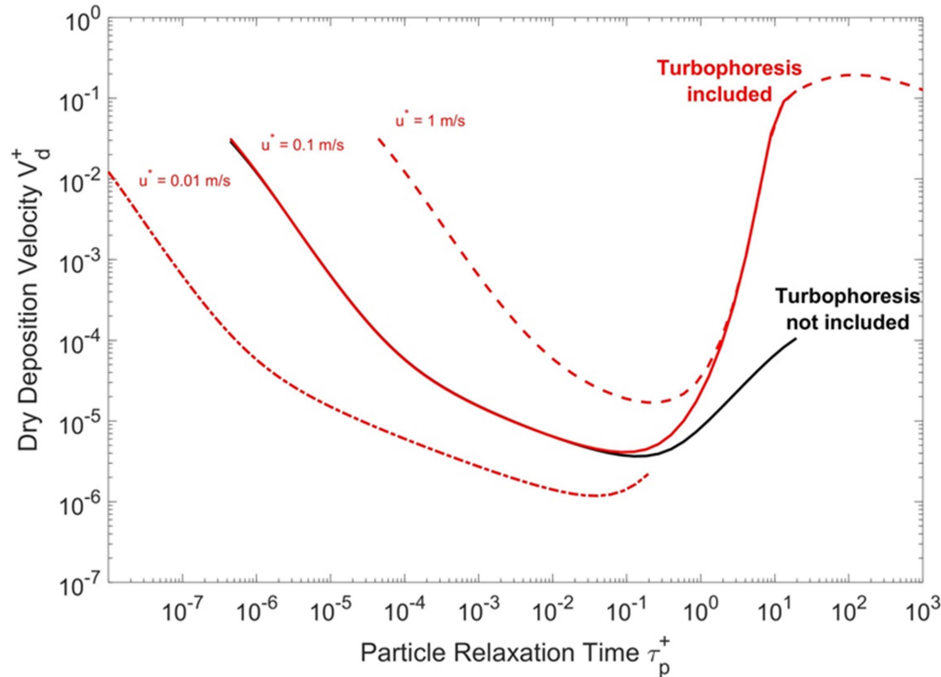


FIG. 4. Dimensionless dry deposition velocity (V_d^+) versus dimensionless particle relaxation time (τ_p^+) illustrating the effect of turbophoresis at three friction velocity (u^*) values. The model calculations were made for a vertical surface at standard air conditions ($T = 21$ °C and $P = 1$ atm) and spherical particles with unit density (i.e., $\rho_p = 1000$ kg/m³).

In fact, the inclusion of turbophoresis was a critical step towards explaining the high empirical values of V_d^+ towards vertical surfaces. Hence, the well-known universal dependence of the V_d^+ on τ_p^+ was not possible without this important development (i.e., inclusion of turbophoresis) in three-layer models. As postulated before, there can be distinguished three regimes for V_d curve onto vertical *smooth* surfaces: turbulent particle diffusion regime ($\tau_p^+ < 1$), Eddy diffusion-impaction regime ($\tau_p^+ 0.1-10$) and particle inertia-moderated regime ($\tau_p^+ > 10$). The Brownian and Eddy diffusion perfectly explains the dependence of V_d^+ on τ_p^+ within the first regime, whereas turbophoresis explains the sharp increase of V_d^+ with τ_p^+ within the second

regime. Within the third regime, V_d^+ is saturated with τ_p^+ and eventually decreases with increasing τ_p^+ .

Gravitational Settling

This mechanism is important whenever the deposition surface is not vertical. While moving inside the fluid, the forces acting on the particle are: force of gravity, drag force opposite to the direction of motion and buoyant force making the particle float in the fluid, when its density is less than the density of the fluid. The particle reaches its terminal velocity when the resultant force from all external forces is null; i.e., the particle acceleration is zero and its speed is constant.

Eq. (5) was derived according to the terminal velocity conditions. Its direction is always downwards. For a surface that is horizontal and facing up (e.g. a floor), the gravitational settling is towards the surface in a direction parallel with the effect of Fickian and turbophoresis mechanisms; i.e., V_d^+ is increased (Fig. 5). For a horizontal surface facing down (e.g. a ceiling), the gravitation settling is away from the surface in a direction antiparallel with the effect of Fickian and turbophoresis mechanisms; i.e., V_d^+ is decreased (Fig. 6). For a surface that is inclined with an angle, the scalar product between the direction of the settling velocity and the normal to the surface needs to be taken into account.

As can be seen for the model simulations (Figs. 5 and 6), V_d^+ increases with τ_p^+ , because the larger the particle is, the more massive is the particle. For a 2 μm particle diameter ($\tau_p^+ = 0.1$), V_d^+ on a horizontal facing up surface is increased by four orders of magnitude when compared to deposition on a vertical surface (Fig. 5). One order of magnitude change in the particle density results in V_d^+ increasing by one order of magnitude.

Thermophoresis

This mechanism is usually well observed on the walls nearby heaters, where particles are deposited on the walls due to the high air temperature and cold wall; i.e., temperature

gradient towards the wall forces particle to migrate towards the wall. This mechanism is also utilized in air purifiers, where the air stream is heated to generate a temperature gradient to force air pollution to migrate towards collection surfaces as a method to clean indoor air.

Fig. 7 illustrates the effect of thermophoresis on V_d^+ for two temperature differences in either directions towards and away from a vertical surface. This mechanism has its significant effect within the particle diameter range, where neither diffusion nor inertial forces are significant; i.e., τ_p^+ in the range 0.001–0.1 (or in other words D_p in the range 0.1–1 μm).

Electrophoresis

This mechanism has a wide range of applications, such as in agriculture, industry, materials science, medical sciences, ... etc. Simply, a charge accumulation on a surface will force particles with a certain charge to either get an enhanced deposition or *vice versa*. For example, a certain type of matter can be deposited in patterns as thin films on substrates by creating a charge pattern that attracts the particles and make them deposit efficiently in the wanted pattern. Fig. 8 illustrates the effect of electrophoresis on V_d^+ for two values of nearby-surface electric field. This mechanism has its significant effect for submicron particles ($D_p < 1 \mu\text{m}$).

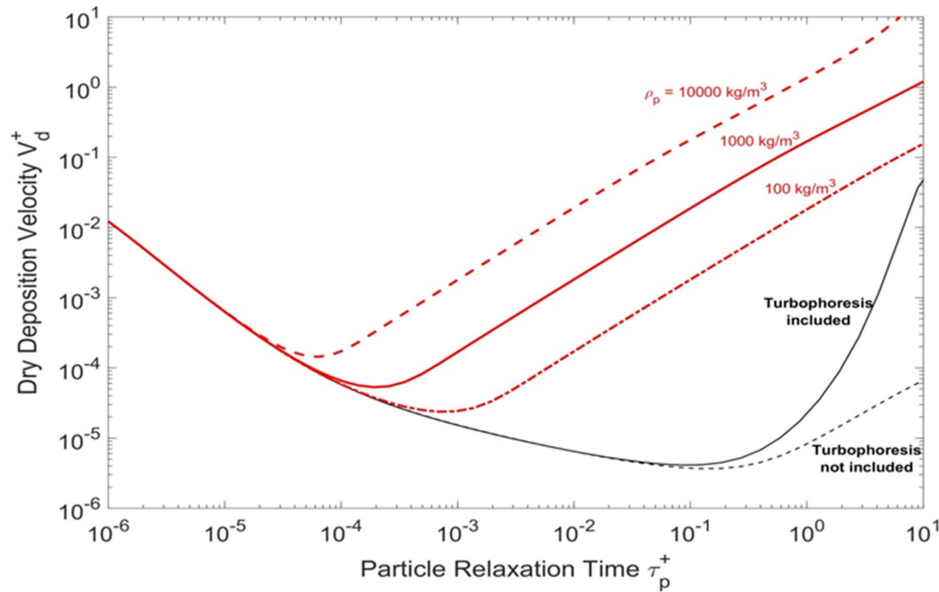


FIG. 5. Dimensionless dry deposition velocity (V_d^+) versus particle relaxation time (τ_p^+) illustrating the effect of gravitational settling for three densities (ρ_p) and compared to two models without including gravitational settling (black curves, $\rho_p = 1000 \text{ kg/m}^3$). The model calculations were made for a vertical surface (black curves) and horizontal facing up surfaces (red curves) at standard air conditions ($T = 21 \text{ }^\circ\text{C}$ and $P = 1 \text{ atm}$).

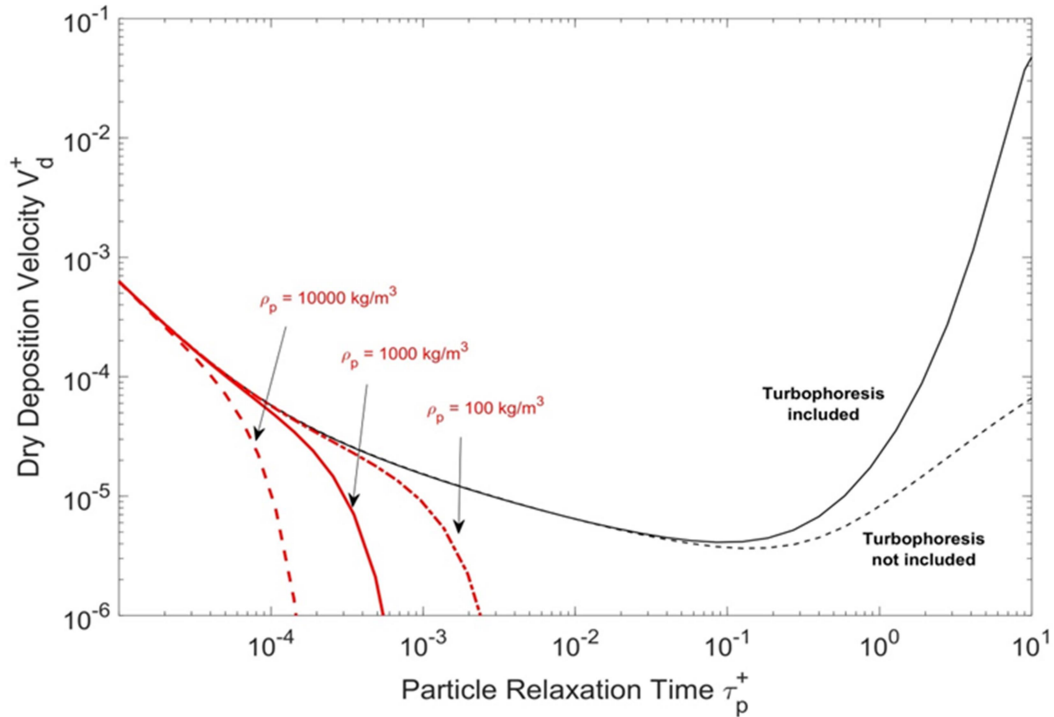


FIG. 6. Dimensionless dry deposition velocity (V_d^+) versus dimensionless particle relaxation time (τ_p^+) illustrating the effect of gravitational settling for three particle densities (ρ_p) and compared to two other models without including gravitational settling (black curves, $\rho_p = 1000 \text{ kg/m}^3$). The model calculations were made for a vertical surface (black curves) and horizontal facing down surfaces (red curves) at standard air conditions ($T = 21^\circ\text{C}$ and $P = 1 \text{ atm}$).

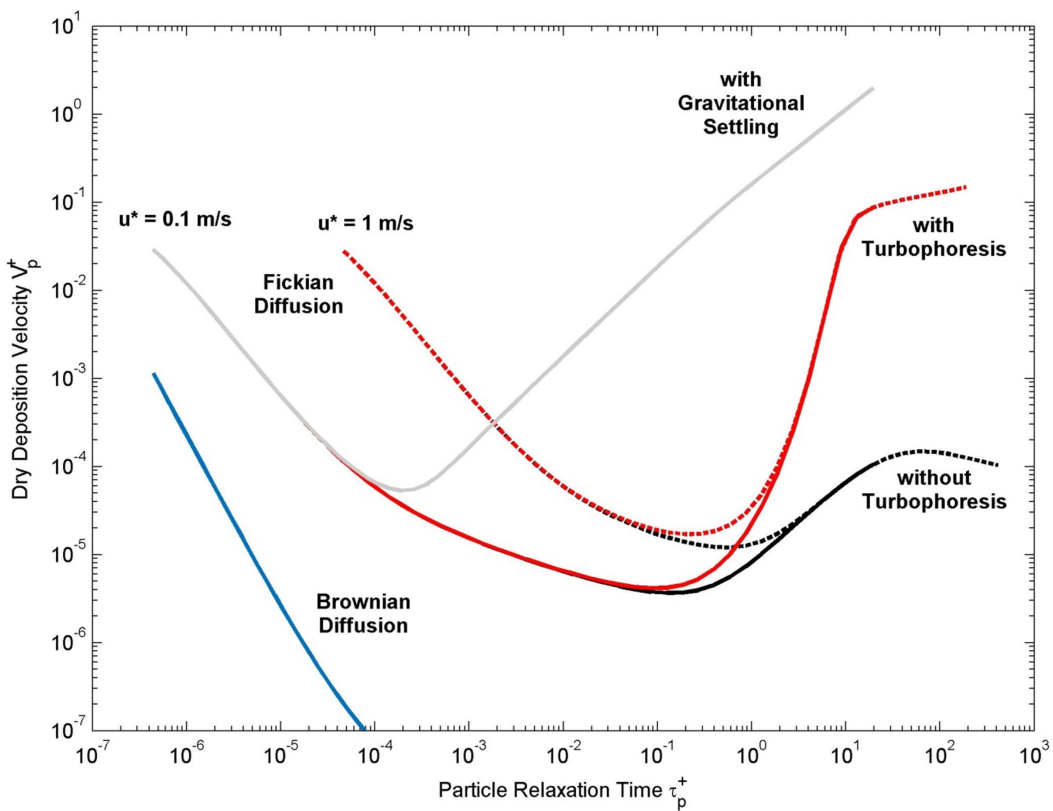


FIG. 7. Model simulations showing the difference between the main processes included in three-layer deposition models. The model calculations were made for a vertical surface (all curves except for the gray curve, which was made for a horizontal facing up surface) at standard air conditions ($T = 21^\circ\text{C}$ and $P = 1 \text{ atm}$) and spherical particles with unit density (i.e., $\rho_p = 1000 \text{ kg/m}^3$).

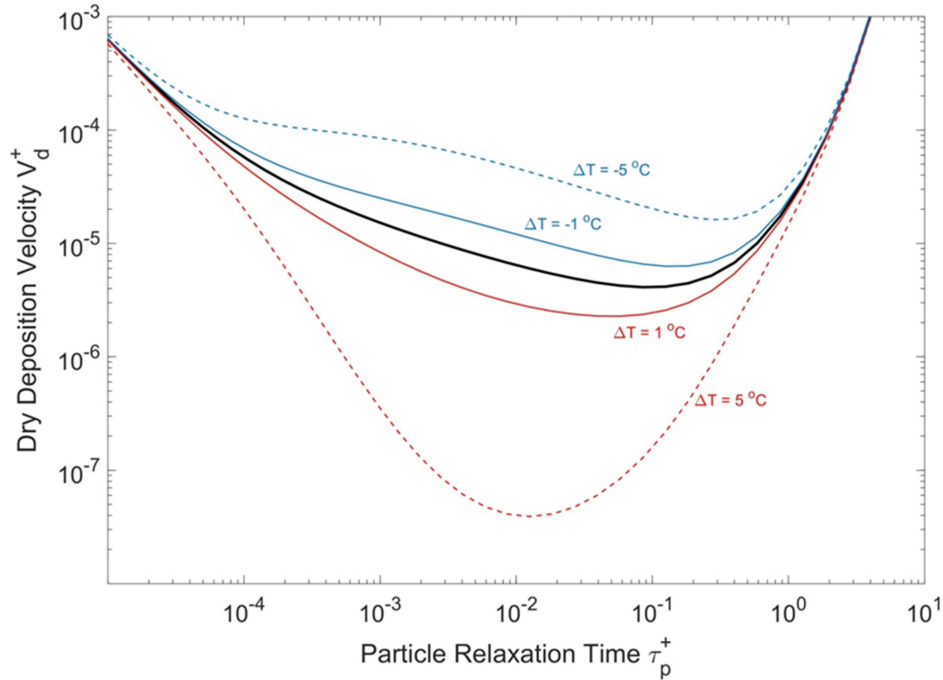


FIG. 8. Dimensionless dry deposition velocity (V_d^+) versus dimensionless particle relaxation time (τ_p^+) illustrating the effect of thermophoresis with two different temperature gradients causing thermophoresis migration parallel (blue curves) or antiparallel (red curves) with the effect of Fickian diffusion mechanism. The model calculations were made for a vertical surface at standard air conditions ($T = 21\text{ }^\circ\text{C}$ and $P = 1\text{ atm}$), friction velocity $u^* = 0.1\text{ m/s}$ and spherical particles with unit density (i.e., $\rho_p = 1000\text{ kg/m}^3$).

Magnetophoresis

This mechanism has not been very popular, because it requires a strong magnetic field to have significant effects. In the near future and with the help of advanced technology to generate magnetic fields with high intensity, this mechanism might have important applications in the field of materials science and the development of thin films and nanotechnology.

Fig. 9 illustrates the effect of magnetophoresis on V_d^+ for two magnetic field intensities to migrate particles in either directions towards and away from a vertical surface. This mechanism has its significant effect for nanoparticles ($D_p < 40\text{ nm}$); the smaller the particles are, the more significant is the effect of this mechanism.

As an overall comparison between different processes, Figure 10 illustrates them on the same plot.

Rough Surface

In practice, surfaces are not ideally smooth. To be more specific, surfaces are not hydraulically smooth. This is an important fact when dealing with environmental surfaces for

the purpose of estimating particle losses. The surface roughness of environmental surfaces can vary from a couple of microns to several millimeters. Fig. 11 illustrates the effect of surface roughness (summarized by F^+) on V_d^+ for an ordinary rough surface ($F^+ = 0.1$) and an extremely rough surface ($F^+ = 1$). The surface roughness affects a wide range of particle sizes including submicron and micron particles.

3.1 Comparison with Empirical Data

In practice, the evaluation of the model calculations against experimental observations is not solely made for a certain process. For example, the Fickian diffusion can't be neglected. To start with, let us consider the experimental data made by Liu and Agarwal [18] to empirically determine the particle deposition inside vertical glass tubes (Fig. 12). This is considered a benchmark for dry deposition model calculations for spherical particles ($\rho_p = 0.92\text{ g/cm}^3$, $\tau_p^+ = 0.21\text{--}774$) deposited on vertical surfaces. Later, El-Shobakshy [37] repeated this experiment by taking into consideration spherical particles ($\rho_p = 1.5\text{ g/cm}^3$, $\tau_p^+ = 0.1\text{--}10$) deposited inside vertical tubes made of glass or brass (Fig. 12).

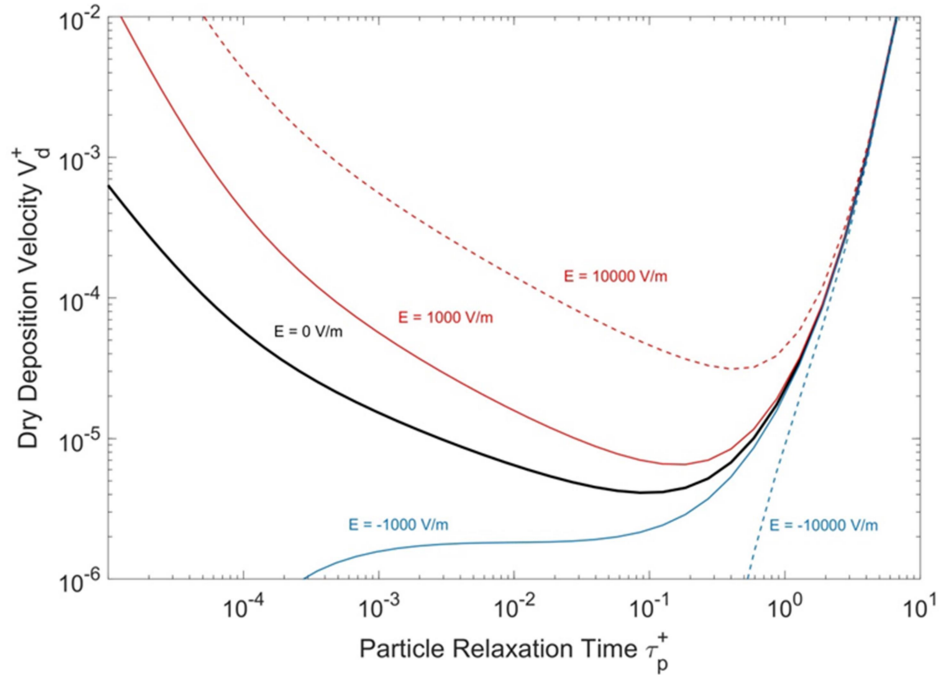


FIG. 9. Dimensionless dry deposition velocity (V_d^+) versus dimensionless particle relaxation time (τ_p^+) illustrating the effect of electrophoresis with two different electrostatic field strengths causing electrostatic drifting parallel (red curves) or antiparallel (blue curves) with the effect of Fickian diffusion mechanism. The model calculations were made for a vertical surface at standard air conditions ($T = 21^\circ\text{C}$ and $P = 1\text{ atm}$), friction velocity $u^* = 0.1\text{ m/s}$ and spherical particles with unit density (i.e., $\rho_p = 1000\text{ kg/m}^3$) carrying a negative charge ($-3e$).

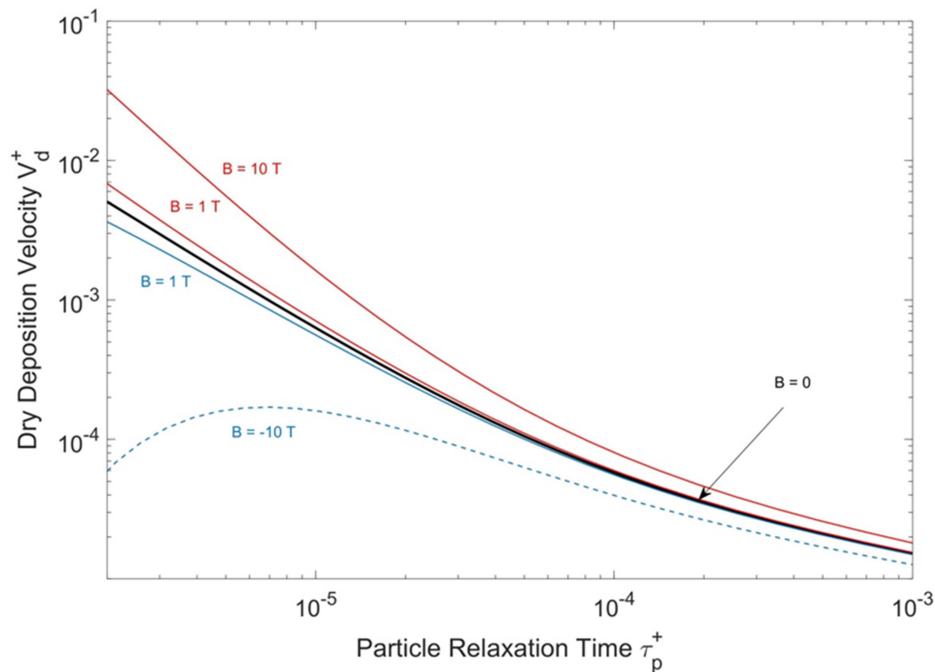


FIG. 10. Dimensionless dry deposition velocity (V_d^+) versus dimensionless particle relaxation time (τ_p^+) illustrating the effect of magnetophoresis with two different magnetic field strengths causing electrostatic drifting parallel (red curves) or antiparallel (blue curves) with the effect of Fickian diffusion mechanism. The model calculations were made for a vertical surface at standard air conditions ($T = 21^\circ\text{C}$ and $P = 1\text{ atm}$), friction velocity $u^* = 0.1\text{ m/s}$ and spherical particles with unit density (i.e., $\rho_p = 1000\text{ kg/m}^3$) carrying a negative charge ($-3e$) and having a velocity component ($v_0 = 10\text{ m/s}$) parallel to the surface.

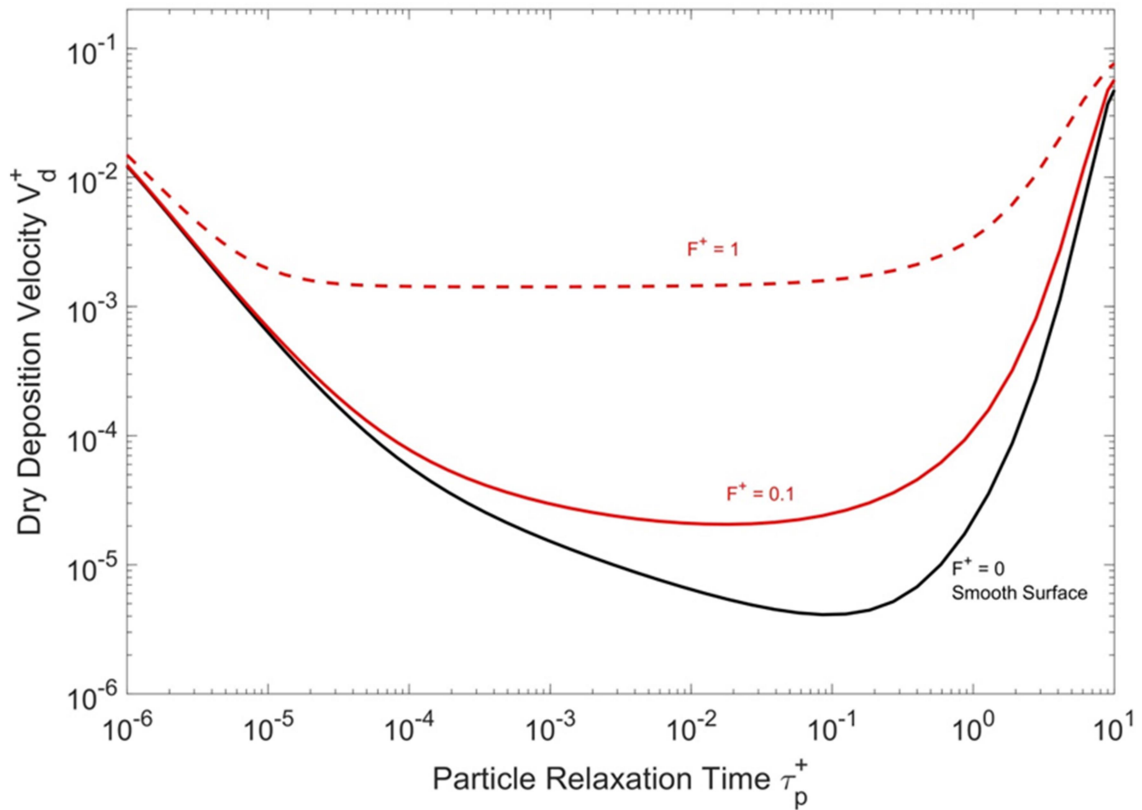


FIG. 11. Dimensionless dry deposition velocity (V_d^+) versus dimensionless particle relaxation time (τ_p^+) illustrating the effect of surface roughness. The model calculations were made at standard air conditions ($T = 21^\circ\text{C}$ and $P = 1\text{ atm}$), friction velocity $u^* = 0.1\text{ m/s}$ and spherical particles with unit density (i.e., $\rho_p = 1000\text{ kg/m}^3$).

The dry deposition model calculations for V_d^+ compare well with the empirical data provided by both Liu and Agarwal [18] and El-Shobakshy [37]. It is presumed that glass is smooth, but in practice, it is not. The model calculations showed a deviation from the empirical data when considering that the vertical glass tubes are smooth; therefore, a surface roughness parameter $F^+ = 0.2$ was needed to match the model calculations with the empirical data. As for the brass surfaces reported by El-Shobakshy [37], the surface roughness parameter was needed to be $F^+ = 1$ and 3. The surface roughness height provided by El-Shobakshy [37] was $K^+ = 0.56$ and 1.65. As mentioned before, when introducing F^+ parameter, it describes the surface roughness based on the mean surface roughness height (K^+) and the mean inter-distance between roughness elements (L^+). This description is more comprehensive than just taking the surface roughness height (K^+) alone into account.

Before trying model evaluation against environmental surfaces, we shall consider the simplest case reported by Sehmel [38], which was the deposition of spherical particles ($\rho_p = 1.5\text{ g/cm}^3$, $\tau_p^+ = 0.005\text{--}40$) on a horizontal smooth surface setup in a wind tunnel (Fig. 13). Since the surfaces were smooth, we used $F^+ = 0$ in the model calculations and the result agrees well with the empirical data.

Slinn [39] reviewed the deposition of spherical particles ($\rho_p = 1.5\text{ g/cm}^3$) on rough surfaces: artificial grass, gravel, water and grass [38, 40–42] with friction velocity $u^* = 19, 22, 40$ and 36 cm/s , respectively (Fig. 14). The model calculation was made by using $F^+ \sim 0.5$ for gravel, water and grass, whereas $F^+ \sim 1.6$ was assumed for artificial grass. Fig. 15 also presents additional model calculations compared to spherical particle deposition on artificial grass reported by Chamberlain [43]. In fact, the model calculations can be extended to reproduce particle deposition on many vegetation types (Fig. 16).

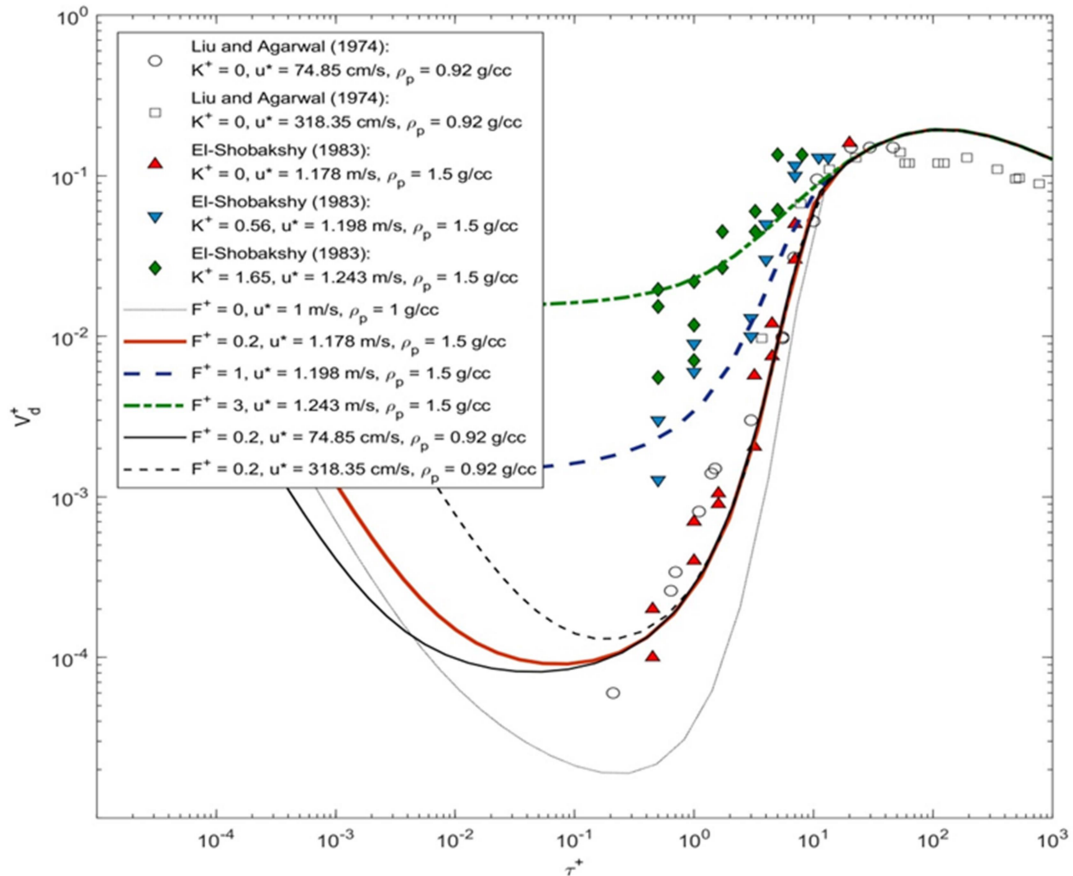


FIG. 12. Dry deposition velocity model calculations compared to empirical data observed for spherical particles deposited inside vertical tubes (glass or brass) as reported by Liu and Agarwal [18] and El-Shobakshy [37].

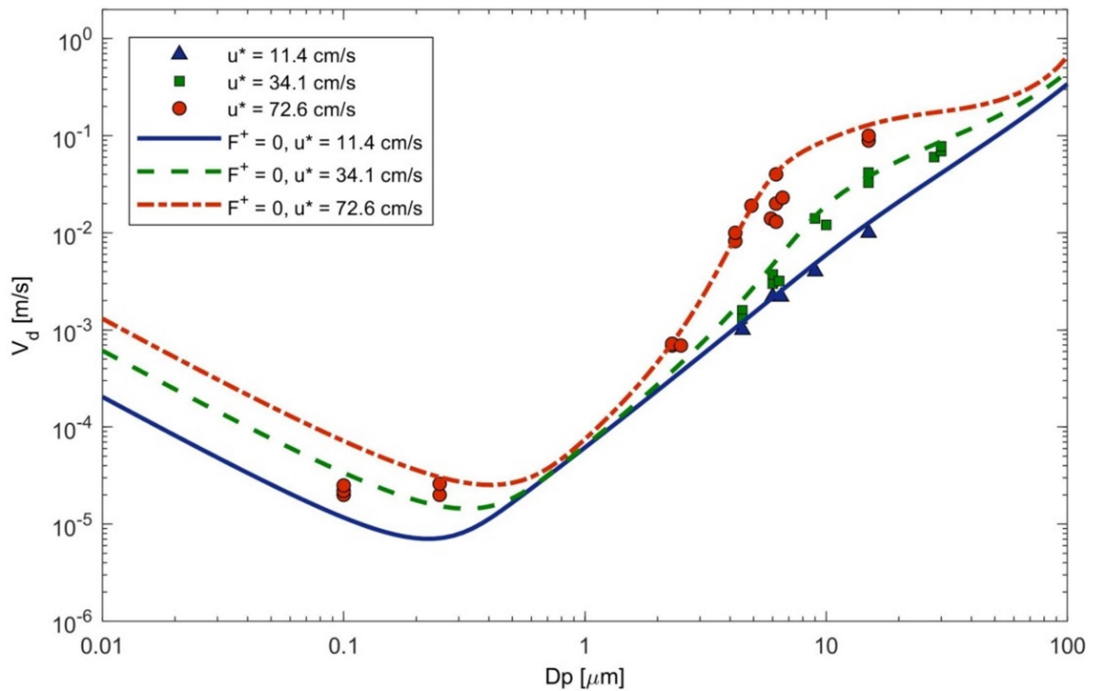


FIG. 13. Dry deposition velocity model calculations compared to empirical data observed for spherical particle ($\rho_p = 1.5 \text{ g/cm}^3$) deposition onto horizontal smooth surfaces as reported by Sehmel [38].

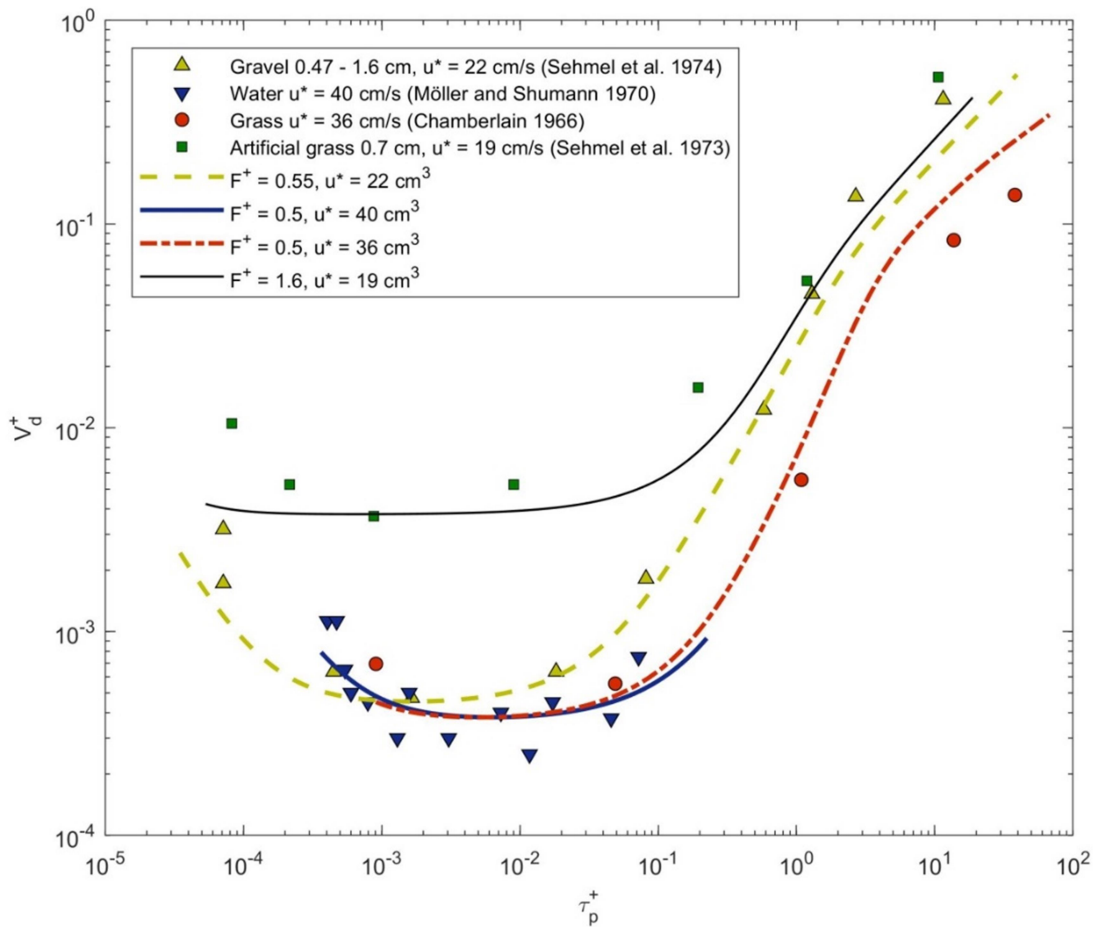


FIG. 14. Dry deposition velocity model calculations compared to empirical data observed for spherical particle ($\rho_p = 1.5 \text{ g/cm}^3$) deposition onto horizontal rough surfaces: grass [42], artificial grass [38], gravel [40] and water [41].

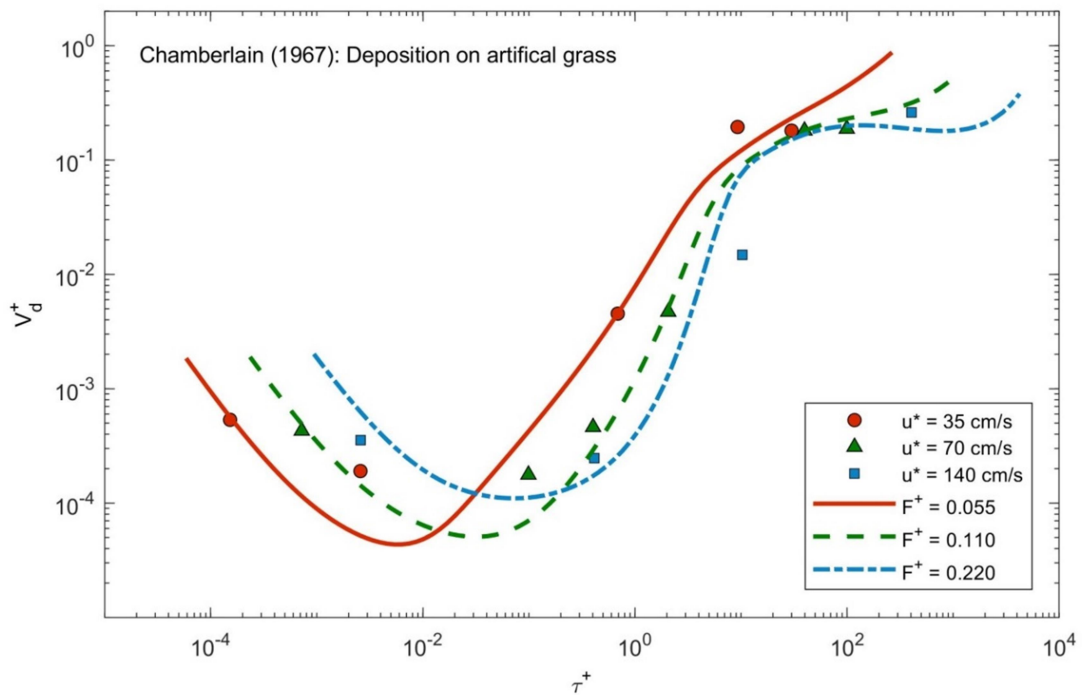


FIG. 15. Dry deposition velocity model calculations compared to empirical data observed for spherical particle ($\rho_p = 1.5 \text{ g/cm}^3$) deposition onto horizontal rough surfaces of artificial grass [43].

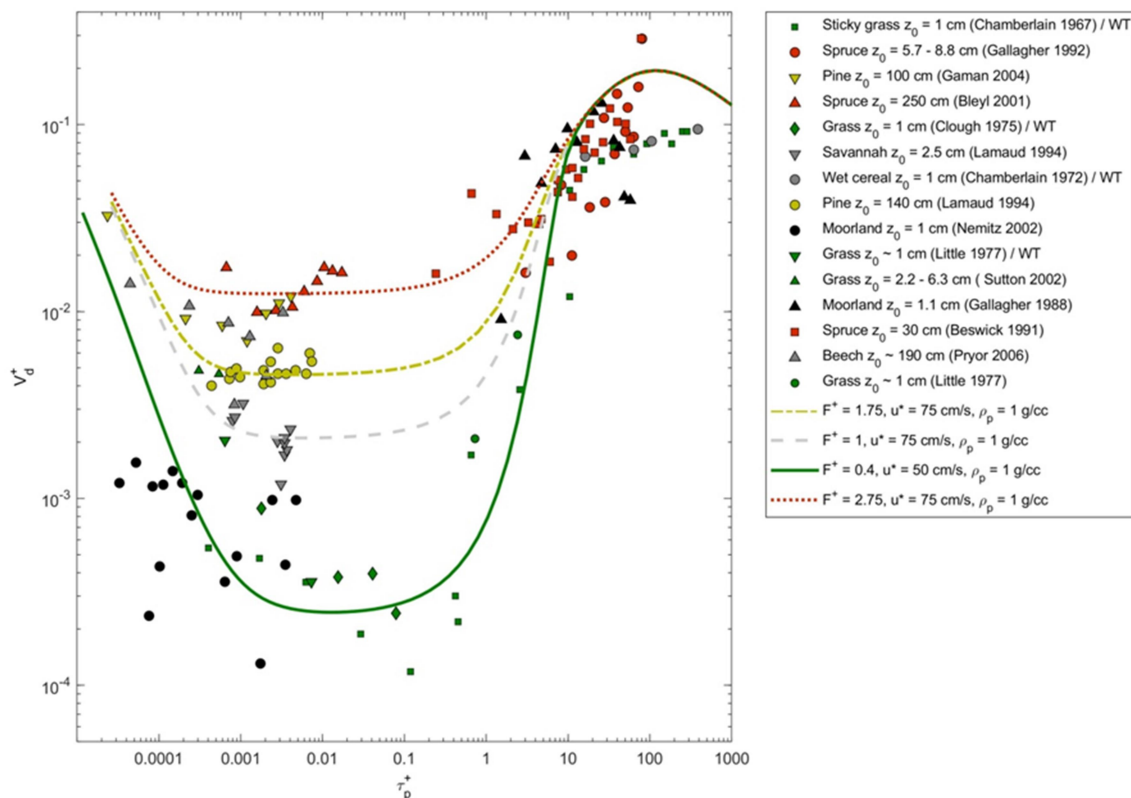


FIG. 16. Dry deposition velocity model calculations compared to empirical data observed for deposition onto different types of vegetation [50–62].

4. Summary and Conclusions

The development of dry deposition modelling is dated back to the early era of the 20th century. Meanwhile, several experimental setups emerged to fulfill the need of testing the performance of model approaches; that was clearly seen in the literature published in the beginning of the 1960s and until the end of the 1980s. During the past twenty years, the model accuracy was significantly enhanced in line with the development of more precise experimental setups and the introduction of advanced technologies. To the date, dry deposition models are capable of simulating particle deposition on a vast range of surfaces and have been used in many applications, such as atmospheric climate and air quality models, industrial processes, nanomaterials, clean rooms, building engineering, particle losses inside sampling lines, health effect of atmospheric particles and pharmaceuticals.

In this paper, we presented the basic concepts that have been developed and implemented in dry deposition models and illustrated the effect

of different processes on the transport rate of suspended particles in the fluids towards surfaces. As a benchmark for the accuracy of the current dry deposition modelling, we presented a comparison between model calculations and experimental data-bases found in the literature. As a main conclusion, the current dry deposition models are capable of accurately predicting the dry deposition velocities onto almost any surface type and can cover a wide range of particle size (diameter 0.001–100 μm). However, additional research is needed to further develop the current model concepts, so that they include other processes that have specific industrial applications. It is also very important to develop the experimental setup of dry deposition measurements by implementing state-of-the-art technology. For instance, investigations on extreme surface conditions and fluid characteristics are also valuable.

Acknowledgments

The authors would like to acknowledge Prof. Laila Abu-Hassan for her precious advice and encouragement for preparing this review.

References

- [1] Corner, J. and Pendlebury, E.D., *Proceedings Phys. Soc.*, B64 (1951) 645.
- [2] Guha, A., *J. Aerosol Sci.*, 28 (1997) 1517.
- [3] Lai, A.C.K. and Nazaroff, W.W., *J. Aerosol Sci.*, 31 (2000) 463.
- [4] Zhao, B. and Wu, J., *Atmos. Environ.*, 40 (2006) 457.
- [5] Browne, L.W.B., *Atmos. Environ.*, 8 (1974) 801.
- [6] Wan, S.G., *Chinese Sci. Bull.*, 26 (1981) 1145.
- [7] Wood, N.B., *J. Aerosol Sci.*, 12 (1980) 275.
- [8] McMurry, P.H. and Rader, D. J., *Aerosol Sci. Technol.*, 4 (1985) 249.
- [9] Nazaroff, W.W. and Cass, G.R., *Environ. Intern.*, 15 (1989) 567.
- [10] Lai, A.C.K., *Atmos. Environ.*, 39 (2005) 3823.
- [11] Zhao, B. and Wu, J., *Atmos. Environ.*, 40 (2006) 6918.
- [12] Hussein, T., Kubincová, L., Dohányosová, P., Hruška, A., Džumbová, L., Hemerka, J., Kulmala, M. and Smolik, J., *Build. Environ.*, 44 (2009) 2056.
- [13] Hussein, T., Hruška, A., Dohányosová, P., Džumbová, L., Hemerka, J., Kulmala, M. and Smolik, J., *Atmos. Environ.*, 43 (2009) 905.
- [14] Hussein, T., Smolik, J., Kerminen, V.-M. and Kulmala, M., *Aerosol Sci. Technol.*, 46 (2012) 44.
- [15] Friedlander, S.K. and Johnstone, H.F., *Ind. Engng. Chem.*, 40 (1957) 1151.
- [16] Davies, C.N., “*Aerosol Science*”, (Academic Press, London, 1966).
- [17] Gardner, G.C., *Int. J. Multiphase Flow*, 2 (1975) 213.
- [18] Liu, B.Y.H. and Agarwal, J.K., *J. Aerosol Sci.*, 5 (1974) 145.
- [19] Kallio, G.A. and Reeks, M.W., *Int. J. Multiphase Flow*, 15 (1989) 433.
- [20] Young, J.A., *J. Fluid Mech.*, 340 (1997) 129.
- [21] Millikan, R.A., *Phys. Rev.*, 22 (1923) 1.
- [22] Langstroth, G.O. and Gillespie, T., *Canad. J. Res.*, B25 (1947) 455.
- [23] Crump, J.G., Flagan, R.C. and Seinfeld, J.H., *Aerosol Sci. Technol.*, 2 (1983) 303.
- [24] Bejan, A., “*Convection Heat Transfer*”, 2nd Ed., (Wiley, New York, 1995).
- [25] Fogh, C.L., Byrne, M.A., Roed, J. and Goddard, A.J.H., *Atmos. Environ.*, 31 (1997) 2193.
- [26] Abadie, M., Limam, K. and Allard, F., *Build. Environ.*, 36 (2001) 821.
- [27] Thatcher, T.L., Lai, A.C.K., Moreno-Jackson, R., Sextro, R.G. and Nazaroff, W.W., *Atmos. Environ.*, 36 (2002) 1811.
- [28] Sippola, M.R. and Nazaroff, W.W., *Aerosol Sci. Technol.*, 38 (2004) 914.
- [29] Seinfeld, J.H. and Pandis, S.N., “*Atmospheric Chemistry and Physics*”, (Wiley, New York, 1998).
- [30] Hinds, W.C., “*Aerosol Technology: Properties, Behavior and Measurement of Airborne Particles*”, (Wiley, New York, 1999).
- [31] Reeks, M.W., *J. Aerosol Sci.*, 14, (1983) 729.
- [32] Johansen, S.T., *Int. J. Multiphase Flow*, 17 (1991) 355.
- [33] Talbot, L., Cheng, R.K., Schefer, R.W. and Willis, D.R., *J. Fluid Mech.*, 101 (1980) 737.
- [34] Othmane, M.B., Havet, M., Gehin, E., Sollic, C. and Arroyo, G., *J. Food Eng.*, 105 (2011) 400.
- [35] Nerisson, P., Ph.D. Thesis, University of Toulouse, France, (2009).
- [36] Boyce, W.E. and DiPrima, R.C., “*Elementary Differential Equations and Boundary Value Problems*”, 2nd Ed., (John Wiley & Sons, Canada, 1992).
- [37] El-Shobokshy, M.S., *Atmos. Environ.*, 17 (1983) 639.
- [38] Sehmel, G.A., *J. Aerosol Sci.*, 4 (1973) 125.
- [39] Slinn, W.G.N., *Nuclear Safety*, 19 (1978) 205.

- [40] Sehmel, G.A., Hodgson, W.H. and Sutter, S.L. "Dry deposition of particles", Pacific Northwest Laboratory Annual Report for 1973 to the USAEC Division of Biomedical and Environmental Research, Part 3, Atmospheric Series, USAEC Report BNWL-1850 (Pt. 3), (1974) p157.
- [41] Möller, U. and Shumann, G., *J. Geophys. Res.*, 75 (1970) 3013.
- [42] Chamberlain, A.C., *Proc. R. Soc. London Ser. A*, 290 (1966) 236.
- [43] Chamberlain, A.C., *Proceed. Royal Soc. London*, 296 (1967) 45.
- [44] Hinze, J.O., "Turbulence", 2nd Ed., (McGraw-Hill, New York, 1975).
- [45] Lin, C.S., Moulton, R.W. and Putnam, G.L., *Ind. Engng. Chem.*, 45 (1953) 636.
- [46] Kim, J., Moin, P. and Moser, R., *J. Fluid Mech.*, 177 (1987) 133.
- [47] Chapman, D.R. and Kuhn, G.D., *J. Fluid Mech.*, 170 (1986) 265.
- [48] Karlsson, R.I. and Johansson, T.G., "LDV Measurements of Higher Order Moments of Velocity Fluctuations in a Turbulent Boundary Layer", in: "Laser Anemometry in Fluid Mechanics", Eds., Adrian R.J. et al., (Ladoan-Instituto Superior Tecnico, Portugal, 1988) p. 273.
- [49] Meneveau, C., Lund, T.S. and Cabot, W.H., *J. Fluid Mech.*, 319 (1996) 353.
- [50] Gallagher, M.W., Beswick, K.M. and Choularton, T.W., *Atmos. Environ.*, 26A (1992) 2893.
- [51] Gaman, A., Rannik, U., Aalto, P., Pohja, T., Siivola, E., Kumala, M. and Vesala, T., *J. Atmos. Ocean. Technol.*, 21 (2004) 933.
- [52] Bleyl, M.R., Ph.D. Thesis, Georg-August-Universität, (2001), Göttingen, Germany.
- [53] Clough, W.S., *Atmos. Environ.*, 9 (1975) 1113.
- [54] Lamaud, E., Brunet, Y., Labatut, A., Lopez, A., Fontan, J. and Druilhet, A., *J. Geophys. Res.*, 99 (1994) 16511.
- [55] Lamaud, E., Chapuis, A., Fontan, J. and Serie, E., *Atmos. Environ.*, 28 (1994) 2461.
- [56] Chamberlain, A.C. and Chadwick, R.C., *Annals App. Bio.*, 71 (1972) 141.
- [57] Nemitz, E., Gallagher, M.W., Duyzer, J.H. and Fowler, D., *Quart. J. Royal Meteorol. Soc.*, 128 (2002) 2281.
- [58] Little, P. and Wiffen, R.D., *Atmosph. Environ.*, 11 (1977) 437.
- [59] Sutton M.A., Milford C., Nemitz E., Theobald, M.R., Hill, P.W., Fowler, D. et al., *Plant Soil*, 228 (2001) 131.
- [60] Gallagher, W.M., Choularton, T.W., Morse, A.P. and Fowler, D., *Quart. J. Royal Meteorol. Soc.*, 114 (1988) 1291.
- [61] Beswick, K.M., Hargreaves, K.L., Gallagher, M.W., Choularton, T.W. and Fowler, D., *Quart. J. Royal Meteorol. Soc.*, 117 (1991) 623.
- [62] Pryor, S., *Atmos. Environ.*, 40 (2006) 6192.

Structural, Spectroscopic and Magnetic Characterization of $\text{Bi}_{0.9}\text{X}_{0.1}\text{Fe}_{0.98}\text{Mg}_{0.02}\text{O}_3$ (X = Gd, Sm, Ba) Multiferroic Compounds

Mansour M. Al-Haj

Physics Department, Mutah University, Mutah, Al-Karak, Jordan.

Received on: 08/06/2018;

Accepted on: 8/10/2018

Abstract: The compounds $\text{Bi}_{0.9}\text{Gd}_{0.1}\text{Fe}_{0.98}\text{Mg}_{0.02}\text{O}_3$, $\text{Bi}_{0.9}\text{Sm}_{0.1}\text{Fe}_{0.98}\text{Mg}_{0.02}\text{O}_3$ and $\text{Bi}_{0.9}\text{Ba}_{0.1}\text{Fe}_{0.98}\text{Mg}_{0.02}\text{O}_3$ were found to have a rhombohedral perovskite-like structure. The structural parameters were extracted from the X-ray diffraction data. Fourier transform infrared spectroscopy revealed traces of the $\alpha\text{-Fe}_2\text{O}_3$ magnetic phase in the $\text{Bi}_{0.9}\text{Ba}_{0.1}\text{Fe}_{0.98}\text{Mg}_{0.02}\text{O}_3$ compound. The $\text{Bi}_{0.9}\text{Gd}_{0.1}\text{Fe}_{0.98}\text{Mg}_{0.02}\text{O}_3$ and $\text{Bi}_{0.9}\text{Sm}_{0.1}\text{Fe}_{0.98}\text{Mg}_{0.02}\text{O}_3$ compounds were found to show a weak intrinsic ferromagnetic behavior, whereas the ferromagnetism of the $\text{Bi}_{0.9}\text{Ba}_{0.1}\text{Fe}_{0.98}\text{Mg}_{0.02}\text{O}_3$ compound was found to be non-intrinsic in origin. The magnetic transition temperatures were found to be around 340 °C.

Keywords: X-ray diffraction, Spectroscopy, Magnetization, Transition temperature.

PACS: 61.05.cp; 75.50.Ee; 75.60.Ej.

1. Introduction

Multiferroics are materials that exhibit more than one ferro-property (ferromagnetism, ferroelectricity, ferroelasticity) simultaneously in the same phase. Multiferroics include also non-primary order parameters, such as antiferromagnetism or ferrimagnetism. The inorganic compound BiFeO_3 (BFO) with perovskite-like structure is one of the most fascinating multiferroic materials [1]. The room-temperature phase of BFO is classified as rhombohedral with space group $R3c$. It is synthesized in bulk [2], nanoparticles [3-5], single crystal [6], thin film [7], nanotubes [8] or nanowires [9] form. Its antiferromagnetic (G-type magnetic ordering) Neel temperature $T_N \cong 370$ °C and its ferroelectric Curie temperature $T_C \cong 827$ °C. Ferroelectric polarization occurs along the pseudocubic direction $\langle 111 \rangle_c$ with a magnitude of 90-100 $\mu\text{C}/\text{cm}^2$, depending on the material's form. However, the bulk form is suffering from shortcomings, such as weak magnetization and high leakage current, which prohibit its applicability in future electronic

devices. Therefore, there has been an extensive research work in order to improve the performance of this material. Partial substitution of Bi^{3+} by ions such as Y^{3+} [10, 11], Dy^{3+} [12], Gd^{3+} [13, 14], Ho^{3+} [15], Nd^{3+} [16], Tb^{3+} [17], Sr^{2+} [18]; partial substitution of Fe^{3+} by ions such as Mn^{3+} and Co^{3+} [19]; or partial co-substitution of Bi^{3+} and Fe^{3+} by ions such as (Sm^{3+} , Sc^{3+}) [20], (Ba^{2+} , Mn^{3+}) [21], (In^{3+} , Mn^{3+}) [22], (Gd^{3+} , Ti^{4+}) [23], (Ca^{2+} , Ti^{4+}) [24], (La^{3+} , Ti^{4+}) [25], (K^+ , Ta^{5+}) [26], (Eu^{3+} , Mn^{2+}) [27], (La^{3+} , V^{5+}) [28], all these substitutions were found to enhance the structural, electric, magnetic, dielectric, optical, and ferroelectric properties of BFO and helped understand the behavior of this material. Despite the progress achieved, the story is not ending. There are still unanswered questions about the true origin of magnetism in BFO-substituted materials.

In this work, we investigate the multiferroic compounds $\text{Bi}_{0.9}\text{Gd}_{0.1}\text{Fe}_{0.98}\text{Mg}_{0.02}\text{O}_3$, $\text{Bi}_{0.9}\text{Sm}_{0.1}\text{Fe}_{0.98}\text{Mg}_{0.02}\text{O}_3$ and $\text{Bi}_{0.9}\text{Ba}_{0.1}\text{Fe}_{0.98}\text{Mg}_{0.02}\text{O}_3$ by several techniques.

Throughout this paper, we refer to them as GdMg, SmMg and BaMg, respectively. Since the ionic radius $r(\text{Mg}^{2+}) = 0.720 \text{ \AA} > r(\text{Fe}^{3+}) = 0.645 \text{ \AA}$, only 2% of Fe^{3+} ions were replaced by Mg^{2+} ions to make sure that they go into the Fe^{3+} sites and stabilize the crystal structure.

2. Experimental Methods

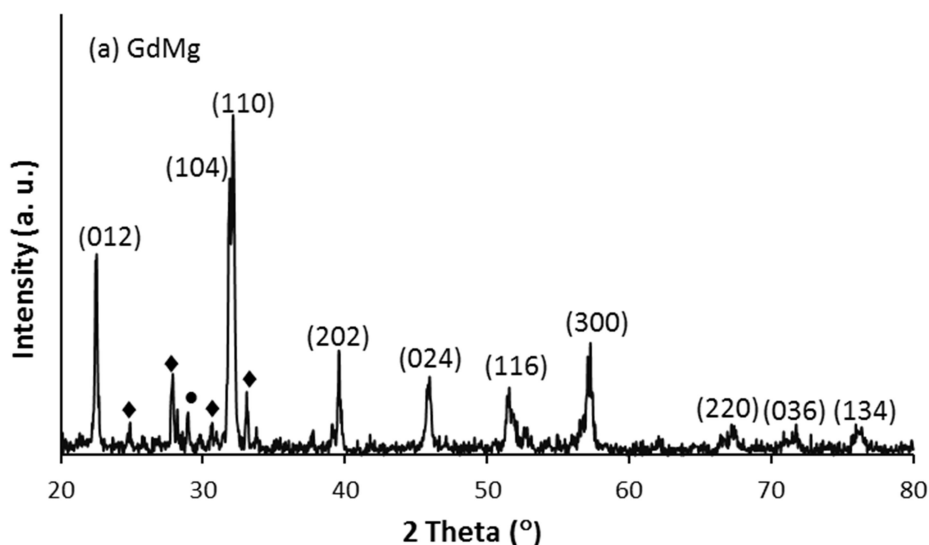
The compounds were prepared by the conventional mixed oxide method. Stoichiometric amounts of pure oxides of Bi_2O_3 , Gd_2O_3 , Sm_2O_3 , Fe_2O_3 and MgO were mixed and ground in an agate mortar and pestle for half an hour. The GdMg and SmMg mixtures were calcined at $825 \text{ }^\circ\text{C}$ in a tube furnace for 90 min. After the calcination process, the two mixtures were cooled to room temperature, ground and calcined again at $825 \text{ }^\circ\text{C}$ for 90 min. Then, the mixtures were cooled to room temperature and ground to get a fine powder. The same procedure was done to the BaMg mixture, but with the first calcination at $825 \text{ }^\circ\text{C}$ for 60 min and the second one at $825 \text{ }^\circ\text{C}$ for 75 min. The x-ray diffraction (XRD) patterns were collected by a Seifert 3003TT powder diffractometer using CuK_α radiation. The Fourier transform infrared (FTIR) spectra of the samples were collected by a JASCO E300 spectrometer (range: $400 - 4000 \text{ cm}^{-1}$). Since potassium bromide (KBr) does not show any absorption spectrum in the IR region, a small amount of each powder (1% by weight) is mixed by KBr (99% by weight) and then pressed into thin pellets (thickness $< 1 \text{ mm}$) for FTIR spectra collection. The magnetic hysteresis loops were recorded by a conventional vibrating sample magnetometer (VSM) calibrated with a

nickel sphere. The magnetic transition temperature was measured by a Mettler differential scanning calorimeter (DSC) with a maximum operating temperature of $450 \text{ }^\circ\text{C}$. The instrument was calibrated with an indium standard and aluminum sample holders were used for measurement.

3. Results and Discussion

Fig. 1 shows the XRD patterns of the GdMg, SmMg, and BaMg compounds. The reflection peaks in these patterns were indexed according to the BiFeO_3 diffraction pattern (PDF # 86-1518), confirming the rhombohedral perovskite-like structure with space group $R3c$. However, small traces of the impurity nonmagnetic phases mullite $\text{Bi}_2\text{Fe}_4\text{O}_9$ (indicated by \bullet) and sillenite $\text{Bi}_{25}\text{FeO}_{40}$ (indicated by \blacklozenge) are existent. These are the inevitable impurity phases that were reported to form during the synthesis of related BFO-substituted compounds [29] and are attributed to the volatilization of Bi.

In order to extract accurate values of the structural parameters of the studied materials, we carried out a least-squares refinement calculation of the XRD data using the UnitCell program [30]. The lattice parameters a and c , as well as the volume V of the hexagonal unit cell are listed in Table 1. Since $r(\text{Ba}^{2+}) = 1.35 \text{ \AA} > r(\text{Sm}^{3+}) = 0.958 \text{ \AA} > r(\text{Gd}^{3+}) = 0.938 \text{ \AA}$, the general trend is that the structural parameters increase as the radius of the substituting ion is increased (the c value of BaMg has undergone a slight decrease, but the a and V values have increased).



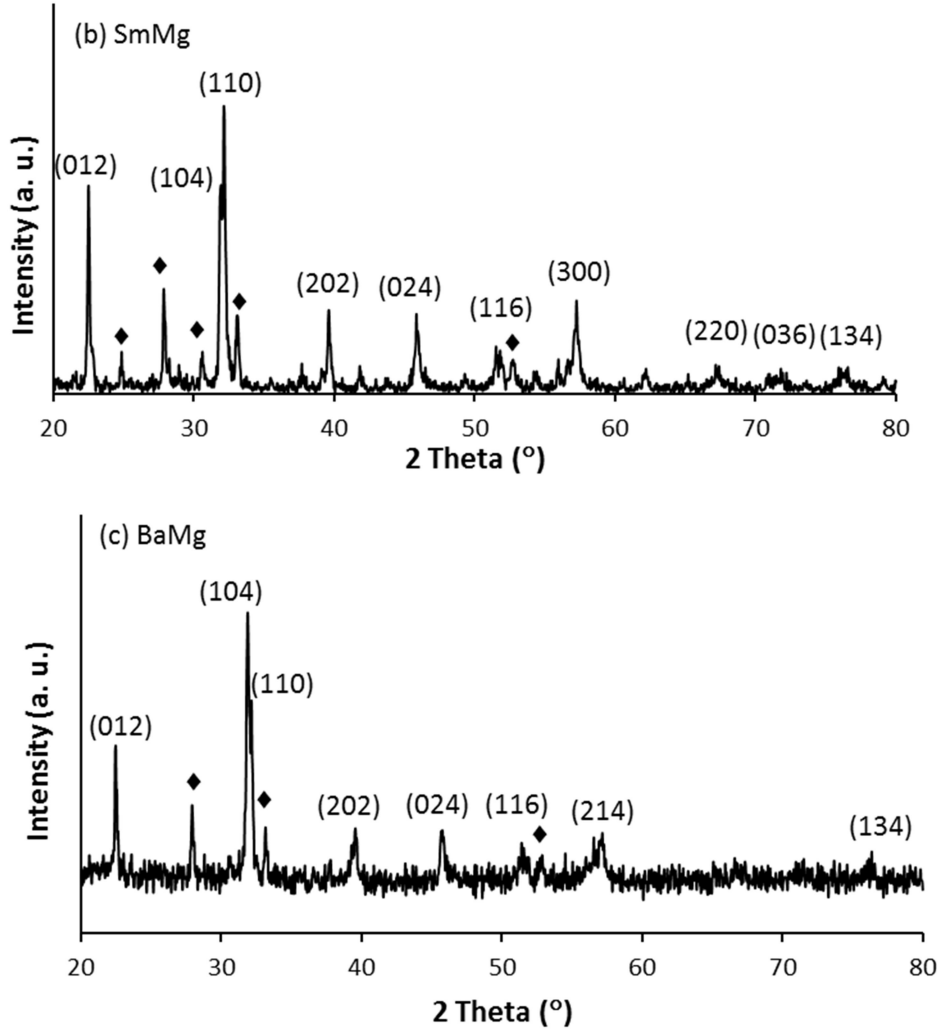


FIG. 1. The XRD patterns of (a) GdMg, (b) SmMg and (c) BaMg.

TABLE 1. The structural parameters of the studied compounds.

Compound	a (\AA)	c (\AA)	V (\AA^3)
GdMg	5.5685 ± 0.0003	13.7794 ± 0.0018	370.04 ± 0.05
SmMg	5.5691 ± 0.0003	13.7900 ± 0.0018	370.39 ± 0.05
BaMg	5.5767 ± 0.0005	13.7863 ± 0.0020	371.31 ± 0.05

It should be observed from the table that, due to the small difference between the radii of Gd^{3+} and Sm^{3+} , the cell volume has undergone a small change, but this is not the case for Ba^{2+} which has a relatively large radius. In conclusion, the substituting process has caused a lattice distortion (greatest for BaMg) which manifests itself in a change in the Bi/Fe-O bond length and the Fe-O-Fe bond angle [15, 27].

Another important point that we want to consider is the existence of traces of the magnetic phases Fe_3O_4 (PDF # 87-2334), BaFe_2O_4 (PDF # 70-1441) and/or $\alpha\text{-Fe}_2\text{O}_3$ (PDF # 33-0664). In fact, a careful search-match process did not reveal any traces of the ferrite phases Fe_3O_4 and BaFe_2O_4 in all compounds.

Moreover, it was hard to discover traces of the hematite phase $\alpha\text{-Fe}_2\text{O}_3$ using the search-match process due to the proximity of the strong (104) reflection peak of $\alpha\text{-Fe}_2\text{O}_3$ to the (321) reflection peak of $\text{Bi}_{25}\text{FeO}_{40}$ (PDF # 78-1543). But, as we will see, traces of the hematite phase do exist in the BaMg compound.

FTIR spectroscopy is an analytical technique used to measure the absorption of infrared radiation by the sample material *versus* wavelength. The infrared absorption bands identify the vibrational modes of the building units. Fig. 2 shows the FTIR spectra for the GdMg, SmMg and BaMg compounds in the wavenumber range $400 - 2000 \text{ cm}^{-1}$. The absorption peaks at $573, 575$ and 567 cm^{-1}

(indicated by vertical lines) correspond to the Fe-O stretching vibrations in the FeO_6 octahedral unit of each compound. In the FTIR spectra of GdMg and SmMg, we can see two prominent peaks at 455 and 457 cm^{-1} (indicated by x's),

corresponding to the O-Fe-O bending vibrations. Four additional non-intrinsic prominent absorption peaks (at 824, 877, 1036 and 1449 cm^{-1}) can be observed in the BaMg spectrum.

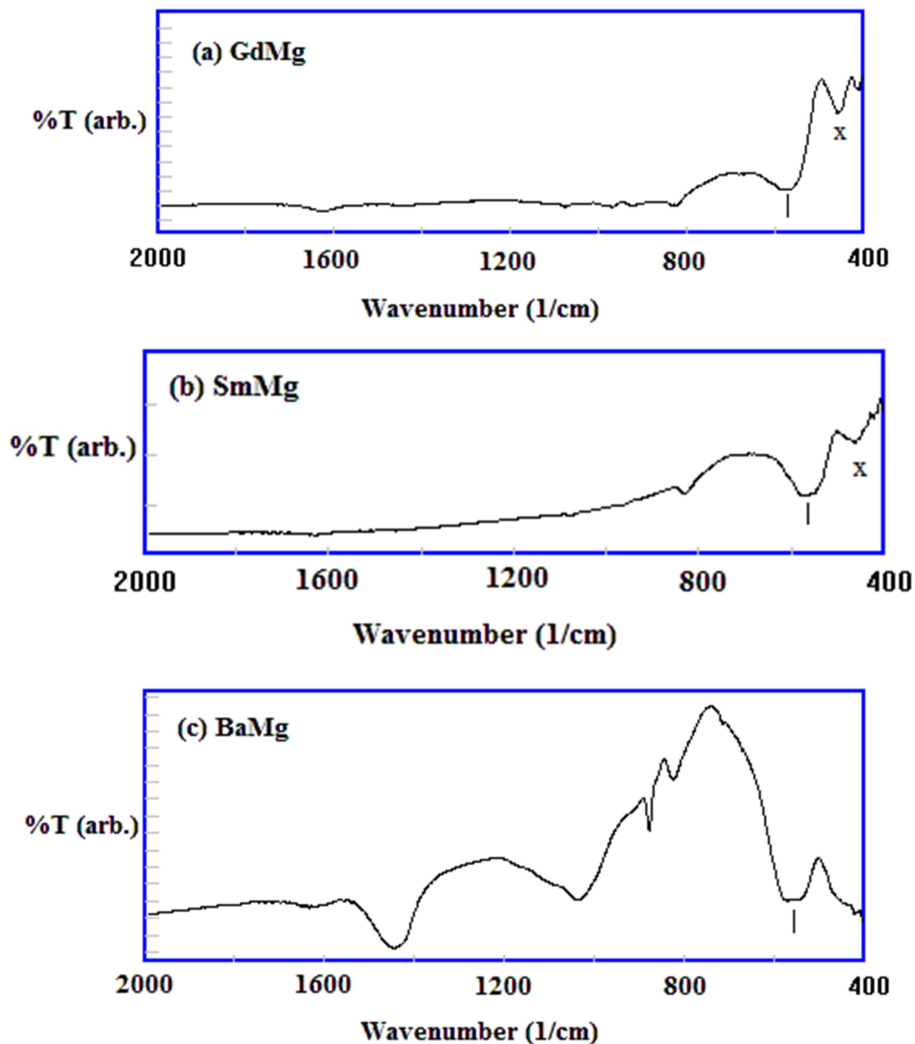


FIG. 2. The FTIR spectra of (a) GdMg, (b) SmMg and (c) BaMg.

Some researchers reported two peaks at 815 and 878 cm^{-1} (close to our first two values) in the FTIR spectrum of Ho-substituted BFO [15] that were attributed to the absorption of water and CO_2 from the environment. In fact, we checked up the FTIR spectra of water and CO_2 in the NIST WebBook and found that these peaks cannot be attributed to water and CO_2 ; they are better attributed to the $\alpha\text{-Fe}_2\text{O}_3$ hematite phase (the NIST WebBook). The last two peaks in the BaMg spectrum could have resulted from other unidentified impurities (probably in KBr).

The room temperature hysteresis loops of the compounds are shown in Fig. 3. It is seen that the compounds GdMg and SmMg exhibit weak ferromagnetism with unsaturated magnetization.

The BaMg compound exhibits an enhanced ferromagnetic behavior with an open hysteresis loop. Since the concentration of Mg^{2+} ions in all compounds is the same, the effect of these ions on the magnetization is invariant. The values of the remnant magnetization M_r and coercive field H_c are listed in Table 2. It is known that there are several reasons for the appearance of weak ferromagnetism in BFO-substituted compounds. They include suppression of the helical spin structure of BFO due to lattice distortion, change of the oxidation state of the substituting ions, creation of oxygen vacancies, magnetic impurities and/or chemical inhomogeneity. As seen in Table 2, the M_r value of SmMg is 0.0388 emu/g and that of GdMg is 0.0924 emu/g, which

is about 2.4 greater than that of SmMg. Such a difference cannot be explained solely based on lattice distortion and/or oxygen vacancies, since, as we mentioned earlier, the lattice distortion in each compound is nearly the same as there is no much difference between the ionic radii of Gd^{3+} and Sm^{3+} and both ions have the same oxidation state so the that effect of oxygen vacancies is nullified. We think that the plausible explanation is that, since the magnetic moment of Gd^{3+} is greater than that of Sm^{3+} , both ions doped at the Bi^{3+} sites would cause magnetic coupling interactions with the Fe^{3+} ions (the Gd^{3+} - Fe^{3+} interaction is greater and would lead to enhancement of ferromagnetism in the GdMg compound).

Now let's get back to BaMg, which has an M_r value of 0.857 emu/g (greater than the GdMg value by a factor of about 9.3). Ba^{2+} ions doped

at the Bi^{3+} sites are not magnetic and as we have seen, lattice distortion is the greatest in BaMg. But, this is not sufficient to cause such a large change in ferromagnetism. We think that the real cause of such a relatively large magnetization is the parasitic $\alpha\text{-Fe}_2\text{O}_3$ hematite phase, which is a soft ferromagnet at room temperature and masks the intrinsic magnetization of the sample. This result is in agreement with other reported investigations [31, 32]. But, what is the reason for the large value of H_c ? In fact, the role of oxygen vacancies cannot be overlooked. Since the oxidation state of Ba^{2+} is different from that of Bi^{3+} , charge neutrality in BaMg is accomplished *via* the creation of oxygen vacancies: structural defects that increase magnetic anisotropy and, consequently, increase the value of H_c .

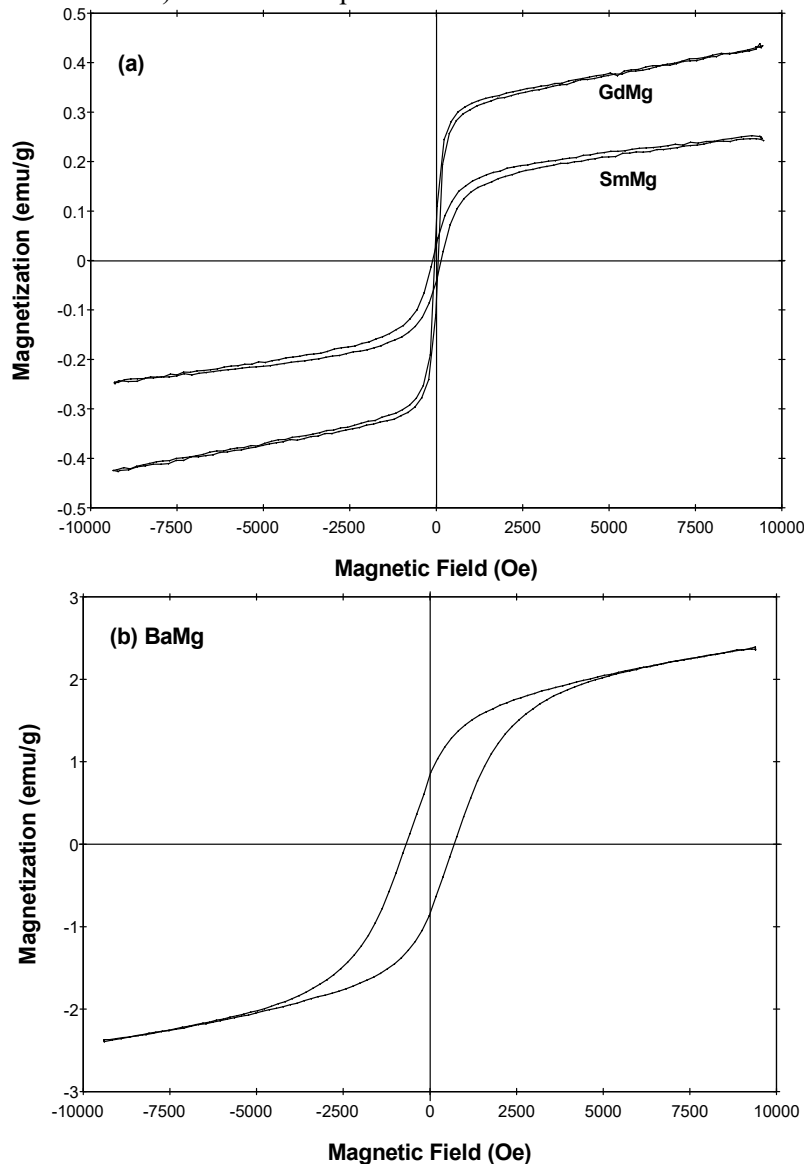


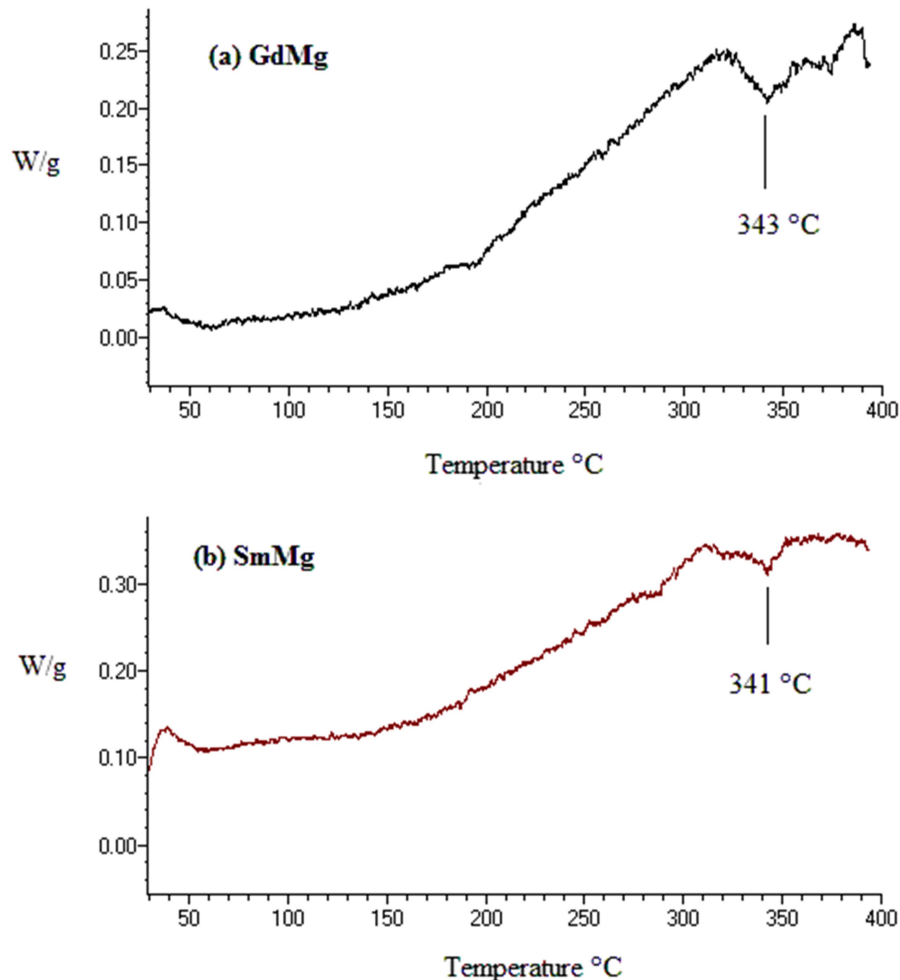
FIG. 3. The magnetic hysteresis loops of (a) GdMg; SmMg and (b) BaMg.

TABLE 2. Some magnetic parameters of the compounds.

Compound	M_r (emu/g)	H_c (Oe)	T_N (°C)
GdMg	0.0924	70	343
SmMg	0.0388	107	341
BaMg	0.857	693	340

DSC is a thermal technique that can be used to measure a number of characteristic properties of a sample, such as fusion, crystallization, oxidation and glass transition. One less common use of DSC is to identify the magnetic transition temperature T_N , which is revealed by a weak endothermic peak on the DSC scan. In practice, such a peak is hard to detect, because it could overlap with other noisy signals, especially if the baseline is fluctuating with temperature. Nonetheless, by the proper choice of sample mass and heating rate, the transition can be

detected. Fig. 4 shows the DSC scans of the compounds and their magnetic transition temperatures are listed in Table 2. Taking into consideration that $T_N \cong 370$ °C for pure BFO, the obtained values seem to be reasonable. Comparatively, a magnetic transition temperature of 350 °C was reported for $\text{Bi}_{0.95}\text{Sr}_{0.05}\text{FeO}_3$ using DSC [18]. Based on the weak magnetism of these materials, the T_N values obtained are nearly the same.



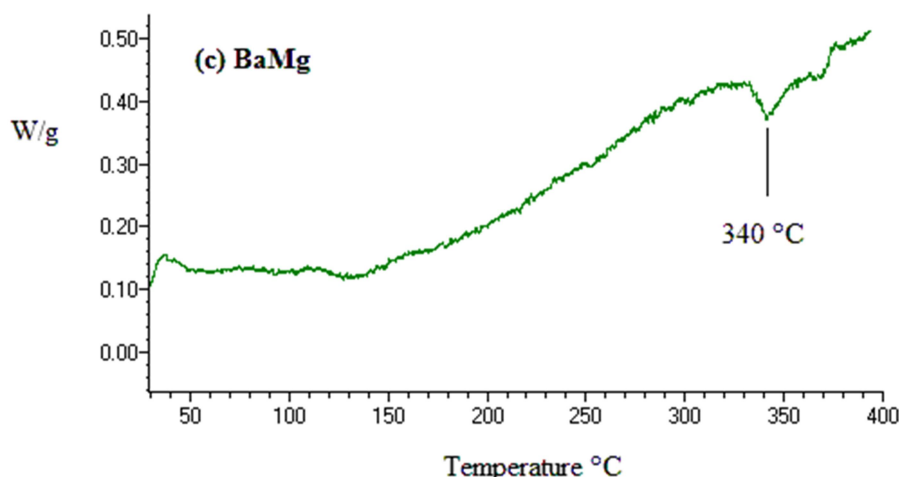


FIG. 4. The DSC curves of (a) GdMg, (b) SmMg and (c) BaMg.

4. Conclusions

We have carried out a comparative study of the structural and magnetic properties of the compounds GdMg, SmMg and BaMg, prepared by the mixed oxide method. They have been explored by structural, spectroscopic, magnetic

and thermal techniques. We have found that the magnetization of GdMg and SmGd is intrinsic in origin, while that of BaMg is masked by the impurity magnetic phase. One has to be very careful in explaining the magnetic data, because otherwise misleading results would be obtained.

References

- [1] Catalan, G. and Scott, J.F., *Adv. Mater.*, 21 (2009) 2463.
- [2] Singh, H. and Yadav, K.L., *Ceramics Inter.*, 41 (2015) 9285.
- [3] Wei, J. and Xue, D., *Mater. Res. Bull.*, 43 (2008) 3368.
- [4] Alemi, A. and Purhasan, A., *J. Mater. Sci.: Mater. Electron.*, 28 (2017) 14476.
- [5] Maleki, H., Haselpour, M. and Fathi, R., *J. Mater. Sci.: Mater. Electron.*, 29 (2018) 4320.
- [6] Haumont, R., Saint-Martin, R. and Byl, C., *Phase Trans.*, 81 (2008) 881.
- [7] Ali, Z., Atta, A., Abbas, Y., Sedeek, K., Adam, A. and Abdeltwab, E., *Thin Solid Films*, 577 (2015) 124.
- [8] Wu, L., Sui, W., Dong, C., Zhang, C. and Jiang, C., *Appl. Surf. Sci.*, 384 (2016) 368.
- [9] Lotey, G.S. and Verma, N.K., *Mater. Sci. Semicond. Process.*, 21 (2014) 206.
- [10] Gómez, J., Canaria, C., Burgos, R., Ortiz, C., Supelano, G. and Vargas, C., *J. Phys.: Conf. Ser.*, 687 (2016) 012091.
- [11] Wu, Y.J., Qin, Z.X., Chen, X.K., Zhang, J., Liu, J., Wu, Z. and Chen, X.J., *J. Phys.: Condens. Matter*, 25 (2013) 365401.
- [12] Uniyal, P. and Yadav, K.L., *J. Phys.: Condens. Matter*, 21 (2009) 012205.
- [13] Kumar, S., *J. Mater. Sci.: Mater. Electron.*, 24 (2013) 2112.
- [14] Sharma, S., Mishra, A., Saravanan, P., Pandey, O.P. and Sharma, P., *J. Magn. Magn. Mater.*, 418 (2016) 188.
- [15] Singh, H. and Yadav, K.L., *J. Phys. D: Appl. Phys.*, 48 (2015) 205001.
- [16] Zhang, H., Liu, W.F., Wu, P., Hai, X., Wang, S.Y., Liu, G.Y. and Rao, G.H., *J. Nanopart. Res.*, 16 (2014) 2205.
- [17] Guo, M.C., Liu, W.F., Wu, P., Zhang, H., Xu, X.L., Wang, S.Y. and Rao, G.H., *Chin. Phys. Lett.*, 32 (2015) 066101.
- [18] Mandal, S., Rakshit, T., Ray, S., Mishra, S., Krishna, P. and Chandra, A., *J. Phys.: Condens. Matter*, 25 (2013) 055303.
- [19] Ma, Y., Tang, X., Lu, M., Zheng, K., Mao, W., Zhang, J., Yang, J. and Li, X., *J. Supercond. Nov. Magn.*, 28 (2015) 3593.

- [20] Wang, C.A., Pang, H.Z., Zhang, A.H., Qin, M.H., Lu, X.B., Gao, X.S., Zeng, M. and Liu, J.M., *J. Phys. D: Appl. Phys.*, 48 (2015) 395302.
- [21] Kumar, K.S., Venkateswaran, C., Kannan, D., Tiwari, B. and Rao, M.S.R., *J. Phys. D: Appl. Phys.*, 45 (2012) 415302.
- [22] Arya, G.S. and Negi, N.S., *J. Phys. D: Appl. Phys.*, 46 (2013) 095004.
- [23] Ahmmad, B., Islam, M., Billah, A. and Basith, M., *J. Phys. D: Appl. Phys.*, 49 (2016) 095001.
- [24] Khomchenko, V. and Paixão, J., *J. Phys.: Condens. Matter*, 27 (2015) 436002.
- [25] Kumar, P., Panda, C. and Kar, M., *Smart Mater. Struct.*, 24 (2015) 045028.
- [26] Mohanty, S., Kumar, A. and Choudhary, R.N.P., *J. Mater. Sci.: Mater. Electron.*, 26 (2015) 9640.
- [27] Zhu, Y., Quan, C., Ma, Y., Wang, Q., Mao, W., Wang, X., Zhang, J., Min, Y., Yang, J., Li, X. and Huang, W., *Mater. Sci. Semicond. Process.*, 57 (2017) 178.
- [28] Yu, B., Li, M., Wang, J., Pei, L., Guo, D. and Zhao, X., *J. Phys. D: Appl. Phys.*, 41 (2008) 185401.
- [29] Al-Haj, M., *Turk. J. Phys.*, 36 (2012) 415.
- [30] Holland, T. and Redfern, S., *Mineral. Mag.*, 61 (1997) 65.
- [31] Al-Haj, M., *Cryst. Res. Technol.*, 45 (2010) 1145.
- [32] Nayek, C., Tamilselvan, A., Thirimal, C., Murugavel, P. and Balakumar, S., *J. Appl. Phys.*, 115 (2014) 073902.

Structural and Magnetic Properties of $\text{La}_{2/3}\text{D}_{1/3}\text{MnO}_3$ (D = Ca, Sr, Ba) Manganites Prepared By Ball Milling

Sami Mahmood^a, Haneen Badran^a, Eman Al-Hwaitat^a, Ibrahim Bsoul^b and Rola Bqaen^c

^a Department of Physics, The University of Jordan, Amman 11942, Jordan.

^b Department of Physics, Al al-Bayt University, Al-Mafraq 13040, Jordan.

^c Cell Therapy Center, The University of Jordan, Amman 11942, Jordan.

Received on: 1/10/2018;

Accepted on: 8/10/2018

Abstract: In this research, we report on the synthesis and characterization of $\text{La}_{0.67}\text{Ca}_{0.33}\text{MnO}_3$ (LCMO), $\text{La}_{0.67}\text{Ba}_{0.33}\text{MnO}_3$ (LBMO) and $\text{La}_{0.67}\text{Sr}_{0.33}\text{MnO}_3$ (LSMO) perovskites. Precursor powders for the perovskite samples were prepared using ball milling technique. The resulting powder was pressed into disks which were subsequently sintered at 1000°C for 2h. The structural characteristics of the prepared samples were investigated using X-ray diffraction (XRD) and scanning electron microscope (SEM), while the magnetic properties were investigated using vibrating sample magnetometry (VSM). XRD pattern of LCMO sample revealed a pure perovskite phase with $Pnma$ space group, while the pattern of LSMO sample revealed a pure perovskite with $R\bar{3}c$ space group. XRD pattern of LBMO sample, however, demonstrated the presence of a major perovskite phase with $R\bar{3}c$ symmetry, together with a secondary BaMnO_3 phase. This secondary phase disappeared upon sintering LBMO at a higher temperature of 1100°C . Isothermal magnetic measurements and thermomagnetic curves revealed that LCMO was paramagnetic at room temperature. However, LSMO exhibited soft ferromagnetic behavior at room temperature, with $T_c = 380\text{K}$ and $M_s = 50.9\text{emu/g}$. Also, LBMO sample sintered at 1000°C exhibited soft ferromagnetic behavior at room temperature, with Curie temperature $T_c = 343\text{K}$ and a rather low saturation magnetization of $M_s = 30.7\text{emu/g}$. The higher sintering temperature of LBMO compound resulted in a significant increase of the saturation magnetization to 50.8emu/g for the sample sintered at 1100°C .

Keywords: Perovskites, Structural properties, Magnetic properties, Thermomagnetic curves.

1. Introduction

Doped perovskite manganites with the general formula $\text{T}_{1-x}\text{D}_x\text{MnO}_3$, where T is a trivalent lanthanide cation and D is a divalent cation, have been the focus of many studies due to their interesting structural, magnetic, transport and electronic structure properties [1]. Perovskites are of vital interest to a wide community of material scientists, not only because of the fascinating phenomena and properties exhibited (such as colossal magneto-

resistance (CMR), metal-insulator transition, charge ordering (CO), phase separation and magneto-caloric effect (MCE) [2-5]), but also due to their potential technological applications in magnetic recording [6] and gas sensors [7-9].

LaMnO_3 compound is an antiferromagnetic insulator below Néel temperature ($T_N = 143\text{K}$) [10]. The partial substitution of La^{3+} ions by a divalent ion D^{2+} (such as Ba^{2+} , Sr^{2+} , Ca^{2+} , Pb^{2+}) induces the conversion of some of the Mn^{3+} ions

into tetravalent (Mn^{4+}) ionic state, where the fraction of the tetravalent ions is equal to the fraction of the divalent ions according to the formula $\text{La}_{1-x}\text{D}_x\text{Mn}_{1-x}^{3+}\text{Mn}_x^{4+}\text{O}_3$. This is responsible for the development of a ferromagnetic state in the manganites and the wealth of fascinating structural, magnetic, magnetocaloric, magnetotransport and other phenomena observed in these compounds. Traditionally, double exchange (DE) interactions between Mn^{3+} and Mn^{4+} ions were proposed to explain the magnetic and magnetotransport behavior in these compounds. Theoretical studies, however, have demonstrated that DE alone does not explain the magnetotransport behavior in $\text{La}_{1-x}\text{D}_x\text{MnO}_3$ [11, 12]. The structural characteristics, magnetic properties and Curie

temperature of the compound are critically sensitive to the type and concentration of the divalent ion [1]. The Ca^{2+} doped manganites (LCMO) were found to exhibit ferromagnetic behavior below room temperature, which is a disadvantage in using these materials in devices operating at room temperature. Also, significant fluctuations in the Curie temperature of this compound were found in the literature, which cannot be associated with Ca^{2+} concentration (x) in the compound or the method of preparation in a systematic manner. Examples of reported values of Curie temperatures for $\text{La}_{1-x}\text{Ca}_x\text{MnO}_3$ compounds are listed in Table 1. It is important to remember that variations from $x = 0.3$ to $x = 0.33$ are negligible [13].

TABLE 1. Curie temperature of $\text{La}_{1-x}\text{Ca}_x\text{MnO}_3$ compounds prepared by different methods.

x	T_c (K)	Preparation method (Heat treatment)	Reference
0.20	256	Sol-gel method (1000° C)	[14]
0.20	236	Sol-gel method (1000° C)	[15]
0.25	224	Sol-gel method (1000° C, 1400° C)	[16]
0.30	220	Solid State Reaction (1200° C)	[17]
0.30	255	Solid State Reaction (1250° C, 1400° C)	[18]
0.33	260	Solid State Reaction (1100° C, 1200° C, 1300° C)	[13]
0.33	260.4	Solid State Reaction (800° C, 1300° C)	[19]
0.50	230	Pyrophoric method (1000° C)	[20]

Upon substituting La^{3+} by Pb^{2+} (LPMO), Ba^{2+} (LBMO) or Sr^{2+} (LSMO), the Curie temperature was found to increase to room temperature and above. At $x = 0.3$, Curie temperature for LPMO, LBMO and LSMO were found to be 300 K, 330 K and 370 K, respectively [13, 17]. Also, Curie temperature for $\text{La}_{0.67}\text{Ba}_{0.33}\text{MnO}_3$ was reported to be 335.1 K [19] and 332 K [21] and Curie temperature for $\text{La}_{0.7}\text{Sr}_{0.3}\text{MnO}_3$ reported by different research groups was found to be 342.6 K [19], 354 K [22], 369 K [10] and 378.1 K [23]. In addition, a systematic study of the effect of partial substitution of La^{3+} by Pb^{2+} revealed transformation of the compound to a ferromagnetic state, with Curie temperature increasing with the level of substitution from 235 K for $x = 0.1$ to 360 K for $x = 0.4$ and improvement of the magnetocaloric effect [24]. Others, however, reported a rather low Curie temperature of 150 K for $\text{La}_{0.67}\text{Sr}_{0.33}\text{MnO}_3$ and weak magnetization with almost linear behavior in the field range > 2000 Oe [25]. Further, the substitution of La^{3+} by mixtures of divalent ions was used to tailor the Curie temperature and

properties of the perovskites for application in specific working temperature regimes [3, 26-30]. However, unsystematic variations of the Curie temperature of manganites produced by different methods at different research laboratories were observed for compounds with nominally identical compositions [1].

A large amount of research work was dedicated to understand the rich structural and magnetic phase diagram exhibited by these compounds [10, 13, 31, 32]. The room-temperature structural results of Urushibara et al. [10] indicated that $\text{La}_{1-x}\text{Sr}_x\text{MnO}_3$ perovskite exhibited orthorhombic $Pbnm$ symmetry in the range $0 < x < 0.175$, with lattice parameters: $5.54 \text{ \AA} > a > 5.51 \text{ \AA}$, $5.75 \text{ \AA} > b > 5.51 \text{ \AA}$ and $7.69 \text{ \AA} < c < 7.80 \text{ \AA}$. At higher Sr doping up to $x = 0.4$, the structure changes to rhombohedral symmetry with $R\bar{3}c$ space group. In another study, the lattice parameters of the compound (LSMO, $x = 0.33$) were found to be: $a = b = 5.4879 \text{ \AA}$, $c = 13.3622 \text{ \AA}$ [33]. These parameters are somewhat lower than the values observed by Zhang et al. (a

$= b = 5.5212 \text{ \AA}$, $c = 13.3797 \text{ \AA}$) [19] and are in better agreement with the lattice parameters of $a = b = 5.5039 \text{ \AA}$, $c = 13.3553 \text{ \AA}$ reported for (LSMO, $x = 0.3$) [34]. On the other hand, $\text{La}_{0.67}\text{Ca}_{0.33}\text{MnO}_3$ (LCMO, $x = 0.33$) was characterized by orthorhombic $Pnma$ structure with lattice parameters: $a = 5.435 \text{ \AA}$, $b = 7.691 \text{ \AA}$, $c = 5.436 \text{ \AA}$ [35]. Zhang et al., however, reported an orthorhombic $Pbnm$ structure with lattice parameters of $a = 5.4744 \text{ \AA}$, $b = 5.4601 \text{ \AA}$, $c = 7.7147 \text{ \AA}$ for (LCMO, $x = 0.33$) [19]. Also, LCMO, $x = 0.3$ exhibited orthorhombic $Pbnm$ symmetry with lattice parameters $a = 5.462 \text{ \AA}$, $b = 5.478 \text{ \AA}$, $c = 7.720 \text{ \AA}$ [18]. In addition, the structural characterization of $\text{La}_{2/3}(\text{Ca}_{1-x}\text{Sr}_x)_{1/3}\text{MnO}_3$ indicated that the structure of the compound with $x = 0$ is orthorhombic with $Pbnm$ space group and that Sr doping levels above 0.05 ($x \geq 0.15$) transform the structure to rhombohedral with $R\bar{3}c$ space group [32]. At this point, it is worth mentioning that $Pbnm$ space group is equivalent to $Pnma$ with a different choice of axes, where a , b , c in $Pbnm$ become c , a , b in $Pnma$ [1]. Further, a comprehensive neutron diffraction study of $\text{A}_{0.7}\text{A}'_{0.3}\text{MnO}_3$ (A = Pr, La, La-Pr; A' = Ca, Sr, Ba, Ca-Sr, Ba-Sr) perovskites was conducted by Radaelli et al. [36]. Room temperature neutron diffraction results indicated that all compounds with Ca^{2+} fraction ≥ 0.17 are orthorhombic with $Pnma$ space group and lattice parameters: $5.4585 \text{ \AA} < a < 5.4690 \text{ \AA}$, $7.6749 \text{ \AA} < b < 7.7292 \text{ \AA}$ and $5.4308 \text{ \AA} < c < 5.5045 \text{ \AA}$. However, all LSMO, LBMO and LBSMO compounds revealed rhombohedral $R\bar{3}c$ symmetry with lattice parameters: $a = b = 5.5022 \text{ \AA} - 5.5378 \text{ \AA}$ and $c = 13.3291 \text{ \AA} - 13.5011 \text{ \AA}$.

Several experimental techniques were used for the preparation of precursor powders of magnetic oxides [37-42]. Ball milling is one of the important commonly used methods due to its simplicity and flexibility of controlling the processing parameters in producing a wide range of materials [43-45]. In this work, we report on the ball-milling synthesis, as well as structural and magnetic studies of $\text{La}_{0.67}\text{D}_{0.33}\text{MnO}_3$ (D = Ca, Sr, Ba) perovskites. This work focuses on the effects of the type of divalent ion on the magnetic properties and magnetocrystalline anisotropy in these compounds.

2. Experimental

2.1 Material Preparation

In this study, homogeneous precursor powder mixtures of $\text{La}_{0.67}\text{D}_{0.33}\text{MnO}_3$ manganites (D = Ca, Sr, and Ba) were prepared by ball milling stoichiometric amounts of the starting powders. The starting powders were high-purity La_2O_3 , DCO_3 and MnO with molar ratios of 0.335:0.330:1.000. The powders were mixed and milled in a planetary ball mill (Pulverisette-7) with a powder to ball mass ratio of 1:12. The milling was carried out for 16 h at a rotational speed of 250 rpm. Disc-shape pellets were made by pressing parts of the powder mixtures in a stainless steel die under a pressure of 5 T. Then, the pellets were sintered in a box oven at 1000°C for 2 h using a temperature rate of increase of $10^\circ\text{C}/\text{min}$. Since LBMO was not a pure phase as revealed by XRD data, a sample of this compound was sintered at 1100°C in order to investigate the effect of sintering temperature on the structural properties of this compound.

2.2 Material Characterization

The structural characteristics of the synthesized samples were examined by X-ray diffraction (XRD). XRD patterns were collected in the angular range $20^\circ \leq 2\theta \leq 70^\circ$ with a step of 0.01° and a scan speed of $0.5^\circ/\text{min}$. The particle size and morphology of the prepared materials were examined by scanning electron microscopy (SEM). The magnetic properties of the samples were investigated using a conventional vibrating sample magnetometry (VSM) operating at an applied magnetic field up to 10 kOe.

3. Results and Discussion

3.1 XRD Measurements

Fig. 1 shows that the XRD patterns of $\text{La}_{0.67}\text{Sr}_{0.33}\text{MnO}_3$ (LSMO) and $\text{La}_{0.67}\text{Ca}_{0.33}\text{MnO}_3$ (LCMO) samples revealed the presence of a single perovskite phase with no detectable secondary phases. However, XRD pattern of $\text{La}_{0.67}\text{Ba}_{0.33}\text{MnO}_3$ sintered at 1000°C (LBMO 1000) showed a perovskite phase and a secondary phase as revealed by the additional reflections at $2\theta = 25.8^\circ$ and 31.356° , 41.1° and 55.9° (Fig. 2). These reflections are consistent with those of the standard pattern for BaMnO_3 (JCPDS: 00-026-0168). The appearance of a secondary phase in (LBMO 1000) sample is an indication of incomplete crystallization of the

perovskite phase at a sintering temperature of 1000° C and the attainment of a pure perovskite LBMO phase may require modifications of the synthesis route and heat treatment. Accordingly,

another sample of LBMO was sintered at 1100° C (LBMO 1100) and studied to examine the effect of sintering temperature on the structural and magnetic properties of this compound.

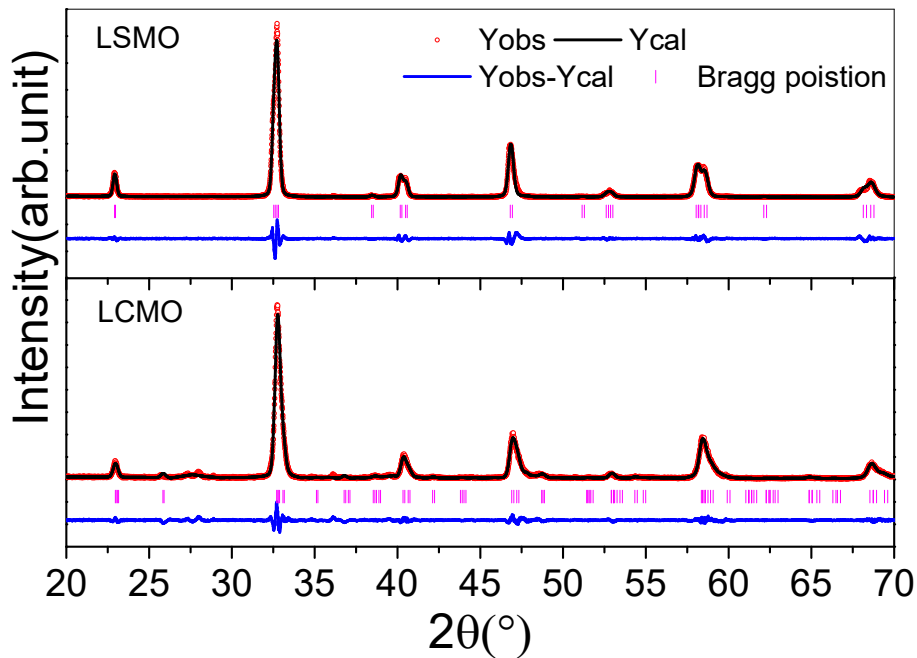


FIG. 1. Rietveld plots of XRD data of $\text{La}_{0.67}\text{Ca}_{0.33}\text{MnO}_3$ (LCMO) and $\text{La}_{0.67}\text{Sr}_{0.33}\text{MnO}_3$ (LSMO) compounds.

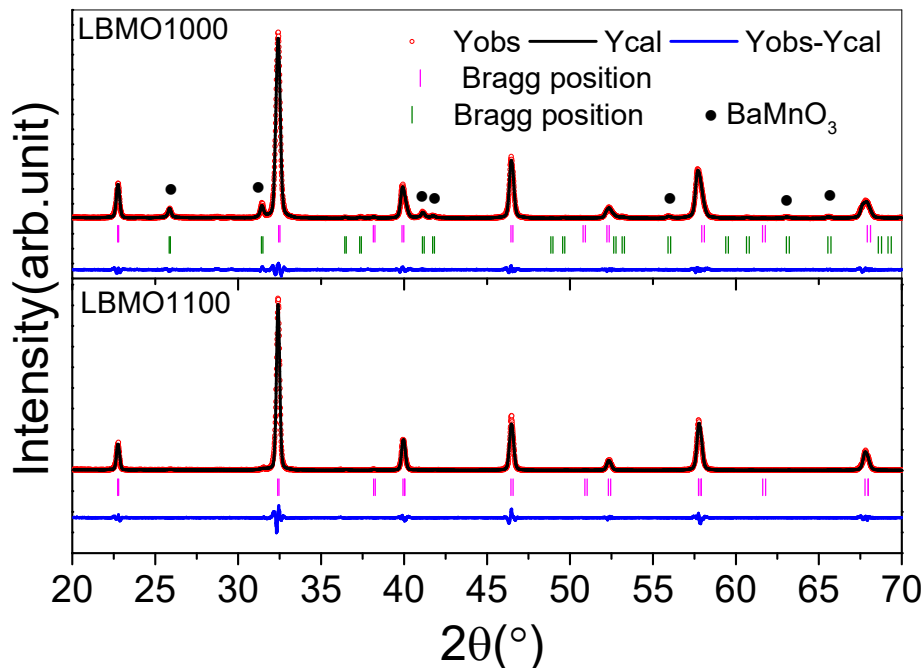


FIG. 2. Rietveld plots of XRD data of $\text{La}_{0.67}\text{Ba}_{0.33}\text{MnO}_3$ samples sintered at 1000° C (LBMO 1000) and at 1100° C (LBMO 1100).

Comparison of the XRD patterns of (LBMO 1000) and (LBMO 1100) samples in Fig. 2 revealed significant improvement of the crystallization of the perovskite phase at 1100° C. This improvement was demonstrated by the disappearance of the reflections corresponding to the secondary BaMnO_3 phase and the reduction

of the width of the structural peaks of LBMO perovskite phase, indicating that LBMO perovskite phase requires higher formation temperature in comparison with LSMO and LCMO.

Rietveld analysis of the diffraction patterns of all samples was carried out to investigate the

microstructural characteristics and obtain the refined structural parameters of each sample. The refined lattice parameters a , b and c , as well as the cell volume V and X-ray density ρ_x of the samples, are listed in Table 2. The analysis revealed that the LCMO sample consisted of a single perovskite phase with orthorhombic $Pnma$ symmetry. This structural symmetry and observed lattice parameters are consistent with previously reported structural results of LCMO [19, 32, 35]. However, both (LBMO 1100) and LSMO samples revealed the presence of a single perovskite phase with rhombohedral $R\bar{3}c$ symmetry. The lattice parameters of LSMO are in good agreement with previously reported values based on XRD and neutron diffraction data for LSMO, $x = 0.3, 0.33$ [33, 34, 36]. Also, the lattice parameters of LBMO samples are in very good agreement with the values ($a = 5.5378$

\AA , $c = 13.5011 \text{\AA}$) derived from neutron diffraction data [36] and the values ($a = 5.5320 \text{\AA}$, $c = 13.5273 \text{\AA}$) [19] and ($a = 5.5191 \text{\AA}$, $c = 13.5509 \text{\AA}$) [46] derived from XRD data for (LBMO; $x = 0.33$). Further, the observed refined lattice parameters for (LBMO; $x = 0.33$) are in agreement with the values ($a = 5.5336 \text{\AA}$, $c = 13.4838 \text{\AA}$) derived from XRD data for (LBMO; $x = 0.3$) [47]. The structural symmetry of our LBMO samples, however, is different from the reported cubic $Pm\bar{3}m$ symmetry with lattice parameter $a = 3.9075 \text{\AA}$ [48], even though the reported X-ray density of 6.719 g/cm^3 is almost equal to our observed value. Although the cell volume increases from LCMO to LBMO, the X-ray density increases progressively, which can be associated with the progressive increase of the molecular mass of the perovskite.

TABLE 2. Refined lattice parameters and cell volume, x-ray density, Mn–O bond length and Mn–O–Mn bond angle of the perovskite structure in the samples.

Sample	LCMO	LSMO	LBMO1000	LBMO1100
Space group	$Pnma$	$R\bar{3}c$	$R\bar{3}c$	$R\bar{3}c$
a (\AA)	5.42	5.50	5.54	5.53
b (\AA)	7.75	5.50	5.54	5.53
c (\AA)	5.48	13.35	13.49	13.53
V (\AA^3)	230	350	358	358
ρ_x (g/cm^3)	6.07	6.41	6.72	6.72
Mn–O(1) (\AA)	1.937	-	-	-
Mn–O(2) (\AA)	2.274	-	-	-
	1.680	-	-	-
$\langle \text{Mn–O} \rangle$ (\AA)	1.964	1.954	-	1.958
Mn–O(1)–Mn ($^\circ$)	178.5	-	-	-
Mn–O(2)–Mn ($^\circ$)	153.8	-	-	-
$\langle \text{Mn–O–Mn} \rangle$ ($^\circ$)	162.0	165.2	-	172.4

The increase of the cell volume from LCMO to LBMO is associated with the increase of the mean ionic radius $\langle r_A \rangle$ at the A-site, which results in a reduction of the internal chemical pressure in the perovskite unit cell [19]. This leads to a reduction of the distortion in the MnO_6 octahedra and a consequent structural transition from $Pnma$ to $R\bar{3}c$. Careful examination of the structural characteristics of the samples revealed that while the Mn–O distances along the different octahedral axes vary significantly in LCMO, these distances remained constant in both LSMO and LBMO. Also, examination of the angles between the octahedral axes revealed that these angles in LCMO are $\sim 5^\circ, 9^\circ$ and 11°

different from the ideal value of 90° for a perfect octahedron. However, the angles within LSMO octahedra are only $\sim 0.8^\circ$ off and in LBMO the angles are $< 0.2^\circ$ off the ideal value of 90° . These results confirm the reduction of the octahedral distortions in going from LCMO to LBMO. Further, the $\langle \text{Mn–O–Mn} \rangle$ angle increases toward the ideal 180° value in going from LCMO to LBMO (see the values given in Table 2), indicating a reduction of the structural distortion and an improvement of the long-range structural coherence.

The crystallite size for the perovskite phase was determined using Scherrer equation [49]:

$$D = \frac{k\lambda}{\beta \cos(\theta)} \quad (1)$$

Here, $k = 0.91$ for a Gaussian peak profile, λ ($= 1.54 \text{ \AA}$) is the X-ray radiation wave length and β is the full width at half maximum of the diffraction peak. The main structural peaks at $2\theta = 32.788^\circ$ for LCMO, 32.69° for LSMO and 32.41° for LBMO samples were fitted with Gaussian line shape, from which the peak position and full width at half maximum were determined. The peak width was then corrected for instrumental broadening using a standard silicon sample and the corrected peak width was used to evaluate the mean crystallite size in each sample. The analysis indicated that the mean crystallite size for LCMO, LSMO, LBMO1000 and LBMO1100 were 20 nm, 23 nm, 31 nm and 44 nm, respectively. These results indicated that a significant improvement of the crystallization of the perovskite phase is achieved by Ba substitution for La and the increase of the sintering temperature.

3.2 SEM Measurements

SEM images of all samples indicated that the samples are mainly composed of aggregates of submicron, irregularly-shaped particles (Fig. 3). The images of all samples sintered at 1000°C (LCMO (a); LBMO 1000 (b) and LSMO (d)) revealed that the majority of the samples consisted of particles in the size range of $\sim 100 - 300 \text{ nm}$ and that particles with larger size are present with a smaller fraction. Although differences between the images are not obvious, careful examination of the particle size in the various samples makes us believe that the mean particle size in LBMO 1100 sample is higher than in the samples sintered at 1000°C . This is consistent with XRD data which revealed that LBMO 1100 had the highest crystallite size among all samples. In this sample, the higher sintering temperature is responsible for the improvement of crystallization of the perovskite phase.

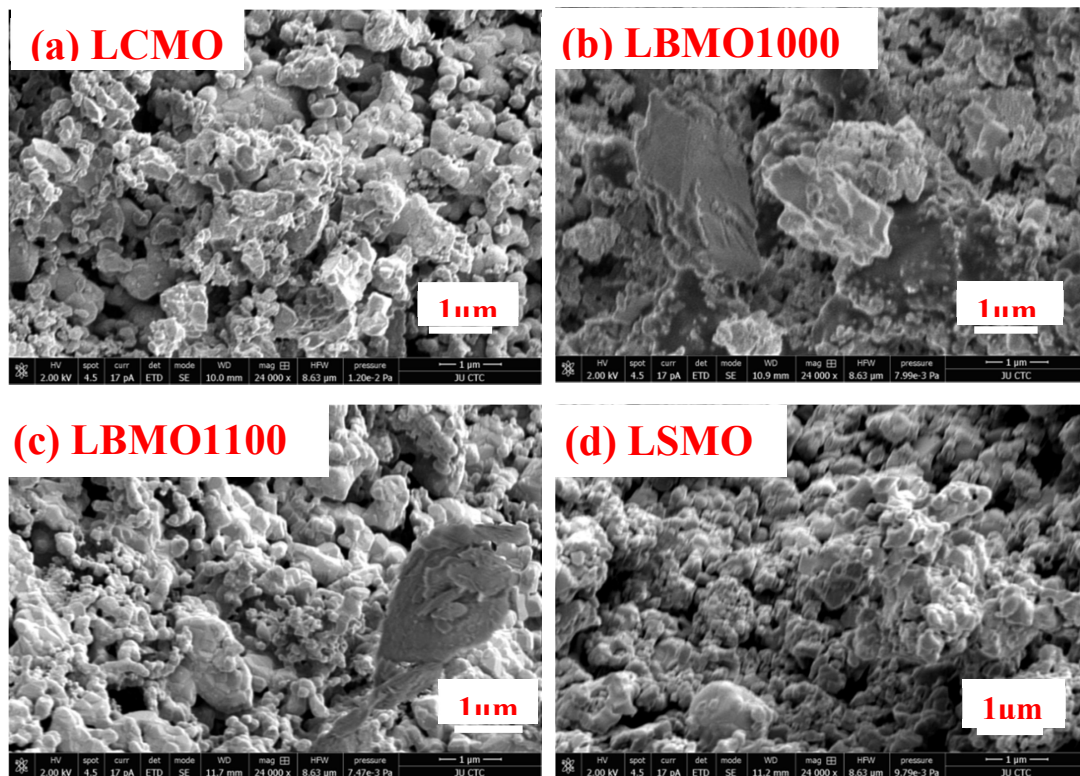


FIG. 3. SEM images for (a) LCMO, (b, c) LBMO and (d) LSMO samples prepared by ball milling.

3.3 Hysteresis Loop Measurements

Room temperature hysteresis loops of all samples were recorded at room temperature using VSM under an applied field up to 10 kOe and are shown in Fig. 4. The hysteresis loops indicated that LCMO is paramagnetic at room

temperature, while LSMO and LBMO samples revealed ferromagnetic behavior with low coercivity as shown in the expanded view (Fig. 5). The saturation magnetization of LBMO sample sintered at 1000°C is significantly lower than that of LSMO, which could be associated with the presence of a nonmagnetic impurity

phase in LBMO 1000. The saturation magnetization of LBMO sintered at 1100°C , however, exhibited a significant increase,

approaching the saturation magnetization of LSMO as demonstrated by Fig. 4.

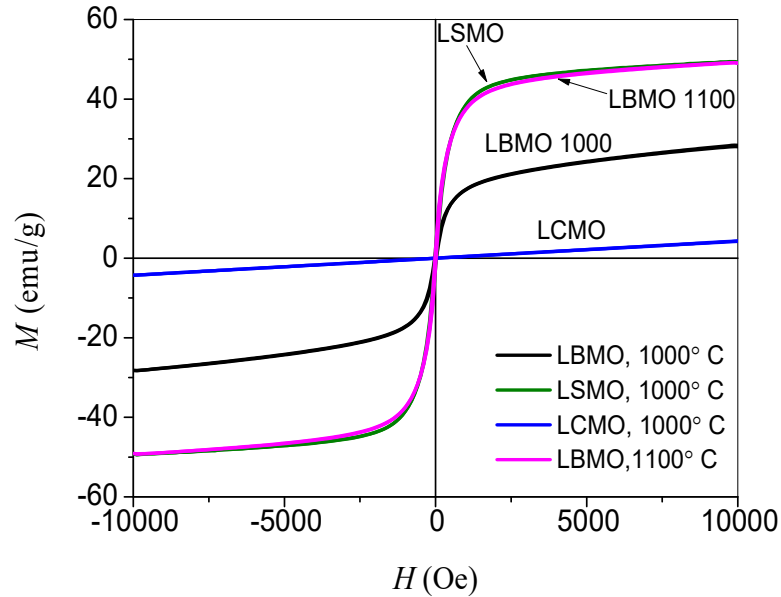


FIG. 4. Hysteresis loops for all samples.

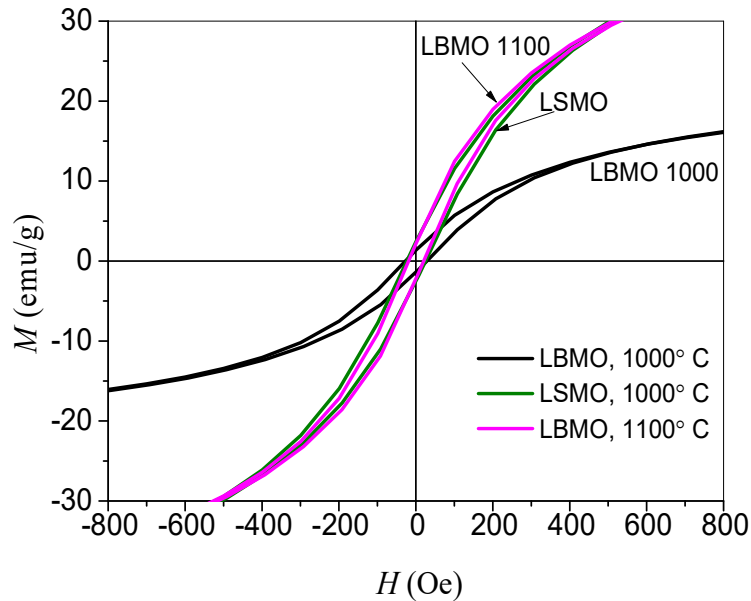


FIG. 5. Expanded hysteresis loops for LBMO and LSMO samples.

Low values of remnant magnetization and coercive fields ($H_c < 20$ Oe) characteristic of soft magnetic materials for LSMO and LBMO samples were determined directly from the hysteresis loops and the results are listed in Table 3. However, accurate determination of the saturation magnetization can be achieved by applying the law of approach to saturation in the high field range. In this range, the rotation of domain magnetization is dominant, where the magnetization is given by [50]:

$$M = M_s \left(1 - \frac{A}{H} - \frac{B}{H^2} \right) + \chi H \quad (2)$$

Here, M_s is the spontaneous saturation magnetization of the domains per unit volume, A is a constant representing the contributions of inclusions/microstress, B is a constant representing the contribution of magnetocrystalline anisotropy and χH is the forced magnetization term. In a uniaxial crystal, the contribution of the magnetocrystalline anisotropy is completely determined by the first

anisotropy constant K_1 , where the constant B for a cubic crystal is given by [51]:

$$B = \frac{0.07619 K_1^2}{M_s^2} \quad (3)$$

Accordingly, the law of approach to saturation was used to obtain the saturation magnetization and magnetocrystalline anisotropy of LSMO and LBMO samples. A plot of M_s vs. $1/H^2$ in the high field region ($8.5 \text{ kOe} < H < 10 \text{ kOe}$) gave a straight line, indicating that the

magnetocrystalline term is dominant in this field range. The saturation magnetization (M_s) was determined from the intercept of the straight line with the magnetization axis, whereas the constant B was determined from the slope, from which the first anisotropy constant was determined using Eq. 3. The derived magnetic parameters of LBMO and LSMO samples are listed in Table 3.

TABLE 3. Saturation magnetization (M_s), remanence (M_r), coercive field (H_c) and first anisotropy constant (K_1) for the samples.

Sample	M_s (emu/g)	M_r (emu/g)	H_c (Oe)	K_1 (10^5 erg/g)
LBMO 1000	30.7	1.03	18.9	3.2
LBMO 1100	50.8	1.43	15.1	3.2
LSMO	50.9	1.63	18.6	3.1

The saturation magnetization of LBMO increased from 30.7 emu/g for the sample sintered at 1000° C to 50.8 emu/g as the sintering temperature increased to 1100° C. This significant improvement of the saturation magnetization is a result of the reduction of the nonmagnetic phase and the improvement of the crystallization of the perovskite phase as a consequence of the increase of the sintering temperature. The saturation magnetization of LBMO 1100 is almost equal to that of LSMO, which is in good agreement with the value of 52 emu/g reported for $\text{La}_{0.67}\text{Ba}_{0.22}\text{Sr}_{0.11}\text{MnO}_3$ prepared by sol – gel and sintering at 1100° C [2]. However, the observed saturation magnetization is higher than the value of ~ 47 emu/g reported for $\text{La}_{0.7}\text{Sr}_{0.3}\text{MnO}_3$ prepared by coprecipitation and sintering at 900° C [52]. As for the magnetocrystalline anisotropy, the first anisotropy constant was found to be almost the same for LSMO and LBMO, indicating similar effect for Ba and Sr on the structural and magnetic properties of the perovskite

manganites. This conclusion is also consistent with the similarity of the saturation magnetization of the pure LSMO and LBMO perovskites.

3.4 Thermomagnetic Measurements

The thermomagnetic curves at a constant applied field of 100 Oe were measured for all samples sintered at 1000° C. A homogeneous sample with sharp magnetic phase-transition at the Curie temperature (T_c) should give a sharp peak in the derivative of the thermomagnetic curve at that temperature. The magnetization curve of LCMO (Fig. 6) exhibited monotonic decrease with the increase of temperature, with no peaks in the derivative curve, indicating that the sample does not exhibit ferromagnetic behavior above room temperature. The derivative curves for LSMO and LBMO samples, however, exhibited peaks corresponding to magnetic phase transitions above room temperature (see Fig. 7).

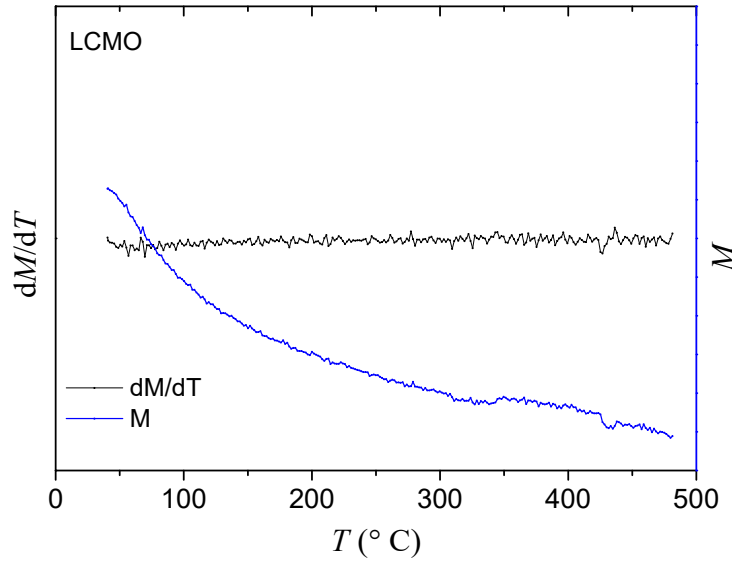


FIG. 6. Thermomagnetic curve (at an applied field of 100 Oe) and its derivative for LCMO sample.

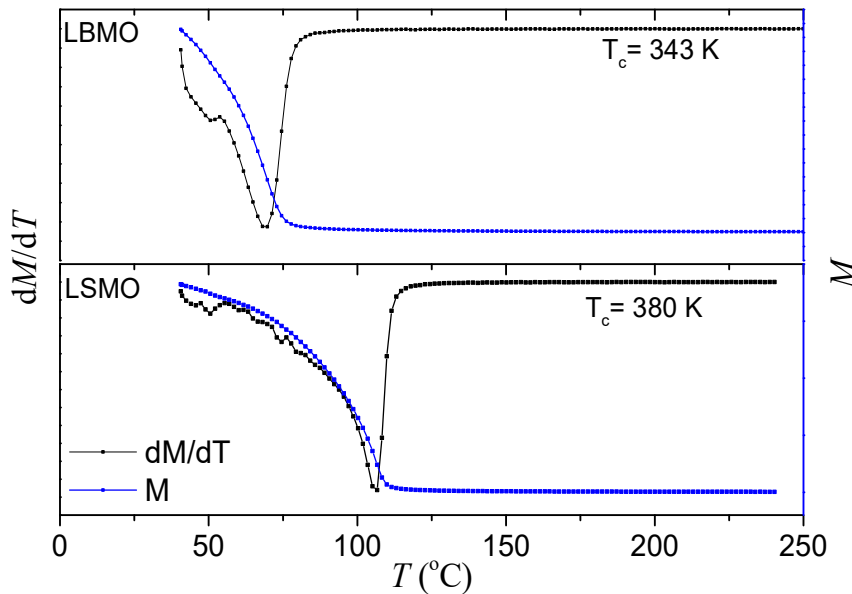


FIG. 7. Thermomagnetic curves (at an applied field of 100 Oe) and their derivatives for LSMO and LBMO samples.

The derivative curve of LSMO sample showed a single peak at 380 K, corresponding to ferromagnetic – paramagnetic phase transition with Curie temperature somewhat higher than previously reported values (see data in Table 4). The broadening of the magnetic transition, however, could be evidence of a small degree of magnetic inhomogeneity arising from small local structural distortions in the sample. On the other hand, the derivative curve of LBMO sample showed a double peak structure, which could be

an indication of magnetic phase separation and the presence of a minority magnetic phase in addition to the major perovskite phase. The temperature (343 K) at which the major peak occurred in the derivative curve is in good agreement with reported values of Curie temperature for LBMO and this peak is therefore associated with ferromagnetic to paramagnetic phase transition of the major magnetic phase in this sample.

TABLE 4. Curie temperatures of LSMO and LBMO compounds compared to values found in the literature.

Sample	T_c (observed)	T_c (from literature)
$\text{La}_{0.67}\text{Sr}_{0.33}\text{MnO}_3$	380 K	342.6 K [19], 370 K [13], 375 K [33], 378 K [1]
$\text{La}_{0.67}\text{Ba}_{0.33}\text{MnO}_3$	343 K	335.1 K [19], 332 K [21], 342 K [47]

4. Conclusions

Pure perovskite $\text{La}_{0.67}\text{Ca}_{0.33}\text{MnO}_3$ and $\text{La}_{0.67}\text{Sr}_{0.33}\text{MnO}_3$ phases were synthesized by high energy ball milling and sintering at 1000° C. This synthesis route, however, was not appropriate to produce a pure $\text{La}_{0.67}\text{Ba}_{0.33}\text{MnO}_3$ phase, where a secondary BaMnO_3 phase appeared in addition to the major perovskite phase. Single LBMO perovskite phase, however, was obtained by sintering the compound at 1100° C and a significant increase of the saturation magnetization from 30.7 emu/g to 50.8 emu/g was observed. The saturation magnetization of the sample sintered at 1100° C was almost equal

to that of LSMO and low coercivity of $H_c < 20$ Oe for all samples was observed. The first magnetic anisotropy constant (K_1) was found to be almost the same for LSMO and LBMO samples. Room temperature isothermal magnetic measurements, however, revealed that LCMO sample was paramagnetic at room temperature. The thermomagnetic measurements showed ferromagnetic–paramagnetic phase transitions for LBMO and LSMO at 343 K and 380 K, respectively and revealed evidence of magnetic inhomogeneity in both samples.

References

- [1] Coey, J.M.D., Viret, M. and Molnár, S.V., *Advances in Physics*, 58 (2009) 571.
- [2] Jemaa, F.B., Mahmood, S., Ellouze, M., Hlil, E.K., Halouani, F., Bsoul, I. and Awawdeh, M., *Solid State Sciences*, 37 (2014) 121.
- [3] Jemaa, F.B., Mahmood, S.H., Ellouze, M., Hlil, E.K. and Halouani, F., *Journal of Materials Science*, 49 (2014) 6883.
- [4] Kolat, V.S., Izgi, T., Kaya, A.O., Bayri, N., Gencer, H. and Atalay, S., *Journal of Magnetism and Magnetic Materials*, 322 (2010) 427.
- [5] Dhahri, Ah., Jemmali, M., Dhahri, E. and Hlil, E.K., *Dalton Transactions*, 44 (2015) 5620.
- [6] Acharya, S., Mondal, J., Ghosh, S., Roy, S.K. and Chakrabarti, P.K., *Materials Letters*, 64 (2010) 415.
- [7] Wang, J., Wu, F.Q., Shi, K.H., Wang, X.H. and Sun, P.P., *Sensors and Actuators B: Chemical*, 99 (2004) 586.
- [8] Suo, H., Wu, F., Wang, Q., Liu, G., Qiu, F., Xu, B. and Zhao, M., *Sensors and Actuators B: Chemical*, 45 (1997) 245.
- [9] Martinelli, G., Carotta, M.C., Ferroni, M., Sadaoka, Y. and Traversa, E., *Sensors and Actuators B: Chemical*, 55 (1999) 99.
- [10] Urushibara, A., Moritomo, Y., Arima, T., Asamitsu, A., Kido, G. and Tokura, Y., *Physical Review B*, 51 (1995) 14103.
- [11] Röder, H., Zang, J. and Bishop, A.R., *Physical Review Letters*, 76 (1996) 1356.
- [12] Millis, A.J., Littlewood, P.B. and Shraiman, B.I., *Physical Review Letters*, 74 (1995) 5144.
- [13] Mira, J., Rivas, J., Rivadulla, F., Vázquez-Vázquez, C. and López-Quintela, M.A., *Physical Review B*, 60 (1999) 2998.
- [14] Turki, D., Cherif, R., Hlil, E., Ellouze, M. and Elhalouani, F., *International Journal of Modern Physics B*, 28 (2014) 1450230.
- [15] Turki, D., Remenyi, G., Mahmood, S., Hlil, E., Ellouze, M. and Halouani, F., *Materials Research Bulletin*, 84 (2016) 245.
- [16] Guo, Z.B., Zhang, J.R., Huang, H., Ding, W.P. and Du, Y.W., *Applied Physics Letters*, 70 (1997) 904.
- [17] Thomas, R.M., Ranno, L. and Coey, J.M.D., *Journal of Applied Physics*, 81 (1997) 5763.

- [18] Kumar, N., Kishan, H., Rao, A. and Awana, V.P.S., *Journal of Applied Physics*, 107 (2010) 083905.
- [19] Zhang, Y.B., Li, S., Sun, C.Q. and Gao, W., *Materials Science and Engineering B*, 98 (2003) 54.
- [20] Doshi, R.R., Solanki, P.S., Khachar, U., Kuberkar, D.G., Krishna, P.S.R., Banerjee, A. and Chaddah, P., *Physica B*, 406 (2011) 4031.
- [21] Baazaoui, M., Zemni, S., Boudard, M., Rahmouni, H., Gasmi, A., Selmi, A. and Oumezzine, M., *Materials Letters*, 63 (2009) 2167.
- [22] Ghosh, K., Lobb, C.J., Greene, L., Karabashev, S.G., Shulyatev, D.A., Arsenov, A.A. and Mukovskii, Y., *Physical Review B*, 81 (1998) 4740.
- [23] Martin, M.C., Shirane, G., Endoh, Y., Herota, K., Moritomo, Y. and Tokura, Y., *Physical Review B*, 53 (1996) 14285.
- [24] Chau, N., Nhat, H.N., Luong, N.H., Minh, D.L., Tho, N.D. and Chau, N.N., *Physica B*, 327 (2003) 270.
- [25] Chérif, W., Ellouze, M., Lehlooh, A.F., Mahmood, S.H. and Elhalouani, F., *Hyperfine Interactions*, 211 (2012) 153.
- [26] Dhahri, Ah., Jemmali, M., Taibi, T., Dhahri, E. and Hlil, E.K., *Journal of Alloys and Compounds*, 618 (2015) 488.
- [27] Mohamed, Za., Tka, E., Dhahri, J. and Hlil, E.K., *Journal of Alloys and Compounds*, 619 (2015) 520.
- [28] Jemaa, F.B., Mahmood, S.H., Ellouze, M., Hlil, E.K. and Halouani, F., *Journal of Materials Science: Materials in Electronics*, 26 (2015) 5381.
- [29] Jemaa, F.B., Mahmood, S.H., Ellouze, M., Hlil, E.K. and Halouani, F., *Ceramics International*, 41 (2015) 8191.
- [30] Jemaa, F.B., Mahmood, S.H., Ellouze, M., Hlil, E.K. and Halouani, F., *Journal of Materials Science*, 50 (2015) 620.
- [31] Paraskevopoulos, M., Mayr, F., Hemberger, J., Loidl, A., Heichele, R., Maurer, D., Müller, V., Mukhin, A.A. and Balbashov, A.M., *Journal of Physics: Condensed Matter*, 12 (2000) 3993.
- [32] Mira, J., Rivas, J., Rivadulla, F. and Quintela, M.A.L., *Physica B*, 320 (2002) 23.
- [33] Rostamnejadi, A., Venkatesan, M., Kameli, P., Salamati, H. and Coey, J., *Journal of Magnetism and Magnetic Materials*, 323 (2011) 2214.
- [34] Kim, M.S., Yang, J.B., Medvedeva, J., Yelon, W.B., Parris, P.E. and James, W.J., *Journal of Physics: Condensed Matter*, 20 (2008) 255228.
- [35] Vázquez-Vázquez, C., Blanco, M.C., López-Quintela, M.A., Sánchez, R.D., Rivas, J. and Oseroff, S.B., *Journal of Materials Chemistry*, 8 (1998) 991.
- [36] Radaelli, P., Iannone, G., Marezio, M., Hwang, H., Cheong, S., Jorgensen, J. and Argyriou, D., *Physical Review B*, 56 (1997) 8265.
- [37] Pullar, R.C., *Progress in Materials Science*, 57 (2012) 1191.
- [38] Mahmood, S.H., "Properties and Synthesis of Hexaferrites", in: S.H. Mahmood and I. Abu-Aljarayesh (Eds.) "Hexaferrite Permanent Magnetic Materials", (Materials Research Forum LLC, Millersville, PA, 2016), pp. 74-110.
- [39] Mahmood, S.H. and Bsoul, I., "Tuning the Magnetic Properties of M-Type Hexaferrites", in: R.B. Jotania and S.H. Mahmood (Eds.) "Magnetic Oxides and Composites", (Materials Research Forum LLC, Millersville, PA, USA, 2018), pp. 49-100.
- [40] Alhwaitat, E.S., Mahmood, S.H., Al-Hussein, M., Mohsen, O.E., Maswadeh, Y., Bsoul, I. and Hammoudeh, A., *Ceramics International*, 44 (2018) 779.
- [41] Mahmood, S.H., Aloqaily, A.N., Maswadeh, Y., Awadallah, A., Bsoul, I., Awawdeh, M. and Juwhari, H.K., *Solid State Phenomena*, 232 (2015) 65.
- [42] Aneesh Kumar, K.S., Bhowmik, R.N. and Mahmood, S.H., *Journal of Magnetism and Magnetic Materials*, 406 (2016) 60-71.
- [43] Mahmood, S.H., Dawood, J., Lehlooh, A.F., Cheikhrouhou, A. and Ammar, A., *Hyperfine Interactions*, 196 (2010) 385.

- [44] Awadallah, A., Mahmood, S.H., Maswadeh, Y., Bsoul, I. and Aloqaily, A., IOP Conference Series: Materials Science and Engineering, 92 (2015) 012006.
- [45] Mohaidat, Q.I., Lataifeh, M., Mahmood, S.H., Bsoul, I. and Awawdeh, M., Journal of Superconductivity and Novel Magnetism, 30 (2017) 2135.
- [46] Baazaoui, M., Zemni, S., Boudard, M., Rahmouni, H., Gasmi, A., Selmi, A. and Oumezzine, M., International Journal of Nanoelectronics and Materials, 3 (2010) 23.
- [47] Kallel, N., Ben Abdelkhalek, S., Kallel, S., Peña, O. and Oumezzine, M., Journal of Alloys and Compounds, 501 (2010) 30.
- [48] Oumezzine, Ma., Zemni, S. and Peña, O., Journal of Alloys and Compounds, 508 (2010) 292.
- [49] Warren, B.E., "X-ray Diffraction", (Addison-Wesley, Reading, Massachusetts, 1969).
- [50] Cullity, B.D. and Graham, C.D., "Introduction to Magnetic Materials", 2nd ed., (John Wiley & Sons, Hoboken, NJ, 2011).
- [51] Grössinger, R., Physica Status Solidi (a), 66 (1981) 665.
- [52] Radelytskyi, I., Dłużewski, P., Dyakonov, V., Aleshkevych, P., Kowalski, W., Jarocki, P. and Szymczak, H., Journal of Magnetism and Magnetic Materials, 335 (2013) 11.

Investigation of Radioactivity Levels and Radiation Hazards in Soil Samples Collected from Different Sites in Tafila Governorate, Jordan

Ahmad M. Al-Qararah^a, Abdallah H. Almahasneh^a, Derar Altarawneh^a and Alaa Jaffal^b

^a Department of Physics, Faculty of Science, Tafila Technical University, P.O.Box 179, Tafila 66110, Jordan.

^b Energy and Minerals Regulatory Commission, P.O. Box 1865, Amman 11821, Jordan.

Received on: 26/9/2018;

Accepted on: 17/12/2018

Abstract: Natural and artificial radioactivity levels in surface soil samples collected from various sites in Tafila governorate in Jordan, have been determined using gamma-ray spectrometry. The average concentrations of ²³⁸U, ²²⁶Ra, ²³²Th, ⁴⁰K and ¹³⁷Cs were 23.6 ± 3.1 , 23.3 ± 0.7 , 16.7 ± 1.0 , 234.1 ± 9.85 and 5.4 ± 0.3 Bq kg⁻¹, respectively. The activity ratio between ²³⁸U and ²²⁶Ra for all samples was close to unity. The average values of radium equivalent activity, gamma-absorbed dose rate in air, annual effective dose equivalent, external hazard index, internal hazard index and excess lifetime cancer risk were 65.2 Bq kg⁻¹, 30.6 nGy h⁻¹, 37.6 μSv y⁻¹, 0.18, 0.24 and 1.39×10^{-4} , respectively. These values for the collected samples do not exceed the permissible limits. Therefore, the studied area does not pose any significant radiation hazard to the public. Furthermore, it has been found that the activity concentration of ¹³⁷Cs radionuclide is within the values of recommended safe levels.

Keywords: Soil samples, Natural radioactivity, Artificial radioactivity, Gamma-ray spectrometry, Radiation hazard assessment.

1. Introduction

Due to Jordan's growing need for electrical power, Jordan government has commissioned the Jordan Atomic Energy Commission JAEC to construct a nuclear power plant capable of generating electricity. Therefore, a need has emerged for a radiological mapping of Jordan, which is intended to enhance our knowledge of the varying radioactivity in our environment. As one of the primary research fields in the Department of Physics in Tafila Technical University (TTU), Jordan, the present study is a corner stone in enhancing and enriching the radiological mapping for different sites in Tafila governorate. Therefore, the main aim of this work is to measure the specific activities of ²³⁸U,

²²⁶Ra, ²³²Th, ⁴⁰K and ¹³⁷Cs and to estimate the radiological hazard associated with these radionuclides in soil samples obtained from different areas in Tafila governorate in Jordan.

²³⁸U, ²²⁶Ra, ²³²Th and ⁴⁰K radionuclides mainly constitute the natural radioactivity which is nearly found everywhere in soil, water and rock [1-5]. ¹³⁷Cs is the most important anthropogenic radionuclide with a relatively long half-life of 30.17 years [6]. It is widely distributed globally due to nuclear weapon testing and nuclear power plant accidents. Humans can get exposed to radiation from these radionuclides in two ways, either by direct exposure or by the accumulation of these

radionuclides in the body through inhaling or food consumption. Soil is considered to be the medium of transferring these radionuclides to human beings and constitutes a serious radiation hazard. Moreover, determining the activity concentrations of natural and anthropogenic radionuclides is important for the purposes of establishing baseline data for ascertaining their radiological levels.

There have been several studies in the past decades conducted for the determination the natural and/or anthropogenic radioactivity levels in Jordan [7-13]. However, these studies were specific to certain geographical areas and did not include all areas of Jordan. In a recent study [14], the natural radioactivity levels and radiation hazard in the south of Jordan were assessed. It focused on determining the natural radioactivity levels and the associated hazards, but did not study the levels of anthropogenic radiation in this region. All the previous reasons and the lack of measurements motivated the authors to determine the activity concentrations of both natural and anthropogenic radionuclides as well as the radiation hazards in Tafila region.

In this paper, the natural and anthropogenic radioactivity levels in surface soil samples in Tafila governorate in Jordan are investigated using gamma-ray spectrometry. This type of work in the study area is distinctive that no prior work has investigated the activity concentrations of anthropogenic radionuclides as well as the natural radionuclides and the radiation hazards in the sites located nearby the Royal highway and other touristic sites; namely, Dana Wildlife Reserve and the old Sela' town in Tafila. Thus, there is a great interest to provide information regarding the radioactivity levels in these areas to the inhabitants and visitors of these areas and to provide them with awareness advices about the radiological effects on their health.

The rest of the paper is organised as follows: In Section 2, details of the soil sample collection and preparation, detector calibration and sample analysis utilized during this study are described. The calculation of radium equivalent activity,

gamma-absorbed dose rate in air, annual effective dose equivalent, external and internal hazard indices and excess lifetime cancer risk are presented in Section 3. The activity concentrations of ^{238}U , ^{226}Ra , ^{232}Th , ^{40}K and ^{137}Cs as well as the results of radiation hazards are presented in Section 4. The last section summarizes the work and conclusions are discussed.

2. Experimental Methods and Materials

2.1 Study Area

Tafila governorate is located in the south of Jordan about 180 km from Amman the capital of Jordan. Its population is nearly 100,000. Its area is approximately 2100 km². It is considered to be one of the oldest areas in the country which was the most populated as result of the succession of different nations. Tafila is mostly a mountainous area as it has mountain chains of a height ranging from 1200 m in the eastern part to 1600 m in the west (Al-Qadisyya). These mountain chains are crossed with deep valleys. Dana Wildlife Reserve which is one of the biggest wildlife reserves in Jordan is part of Tafila governorate. Its area is about 300 km² with curved terrain facing the Afro-Asian Rift-Valley.

2.2 Soil Sample Collection and Preparation

In this study, sixteen soil samples were collected from different sites in Tafila governorate. Soil samples were taken to a depth of 5 cm and Global Positioning System GPS was used for tracking the data recording as seen in Table 1 and Fig. 1.

For homogeneous soils, the samples were sieved in order to separate stones and grasses from the samples. Then, the samples were crushed and placed in an oven at 95 °C for 15 h. Finally, the samples were sealed in plastic containers and left for one month before counting in order to ensure equilibrium between ^{226}Ra and ^{222}Ra and their daughter products.

TABLE 1. Sample identifications and GPS position locations.

Site	Site Name	Altitude (m)	GPS position	
			LAT.	LONG.
Site 1	Sa'wa	1240	30°46' 19"	35°36' 34"
Site 2	Eima	900	30°52' 36"	35°35' 45"
Site3	Rawath	1450	30°42' 16"	35°38' 09"
Site4	Al-Qadisyya	1590	30°39' 53"	35°37' 16"
Site5	Umm Sarab	1270	30°44' 53"	35°38' 01"
Site6	Garandal	1340	30°43' 15"	35°38' 44"
Site7	Zoabar	1370	30°46' 49"	35°36' 46"
Site8	Busira	1170	30°43' 36"	35°37' 15"
Site9	Dana	1290	30°40' 31"	35°36' 47"
Site10	Izhaiqa	1260	30°49' 12"	35°38' 29"
Site11	Lahda	1460	30°41' 52"	35°35' 56"
Site12	Al Ayes	1240	30°50' 44"	35°38' 06"
Site13	Dra'	1365	30°46' 02"	35°37' 47"
Site14	Alhala	1420	30°46' 15"	35°38' 27"
Site15	Sela	1090	30°46' 18"	35°35' 04"
Site16	Rashadiyah	1560	30°40' 59"	35°37' 21"

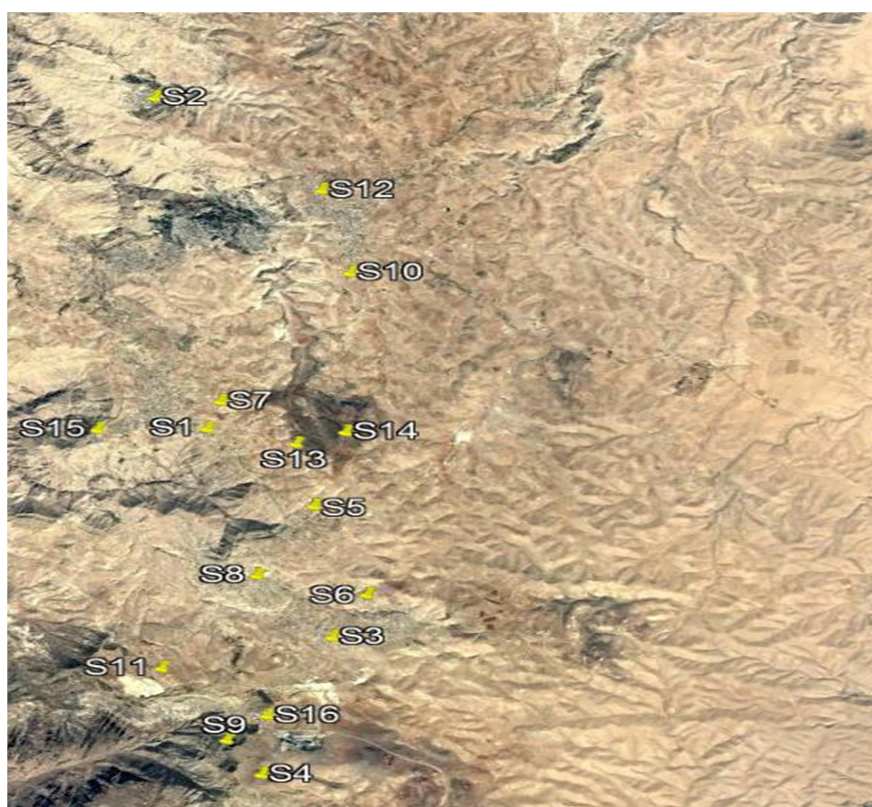


FIG. 1. Location map of the study area (using Google Maps).

2.3 Detector Calibration

For identifying gamma-emitting radionuclides and determining their activity concentrations, a gamma-ray spectrometry with High Purity Germanium (HPGe) detector measuring system of 50 % relative efficiency manufactured by Canberra [22] was used. The

gamma radiation of the environment may influence the gamma spectrometry which in turn might affect the measurement. Therefore, the detector was surrounded by a lead shield. The background spectrum was collected before the measurements and the peaks of the background

spectrum were subtracted using peak area correction.

The energy calibration was performed using radioactive sources (^{137}Cs , ^{57}Co , ^{65}Zn , ^{109}Cd , ^{113}Sn , ^{54}Mn , ^{155}Eu , ^{22}Na and ^{241}Am). These point sources were manufactured by Canberra on 18 January 2010 (except for ^{155}Eu and ^{22}Na , which were produced on 23 June 2009). The initial activity for each point source is 37 kBq. Efficiency calibration has also been done before the measurements using a standard -Petri dish-calibration mixed source. The performed efficiency calibration curve has been corrected for cascade summing effect using a geometry correction software.

2.4 Sample Analysis

Soil samples were placed facing the detector. The counting time for each sample was 24 h. Any thumb rule concerning the acquisition time does not exist, because it depends on achieving the desired counting statistics on the primary line emitted by the nuclide subject of measurement.

The average activity concentrations of the three photopeaks of ^{214}Pb at 295.2 keV and 352.0 keV and ^{214}Bi at 609.3 keV were used to determine the activity concentration of ^{226}Ra . The activity concentration corresponding to the photopeaks of ^{228}Ac at 911.1 keV, ^{212}Pb at 238.6 keV and ^{208}Tl at 583.1 keV was used in order to determine the activity concentration of ^{232}Th . The activity concentration corresponding to the photopeak of ^{234}Th at 63.3 keV was used in determining the activity concentration of ^{238}U . The activity concentrations of ^{40}K and ^{137}Cs were determined directly using the photopeaks at 1460.8 keV and 661.6 keV, respectively.

3. Calculations

3.1 Activity Concentration

The activity concentration, A , of the radionuclides present in the sample was calculated based on the following expression:

$$A = \frac{C}{\epsilon \times I_{\gamma} \times w} \quad (1)$$

where A is the activity concentration in Bq kg^{-1} , C is the net count rate in counts per second, ϵ is the detector efficiency, I_{γ} is the fractional number of decays that yield the radiation to be detected and w is the sample weight in kg.

3.2 Radium Equivalent Activity

Radium equivalent activity Ra_{eq} is a common index used for the assessment of radiological hazard of radioactivity. It uses the activity concentrations of ^{226}Ra , ^{232}Th and ^{40}K to create an index of a single quantity. It was calculated, as shown in Eq. 2, based on the assumption that 370 Bq kg^{-1} of ^{226}Ra , 259 Bq kg^{-1} of ^{232}Th and 4810 Bq kg^{-1} of ^{40}K produce the same gamma ray dose rate [15].

$$Ra_{eq}(\text{Bq kg}^{-1}) = A_{Ra-22} + 1.43 A_{Th-232} + 0.077 A_{K-40} \quad (2)$$

where A_{Ra-22} , A_{Th-232} and A_{K-40} are the activity concentrations of ^{226}Ra , ^{232}Th and ^{40}K in Bq kg^{-1} , respectively.

3.3 Absorbed Dose Rate

Gamma-absorbed dose rate D in air outdoors at a height of 1 m above the ground surface can be calculated using the activity concentrations of ^{238}U , ^{232}Th and ^{40}K . Gamma-absorbed dose rate D can be calculated based on the guidelines provided by UNSCEAR [16]:

$$D(\text{nGy h}^{-1}) = 0.462 A_{Ra-2} + 0.604 A_{Th-23} + 0.0417 A_{K-40} \quad (3)$$

where A_{Ra-226} , A_{Th-2} and A_{K-40} are the activity concentrations of ^{226}Ra , ^{232}Th and ^{40}K in Bq kg^{-1} and D is in nGy h^{-1} , respectively.

3.4. Annual Effective Dose Equivalent (AEDE)

To estimate the annual effective dose received by the public due to soil radioactivity, the following formula provided by UNSCEAR [16] was used:

$$AEDE(\mu\text{Sv y}^{-1}) = D(\text{nGy h}^{-1}) \times 8760 \text{ h} \times 0.2 \times 0.7 \text{ Sv Gy}^{-1} \times 10^{-3} \quad (4)$$

where 0.7 Sv Gy^{-1} is the conversion coefficient from absorbed dose in air to effective dose received by adults and 0.2 for the outdoor occupancy factor.

3.5 External and Internal Hazard Indices

The external hazard index H_{ex} deals with the external radiation effects and can be calculated using the following expression:

$$H_{ex} = \frac{A_{Ra-226}}{370} + \frac{A_{Th-232}}{259} + \frac{A_{K-40}}{4810} < 1. \quad (5)$$

The value of H_{ex} must not exceed the limit of unity for the radiation hazard to be negligible, which corresponds to the upper limit of Ra_{eq} (370 Bq kg^{-1}).

The internal hazard index H_{in} is used for internal exposure from radon²²²Rn and its short-lived progeny in building material. Internal hazard index H_{in} can be calculated using the following formula [17]:

$$H_{in} = \frac{A_{Ra-226}}{185} + \frac{A_{Th-232}}{259} + \frac{A_{K-40}}{4810} < 1. \quad (6)$$

3.6 Excess Lifetime Cancer Risk

To estimate the probability of developing cancer due to the radiation exposure effects for a specific lifetime of a person, the excess lifetime cancer risk, ELCR, is calculated using the following relation:

$$ELCR = AEDE \times LE \times RF \quad (7)$$

where AEDE is in $\mu Sv y^{-1}$, LE is the life expectancy in Jordan that is 74 years and RF is the fatal cancer risk per Sievert which is 0.05 Sv^{-1} .

4. Results and Discussion

4.1 Activity Concentration of ²³⁵U, ²²⁶Ra, ²³²Th and ⁴⁰K

Table 2 summarizes the activity concentrations of ²³⁵U, ²²⁶Ra, ²³²Th and ⁴⁰K collected from sixteen different locations in Tafila governorate soil. The table illustrates the activity concentration of radionuclides for each sample followed by the minimum, maximum and average values of all samples. Activity concentrations of ²³⁸U for all the soil samples were found to be ranging from 11.6 to 44.3 Bq kg^{-1} with an average value of 23.6 Bq kg^{-1} . The activity concentration of ²²⁶Ra ranged from 21.1 to 41.4 Bq kg^{-1} with an average value of 23.3 Bq kg^{-1} . The activity concentration of ²³²Th varied from 7.3 to 28.8 Bq kg^{-1} with an average value of 16.7 Bq kg^{-1} . The activity concentration of ⁴⁰K ranged from 115.6 to 435.5 Bq kg^{-1} with an

average value of 234.1 Bq kg^{-1} . Site 15 had the highest values of ²³⁸U, ²²⁶Ra and ⁴⁰K, while site 13 had the highest value of ²³²Th. The differences in the activity concentrations among the samples depend primarily on the geological conditions [18]. However, the average activity concentrations of ²³⁸U, ²²⁶Ra, ²³²Th and ⁴⁰K in the studied area were lower than the worldwide average concentrations in soils of various countries which are 33 Bq kg^{-1} for ²³⁸U, 32 Bq kg^{-1} for ²²⁶Ra, 45 Bq kg^{-1} for ²³²Th and 412 Bq kg^{-1} for ⁴⁰K [4].

Table 3 compares the results of this work with results for other regions in Jordan. It is clear that the natural activity concentrations of ²³⁸U, ²²⁶Ra and ²³²Th in other regions are higher. The average activity concentration of ⁴⁰K in Tafila is not the least, but the value is close to the values of the other regions.

In another study, Ahmad et al. [19] reported that the specific activities in soil samples collected in Amman, the capital of Jordan, were 56.4, 28.8 and 501.3 Bq kg^{-1} for ²³⁸U, ²³²Th and ⁴⁰K, respectively. Moreover, they reported that the specific activities in Jerash soils were 27.9, 12.4 and 120 Bq kg^{-1} for ²³⁸U, ²³²Th and ⁴⁰K, respectively. The activity concentrations in soil samples taken along the Amman-Aqaba highway have been investigated by Al-Jundi et al. [9]. They found that the activity concentrations varied from 22 to 104 Bq kg^{-1} for ²³⁸U, from 21 to 103 Bq kg^{-1} for ²³²Th and from 138 to 601 Bq kg^{-1} for ⁴⁰K. Also, a recent study [14] reported that the average activity concentrations in areas in the southern governorates of Jordan were 45, 39, 23 and 233 Bq kg^{-1} for ²³⁸U, ²²⁶Ra, ²³²Th and ⁴⁰K, respectively. Table 3 shows that the average values of the activity concentrations in this study are in agreement with the previous cited results.

Fig. 2 shows the relationship between uranium and radium concentrations in soil samples collected in Tafila. A strong correlation between ²³⁸U and ²²⁶Ra can be seen. The ratio of ²³⁸U / ²²⁶Ra is very close to unity. This result is expected, since they belong to the same series and should be in equilibrium. The strong correlation between ²³⁸U and ²²⁶Ra indicate that the results for anyone of them represent a good predictor for the other.

TABLE 2. Activity concentrations of ^{238}U , ^{226}Ra , ^{232}Th and ^{40}K , in Tafila governorate soil.

Site	^{238}U (Bq kg $^{-1}$)	^{226}Ra (Bq kg $^{-1}$)	^{232}Th (Bq kg $^{-1}$)	^{40}K (Bq kg $^{-1}$)
Site 1	11.6 ± 1.6	12.1 ± 0.5	8.5 ± 0.6	115.6 ± 5.9
Site 2	28.1 ± 2.4	30.7 ± 0.6	17.9 ± 0.8	225.2 ± 8.2
Site 3	21.4 ± 2.0	20.8 ± 0.6	19.9 ± 0.9	264.4 ± 8.6
Site 4	27.6 ± 3.6	29.9 ± 0.7	20.9 ± 1.2	163.6 ± 11.9
Site 5	17.6 ± 2.0	17.7 ± 0.6	12.9 ± 0.7	203.7 ± 7.8
Site 6	19.9 ± 1.1	20.7 ± 0.4	17.4 ± 0.5	208.4 ± 5.7
Site 7	28.4 ± 5.9	24.7 ± 0.9	20.5 ± 1.2	225.1 ± 9.4
Site 8	23.2 ± 2.2	24.2 ± 0.7	18.9 ± 0.8	267.6 ± 9.1
Site 9	18.3 ± 3.2	17.8 ± 0.6	15.7 ± 0.8	419.9 ± 9.8
Site 10	19.6 ± 5.6	19.0 ± 1.0	14.2 ± 1.8	149.2 ± 18.0
Site 11	22.9 ± 2.2	23.8 ± 0.6	19.4 ± 1.1	202.5 ± 8.2
Site 12	23.4 ± 2.3	24.2 ± 0.6	19.7 ± 0.8	272.1 ± 8.8
Site 13	27.2 ± 4.7	27.2 ± 0.9	28.8 ± 1.7	289.8 ± 15.5
Site 14	22.7 ± 5.4	23.5 ± 0.9	7.3 ± 1.0	173.4 ± 8.5
Site 15	44.3 ± 2.4	41.4 ± 0.9	13.5 ± 0.8	435.5 ± 11.4
Site 16	21.4 ± 3.7	16.0 ± 0.8	11.4 ± 1.2	130.0 ± 10.9
Min.	11.6 ± 1.6	12.1 ± 0.5	7.3 ± 1.0	115.6 ± 5.9
Max.	44.3 ± 2.4	41.4 ± 0.9	28.8 ± 1.7	435.5 ± 11.4
Average	23.6 ± 3.1	23.3 ± 0.7	16.7 ± 1.0	234.1 ± 9.9

TABLE 3. Comparison of the average activity concentrations of ^{238}U , ^{226}Ra , ^{232}Th and ^{40}K with other parts of Jordan's soil.

Governorate	^{238}U (Bq kg $^{-1}$)	^{226}Ra (Bq kg $^{-1}$)	^{232}Th (Bq kg $^{-1}$)	^{40}K (Bq kg $^{-1}$)	Reference
Irbid	43.9 ± 34.9	36.0 ± 42.9	25.3 ± 10.9	226.3 ± 84.2	[7]
Ma'raq	33.3 ± 14.3	25.6 ± 7.4	27.6 ± 6.0	350.2 ± 78.1	[7]
Ajloun	31.2 ± 14.3	31.0 ± 12.9	28.0 ± 10.5	298.4 ± 113.1	[7]
Jerash	33.2 ± 15.5	30.1 ± 10.8	29.5 ± 7.2	315.3 ± 71.4	[7]
Balqa	37.4 ± 27.5	26.6 ± 26.7	26.0 ± 9.1	277.3 ± 101.5	[7]
Zarqa	257.8 ± 355.5	213.9 ± 315.4	21.5 ± 9.1	248.5 ± 121.5	[7]
Amman	47.0 ± 71.5	44.0 ± 69.8	20.9 ± 10.6	241.6 ± 120.8	[7]
Madaba	28.0 ± 14.4	28.0 ± 10.4	27.4 ± 5.1	303.6 ± 47.3	[7]
Ma'an	44.9 ± 6.3	57.7 ± 5.4	18.1 ± 1.4	138.1 ± 40.8	[10]
Tafila	23.6 ± 3.1	23.3 ± 0.7	16.7 ± 1.0	234.1 ± 9.9	

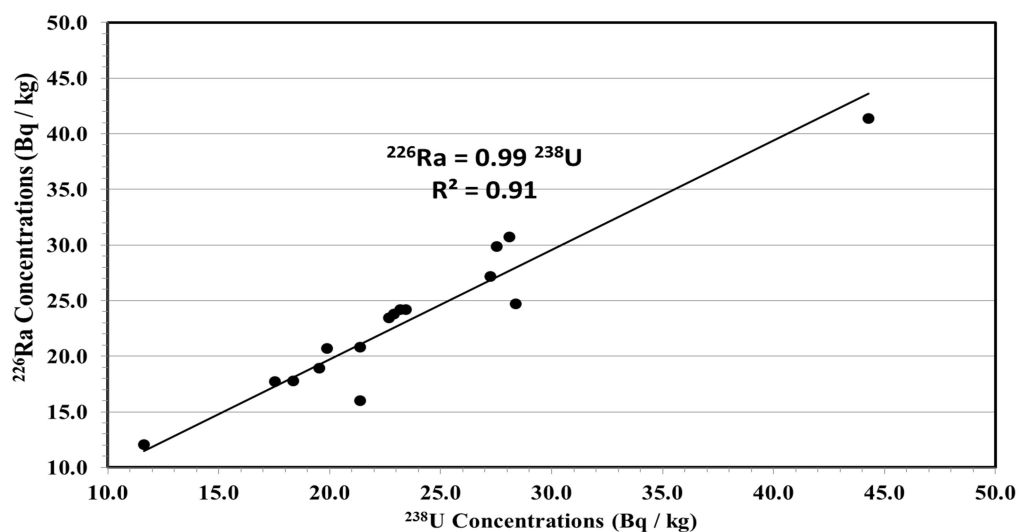


FIG. 2. Uranium vs. radium concentrations.

4.2 Activity Concentration of ^{137}Cs

Fig. 3 displays the activity concentrations of anthropogenic ^{137}Cs in soil samples collected from Tafila governorate. Activity concentrations of ^{137}Cs were determined for 13 soil samples, since there is no ^{137}Cs in the collected soil samples from sites 14-16. Those concentrations ranged from 0.58 to 10.57 Bq kg⁻¹ with an average value of 5.41 Bq kg⁻¹. The highest activity value of ^{137}Cs is for Garandal sample (site 6). The lowest activity is for Sa'wa sample (site 1). Hamarneh and coworkers [20] found

that the activity concentrations of ^{137}Cs in Irbid region varied from 12.11 to 24.83 Bq kg⁻¹. However, most of the activity concentrations of ^{137}Cs in Tafila region were less than those in Irbid region. It is worth mentioning that the reported data by IAEA expert missions mentioned that the activity concentration of ^{137}Cs should be ranging between 5 and 100 Bq kg⁻¹ [16]. Globally, all soil samples in this work showed that the values of activity concentration of ^{137}Cs were much below this range.

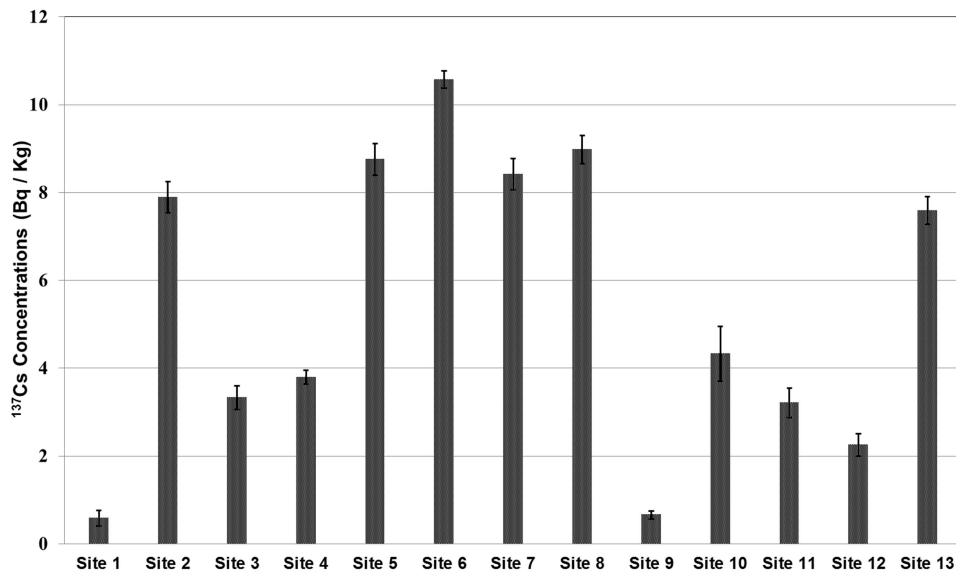


Fig. 3: ^{137}Cs activity concentrations at different locations.

4.3 Radiological Effects

The main objective of studying the radioactivity levels in soils is to calculate the radiation dose to public. Fig. 4a displays the radium equivalent activity for the soil samples collected from Tafila region. It can be clearly seen that the radium equivalent activity for all the 16 soil samples in the present work ranged from 33.1 to 90.6 Bq kg⁻¹, with an average value of 65.2 Bq kg⁻¹. The highest value is in Dra' sample (site 13) and the lowest is in Sa'wa sample (site 1). The average value of the radium equivalent activity in the present study is lower than the allowed maximum value of 370 Bq kg⁻¹ [16].

Fig. 4b shows the gamma-absorbed dose rate in air for the soil samples collected from Tafila region. The gamma-absorbed dose rate varied from 15.5 nGy h⁻¹ for Sa'wa sample (site 1) to 45.4 nGy h⁻¹ for Sale sample (site 15), with an average value of 30.6 nGy h⁻¹ which is lower

than the world's average value of 60 nGy h⁻¹ [16].

Results for the outdoor annual effective dose are shown in Fig. 4c. The outdoor annual effective dose varied from 19.0 to 55.7 $\mu\text{Sv y}^{-1}$ with an average of 37.6 $\mu\text{Sv y}^{-1}$. This value is lower than the world's average value of 70 $\mu\text{Sv y}^{-1}$ [16].

Results for the external and internal hazard indices are shown in Fig. 4d and Fig. 4e. The external hazard index ranged from 0.09 to 0.25 with an average of 0.18, whereas the internal hazard index ranged from 0.12 to 0.37 with an average of 0.24. These values are much less than unity [17].

The values of the excess lifetime cancer risk ranged from 7.04×10^{-5} to 2.06×10^{-4} with an average value of 1.39×10^{-4} . The present average is below the world average limit of 2.9×10^{-4} [21].

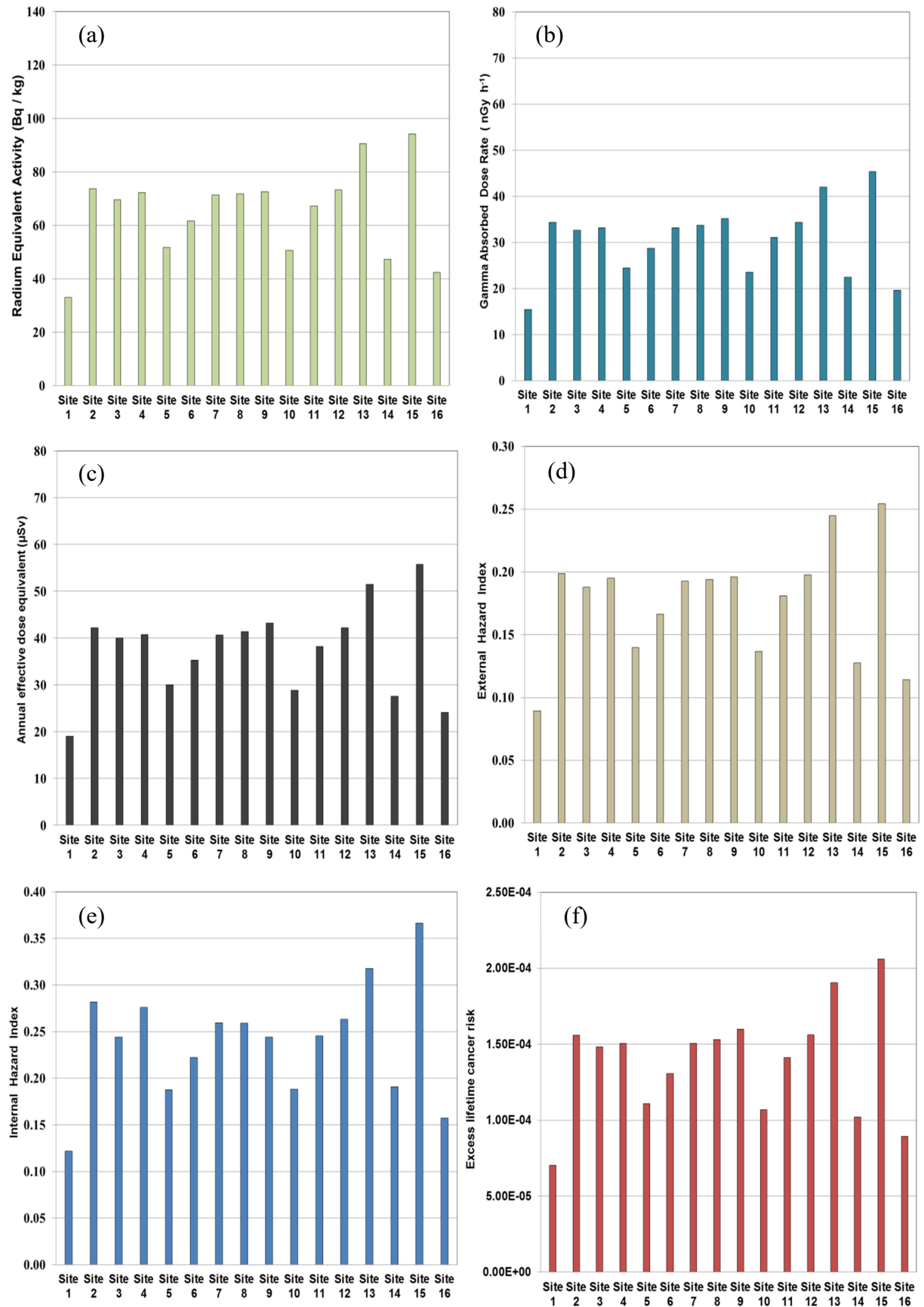


FIG. 4. Illustration of (a) Radium equivalent activity (b) Gamma-absorbed dose rate in air (c) Annual effective dose equivalent (d) External hazard index (e) internal hazard index and (f) Excess lifetime cancer risk from ^{238}U , ^{226}Ra , ^{232}Th and ^{40}K , for soil samples collected from Tafila region.

Conclusion

The natural and anthropogenic radioactivity levels have been determined for 16 surface soil samples collected from various locations in Tafila governorate in Jordan. The activity concentrations were determined using gamma-ray spectrometry. The average concentrations of natural radionuclides ^{238}U , ^{226}Ra , ^{232}Th and ^{40}K were found to be lower than the worldwide average values. The ratio between ^{238}U and ^{226}Ra for all samples was close to unity. Among the anthropogenic radionuclides, only ^{137}Cs was detected, but with very low values compared to the worldwide range. The average values of

radium equivalent activity, gamma-absorbed dose rate in air, annual effective dose equivalent, external and internal hazard indices and excess lifetime cancer risk were lower than the world's average values. Our results show that the studied area does not pose any significant radiation hazard to the public.

Acknowledgements

The authors would like to thank the Energy and Minerals Regulatory Commission (EMRC) for granting permission to analyze the samples in their laboratory facilities.

References

- [1] Knoll, G., "Radiation detection and measurement", 3rd Ed., (Wiley, New York, 2010).
- [2] Martin, E., "Physics for radiation protection", 3rd Ed., (Wiley-VCH Verlag, Weinheim, 2013).
- [3] NCRP Report No. 77, "Exposures from the uranium series with emphasis on radon and its daughters", Bethesda, Maryland, (1984).
- [4] UNSCEAR, "Sources and effects of ionizing radiation", United Nations Publications, New York, (2008).
- [5] International Commission on Radiological Protection (ICRP), "The 2007 Recommendations of the International Commission on Radiological Protection", ICRP Publication 103, (2007).
- [6] Al-Shboul, K.F., Alali, A.E., Al-Khodire, H.Y., Batayneh, I.M. and AlShurafat, A.W., J. Radioanal. Nucl. Chem., 314 (2) (2017) 1353.
- [7] Al-Hamarneh, I.F. and Awadallah, M.I., Radiat. Meas., 44 (1) (2009) 102.
- [8] Hamideen, M. and Sharaf, J., Radiat. Phys. Chem., 81 (10) (2012) 1559.
- [9] Al-Jundi, J., Al-Bataina, B., Abu-Rukah, Y. and Shehadeh, H., Radiat. Meas., 36 (1-6) (2003) 555.
- [10] Saleh, H. and Abu Shayeb, M., Ann. Nucl. Energy, 65 (2014) 184.
- [11] Al-Kharouf, S., Al-Hamarneh, I. and Dababneh, M., J. Environ. Radioact., 99 (2008) 1192.
- [12] Abusini, M., Al-Ayasreh, K. and Al-Jundi, J., Radiat. Protect. Dosimet., 128 (2008) 213.
- [13] Abumurad, K. and Al-Tamimi, M., Radiat. Meas., 39 (2005) 77.
- [14] Al-Hamarneh, I., J. Radioanal. Nucl. Chem., 316 (2018) 139.
- [15] Singh, P., Singh, P., Bajwa, B. and Sahoo, B., J. Radioanal. Nucl. Chem., 311 (1) (2017) 253.
- [16] UNSCEAR, "Sources and effects of ionizing radiation", United Nations Publications, New York, (2000).
- [17] ICRP 60 "Recommendations of the International Commission on Radiological Protection", Annals of the ICRP, Pergamon Press, Oxford, (1990).
- [18] Zaim, N. and Atlas, H., J. Radioanal. Nucl. Chem., 310 (3) (2016) 959.
- [19] Ahmad, N., Matiullah, L. and Khataibeh, A., Radiat. Prot. Dosim., 71 (3) (1997) 231.
- [20] Al-Hamarneh, I., Wreikat, A. and Toukan, K., J. Environ. Radioact., 67 (2003) 53.
- [21] Kritsanuwat, R., Sahoo, S., Fukushi, M., Pangza, K. and Chanyotha, S., J. Radioanal. Nucl. Chem., 303 (1) (2015) 325.
- [22] <https://www.mirion.com/products/germanium-detectors>.

Classification of LRS Bianchi Type I Spacetime through Its Conformal Killing Vector Fields

Suhail Khan^a, Syed Zaheer Ullah^a, M. Ramzan^b and Muhammad Ayaz^c

^aDepartment of Mathematics, University of Peshawar, Peshawar Khyber Pukhtoonkhwa, Pakistan.

^bDepartment of Mathematics, The Islamiya University Bahawalpur 63100, Pakistan.

^cDepartment of Mathematics, Abdul Wali Khan University Mardan, Khyber Pukhtoonkhwa, Pakistan.

Received on: 27/2/2018;

Accepted on: 6/1/2019

Abstract: In this paper, we investigate Conformal Killing Vector Fields (CKVFs) of Locally Rotationally Symmetric (LRS) Bianchi type I spacetime. Ten conformal Killing equations and the CKVF components having unknown functions of integration are derived. Specific solutions of these conformal Killing equations are subject to the twelve integrability conditions. Integrability conditions are solved completely in different cases and CKVFs of dimensions four, five and six are obtained along with their conformal factors. In each case, the exact form of the metric which admits CKVFs is obtained. The inheriting CKVFs are obtained. It is also shown that a particular vacuum solution of LRS Bianchi type I spacetime does not admit proper homothetic or proper CKVF.

Keywords: Conformal symmetries, Direct integration technique, Particular solutions.

1. Introduction

The highly non-linear Einstein's Field Equations (EFEs) are used to treat the general theory of relativity. The exact solutions of these equations are extremely difficult because of their non-linear behavior. Some of the physically remarkable exact solutions of EFEs are presented in [1]. Exact solutions of EFEs can be classified according to different symmetries in order to find out the link between structure of spacetime and gravitational interaction. In general relativity, the spacetime symmetries play an important role because of their direct relation with conservation laws. When a physical system is subject to energy conservation law, it remains invariant under time translation. In general relativity, this phenomenon is defined as the invariance property of spacetime metric under a time translation [2]. By spacetime symmetry, we mean a smooth vector field whose

local flow preserves some geometrical features of the spacetime, which refer to a specific tensor, such as the energy momentum tensor, the metric tensor or any other aspect of the spacetime, such as geodesic structure [3]. The motion along which spacetime metric remains constant up to some scale factor is called CKVFs. while the scale factor is known as conformal factor. It is considered that the CKVF is a global smooth vector field X over a manifold W , such that $\xi : W \rightarrow R$ of X ; the relation $X_{a;b} = \xi g_{ab} + N_{ab}$ holds, where ξ is a smooth conformal function, g_{ab} are the components of metric tensor and $N_{ab} = (-N_{ba})$ is the bivector of X . In terms of Lie derivative, the above relation can be written as [3]:

$$L_X g_{ab} = 2\xi g_{ab} \quad (1)$$

where L_X is the Lie derivative along the vector field X . It is to be noted that the conformal function ξ depends on the chosen coordinate system. In an explicit form, Eq. (1) can be written as:

$$g_{ab,d}X^d + g_{bd}X_{,a}^d + g_{ad}X_{,b}^d = 2\xi g_{ab}. \quad (2)$$

In Eq. (2), comma represents partial derivative. From the above equation, it is clear that if ξ is constant, then the vector field reduces to Homothetic Vector Field (HVF) and if ξ vanishes, then the vector field becomes Killing Vector Field (KVF). Hall and Steele [4] worked on the CKVFs in general relativity. According to their work, the maximum dimension for conformally flat spacetime is fifteen, while for non-conformally flat spacetime, the maximum dimension is seven. Khan et al. [2] explored CKVFs for plane symmetric spacetimes. They have solved the integrability conditions completely for some known conformally and non-conformally flat classes of plane symmetric spacetimes. Khan et al. [5] found out CKVFs for LRS Bianchi Type V spacetimes. They solved integrability conditions for some particular cases. They have also determined the inheriting CKVFs for LRS Bianchi Type V spacetime. Maartens et al. [6] have classified spherically symmetric static spacetimes on the basis of their conformal motion. They revealed that for non-conformally flat spacetime, there are two proper conformal motions. The spherical conformal symmetries in non-static spacetime have been studied by Moopanar and Maharaj [7]. Moopanar and Maharaj [8] have also studied a complete conformal geometry of shear-free spacetime with spherical symmetry without specifying the form of matter content. Shabbir et al. [9, 10] investigated that Bianchi Types VIII and IX spacetimes admit proper CKVFs, while spatially homogeneous rotating spacetime does not admit proper CKVFs. In [11], the authors explored LRS spacetimes which are hypersurface homogeneous and admit proper conformal Killing vector fields. Recently, a method have been developed [12] and with their method, the authors classified Bianchi type I spacetime according to its proper conformal vector fields. The authors of this paper showed that only two non-conformally flat families of Bianchi type I spacetimes admit proper conformal vector fields.

In general theory of relativity, CKVFs have a large number of applications. They play a vital role at the geometric level as well as at the

dynamics and kinematics levels [12]. In kinematics, variables like expansion, rotation and shear can be studied by assuming that the spacetime admits CKVFs. These vector fields are also used for the investigation of these variables by implementing some constraints on them. These variables are then used to produce well known results, some of which can be seen in [6, 13, 14]. Similarly, the CKVFs have a vital role at the dynamics level. In [15, 16, 17], some of the plausible solutions of EFEs have been obtained by assuming that the spacetimes admit CKVFs. At the geometric level, the CKVFs are used to simplify the metric by taking possible coordinates which are discussed in [18]. These important applications motivated us to explore CKVFs of LRS Bianchi Type I spacetimes in explicit form and obtain the exact form of the metric. Without going into developing complicated methods, we will solve the conformal Killing equations by direct integration and some simple algebraic techniques.

This paper is organized as follows: In Sect. 2, we write ten conformal Killing equations for LRS Bianchi Type I spacetime. In the subsections of 2, we discuss different cases for integrability conditions. An in detail discussion of CKVFs of particular form, including time-like and inheriting conditions, is presented in Section 3. In Sect. 4, we find vacuum solution and its corresponding CKVFs. A summary of the study is presented in Sec. 5.

2. General Forms of Conformal Killing Equations and Conformal Vector Fields

The line element in usual coordinates (t, x, y, z) (labeled by (x^0, x^1, x^2, x^3) , respectively) for LRS Bianchi type I spacetime is given by

$$ds^2 = -dt^2 + A^2(t)dx^2 + B^2(t)(dy^2 + dz^2), \quad (3)$$

where $A(t)$ and $B(t)$ are no-where zero functions of t only. The conformal Killing equations are obtained as follows (from Eqs.(2) and (3))

$$X_{,0}^0 = \xi(t, x, y, z), \quad (4)$$

$$A^2 X_{,0}^1 - X_{,1}^0 = 0, \quad (5)$$

$$B^2 X_{,0}^2 - X_{,2}^0 = 0, \quad (6)$$

$$B^2 X_{,0}^3 - X_{,3}^0 = 0, \quad (7)$$

$$\dot{A}X^0 + AX^1_1 = A\xi(t, x, y, z), \tag{8}$$

$$B^2X^2_1 + A^2X^1_2 = 0, \tag{9}$$

$$B^2X^3_1 + A^2X^1_3 = 0, \tag{10}$$

$$\dot{B}X^0 + BX^2_2 = B\xi(t, x, y, z), \tag{11}$$

$$X^3_2 + X^2_3 = 0, \tag{12}$$

$$\dot{B}X^0 + BX^3_3 = B\xi(t, x, y, z), \tag{13}$$

In this paper, throughout dot denotes derivative with respect to t . In the first step, some of the above ten equations are used to obtain vector field components X^0, X^1, X^2, X^3 and conformal factor $\xi(t, x, y, z)$. These components are obtained by the following process:

Differentiating Eqs. (6), (7) and (12) with respect to z, y and t respectively, we have the following relation

$$X^0_{23} = X^2_{03} = 0, \tag{14}$$

Similarly, differentiating Eqs. (9), (10) and (12) with respect to z, y and x , respectively, we get the following relation:

$$X^1_{23} = X^2_{13} = 0, \tag{15}$$

Comparing Eqs. (4) and (11) followed by using relation (14), we have $X^2_3 = yB^1(t, x, z) + B^2(t, x, z)$, where $B^1(t, x, z)$ and $B^2(t, x, z)$ are functions of integration. Using Eq.(12) and the last equation, keeping relation (14) in mind, we have:

$$X^2_3 = yF^1(x, z) + F^2(x, z), \tag{16}$$

$$X^3 = -\frac{y^2}{2}F^1(x, z) - yF^2(x, z) + B^3(t, x, z), \tag{17}$$

where $F^1(x, z), F^2(x, z)$ and $B^3(t, x, z)$ are functions of integration. Comparing Eqs.(11) and (13) and differentiating with respect to z , we have $X^2_{23} = X^3_{33}$. Then, Eqs. (16) and (17) become:

$$\left\{ \begin{aligned} X^2 &= y \left[\frac{z^2}{2} J^1(x) + z J^2(x) \right] + \frac{z^2}{2} J^3(x) \\ &+ z J^4(x) - \frac{y^3}{6} J^1(x) - \frac{y^2}{2} J^3(x) \\ &+ y F^3(t, x) + F^5(t, x), \end{aligned} \right.$$

$$\left\{ \begin{aligned} X^3 &= -\frac{y^2}{2} [z J^1(x) + J^2(x)] - y [z J^3(x) \\ &+ J^4(x)] + \frac{z^3}{6} J^1(x) + \frac{z^2}{2} J^2(x) \\ &+ z F^3(t, x) + F^4(t, x), \end{aligned} \right.$$

where $J^p(x)$ for $p = 1, 2, 3, 4$ and $F^q(t, x)$ for $q = 3, 4, 5$ are functions of integration. Substituting the values of X^2 and X^3 in Eqs. (6), (7), (9) and (10) and using relation (15), we have the following general form of the components of conformal Killing vector fields:

$$\left\{ \begin{aligned} X^0 &= B^2 \left[\frac{z^2}{2} F_t^3(t, x) + z F_t^4(t, x) \right] \\ &+ B^2 \left[\frac{y^2}{2} F_t^3(t, x) + y F_t^5(t, x) \right] + F^6(t, x), \end{aligned} \right.$$

$$\left\{ \begin{aligned} X^1 &= -\frac{B^2}{A^2} \left[\frac{z^2}{2} F_x^3(t, x) + z F_x^4(t, x) \right] \\ &- \frac{B^2}{A^2} \left[\frac{y^2}{2} F_x^3(t, x) + y F_x^5(t, x) \right] + F^7(t, x), \end{aligned} \right.$$

$$\left\{ \begin{aligned} X^2 &= y \left[\frac{z^2}{2} c_1 + z c_2 \right] + \frac{z^2}{2} c_3 + z c_4 - \frac{y^3}{6} c_1 \\ &- \frac{y^2}{2} c_3 + y F^3(t, x) + F^5(t, x), \end{aligned} \right.$$

$$\left\{ \begin{aligned} X^3 &= -\frac{y^2}{2} [z c_1 + c_2] - y [z c_3 + c_4] + \frac{z^3}{6} c_1 \\ &+ \frac{z^2}{2} c_2 + z F^3(t, x) + F^4(t, x), \end{aligned} \right.$$

The general form of the conformal factor takes the following form:

$$\left\{ \begin{aligned} \xi(t, x, y, z) &= \xi(t, x) = \\ &2B \dot{B} \left[\frac{z^2}{2} F_t^3(t, x) + z F_t^4(t, x) \right] \\ &+ B^2 \left[\frac{z^2}{2} F_u^3(t, x) + z F_u^4(t, x) \right] \\ &+ 2B \dot{B} \left[\frac{y^2}{2} F_t^3(t, x) + y F_t^5(t, x) \right] \\ &+ B^2 \left[\frac{y^2}{2} F_u^3(t, x) + y F_u^5(t, x) \right] + F_t^6(t, x), \end{aligned} \right.$$

The final form of conformal Killing vector fields and conformal factor is subject to the following twelve integrability conditions:

$$2B^2 F_{xx}^3(t, x) + A^2 \left(\frac{B^2}{A^2} \right) F_x^3(t, x) = 0, \tag{18}$$

$$2B^2 F_{xx}^4(t, x) + A^2 \left(\frac{B^2}{A^2} \right) F_x^4(t, x) = 0, \tag{19}$$

$$2B^2 F_{xx}^5(t, x) + A^2 \left(\frac{B^2}{A^2} \right) F_x^5(t, x) = 0, \tag{20}$$

$$A^2 F_t^7(t, x) - F_x^6(t, x) = 0, \tag{21}$$

$$\left\{ \begin{aligned} (\dot{A} B - 2A \dot{B}) F_t^3(t, x) - \frac{B}{A} F_{xx}^3(t, x) \\ - AB F_u^3(t, x) = 0, \end{aligned} \right. \tag{22}$$

$$\left\{ \begin{aligned} (\dot{A} B - 2A \dot{B}) F_t^4(t, x) - \frac{B}{A} F_{xx}^4(t, x) \\ - AB F_u^4(t, x) = 0, \end{aligned} \right. \tag{23}$$

$$\left\{ \begin{aligned} (\dot{A} B - 2A \dot{B}) F_t^5(t, x) - \frac{B}{A} F_{xx}^5(t, x) \\ - AB F_u^5(t, x) = 0, \end{aligned} \right. \tag{24}$$

$$A F^6(t, x) - A F_t^6(t, x) + A F_x^7(t, x) = 0, \tag{25}$$

$$\dot{B} F_t^3(t, x) + B F_u^3(t, x) = 0, \tag{26}$$

$$\dot{B} B F_t^4(t, x) - c_2 + B^2 F_u^4(t, x) = 0, \tag{27}$$

$$\dot{B} B F_t^5(t, x) + c_3 + B^2 F_u^5(t, x) = 0, \tag{28}$$

$$\dot{B} F^6(t, x) + B F^3(t, x) - B F_t^6(t, x) = 0, \tag{29}$$

The components of CKVFs and integrability conditions may be simplified and expressed in a more compact form. We introduce the new variables $\zeta = (\zeta_3, \zeta_4, \zeta_5) = \left(\frac{z^2+y^2}{2}, z, y \right)$ and $F^p = (F^3, F^4, F^5)$, then the components of conformal Killing vector fields along with conformal factor are given as:

$$X^0 = B^2 \zeta_p F_t^p(t, x) + F^6(t, x),$$

$$X^1 = -\frac{B^2}{A^2} \zeta_p F_x^p(t, x) + F^7(t, x),$$

$$\left\{ \begin{aligned} X^2 &= (\zeta)_2 F^p(t, x) + y z c_2 \\ &+ \frac{c_3}{2} (z^2 - y^2) + z c_4, \end{aligned} \right.$$

$$\left\{ \begin{aligned} X^3 &= (\zeta)_3 F^p(t, x) + \frac{c_2}{2} [z^2 - y^2] \\ &- y [z c_3 + c_4], \end{aligned} \right.$$

$$\left\{ \begin{aligned} \xi(t, x, y, z) &= \xi(t, x) = 2B \dot{B} \zeta_p F_t^p(t, x) \\ &+ B^2 \zeta_p F_u^p(t, x) + F_t^6(t, x), \end{aligned} \right.$$

and the integrability conditions become:

$$2B^2 F_{xx}^p(t, x) + A^2 \left(\frac{B^2}{A^2} \right) F_x^p(t, x) = 0, \tag{30}$$

$$\left\{ \begin{aligned} (\dot{A} B - 2A \dot{B}) F_t^p(t, x) - \frac{B}{A} F_{xx}^p(t, x) \\ - AB F_u^p(t, x) = 0, \end{aligned} \right. \tag{31}$$

$$\dot{B} B F_t^p(t, x) + B^2 F_u^p = H_p, \tag{32}$$

$$A^2 F_t^7(t, x) - F_x^6(t, x) = 0, \tag{33}$$

$$\dot{A} F^6(t, x) - A F_t^6(t, x) + A F_x^7(t, x) = 0, \tag{34}$$

$$\dot{B} F^6(t, x) + B F^3(t, x) - B F_t^6(t, x) = 0, \tag{35}$$

where, $H_p = 0, c_2, -c_3$ for $p = 3, 4, 5$, respectively. These integrability conditions are solved by separating the variables as product functions for unknown functions $F^p(t, x) = K^p(t)K^q(x)$ with $p = 3, 4, 5, 6, 7$ and $q = 8, 9, 10, 11, 12$, respectively. From Eq. (32) and Eq. (30), we have $F^p(t, x) = c_{12}, c_{14}, c_{16}$ for $p = 3, 4, 5$, respectively. Also for $p = 6$,

substituting the value of $F^p(t, x)$ in Eq. (35), we have:

$$\dot{B}K^6(t)K^{11}(x) + Bc_{12} - BK_t^6(t)K^{11}(x) = 0, \quad (36)$$

Differentiating Eq.(36) with respect to x , we have three different cases.

$$(1). K_x^{11}(x) = 0 \text{ and } (\dot{B}K^6(t) - BK_t^6(t)) = 0$$

$$(2). K_x^{11}(x) = 0 \text{ and } (\dot{B}K^6(t) - BK_t^6(t)) \neq 0$$

$$(3). K_x^{11}(x) \neq 0 \text{ and } (\dot{B}K^6(t) - BK_t^6(t)) = 0$$

In the following part, we will discuss each case in turn. It is to be noted that throughout the following sub-section, constants h_i are labeled such that h_1, h_2, h_3 and h_4 represent four spatial Killing vector fields $\frac{\partial}{\partial x}, \frac{\partial}{\partial y}, \frac{\partial}{\partial z}$ and $z\frac{\partial}{\partial y} - y\frac{\partial}{\partial z}$, respectively, representing three linear momentum (along x, y and z) and one angular momentum conservation.

2.1 Case 1

In this case, we consider $K_x^{11}(x) = 0 \Rightarrow K^{11}(x) = c_{17}$ and $(\dot{B}K^6(t) - BK_t^6(t)) = 0 \Rightarrow K^6(t) = Bc_{18}$. Substituting these values back in Eq. (33) and Eq. (34), we have $A = \frac{a}{2}h_5t^2e^{-\frac{2h_6}{at}}$ and $B = \frac{at^2}{2}$, where a is a non-zero integration constant. Now, the metric given by Eq. (3) can be written as:

$$\begin{cases} ds^2 = -dt^2 + \left(\frac{a}{2}h_5t^2e^{-\frac{2h_6}{at}}\right)^2 dx^2 \\ \quad + \left(\frac{at^2}{2}\right)^2 (dy^2 + dz^2), \end{cases} \quad (37)$$

The CKVFs admitted by the above metric along with the conformal factor are given as:

$$\begin{cases} X^0 = \frac{a}{2}h_7t^2, & X^1 = h_8x + h_1, \\ X^2 = h_4z + h_2, & X^3 = -h_4y + h_3, \end{cases} \quad (38)$$

$$\xi(t, x, y, z) = ah_7t, \quad (38)$$

where $h_i \in R$, for $i = 1, 2, 3, \dots, 8$ with $h_8 = -h_6h_7$ and $h_5 \neq 0, h_6 \neq 0$. This solution of CKVFs shows that the above LRS Bianchi type I metric admits five independent CKVFs, of

which one is proper CKVF given by $\frac{a}{2}t^2\frac{\partial}{\partial t}$. Note that the same spacetime metric does not admit proper HVF. Also, the dimension of the isometry group is four. It is well known that a CKVF is called special when $\zeta_{,ab} = 0$ [3]. Examining the above CKVFs, one can easily conclude that the obtained CKVFs are special CKVFs.

2.2 Case 2

In this case, we consider $K_x^{11}(x) = 0 \Rightarrow K^{11}(x) = h_9$ and $(\dot{B}K^6(t) - BK_t^6(t)) \neq 0$. Substituting these values back in Eq. (33) and Eq. (34), we have $A = \frac{at^2}{2}$ and $B = \frac{a}{2}h_7t^2e^{\frac{h_8}{at}}$, where a is non-zero integration constant. Thus, the metric given by Eq. (3) can be written as:

$$\begin{cases} ds^2 = -dt^2 + \left(\frac{at^2}{2}\right) dx^2 \\ \quad + \left(\frac{a}{2}\right)(dy^2 + dz^2). \end{cases} \quad (39)$$

The CKVFs and the conformal factor for the above metric take the form:

$$\begin{aligned} X^0 &= \frac{a}{2}h_5t^2, & X^1 &= h_1, & X^2 &= h_4z + h_6y + h_2, \\ X^3 &= -h_4y + h_6z + c_3, \\ \xi(t, x, y, z) &= ac_5t, \end{aligned} \quad (40)$$

where $h_8 = \frac{2h_6}{h_7h_9}$ and $h_1, h_2, h_3, \dots, h_9 \in R$. These CKVFs show that the above LRS Bianchi type I metric admits five independent CKVFs, of which one is proper CKVF given by $\frac{a}{2}t^2\frac{\partial}{\partial t}$ and no proper HVF. Also, the dimension of the isometry group is four. It is well known that a CKVF is called special when $\zeta_{,ab} = 0$ [3]. Examining the above CKVFs, one can easily conclude that the obtained CKVFs are special CKVFs.

2.3 Case 3

In this case, we consider $K_x^{11}(x) \neq 0$ and $(\dot{B}K^6(t) - BK_t^6(t)) = 0 \Rightarrow K^6(t) = Bc_{17}$. Substituting these values back in Eq. (34), we have:

$$\frac{K_{xx}^{11}(x)}{K^{11}(x)} = -\frac{A^2}{B} \left(\frac{\dot{A}B - A\dot{B}}{A} \right) = \gamma. \quad (41)$$

This equation suggests that we have to discuss further three different cases, such as

(3.1): when γ is positive, (3.2): when γ is negative and (3.3): when γ is zero.

2.3.1 Case 3.1

In this case, we consider γ as positive and solve Eq. (41); we get $A = 1$ and $B = h_5 \cosh \sqrt{\gamma t} + h_6 \sinh \sqrt{\gamma t}$. Thus, we obtained the metric for LRS Bianchi type I as:

$$\begin{cases} ds^2 = -dt^2 + dx^2 + \\ (h_5 \cosh \sqrt{\gamma t} + h_6 \sinh \sqrt{\gamma t})^2 (dy^2 + dz^2). \end{cases} \tag{42}$$

For this metric, the six dimensional conformal Killing vector fields and the conformal factor are as follows:

$$\begin{cases} X^0 = (h_7 \cosh \sqrt{\gamma x} + h_8 \sinh \sqrt{\gamma x}) \times \\ (h_5 \cosh \sqrt{\gamma t} + h_6 \sinh \sqrt{\gamma t}), \\ X^1 = (h_7 \sinh \sqrt{\gamma x} + h_8 \cosh \sqrt{\gamma x}) \times \\ (h_5 \sinh \sqrt{\gamma t} + h_6 \cosh \sqrt{\gamma t}) + h_1, \end{cases}$$

$$X^2 = h_4 z + h_2, \quad X^3 = -h_4 y + h_3,$$

$$\begin{cases} \xi(t, x, y, z) = (h_7 \cosh \sqrt{\gamma x} + h_8 \sinh \sqrt{\gamma x}) \\ \times (h_5 \sqrt{\gamma} \sinh \sqrt{\gamma t} + h_6 \sqrt{\gamma} \cosh \sqrt{\gamma t}), \end{cases}$$

where $h_1, h_2, h_3, \dots, h_8 \in R$, such that $h_5, h_6, h_7, h_8 \neq 0$. From the above result, it is clear that there are two proper conformal Killing vector fields and no proper homothetic vector field exists.

Note that in **Case 3.2**, when we take γ as negative and solve Eq. (41), we get the same result except that the hyperbolic functions are replaced by circular functions.

2.3.2 Case 3.3

When considering γ as zero, we obtain $F^6(t, x) = 0$ and $F^7(t, x) = h_1$. Substituting all the values in general form of conformal Killing vector fields and conformal factor, we get:

$$\begin{cases} X^0 = 0, \quad X^1 = h_1, \quad X^2 = h_4 z + h_2, \\ X^3 = -h_4 y + h_3, \\ \xi(t, x, y, z) = 0, \end{cases} \tag{43}$$

where $h_1, h_2, h_3, h_4 \in R$.

2.4 Case 4

Here, we try to solve the integrability conditions by separating the variables as the sum of the unknown functions $F^p(t, x) = G^p(x) + H^p(t)$, where $p = 3, 4, 5, 6, 7$. From Eqs. (30) – (32), we have $F^3(t, x) = c_5$, $F^4(t, x) = c_7$ and $F^5(t, x) = c_9$. Putting the value of $F^3(t, x)$ in Eq. (35) and using Eq. (33), we get $G^7(t) = c_{11}$ and $G^6(t) = c_{12}B$. Substituting these values in Eq. (34), we have $F^6(t, x) = 0$ and $F^7(t, x) = c_{11}$. Putting all these values back in the general form of conformal vector fields and re-labeling the constants of integration, we get the conformal Killing vector fields and conformal factor as:

$$\begin{cases} X^0 = 0, \quad X^1 = h_1, \quad X^2 = h_4 z + h_2, \\ X^3 = -h_4 y + h_3, \\ \xi(t, x, y, z) = 0, \end{cases} \tag{44}$$

where $h_1, h_2, h_3, h_4 \in R$.

2.5 Case 5

In this sub-section, we do not separate the functions $F^p(t, x), p = 3, 4, 5, 6, 7$ as sum or product of the unknown functions, but impose conditions on the metric functions. First, considering $\dot{A}(t) \neq 0$ and $\dot{B} = 0 \Rightarrow B = constant$ and solving Eqs. (33), (34) and (35), we obtain $F^6(t, x) = h_5 t + h_6$ and $F^7(t, x) = h_7 x + h_1$. Substituting all these values back in the general form, the conformal vector fields and the conformal factor reduce to the following form:

$$\begin{cases} X^0 = h_5 t + h_6, \quad X^1 = h_7 x + h_1, \\ X^2 = h_4 z + h_5 y + h_2, \quad X^3 = -h_4 y + h_5 z + h_3, \\ \xi(t, x, y, z) = h_5, \end{cases} \tag{45}$$

where $h_1, h_2, \dots, h_7 \in R$. The metric function also took the form $(t) = (h_5 t + h_6)^{1-\frac{h_7}{h_5}}$. This result shows that for the above particular metric functions, the LRS Bianchi type I spacetime does not admit proper conformal Killing vector field and the five dimensional CKVFs are just the homothetic vector fields with one proper homothetic and four Killing vector fields.

3. Time-like and Inheriting Conformal Killing Vector Fields

For a purely time-like vector field, we must have the consistency $F^p(t, x) = F^7(t, x) = c_2 = c_3 = c_4 = 0$ and assume that $X = (F^6(t), 0, 0, 0)$. Also, Eq. (33) implies that $F^6 \neq 0$; thus, from Eq. (34), we have $F^6(t) = cA(t)$, $c \in R - 0$. This indicates the existence of a CKVF parallel to the time-like vector u^a , defined as $u^a = \delta_0^a$.

The equation

$$L_X u_a = \xi u_a, \quad (46)$$

known as inheriting condition, was introduced by Herrera et al. [19] and Maartens et al. [14] and studied thoroughly by Coley and Tupper [15-17] amongst others. We will use this inheriting condition for time-like vector $u^a = \delta_0^a$. The above condition (46) can be written in an explicit form as:

$$u_{a,b} X^b + u_b X_{,a}^b = \xi u_a. \quad (47)$$

Solving Eq. (47), it is easy to obtain $X_p^0 = 0$ for $p = 1, 2, 3$, such that $X^0 = X^0(t)$ and the corresponding conformal factor takes the form $\xi = X_0^0$. This suggests that F^6 depends on t only, with $F_t^p = 0$ for $p = 3, 4, 5$. Also, Eq. (33) implies that $F_t^7 = 0$. The remaining integrability conditions take the form:

$$\left(\frac{B^2}{A^2}\right) F_x^p(t, x) = 0, \quad (48)$$

$$\frac{B}{A} F_{xx}^p(t, x) = 0, \quad (49)$$

$$\dot{A} F^6(t, x) - A F_t^6(t, x) + A F_x^7(t, x) = 0, \quad (50)$$

$$\dot{B} F^6(t, x) - B F_t^6(t, x) + B F^3(t, x) = 0, \quad (51)$$

From Eq. (48), two possibilities arise; namely, $\left(\frac{B^2}{A^2}\right) \neq 0$ and $\left(\frac{B^2}{A^2}\right) = 0$. A complete solution of the integrability conditions is found in the first case, while in the second case, the solutions are arbitrary and will not be presented here. As $\left(\frac{B^2}{A^2}\right) \neq 0$, thus $F_x^p(t, x) = 0$ and hence $F_{xx}^p(t, x) = 0$. Now, subtracting Eqs. (50) and (51), we obtain:

$$\begin{cases} (\dot{B} - \dot{A})F^6 + BF^3 - AF_x^7 \\ + (A - B)F_t^6(t, x) = 0. \end{cases} \quad (52)$$

After some manipulations, we get the metric functions as $A = t^2$ and $B = h_5 t^2 e^{\left(\frac{h_6}{h_5}\right)\frac{1}{t}}$ and the corresponding CKVFs along with conformal factor are obtained as:

$$\begin{aligned} X^0 &= h_5 t^2, & X^1 &= h_1, & X^2 &= h_4 z + y h_6 + h_2, \\ X^3 &= -h_4 y + h_6 z + h_3, \end{aligned}$$

$$\xi(t, x, y, z) = 2h_5 t. \quad (53)$$

4. Vacuum Solution for LRS Bianchi Type I Spacetime

The vacuum solution for LRS Bianchi type I spacetime can be obtained by setting the Ricci tensor components R_{ab} equal to zero, as follows:

$$B \ddot{A} + 2A \ddot{B} = 0, \quad (54)$$

$$\ddot{A} B + 2\dot{A} \dot{B} = 0, \quad (55)$$

$$A \ddot{B} + \dot{A} \dot{B} + \frac{A \dot{B}^2}{B} = 0, \quad (56)$$

Solving these three differential equations simultaneously, we have the following solution:

$$A = c_3 \left[\frac{3}{2} (c_1 t + c_2) \right]^{-\frac{1}{3}} \text{ and } B = \left[\frac{3}{2} (c_1 t + c_2) \right]^{\frac{2}{3}},$$

where c_1, c_2 and c_3 are constants, such that $c_1, c_3 \neq 0$. Solving the integrability conditions for these particular metric functions, conformal Killing vector fields and conformal factor are obtained as follows:

$$\begin{aligned} X^0 &= 0, & X^1 &= h_1, & X^2 &= h_4 z + h_2, \\ X^3 &= -h_4 y + h_3, \end{aligned}$$

$$\xi(t, x, y, z) = 0. \quad (57)$$

We see that LRS Bianchi type I vacuum solution does not admit proper conformal or proper homothetic vector fields and the conformal Killing vector fields are just the Killing vector fields.

5. Summary

In this paper, we have given a classification of LRS Bianchi type I spacetime according to its conformal Killing vector fields. We have solved ten conformal Killing equations by using direct integration and some algebraic techniques. Conformal Killing vector field components are obtained along with conformal factors and exact forms of the metrics are also obtained which possess these conformal Killing vector fields. The whole problem is divided into different possible cases, where the spacetime metric may possess conformal Killing vector fields. In the first case of **Section 2**, we determined the exact form of the metric (Eq.(37)) which admits five dimensional CKVFs with only one proper time-like CKVF and no proper homothetic vector field. A similar result is obtained for the metric

(39) as well. **Case 3** is divided into three sub-cases. In **Sub-cases (3.1)** and **(3.2)**, we obtained six dimensional CKVFs with two proper CKVFs and no proper HVF. In **Sub-case (3.3)**, four dimensional CKVFs are obtained which are just the minimum KVFs admitted by LRS Bianchi type I spacetime. In **Case (5)**, we obtained five dimensional CKVFs which are just HVFs with one proper HVF.

In **Section 3**, we obtained the inheriting CKVFs and the exact form of the metric functions are also determined. In **Section 4**, we solved the field equations for Vacuum LRS Bianchi type-I spacetime and showed that this spacetime metric does not admit proper CKVF or proper HVF and the CKVFs are just the KVFs.

References

- [1] Stephani, H., Kramer, D., Maccallum, M., Hoenselaers, C. and Herlt, E., "Exact Solutions of Einstein's Field Equations", 2nd Ed., (Cambridge University Press, Cambridge, 2003), p. 157.
- [2] Khan, S., Hussain, T., Bokhari, A.H. and Khan, G.A., Eur. Phys. J. C., 75 (2015) 523.
- [3] Hall, G.S., "Symmetries and Curvature Structure in General Relativity", (World Scientific, Singapore, 2004), p. 285.
- [4] Hall, G.S. and Steele, J.D., J. Math. Phys., 32 (1991) 1847.
- [5] Khan, S., Hussain, T., Bokhari, A.H. and Khan, G.A., Commun. Theor. Phys., 65 (2016) 315.
- [6] Maartens, R., Maharaj, S.D. and Tupper, B.O.J., Class. Quantum Grav., 12 (1995) 2577.
- [7] Moopanar, S. and Maharaj, S.D., Int. J. Theor. Phys., 49 (2010) 1878.
- [8] Moopanar, S. and Maharaj, S.D., J. Eng. Math., 82 (2013) 125.
- [9] Shabbir, G. and Ali, A., Adv. Stud. Theor. Phys., 3 (2009) 93.
- [10] Shabbir, G. and Ali, A., Appl. Math. Sci., 3 (2009) 869.
- [11] Apostolopoulos, P.S. and Tsamparlis, M., Class. Quantum Grav., 18 (2001) 3775.
- [12] Tsamparlis, M., Paliathanasis, A. and Karpathopoulos, L., Gen. Rel. Grav., 47 (2015) 15.
- [13] Maartens, R., Mason, D.P. and Tsamparlis, M., J. Math. Phys., 27 (1986) 2987.
- [14] Maartens, R., Maharaj, S.D. and Tupper, B.O.J., Class. Quantum Grav., 13 (1996) 317.
- [15] Coley, A.A. and Tupper, B.O.J., Class. Quantum Gravity, 7 (1990) 1961.
- [16] Coley, A.A. and Tupper, B.O.J., Class. Quantum Gravity, 7 (1990) 2195.
- [17] Coley, A.A. and Tupper, B.O.J., J. Math. Phys., 33 (1992) 1754.
- [18] Tsamparlis, M., Class. Quantum Grav., 15 (1998) 2901.
- [19] Herrera, L., Jimenez, J., Leal, L., Poncede, J.L., Esculpi, M. and Galina, V., J. Math. Phys., 25 (1984) 3274.

Wireless Electricity Transmission by Coupled Magnetic Resonances

DaifAoula Nasser, Ali Daroesho and Abdalrahman H. Alhashim

Physics Department, Faculty of Science, Tishreen University, Lattakia, Syria.

Received on: 31/7/2018;

Accepted on: 14/1/2019

Abstract: In this work, we have experimentally demonstrated the ability of transferring electrical power wirelessly using coupled magnetic resonance technique. This technique has been improved by using four resonators, thus maintaining the efficiency of transferring electricity wirelessly during the change of the transfer distance between the transmitter and the receiver coils. We also introduce the concepts of this technique, analyze the used circuit and extract the theoretical model which agrees with experimental results. We have experimentally measured the efficiency of transferred electricity at various transfer distances beginning from 30 cm to 130 cm. The efficiency was more than 50% at a distance of less than 70 cm and 22% at a distance of 100 cm.

Keywords: Resonance, Coupled magnetic resonances, Resonant frequency, Coupling coefficient, Mutual induction.

Introduction

Since its discovery, electric power has been transferred *via* wires from energy resources to loads, which could be domestic or industrial devices...etc.

This method of transferring electric power is simple and efficient as long as the load is steady.

Because of the vast technological developments and the existence of many portable electronic gadgets, the interest in wireless electric transferring technique has recently increased. Many research studies and experiments have emerged in this field. There have been many terms to stand for wirelessly transferred electricity, like WPT (Wireless Power Transfer) and Witricity (Wireless electricity). The idea is not newborn; it dates back to the early twentieth century, even to the era before the existence of networks and electric devices, when Nicola Tesla made big steps in this field [1]. In our present time, there are many techniques to transfer electricity wirelessly; it's relevant to classify them according to efficiency and transfer distance. Techniques that use propagating electromagnetic waves work in the

same way in which radio signals do. These techniques have been used successfully as the transfer distance for them was in the order of hundreds of meters. One of the most prominent problems for them was to trade efficiency with range, because transfer is multidirectional [2, 3]. Scientist Brown used this technology in 1964 to operate a 60-foot powered drone helicopter. There are also techniques like HF, RF and Microwaves which use antennas with high gain to wirelessly transfer electric power. These techniques have transfer ranges which reach up to several kilometers and have an efficiency of more than 90%. These systems need constant and complex monitoring alignment equipment to maintain a line-of-sight (point-to-point). This may be very relevant to the transfer of electricity wirelessly for vast distances in uninhabited areas and even to future projects to transfer energy from space to the earth and *vice versa* [4, 5]. In 1975, NASA and Goldstone used this technology in their well-known experiment, where they were able to transfer electricity with a transfer efficiency of about 82% for a transfer distance of 1.5 km. Unfortunately, the cost was high. In

return, the techniques that don't depend on propagating electromagnetic waves and work for distances less than the wave length of the sent signals, have a high efficiency, but their transfer range is limited; about several centimeters. Examples are inductive coupling and capacitive coupling which are used in many applications like rechargeable toothbrushes and power surfaces [6]. Finally, a new technique has been recently suggested. It depends on resonant inductive coupling or coupled magnetic resonances (CMR) [7]. This technique depends on the idea that two circuits with the same resonant frequency could exchange energy with high efficiency so that losses will be neglected. So, power transfer *via* this technique could be so efficient and multidirectional and the medium around the circuit won't affect the transfer process, because interferences and losses resulting from objects around will be small [8]. In 2007, a research team from the MIT (Massachusetts Institute of Technology) successfully performed the first attempt at wireless power transmission using this technique after scientist Tesla's attempts at the end of the 19th century. They were able to transfer electricity wirelessly with a transfer efficiency of 40% and a transfer distance of about 2 meters. Therefore, they used four resonators including helical type as internal resonators (self-resonators) of relatively large size. The used resonant frequency was about 10 MHz and the theoretical model was based on the coupled theory. The article published in this research does not explain the equations necessary to calculate the parameters of the wireless power transfer system, such as coupling coefficient and mutual induction. However, their system didn't adapt with the change of transfer distance. Works in this field adopted various techniques, especially magnetic resonance technology, but most of these works did not explain the theoretical calculations of system parameters and relied on different and complex theories to describe the system, such as coupled mode theory, impedance theory and electromagnetic theory. The practical measurements of most of these works are based on expensive and generally unavailable devices such as VNA (vector network analyzer) and RF techniques for measuring circuit parameters such as Q and f_0 . This research is distinguished for the use of simple physical equations to describe the circuit and system variables based on the laws of Kirchhoff and other simple circuit laws. It also

uses flat spiral coils, because they occupy less space (relatively small dimensions). In our measurements, we used innovative methods, simple available devices, such as an oscilloscope and a high-frequency source to measure all the parameters, such as self-inductance L, capacitance C, resonant frequency f_0 and quality factor Q.

In this research, we will work on this technique, which consists of two or more magnetically coupled resonant circuits. Because of the high efficiency of this technique and its adaptation to the change of transfer distance as well as because of simplicity of its use and its low cost.

Research Importance

The importance of this research comes from the many important applications of it in our daily and future life, with the existence of many electronic gadgets, especially portable devices, such as mobiles and laptops, as well as electric vehicles and medical equipment, such as pulse regulator devices. Most of these devices need constant feeding of electric power to recharge their batteries; so the connectors will become removed as in electric vehicles. These connectors occupy a huge place of the circuit or device while the device is shrinking because of technological advance. The biggest importance comes in the medical field as in recharging the battery of a pulse regulator, which is usually fitted inside the patient's body. In the closer past, there was an inevitable need of surgery in order to recharge or replace that battery. Now, this battery is being recharged wirelessly. With the claim of utilizing electric vehicles to save the environment, the batteries of these vehicles can be recharged wirelessly while passing through a especially made area like a bus stop. Also, a mobile phone can be recharged wirelessly *via* merely putting it on the table or even, in the close future, *via* its existence in an area fitted with a wireless energy feeding system, ... and so on for many other devices. According to what has preceded, the need of an efficient energy transfer system is shown. This research has theoretical and practical contributions to understanding and developing wireless power transfer technology, which has become desired in our days in many fields of application.

In this research, we used simple physical equations to describe the circuit and system variables. In our measurements, we used

innovative methods and simple devices, as we mentioned earlier.

Research Purpose

This research aims to design and execute a circuit depending on wireless power transfer technology using coupled magnetic resonances. It aims to present the main concepts and parameters for this technique, such as transfer distance d , quality factor Q , coupling coefficient K and resonant frequency f_0 . Besides of revealing this technique advantages and getting the maximum efficiency for variable transfer distance, starting from 30 cm to 130 cm, this research aims to study the coil dimensions, the measurement of induction L (self-inductance), self-capacity $C_{\text{parasitic}}$ (parasitic capacity), quality factor Q and self-resonant frequency f_0 , in addition to comparing these parameters to those obtained by theoretical calculations. In addition, transfer efficiency η is measured *via* distance variation and compared to theoretical values of efficiency.

Research Methodology

Throughout this research, we constructed a theoretical model, analyzed this model, executed the practical circuit, conducted measurements to this model parameters and its efficiency and compared the results. Coupled magnetic resonance occurs between two circuits when the magnetic field of the primary circuit interacts with the one of the secondary circuit, which produces an induced current in the secondary circuit. The two circuits exchange power *via* their shared magnetic field. This exchange will be at its maximum when the two circuits are in resonance. These two circuits are called (resonators) and the common frequency of these two circuits is called the resonant frequency f_0 . The two circuits are now coupled, but coupled circuits can show resonance at more than one frequency such as standing waves in trumpets or straight chords [9].

Resonant frequency will change as a function of coupling between coils. This is called frequency splitting. When the amount of

coupling is larger, frequency splitting gets clearer. Coupling amount follows the distance between coils. It determines the energy transfer ratio, not the efficiency [10], while the efficiency is determined *via* losses. To make these losses neglected, energy that can't be transferred to the receiver must stay in the transmitter. Even if the coupling was at its minimum, the efficiency could be very high for coils having a high quality factor Q . This result is somehow unexpected for wireless power transfer systems, while in multidirectional propagation electromagnetic waves technique, the efficiency will be coherent with $\frac{1}{d^2}$.

In inductive coupling technique, efficiency is coherent with $\frac{1}{d^3}$ [11]. In fact, there is a minimal amount of coupling; this will be necessary to each load in the receiver coil for efficiency to stay high and for the system to stay stable[12].

Analyzing the Applied Circuit

Fig. 1 shows a WPT system *via* CMR and Fig. 2 shows the equivalent circuit consisting of our coils (resonators).

Source coil (resonator 1) consists of a single copper loop with a resistor R_1 and self-inductance L_1 connected to a high-frequency source with an internal resistor R_s and an electromotive force V_s and connected to capacitor C_1 in series to make the coil resonant at the required frequency. Load coil (resonator 4) consists of a single copper loop with a resistor R_4 and self-inductance L_4 connected to capacitor C_4 in series. Two coils represent the internal resonators (resonators 3&4) called transmitter and receiver coils; they consist of a round copper conductor with flat spiral shape having number of turns N , resistors R_2, R_3 , self-inductances L_2, L_3 and self-capacitances C_2, C_3 , respectively. The geometry of each coil codetermines parasitic capacity and so it determines resonant frequency. As transmit and receive coils don't contain external resistances, their quality factor will be huge. The usage of two internal coils improves efficiency and range [13, 14].

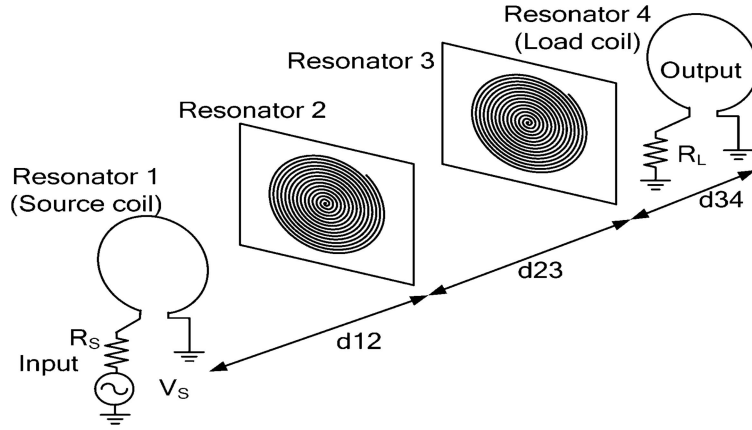


FIG. 1. WPT system via CMR.

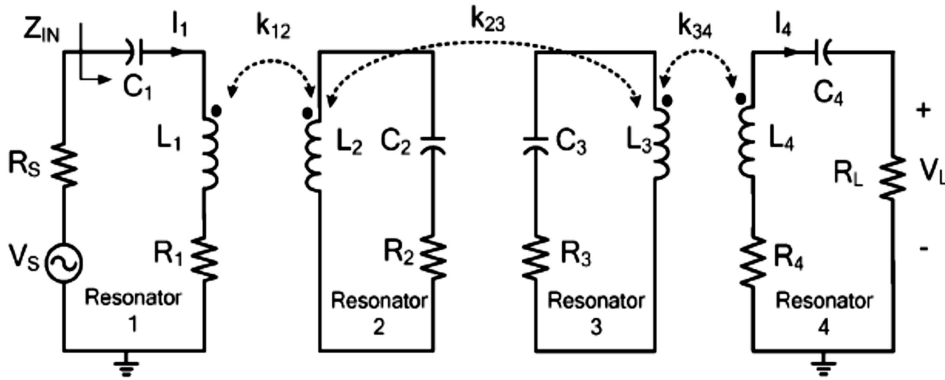


FIG. 2. Equivalent circuit of WPT system via CMR.

In addition, coupling coefficient between source coil and transmit coil on one hand and load coil and receiver coil on the other hand, can be controlled; so, distance change can be adapted without the need of an impedance matching network which can be used for the same purpose, but adding it will result in undesirable additional losses [15].

The suitable selection of the characteristics and geometry of transmitter and receiver coils plays the main role in improving efficiency and transfer range.

The distance between source coil and transmitter coil is d_{12} -Fig.1- and they are magnetically coupled with a coupling coefficient k_{12} as shown in the formula:

$$k_{ij} = \frac{M_{ij}}{\sqrt{L_i L_j}} \quad (1)$$

Here, M_{ij} is the mutual inductance between coils i and j . The subscripts i and j denote the circuit elements in Fig. 2. For example, $i = 1$ denotes the elements in the source coil (loop). In the same way, the distance between transmitter coil and receiver coil is d_{23} and they are magnetically coupled with a coupling coefficient

k_{23} . The distance between receiver coil and load coil is d_{34} and they are magnetically coupled with a coupling coefficient k_{34} .

$$Q_i = \frac{\omega_i L_i}{R_i} \quad (2)$$

And the resonant frequency:

$$\omega_i = \frac{1}{\sqrt{L_i C_i}} \quad (3)$$

In this work, the cross-coupling terms k_{13}, k_{24}, k_{14} are neglected, because they are small and to make calculations easier.

Analyzing the previous circuits can be accomplished using many theories, but we will use Kirchhoff laws and simple circuit laws as mentioned earlier and write:

$$V_s = (R_s + R_1)I_1 + \left(j\omega L_1 - \frac{j}{\omega C_1}\right)I_1 + j\omega M_{12}I_2$$

$$0 = R_2 I_2 + \left(j\omega L_2 - \frac{j}{\omega C_2}\right)I_2 + j\omega M_{12}I_1 - j\omega M_{23}I_3$$

$$0 = R_3 I_3 + \left(j\omega L_3 - \frac{j}{\omega C_3}\right)I_3 + j\omega M_{34}I_4 - j\omega M_{23}I_2$$

$$0 = (R_L + R_4)I_4 + \left(j\omega L_4 - \frac{j}{\omega C_4}\right)I_4 + j\omega M_{34}I_3$$

When $\omega = \omega_0$ for each coil $\omega_i L_i = \frac{1}{\omega_i C_i}$

And $R_1 \ll R_s, R_4 \ll R_L \Rightarrow$

$$R_4 + R_L \cong R_L, R_1 + R_s \cong R_s \Rightarrow$$

$$V_s = R_s I_1 + j\omega M_{12} I_2$$

$$0 = R_2 I_2 + j\omega(M_{12} I_1 - M_{23} I_3)$$

$$0 = R_3 I_3 + j\omega(M_{34} I_4 - M_{23} I_2)$$

$$0 = R_L I_4 + j\omega M_{34} I_3$$

According to the previous equations, we calculate the current in each coil using Q_i and k_{ij}

$$I_1 = \frac{1+k_{23}^2 Q_2 Q_3 + k_{34}^2 Q_3 Q_4}{[(1+k_{12}^2 Q_1 Q_2)(1+k_{34}^2 Q_3 Q_4) + k_{23}^2 Q_2 Q_3]} \frac{V_s}{R_s}$$

$$I_4 = \frac{k_{12} k_{23} k_{34} \sqrt{Q_1 Q_2} \sqrt{Q_2 Q_3} \sqrt{Q_3 Q_4}}{[(1+k_{12}^2 Q_1 Q_2)(1+k_{34}^2 Q_3 Q_4) + k_{23}^2 Q_2 Q_3]} \frac{jV_s}{\sqrt{R_s R_L}}$$

When $k_{12} = k_{34}, Q_2 = Q_3, Q_1 = Q_4$, the transfer function is:

$$\left| \frac{V_L}{V_s} \right| = \frac{k_{23} k_{12} Q_1 Q_2^2}{(1+k_{12}^2 Q_1 Q_2)^2 + k_{23}^2 Q_2^2} \sqrt{\frac{R_L}{R_s}} \quad (4)$$

Here, V_L is the potential between load ends.

The input impedance is:

$$Z_{in} = \frac{V_{in}}{I_1} \Rightarrow Z_{in} = \frac{V_s - R_s I_1}{I_1} \quad (5)$$

$$Z_{in} = R_s \frac{k_{12}^2 Q_1 Q_2 (1+k_{34}^2 Q_3 Q_4)}{1+k_{23}^2 Q_2 Q_3 + k_{34}^2 Q_3 Q_4}$$

To reach maximum efficiency, we consider $Z_{in} = R_s$ and write:

$$(k_{12}^2 Q_1 Q_2 - 1)(k_{34}^2 Q_3 Q_4 + 1) = k_{23}^2 Q_2 Q_3.$$

That is the impedance matching condition.

When $k_{12} = k_{34}, Q_2 = Q_3, Q_1 = Q_4$, we write:

$$k_{12}^2 = \frac{\sqrt{k_{23}^2 Q_2^2 + 1}}{Q_1 Q_2} \quad (6)$$

When we increase the transfer distance d_{23} , k_{23} will decrease and from the last equation, we notice that we should decrease k_{12} or Q_1 to keep the impedance matching condition and maintain efficiency high. Practically, k_{12} decreased when distance d_{12} increased; then, we could maintain efficiency high *via* variation of transfer distance d_{23} without using an impedance matching network. Back to Eq. (5), when $Z_{in} = R_s$, we found that $V_s = 2V_{in}$ is the practical condition to get high efficiency. We can write:

$$\eta = \frac{P_{out}}{P_{in}} = \frac{\frac{V_L^2}{R_L}}{\frac{V_{in}^2}{R_s}} = \frac{\frac{V_L^2}{R_L}}{\frac{V_s^2}{4R_s}}$$

$$\eta = 4 \left(\frac{V_L}{V_s} \right)^2 \frac{R_s}{R_L} \quad (7)$$

From Eq. (4) and Eq. (7) and for $R_s = R_L$:

$$\eta = 4 \left(\frac{k_{23} k_{12}^2 Q_1 Q_2^2}{(1+k_{12}^2 Q_1 Q_2)^2 + k_{23}^2 Q_2^2} \right)^2 \quad (8)$$

Measurement Ways and Devices

The research and measurements have been accomplished in the scientific laboratory-Physics Department, Science Faculty, Tishreen University, Lattakia, Syria.

We used in this research oscilloscope type HAMEG-HM400 -40MHZ, which has an input impedance of $1M\Omega$ for all potential and frequency measurements. And we used a high-frequency generator type PHILIPS-PM 5321 HF GENERATOR giving frequencies from 0.15MHz to 108MHz.

The parameters of the circuit have been measured in more than a simple way. This is what distinguishes this research, as we previously mentioned, including:

A) Measuring L and Q

An LC circuit with an alternative source as in Fig. 3 was used. When the circuit is in resonance by changing the source frequency, the potential between the ends of the capacitor is the largest possible and greater than the potential between the ends of the source by Q times; so, we can measure quality factor Q and self-induction L for each coil from the equations:

$$\omega_0 = \frac{1}{\sqrt{LC}}, \quad Q = \frac{V_C}{V_s}$$

Here, the capacity C is known.

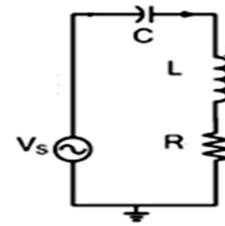


FIG. 3. RLC circuit.

B) Measuring Resonant Frequency of Internal Coils f_0 and Their Parasitic Capacitance $C_{parasitic}$

Measuring parasitic capacitance is not easy, because it is usually small and negligible. It appears in the equivalent circuit in parallel as in Fig. 4. However, the parasitic capacitance was successfully measured using the circuit described in Fig. 5.

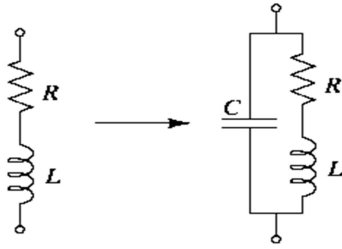


FIG. 4. Equivalent circuit for a coil at high frequency.

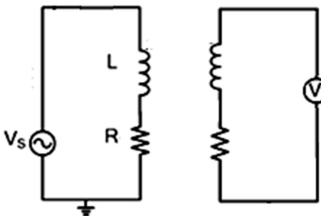


FIG. 5. Measuring resonant frequency.

When the source frequency is changed in the primary circuit (on the right), the potential is maximum in the secondary circuit, which consists of a coil both ends of which are connected to the oscilloscope at a definite frequency. Thus, the secondary circuit is in resonance. In this way, we could measure the resonant frequency. Knowing the self-inductance L of the coil and the resonant frequency, we could measure $C_{parasitic}$ from the equation:

$$\omega_0 = \frac{1}{\sqrt{LC_{parasitic}}}$$

C) Measuring Efficiency η

Efficiency was measured by measuring the load potential V_L , the input potential V_{in} and the electromotive force V_s for each transfer distance. We get efficiency by applying the equation:

$$\eta = 4 \left(\frac{V_L}{V_s} \right)^2 = \left(\frac{V_L}{V_{in}} \right)^2$$

Fig. 1 shows the practical circuit in which the high frequency source is connected to resonator 1 that consists of a source coil and a variable capacitor, so that resonator 1 is in resonance and the resonant frequency is the same frequency as

the self-resonance frequency of the internal coils as well as the resonant frequency of resonator 4.

We could adjust resonator 1 to reach resonance by its variable capacitor.

The first channel of the oscilloscope is connected to the ends of the source in resonator 1; i.e., to the input.

The second channel of the oscilloscope is connected to the ends of the load in resonator 4; i.e., to the output.

What matters is the measurement of V_{in} to apply the practical impedance matching condition $V_{in} = \frac{V_s}{2}$; that is to make the input potential equal to a half of the electromotive force by changing the distance between the source coil and the transmitter coil d_{12} (the same distance between the load coil and the receiver coil).

Results and Discussion

Each of source coil and load coil consists of a single copper conductor with the section diameter of $w = 2r_c = 1.3 \text{ mm}$, round as a single ring with a radius $r_1 = 26 \text{ cm}$. Its inductance can be calculated from the formula [16, 17]:

$$L = \mu_0 r \left[\ln\left(\frac{8r}{r_c}\right) - 2 \right] = 1.98 \mu H$$

Transmitter and receiver coil are made of single copper conductors with a section diameter of $w = 2r_c = 1.8 \text{ mm}$, round in flat spiral shape with a number of turns $N = 7.25$; outer diameter $D_0 = 70 \text{ cm}$, inner diameter $D_{in} = 53.5 \text{ cm}$, average radius $r_2 = 30.8 \text{ cm}$ and pitch $p = 1 \text{ cm}$. Its inductance is calculated from the formula [18]:

$$L = \frac{N^2 [D_0 - N(w+p)]^2}{16D_0 + 28N(w+p)} \frac{39.37}{10^6} = 57.4 \mu H$$

We calculate the resonant frequency for transmitter and receiver coils that is driven by parasitic capacitance from the derived formula:

$$f_0 = \frac{c}{8\pi r N} = 5.34 \text{ MHz}$$

Here, c is the speed of light in free space.

We calculate self-capacitance (parasitic capacitance) $C_{parasitic}$ from:

$$C_p = \frac{1}{\omega^2 L} = 15.4 \text{ PF}$$

The resistance includes ohm resistance and radiation resistance which are calculated for all coils from [19, 20]:

$$R_{rad} = \sqrt{\frac{\mu_0}{\epsilon_0}} \left[\frac{\pi}{12} N^2 \left(\frac{\omega r}{c} \right)^4 \right]$$

$$R_{ohm} = R_{DC} \frac{2r_c}{4\delta}, \delta = \frac{1}{\sqrt{\pi f_0 \mu_0 \sigma}}$$

$$\Rightarrow R_{ohm} = \sqrt{\pi f_0 \mu_0 \rho} N \frac{r}{r_c}.$$

Here, μ_0 is the magnetic permeability of free space, ϵ_0 is the electrical insulation of free space,

δ is the skin depth and $\rho = \frac{1}{\sigma}$ the resistance of the conductor (copper).

$$\Rightarrow R_1 = R_4 = 0.24 \Omega \quad R_2 = R_3 = 1.54 \Omega.$$

We have neglected radiation resistance for its smallness (it is 0.006Ω for coils 2&3). Source resistance and load resistance are $R_s = R_L = 65 \Omega$.

The theoretically calculated parameters for the resonators are given in Table 1.

Table 2 shows the experimentally determined parameters for the resonators.

TABLE 1. Theoretically calculated parameters for the resonators.

	L (μH)	C (PF)	f_0 (MHZ)	$Q_{unloaded}$	Q_{loaded}
Resonator 1 (loop)	1.98	429	5.34	276.8	1.16
Resonator 2 (coil)	57.4	15.4	5.34	1250.5	—
Resonator 3 (coil)	57.4	15.4	5.34	1250.5	—
Resonator 4 (loop)	1.98	429	5.34	276.8	1.16

TABLE 2. Experimentally determined parameters for the resonators.

	L (μH)	C (PF)	f_0 (MHZ)	$Q_{unloaded}$	Q_{loaded}
Resonator 1 (loop)	1.95	398.4	5.71	35	1.22
Resonator 2 (coil)	63	12.33	5.71	150	—
Resonator 3 (coil)	62	12.53	5.71	150	—
Resonator 4 (loop)	1.93	402.5	5.71	34	1.20

Comparing the two tables, we notice the great difference in Q value because of the difference between calculated resistance and measured resistance due to mechanic deformation in the conductor [21]. Bad conductive oxide layer (copper oxide) on the surface of the conductor affects the skin depth making current more limited causing higher resistance [22] and proximity effect makes the same effect on the current. This effect makes precise resistance calculation very difficult [19]. So, we will use the parameters in Table (2) to calculate efficiency.

We calculate coupling coefficient from Eq. (1) and mutual inductance from Neumann's formula [21]:

$$M_{i,j} = \frac{\mu_0 \pi N_i N_j r_i^2 r_j^2}{2d_{i,j}^3}; r_i r_j \ll d_{i,j}.$$

But this formula is limited the in last condition; so, we will use another formula which depends on elliptic integral:

$$M_{i,j} = 2\mu_0 \frac{\sqrt{a+b}}{b} \left[\left(1 - \frac{\beta^2}{2}\right) K(\beta) - E(\beta) \right]$$

Here:

$$a = \frac{r_i^2 + r_j^2 + d_{i,j}^2}{r_i^2 + r_j^2}, b = \frac{2}{r_i r_j}, \beta = \sqrt{\frac{2b}{a+b}}$$

r_i is the radius of loop i of the first coil, r_j is the radius of loop j of the second coil, $d_{i,j}$ is the distance between loop i and loop j and $E(\beta)$ and $K(\beta)$ are the first and second kind elliptic integral:

$$K(\beta) = \int_0^1 \frac{dt}{\sqrt{(1-t^2)(1-\beta^2 t^2)}}$$

$$E(\beta) = \int_0^1 \sqrt{\frac{(1-\beta^2 t^2)}{(1-t^2)}} dt$$

These can be found in the elliptic integral table [25].

Then, the mutual inductance between first and second coils is:

$$M_{a,b} = \sum_{i=1}^N \sum_{j=1}^M M_{i,j}.$$

Here, N and M represent the number of turns for first and second coil, respectively.

Fig. 6 shows the coupling coefficient k_{12} as a function of distance d_{12} , which has been theoretically calculated from the mutual

induction between the coils M_{12} and according to Eq. (1) and Table 2.

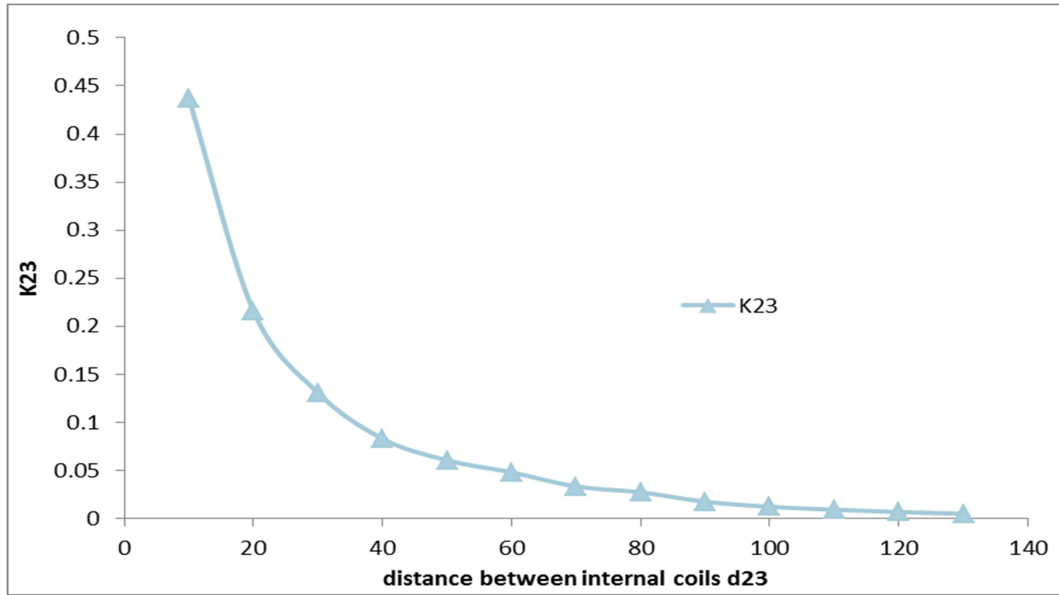


FIG. (6) Coupling coefficient k_{23} versus d_{23} .

Fig. 7 shows the coupling coefficient k_{23} as a function of distance d_{23} , which also has been theoretically calculated from the mutual induction between the coils M_{23} and according to Eq. (1) and Table (2).

The first case: The distance between the source coil and the transmitter coil d_{12} (the same distance between the load coil and the receiver coil) is fixed ($d_{12} = const = 15.5\text{ cm}$); i.e., $k_{12} = const$.

From Figs. 6 and 7, we notice a decrease in coupling coefficient by increasing the distance between coils.

Thus, in Eq. (8), efficiency η and k_{23} remain variable. In this case, there is no impedance matching condition.

Efficiency is theoretically calculated using Eq. (8) and Table 2 parameters in two cases:

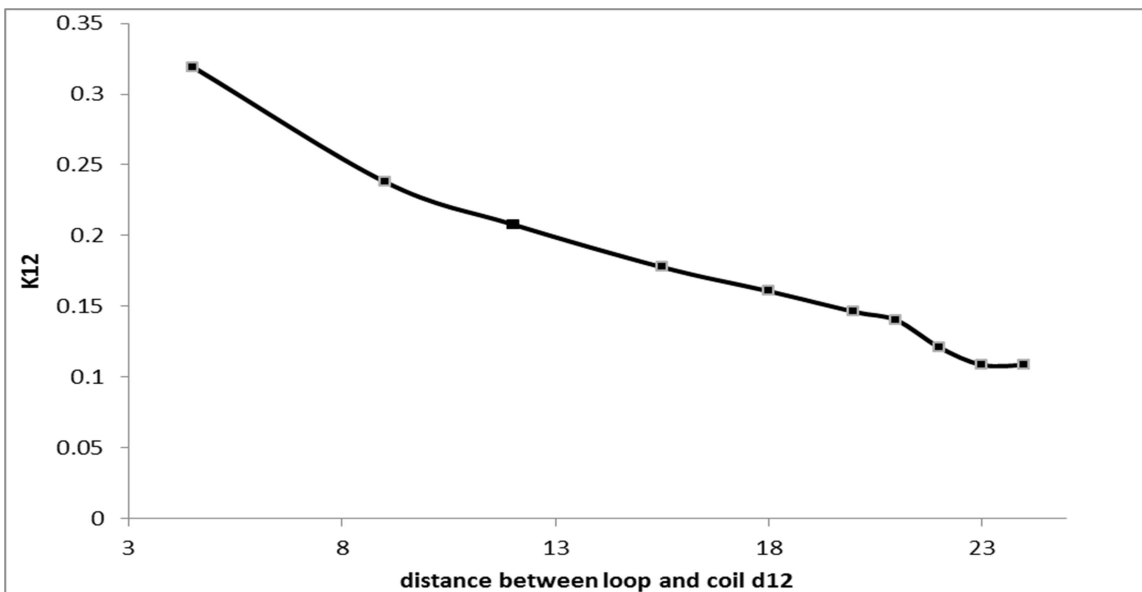


FIG. 7. Coupling coefficient k_{12} versus d_{12} .

The second case: The distance d_{12} is variable by changing the transfer distance d_{23} ; i.e., k_{12} is

variable when k_{23} changes according to the impedance matching condition in Eq. (6), where

by increasing the transfer distance d_{23} , k_{23} will decrease. Therefore, k_{12} should be decreased (i.e., the distance d_{12} should be increased) to keep the efficiency at its maximum as mentioned above. Thus, we calculate the efficiency according to Eqs. (8) and (6). Here, Eq. (8) also has two variables, η and k_{23} , because, according to Eq. (6), k_{12} is related to k_{23} .

Fig. 8 shows the results of theoretical calculation of efficiency in the two preceding cases ($k_{12} = const, k_{12} = variable$).

From Fig. 8, we note the improvement in efficiency in the second case; i.e., the application of impedance matching condition.

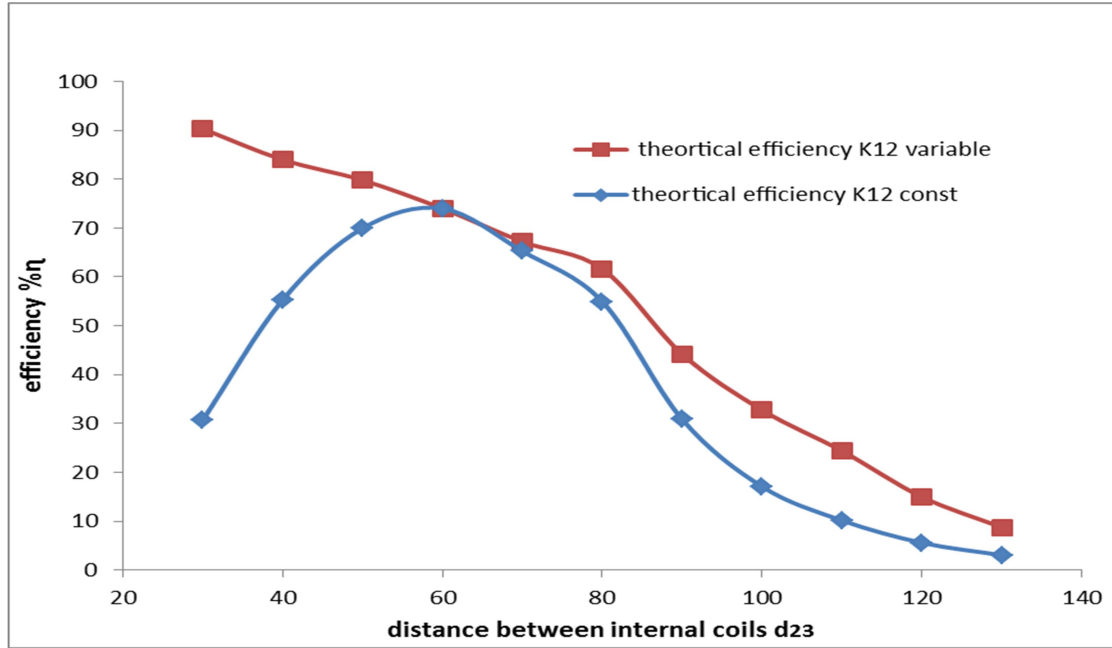


FIG. 8. Theoretical efficiency versus d_{23} .

Efficiency has been measured in two cases and compared to theoretical efficiency:

First: by fixing d_{12} ; i.e., $k_{12} = const$.

Second: by changing d_{12} ; i.e., $k_{12} = variable$, according to the practical impedance matching condition $V_s = 2V_{in}$ which improves

the efficiency and keeps it high by changing the transfer distance.

Fig. 9 illustrates the practical efficiency in the previous two cases. From the figure, we note the improvement in efficiency by applying the impedance matching condition.

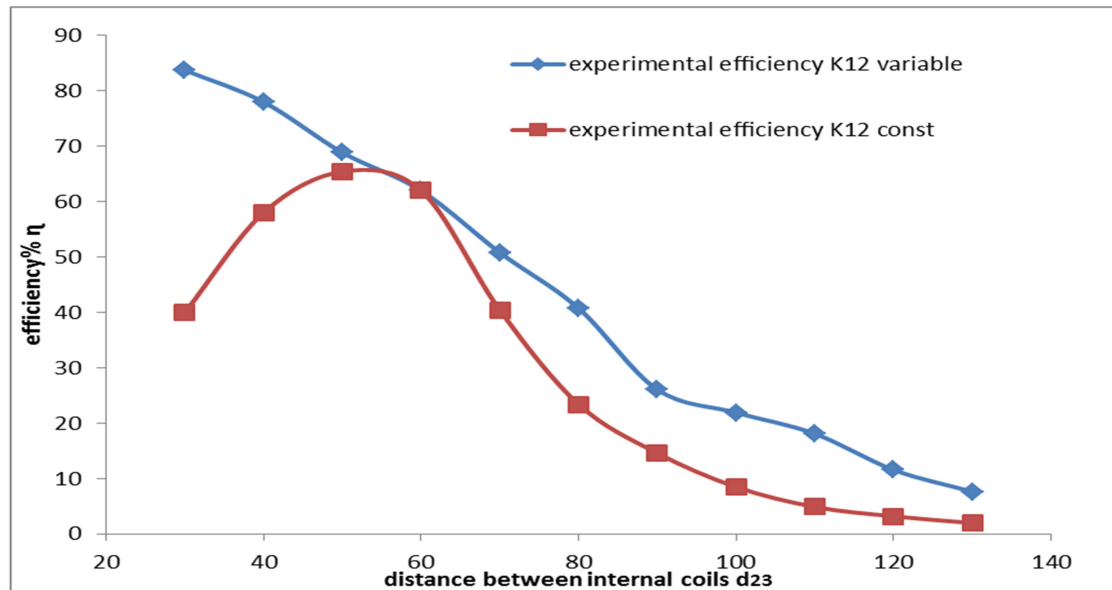


FIG. 9. Experimental efficiency versus d_{23} .

Fig. 10 shows a comparison between theoretical efficiency and practical efficiency in the case of the application of impedance matching condition; i.e., k_{12} is related to k_{23} .

Experimental and theoretical results show that WPT technique *via* Coupled Magnetic Resonances could be efficient for medium ranges and for the case of distance change throughout using the concept of impedance matching (using four coils), where coupling coefficient k_{12} can be changed by changing the distance d_{12} .

We have experimentally measured the maximum efficiency at a distance $d_{23} = 30\text{cm}$ between the two internal resonators and a whole distance $d = 40\text{cm}$ from source coil to load coil. It was found that $\eta = 83.7\%$ and at distances less than $d_{23} = 70\text{cm}$, $d = 106\text{cm}$, it was more than 50%.

$\eta = 22\%$ at a distance $d_{23} = 100\text{cm}$ and a whole distance $d = 142\text{cm}$ and $\eta = 7.6\%$ at a distance $d_{23} = 130\text{cm}$ and a whole distance $d = 178\text{cm}$.

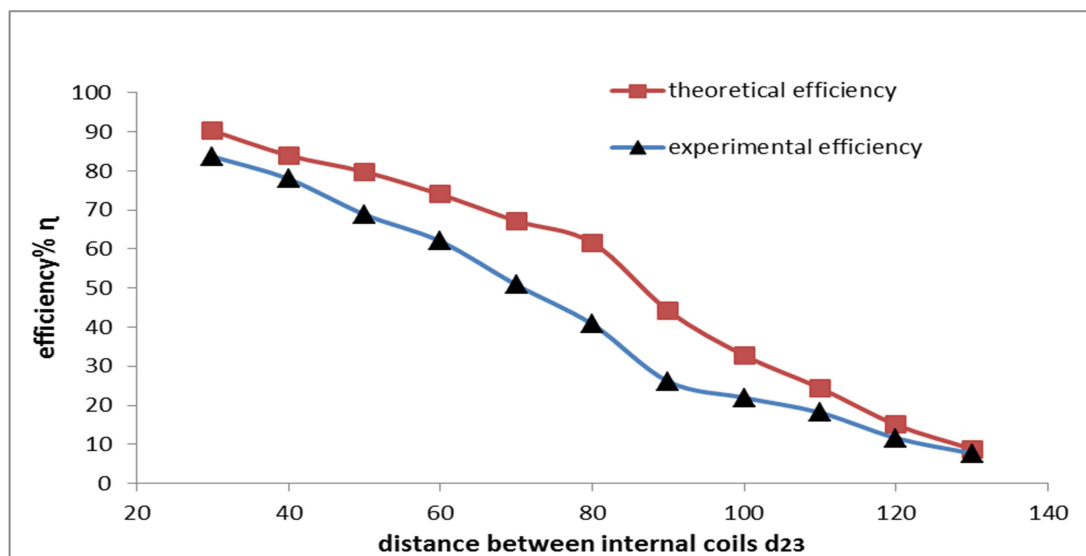


FIG. 10. Experimental and theoretical efficiency *versus* d_{23} .

Conclusions and Recommendations

This work insures the comprehension of WPT *via* Coupled Magnetic Resonances. In addition, the theoretical results approximately match the experimental measurements. It determines the parameters that play vital roles in transfer efficiency and range, such as Q . Bigger Q means higher efficiency. Q is related to coil inductance, coil capacitance, resonant frequency and losses

like Ohmic Resistance, which is mainly responsible for quality factor decrease. In the future, we intend to work on coils that have high quality factor values and fewer losses which means high efficiency and range, working on the coil shape and geometry besides a full theoretical model that is more compatible to experimental measurement.

References

- [1] Tesla, N., U.S. Patent 1,119,732 (1914).
- [2] Ahson, S. and Ilyas, M., "RFID Handbook: Applications, Technology, Security and Privacy". (Boca Raton, FL: CRC Press, 2008).
- [3] Sample, A., Yeager, D., Powledge, P., Mamishev, A. and Smith, J., IEEE Transactions on Instrumentation and Measurement, 57 (11) (2008) 2608.
- [4] Brown, W., IEEE Trans. Microw. Theory Tech., 32 (9) (1984) 1230.
- [5] McSpadden, J. and Mankins, J., IEEE Microw. Mag., 3 (4) (2002) 46.
- [6] Power Mat. Inc., (2009). [Online]. Available: <http://www.powermat.com>.
- [7] Kurs, A., Karalis, A., Moffatt, R., Joannopoulos, J.D., Fisher, P. and Soljacic, M., Science, 317 (5834) (2007).

- [8] Karalis, A., Joannopoulos, J.D. and Soljačić, M., *Ann. Phys.*, 10 (1016) (2007) 4.
- [9] Fletcher, N. and Rossing, T., "The Physics of Musical Instruments". (Berlin, Germany: Springer Verlag, 1998).
- [10] Sample, A. and Smith, J., In: *Proc. IEEE RWS*, Jan. (2009) 16–18.
- [11] Aoki, T. et al., *Nature*, 443 (2006) 671.
- [12] Ka-Lai, L., Hay, J.W. and Beart, P.G.W., U.S. Patent 7, 042, 196 (2006).
- [13] Fernandez, J.M. and Borrás, J.A., U.S. Patent 6, 184, 651 (2001).
- [14] Esser, A. and Skudelny, H.-C., *IEEE Trans. Ind. Appl.*, 27 (1991) 872.
- [15] Giler, E.R., Hall K.L., Kesler, M.P., Soljacic, M., Karalis, A., Kurs, A.B., Li, Q. and Ganem, S.J., U.S. Patent 2010/0259108, Oct. 14, (2010).
- [16] Balanis, C.A., "Antenna Theory: Analysis and Design", (Wiley, New Jersey, 2005).
- [17] Jonah, O., Georgakopoulos, S.V. and Tentzeris, M.M., *IEEE Antennas and Wireless Propagation Letters*, 11 (2012) 1390.
- [18] Grover, F., "Inductance Calculations", Ser. Dover Phoenix Editions. (Dover Publications, Incorporated, 2004).
- [19] Ferreira, J., In: *Power Electronics Specialists Conference, 1990. PESC '90 Record, 21st Annual IEEE*, (1990), 780–785.
- [20] Kaiser, K., "Electromagnetic Compatibility Handbook", Ser. *Electrical Engineering Handbook Series*. (Taylor & Francis, 2004).
- [21] Cheng, D.K., "Field and Wave Electromagnetics", 2nd Ed. Reading, (MA: Addison-Wesley, 1989).
- [22] Sample, A., Waters, B., Wisdom, S. and Smith, J., *IEEE*, 101 (6) (2013) 1343.
- [23] Poon, A.S.Y., *Prog. Electromagn. Res.*, 148 (2014) 171.
- [24] Valenta, C.R., Morys, M.M. and Durgin, G.D., *IEEE Transactions on Microwave Theory and Techniques*, 63 (5) (1967) 1758.
- [25] Hammersley, J.M., *Journal of Research of the National Bureau of Standards*, 50 (1) (1953) 2386.

Radiological Characterization of Settled Dust during a Severe Dust Episode in Jordan

Manal J. Abdallah^a, Molham M. Eyadeh^a, Hamed H. Hamadneh^a,
Abdulrahman N. Akour^b, Mustafa M. Hawamdeh^c and Ibtisam F. Almaaitah^d

^a Physics Department, Faculty of Science, Yarmouk University, Irbid 211-63, Jordan.

^b Department of Basic Science, Al-Huson College, Al-Balqa Applied University, Jordan.

^c Department of physics, Faculty of Engineering Technology, Al-Balqa Applied University, Jordan.

^d Applied Physics Department, Tafila Technical University, Tafila, Jordan.

Received on: 25/9/2018;

Accepted on: 28/1/2019

Abstract: An unusually massive dust storm influenced Jordan and neighboring countries on September 8th to 11th 2015. The dust from this storm was investigated for its radioactive content using gamma-ray spectroscopy. Such storms may carry a large amount of dust and radioactive content, which may impact human health. Samples were collected from different regions in Jordan. The activity concentrations of natural ²³²Th (Thorium), ²³⁸U (Uranium), ⁴⁰K (Potassium) and artificial ¹³⁷Cs (Cesium) radionuclides were measured. The activity concentrations (Bq kg⁻¹) had an average of (\pm Standard Deviation (SD)) 24.7 ± 10 , 34.1 ± 13.3 , 438 ± 124 and 15.7 ± 4.1 for ²³²Th, ²³⁸U, ⁴⁰K, and ¹³⁷Cs, respectively. The activity concentrations of natural and artificial radionuclides were analogous with results obtained from different studies with seasonal storms. The natural radionuclides were comparable to what was found in the local soil, while the activity concentration of ¹³⁷Cs was larger than that found in soil (2.4 ± 1.2 Bq kg⁻¹) and this is attributed to particle size effects. Dose assessment of ¹³⁷Cs showed that it does not contribute significantly to the internal dose of a human during inhalation. The correlation between ²³²Th and ⁴⁰K activity concentration in the measured dust particles is a moderate correlation with a value which is in agreement with those found in other studies worldwide.

Keywords: Radioactivity, Gamma -ray spectrometry, Cesium-137, Unseasonal dust.

PACS number: 29.30.Kv.

1. Introduction

In the past decades, researchers were interested in studying the activities related to nuclear reactions and radioactivity concentrations and its correlated health hazards [1]. Humans are exposed to radionuclides from two main sources, natural and artificial, both of which enter the human body through the food and accumulate in specific organs. Natural radionuclides include the uranium decay series (²³⁵U and ²³⁸U), the thorium decay series (²³²Th)

and Potassium (⁴⁰K) [2]. The artificial radionuclides (¹³⁷Cs, ⁹⁰Sr, ²³⁹Pu, ...etc.) can be released to the environment due to accidents in nuclear reactors such as Chernobyl or from nuclear industry waste, fallout from atmospheric nuclear weapon testing and medical waste [3].

One of the most important artificial nuclides to study is ¹³⁷Cs (with a half-life of 30 years), since it moves easily through the environment

similarly to rubidium and potassium. Its world-wide spread is related to the fallout from atmospheric nuclear weapon testing in the 1950s and 1960s [3]. Among other pathways, humans may directly inhale ^{137}Cs with dust and this pathway may have health consequences [4].

Eastern Mediterranean countries, including Jordan, are affected by seasonal dust storms during the spring season [5, 6]. Besides that, there are unseasonal dust storms that occur under specific weather conditions which meteorologists cannot sometimes predict [7]. These dust storms can affect both weather and human health [8].

A massive dust storm swept through the Middle East on September 8th, 2015, lasting four days, badly reducing visibility, killing at least twelve people and sending thousands of people to hospitals with breathing problems in several Middle Eastern states including Jordan [9, 10, 11]. Broadcast media talked in detail about this unusual event [12, 13, 14, 15]. Health authorities in the affected countries advised and warned people not to leave their homes [16]. Schools in Jordan and Lebanon were closed due to weather and several flights across the region were grounded due to poor visibility. Even the combat was stopped in central Syria [17].

Storms like this are called Haboobs in Arabic culture, which means “violent winds”. Meteorologists were unable to foresee this dense dust storm, because of the unusual weather conditions that are attributed to such a “rare” meteorological phenomenon [7]. These storms can travel for thousands of kilometers, even across the Pacific and can impact many parts of the world.

Papastefanou et al. (2001) studied the radioactivity of radioactive nuclides in colored rain dust samples. It was shown that ^{137}Cs remained after the Chernobyl reactor accident [18]. Papastefanou and Manolopoulou (1989) determined the radioactivity of colored rain in Thessaloniki, Greece by comparing the radioactivity of soil before and after the fall of colored rain. They identified the fission products ^{137}Cs , ^{134}Cs , ^{144}Ce , ^{106}Ru and ^{125}Sb , where all these radionuclides were related to the Chernobyl reactor accident which occurred two years before the study [19].

In Jordan, the first study to assess the radioactivity in seasonal dust storms was in 2015

[20]. The researchers measured the level of natural and artificial radionuclide from large seasonal dust storms in 2012 for samples that were collected from Northern Jordan using gamma-ray spectroscopy. They compared their results with soil samples from the same region.

Recently, a study was conducted to investigate the characteristics of the same unseasonal dust storm as in our present work, at Limassol, Cyprus. The researchers discussed their results based on satellite, lidar vertical profiling and *in situ* aerosol observations [21].

The goal of this study is to measure activity concentrations of natural and artificial radionuclides in this large unseasonal dust storm at different locations in Jordan. For comparison purposes, soil samples from the same regions are analyzed to determine the enrichment of radionuclides (especially ^{137}Cs) to compare the values in dust particles and soil particles.

2. Materials and Methods

Samples of unseasonal dust storm were collected from nine different countryside regions in Jordan which lie at different heights above sea level ranging from 380 to 1000 m based on Google maps [22], (Aqraba, ArRamtha, Huwara, Al Husun, Muhayyam Azmi Almofta, Assarih, Jerash, Jouza and Mo'ta). The study regions were covered with a thin layer of dust. The samples were collected off smooth flat surfaces in the areas (i.e., one sample was gathered from each region). In addition to the dust samples, different soil samples were collected from the same areas for comparison purposes at (0-10) cm depth level all over, packed in plastic bags, assembled in the laboratory and oven dried for at least 2 hrs. at 100°C until a constant weight was reached. Then, the soil samples were sieved through 0.05 mm mesh to remove stones, pebbles and other impurities.

Samples of dust and soil were transferred to standard 100 ml cylindrical cups of 2 cm radius and 6 cm height and sealed. Thereafter, the samples were stored for at least 6 weeks before counting of gamma spectrometric analysis to ensure that secular equilibrium between ^{226}Ra and its decay products was reached.

The activity concentration measurements were performed using high-purity germanium detector (Canberra, Industries, Inc., USA). The detector was of a high resolution; 1.9 keV at 1.33

MeV of ^{60}Co gamma ray peak and a relative efficiency at the same energy peak of 25%. The background radiation was reduced by shielding the detector with a 100mm thick lead cylinder. The data was analyzed using Genie 2000 software containing peak search and nuclide identification modules. A multi-gamma ray reference standard (MGS-5, Canberra, USA) was used for calibration of energy and relative efficiencies for the detector which emits gamma rays of 60-1461 keV . The samples were counted for 86,000 s to reduce the statistical counting error with dead time smaller than 10%. Standard reference materials were used to perform quality control tests obtained from International Atomic Energy Agency (IAEA) (IAEA-375 soil and IAEA-315 marine sediment) in the same geometry as the measured samples. Under the same conditions, an empty cup measurements were also performed to determine the background counts.

The activity concentrations of ^{137}Cs and ^{40}K were directly defined *via* their gamma lines of (yields) 662 keV (0.85) and 1461 keV (0.11), respectively. On the other hand, the activity concentration of ^{232}Th was determined using the gamma line of its daughter (in the decay chain of radioactive substances it's the decay product of parent nuclide ; i.e., ^{232}Th in this case) ^{228}Ac using 911 keV (0.29). For ^{238}U , the activity

concentration was determined using the weighted mean activity concentration of its first daughter ^{234}Th 63.3 keV (0.048). The minimum detectable activities for ^{137}Cs , ^{40}K , ^{238}U and ^{232}Th were 0.17, 8.2, 4.6 and 0.71 $Bq\ kg^{-1}$, respectively.

3. Results and Discussion

Fig. 1 shows the image of the dust storm over the Middle East (AFP photo), captured by the Moderate Resolution Imaging Spectroradiometer (MODIS) instrument on board the Aqua satellite [23]. The image shows that the dust storm affected large parts of Jordan on Tuesday, September 8th 2015. The maximum dust particle mass concentrations for this dust storm were in the order of 10000 $\mu g/m^3$ [21]. For more information about the characterization quantities of this dust storm, see Mamouri et al. (2016).

As shown in Table 1, the radionuclides ^{137}Cs , ^{40}K , ^{232}Th and ^{238}U were identified in all dust and soil sample regions. For dust samples, the activity concentration of ^{137}Cs was in the range of $10.9 \pm 2.0\ Bq\ kg^{-1}$ and $24.6 \pm 4.5\ Bq\ kg^{-1}$ with an average of ($\pm SD$) $15.7 \pm 4.1\ Bq\ kg^{-1}$. This result is less than that of the other study ($1000 \pm 5.0\ Bq\ kg^{-1}$) [19], which can be related to the time period since the nuclear accidents and the weapon testing.

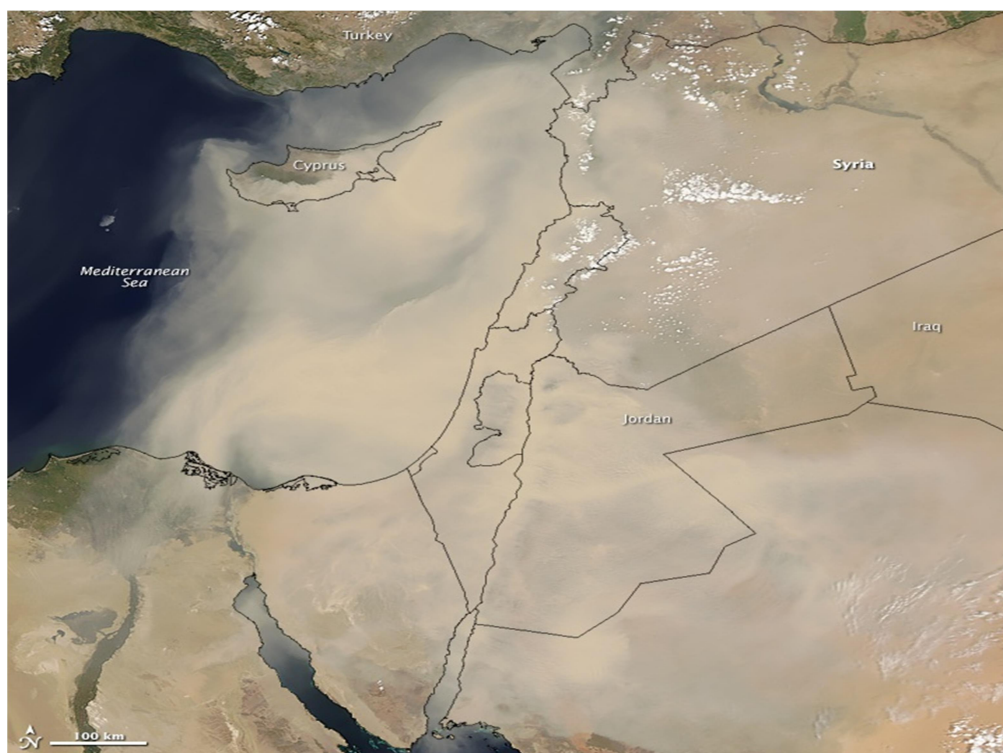


FIG. 1. The image of the dust storm over the Middle East (AFP photo), captured by the Moderate Resolution Imaging Spectroradiometer (MODIS) instrument on board the Aqua satellite on Tuesday, September 8th [23].

TABLE 1. Activity concentrations of measured radionuclides in dust samples and in local soil samples (all activity concentrations were decay corrected for September).

Region	Height above sea level (m) (Google maps)	Activity concentration of radionuclides (Bq kg ⁻¹)							
		Dust Samples				Soil Samples			
		¹³⁷ Cs	⁴⁰ K	²³² Th	²³⁸ U	¹³⁷ Cs	⁴⁰ K	²³² Th	²³⁸ U
Al Husun	600	14.6 ±1.1	404.6 ±34.0	22.1 ±3.2	25.8 ±4.3	0.5 ±0.1	315.9 ±3.9	45.7 ±6.4	39.5 ±6.1
ArRamtha	530	19.9 ±1.9	533.9 ±54.6	28.0 ±4.8	27.4 ±5.7	4.6 ±2.5	160.6 ±38	22.7 ±7.6	20.4 ±4.9
Assarih	700	17.4 ±1.4	417.8 ±39.0	21.2 ±3.7	25.4 ±4.8	1.4 ±0.4	324 ±26.3	29.9 ±3.2	29.7 ±3.0
Aqraba	380	12.8 ±1.3	320.5 ±33.9	23.9 ±4.0	20.8 ±4.6	2.3 ±1.6	172 ±21	26 ±3.7	21.4 ±4.4
Huwara	540	15.6 ±1.2	427.8 ±38.0	20.0 ±3.7	24.9 ±4.5	4.1 ±0.6	495.1 ±58.2	32 ±3.8	38.5 ±7.9
Jerash	700	11.80 ±1.5	402.9 ±46.3	17.2 ±4.5	52.6 ±9.6	2 ±0.6	218.4± 24.4	14.5 ±3.5	19.9 ±4.1
Jouza	800	24.6 ±4.5	751.5 ±14.0	51.7 ±12.3	58.7 ±17.3	2.6 ±0.4	211.9 ±16.5	28.9 ±2.4	20.3 ±3.0
Mo'ta	1000	10.9 ±2.0	385.0 ±6.3	21.7 ±7.1	45.3 ±11.3	1.9 ±0.3	313.5 ±25.2	39.5 ±3.3	29.2 ±4.5
Muhayyam Azmi Almofta	660	13.9 ±1.3	352.9 ±37.5	22.8 ±3.1	26.7 ±5.4	2.2 ±0.3	185.7 ±15.2	26.6 ±2.7	20.6 ±3.0
	MIN.	10.9 ±2.0	320.5 ±33.9	17.2 ±4.5	20.8 ±4.6	0.5 ±0.1	160.6 ±38	14.5 ±3.5	19.9 ±4.1
	MAX.	24.6 ±4.5	751.5 ±14.0	51.7 ±12.3	58.7 ±17.3	4.6 ±2.5	495.1 ±58.2	45.7 ±6.4	39.5 ±6.1
	Average ± (SD)	15.7 ± 4.1	438 ±124	24.7 ±10.0	34.1 ±13.3	2.4 ±1.2	266.3 ± 111	29.5 ±10.8	26.6 ± 8.2

⁴⁰K which is naturally occurring had activity concentrations ranking between 321 ± 34 Bq kg⁻¹ and 752 ± 14 Bq kg⁻¹ with an average of 438 ± 124 Bq kg⁻¹. The activity concentrations of ²³²Th ranged from 17.2 ± 4.5 Bq kg⁻¹ to 51.7 ± 12.3 Bq kg⁻¹ with an average of 24.7 ± 10 Bq kg⁻¹ and for ²³⁸U, the activity concentrations ranged from 20.8 ± 4.6 Bq kg⁻¹ to 58.7 ± 17.3 Bq kg⁻¹ with an average of 34.1 ± 13.3 Bq kg⁻¹. Table 2 compares the activity concentrations of ¹³⁷Cs, ⁴⁰K, ²³²Th and ²³⁸U in the present study and previous studies for dust samples.

For soil samples, the activity concentrations of ¹³⁷Cs were in the range of 0.5 ± 0.1 Bq kg⁻¹ to 4.6 ± 2.5 Bq kg⁻¹ with an average of (\pm SD) $2.4 \pm$

1.2 Bq kg⁻¹. This measured value is comparable with those of previous studies of (0.3 - 41) Bq kg⁻¹ [24] and recent study of 2.3 ± 1.6 Bq kg⁻¹ [20].

For ⁴⁰K, the activity concentrations were in the range from 160.6 ± 38 Bq kg⁻¹ to 495.1 ± 58.2 Bq kg⁻¹ with an average of (\pm SD) 266.3 ± 111 Bq kg⁻¹. For ²³²Th, the activity concentrations were from 14.5 ± 3.5 Bq kg⁻¹ to 45.7 ± 6.4 Bq kg⁻¹ with an average of (\pm SD) 29.5 ± 10.8 Bq kg⁻¹. The activity concentrations of ²³⁸U were in the range between 19.9 ± 4.1 Bq kg⁻¹ and 39.5 ± 6.1 Bq kg⁻¹ with an average of (\pm SD) 26.6 ± 8.2 Bq kg⁻¹.

TABLE 2. Activity concentrations of measured radionuclides in dust samples in the present work and in previous studies.

Radionuclides	Activity concentration of radionuclides (Bq kg ⁻¹) (±SD)	
	Present study	Previous studies
¹³⁷ Cs	15.7 ± 4.1	17.0 ± 2.0 [20] 26.6 ± 4.4 [18]. 402 [19]
⁴⁰ K	438 ± 124	488 [18] 547 ± 56 [20]
²³² Th	24.7 ± 10	30.0 ± 4.9 [20]
²³⁸ U	34.1 ± 13.3	49.3 ± 14 [20]

The internationally reported average values for the natural radionuclides ²³⁸U, ²³²Th and ⁴⁰K are 40, 40 and 370 Bq kg⁻¹, respectively [3]. The obtained results of the present work in dust and soil samples are comparable with the worldwide average concentration values. The average activity concentration of ¹³⁷Cs in dust samples was about eight times its value in soil samples, where the activity concentration increases in the finer size of soil as reported in several studies [25, 26, 27]. The dust samples in the present work have an aerodynamic diameter smaller than 10 µm [21], which is classified as silt and clay with particle sizes of <63 µm according to ISO-14688-1 classification of soil [28].

In spite of the relatively large concentration of ¹³⁷Cs in the dust storm with respect to the concentration in soil, it's not large enough to

affect the potential radiological impact on human health, since the effective dose coefficients for inhalation of ¹³⁷Cs are very small. Based on the ICRP Publication 119 [29], the dose equivalent coefficient of ¹³⁷Cs for adults is 4.8 x 10⁻⁹, which would give rise to a dose of 0.08 µSv per kg of inhaled ¹³⁷Cs in the dust storm studied here. Assuming that the inhaled mass is in the order of milligrams, the expected dose will be in the range of nSv. In addition, the worldwide average effective dose based on UNSCEAR (2000) [3] is 0.22 µSv, which is around 2.7% of the total annual dose from artificial radionuclide.

The correlation between ²³²Th and ⁴⁰K in dust samples is illustrated in Fig. 2. The correlation is moderate. While there is no theoretical basis for this correlation, this result agreed with those revealed other studies worldwide [30, 31, 32].

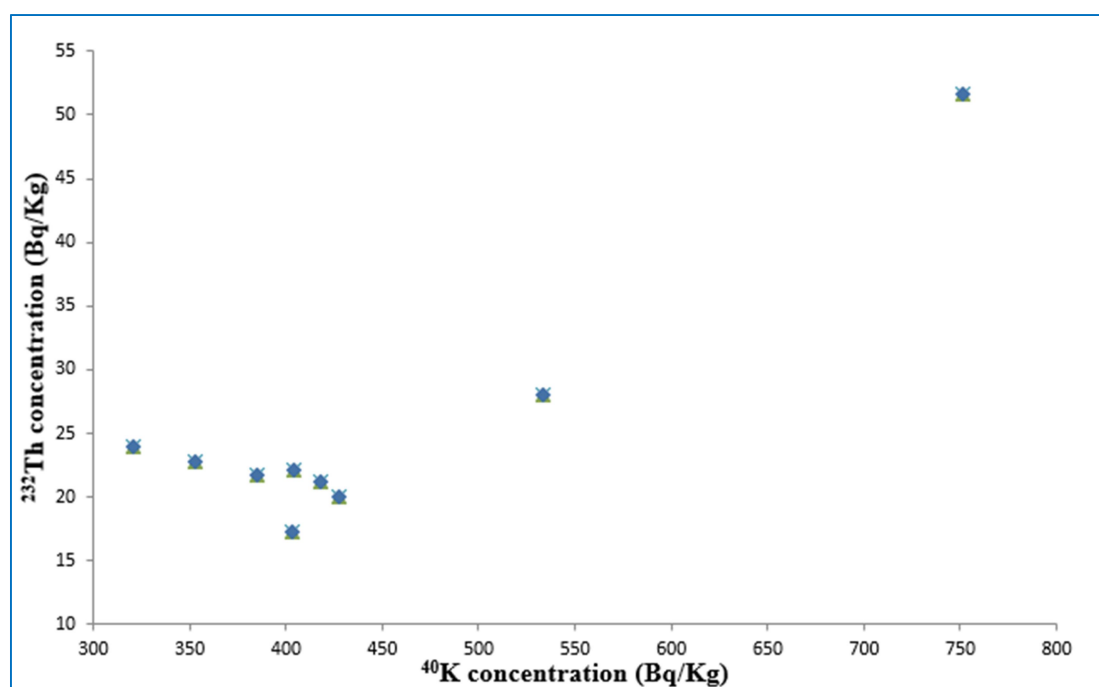


FIG. 2. Potassium vs. thorium concentration in dust samples.

4. Conclusions

A huge unusual dust storm swept through the Middle East on September 8th, 2015, for four days. The activity concentrations of dust and local soil samples were measured in different locations in Jordan using gamma-ray spectroscopy. Terrestrial radioisotopes (²³²Th, ²³⁸U and ⁴⁰K) and the artificial radioisotope ¹³⁷Cs were detected in the samples. In particular, the

activity concentration of ¹³⁷Cs was (\pm SD) 15.7 ± 4.1 Bq kg⁻¹. This high value compared to that in soil (2.4 ± 1.2 Bq kg⁻¹) related to abundance of fine-sized particles, which is consistent with previous studies. The natural radionuclides in dust are comparable to what is found in soil. The dose assessment of ¹³⁷Cs inhalation from dust showed that ¹³⁷Cs contribution to additional effective dose will be negligible.

References

- [1] Altikulac, A., Turhan, S. and Gumus, H., J. Radiat. Research Appl. Sci., 8 (2015) 578.
- [2] Khan, F., "The Physics of Radiation Therapy", 3^{ed} ed., (Lippincott Williams & Wilkins, 2003).
- [3] UNSCEAR, Report to General Assembly, United Nations, New York, 2000.
- [4] Okumura, T., "The Material Flow of Radioactive Cesium-137 in the U.S. 2000". (United States, Environ. Prot. Agency, 2003).
- [5] Abed, A., Al Kuisi, M. and AbulKhair, H., Atmos. Environ., 43 (2009) 2868.
- [6] Kutiel, H. and Furman, H., Indoor Built Environ., 12 (2003) 419.
- [7] Azzeh, L., "Meteorologists 'did not see the sandstorm coming'". Retrieved from: <http://www.jordantimes.com/news/local/meteorologists-did-not-see-sandstorm-coming%E2%80%99>, 10 September 2015.
- [8] Ginoux, P., Prospero, J., Gill, T., Hsu, N. and Zhao, M., Rev. Geophys., 50 (2012) RG3005.
- [9] BBC News, "Incredible photos show what the Levant looks like covered in sand". <http://www.albawaba.com/loop/incredible-photos-show-erie-sandstorm-sweeping-through-middle-east-740938>, 8 September 2015.
- [10] ITV Report, "Hundreds in hospital after deadly sandstorm hits Middle East". Retrieved from: <http://www.itv.com/news/2015-09-08/severe-sandstorm-distrupts-fighting-in-syria-and-hospitalizes-hundreds-in-middle-east/>, 8 September 2015.
- [11] Mashable, "Huge dust storm roars through Middle East, sending hundreds to the hospital". <http://mashable.com/2015/09/08/dust-storm-middle-east-israel-syria/#f19bKO.AuaqD>, 8 September 2015.
- [12] Albawaba, "Incredible photos show what the Levant looks like covered in sand". <http://www.albawaba.com/loop/incredible-photos-show-erie-sandstorm-sweeping-through-middle-east-740938>, 8 September 2015.
- [13] BBC News, "Middle East dust storm puts dozens in hospital". <http://www.bbc.com/news/world-middle-east-34185291>, 8 September 2015.
- [14] Howard, B., "National Geographic, Explaining the Monster Dust Storm Sweeping the Middle East" Retrieved from: <http://news.nationalgeographic.com/2015/09/150908-middle-east-dust-storm-haboob-weather/>, 8 September 2015.
- [15] World Meteorological Organization, "Compared dust forecasts". Retrieved from: <http://sds-was.aemet.es/forecast-products/dust-forecasts/comopared-dust-forecasts>, 7 September 2015.
- [16] Reuters, "Deadly storm engulfs Middle East and slows Syria air strikes". Retrieved from: <http://uk.reuters.com/article/uk-mideast-storm-idUKKCN0R812N20150908>. 8 September 2015.
- [17] The world post, "Deadly Sandstorm Brings Life and War to a Halt in the Middle East". Retrieved from: http://www.huffingtonpost.com/entry/deadly-sandstorm-middle-east_us_55eee28ce4b002d5c0768943, 8 September 2015.

- [18] Papastefanou, C., Manolopoulou, M., Stoulos, S., Ioannidou, A. and Gerasopoulos, E., *J. Environ. Radioact.*, 55 (2001) 109.
- [19] Papastefanou, C. and Manolopoulou, M., *Greece Sci. Total Environ.*, 80 (1989) 225.
- [20] Hamadneh, H., Ababneh, Z., Hamasha, K. and Ababneh, A., *J. Environ. Radioact.*, 140 (2015) 65.
- [21] Mamouri, R., Nisantzil, A., Ansmann, A. and Hadjimitsis, D., *Atmos. Chem. Phys. Discuss.*, 16 (2016) 13711.
- [22] Google maps, <https://www.daftlogic.com/sandbox-google-maps-find-altitude.htm>.
- [23] Schmaltz, J., "Earth Observatory, NASA Images". Retrieved from: <http://earthobservatory.nasa.gov/NaturalHazards/view.php?id=86571>, 7, 8 and 9 September 2015.
- [24] Baggoura, B., Nouredine, A. and Benkrid, M., *Appl. Radiat. Iso.*, 49 (1998) 867.
- [25] Livens, F. and Baxter, M., *Sci. Total Environ.*, 70 (1988) 1.
- [26] Spezzano, P., *J. Environ. Radioact.*, 83 (2005) 117.
- [27] Tsukada, H., Takeda, A., Hisamatsu, S. and Inaba, J., *J. Environ. Radioact.*, 99 (2008) 875.
- [28] Sawai, H., Rahman, I., Lua, C., Tsukagoshi, Y., Begum, Z., Maki, T. and Hasegawa, H., *Microchem. J.*, 118 (2015) 158.
- [29] Eckerman, K., Harrison, J., Menzel, H. and Clement, C., *Ann. ICRP* 41 (Suppl. 1) (2012) 1.
- [30] Al-Jundi, J., *Jordan. Radiat. Meas.*, 35 (2002) 23.
- [31] Papachristodoulou, C., Assimakopoulos, P., Patronis, N. and Ioannides, K., *J. Environ. Radioact.*, 64 (2003) 195.
- [32] Ramzaev, V., Yonehara, H., Hille, R., Barkovsky, A., Mishine, A., Sahoo, S., Kurotaki, K. and Uchiyama, M., *J. Environ. Radioact.*, 85 (2006) 205.

Authors Index

Abdallah H. Almahasneh	153
Abdalahaman H. Alhashim	171
Abdulrahman N. Akour.....	183
Ahmad M. Al-Qararah	153
Alaa Jaffal.....	153
Ali Daroesho.	171
DaifAoulah Nassor	171
Derar Altarawneh.	153
Eman Al-Hwaitat	141
Hamed H. Hamadneh.....	183
Haneen Badran.....	141
Hitler Louis.....	103
Ibrahim Bsoul.....	141
Ibtisam F. Almaaitahd.....	183
Ike V. Chidinma.....	103
Ita I. Benedict.....	103
M. Ramzan.....	163
Manal J. Abdallah.....	183
Mansour M. Al-Haj	133
Molham M. Eyadeh	183
Muhammad Ayaz.....	163
Mustafa M. Hawamdeh.....	183
Najla.A. Elgheryani	97
Nzeata I. Nelson	103
Rola Bqaeen	141
Safa' Ibrahim.	113
Sami Mahmood	141
Sawsan Malek	113
Suhail Khan	163
Syed Zaheer Ullah	163
Tareq Hussein	113

Subject Index

Artificial radioactivity.....	153
Cesium-137.....	183
Conformal symmetries.....	163
Coupled magnetic resonances.....	171
Coupling coefficient.....	171
Dirac equation.....	103
Direct integration technique.....	163
Electrophoresis.....	113
Fickian diffusion.....	113
Gamma-ray spectrometry.....	153,183
Gravitational settling.....	113
Magnetic properties.....	141
Magnetization.....	133
Magnetophoresis.....	113
Manning-Rosen potential.....	103
Mutual induction.....	171
Natural radioactivity.....	153
Nikiforov-Uvarov method.....	103
Particular solutions.....	163
Perovskites.....	141
Polyethylene glycol (PEG).....	97
Polyvinylpyrrolidone (PVP).....	97
Quadratic exponential-type potential.....	103
Radiation hazard assessment.....	153
Radioactivity.....	183
Resonance.....	171
Resonant frequency.....	171
Silver nanoparticles (AgNPs).....	97
Soil samples.....	153
Spectroscopy.....	133
Spin and pseudospin symmetry.....	103
Structural properties.....	141
Surface tension (γ).....	97
Thermomagnetic curves.....	141
Thermophoresis.....	113
Transition temperature.....	133
Turbophoresis.....	113
Unseasonal dust.....	183
Viscosity (η).....	97
X-ray diffraction.....	133

المراجع: يجب طباعة المراجع بأسطر مزدوجة ومرقمة حسب تسلسلها في النص. وتكتب المراجع في النص بين قوسين مربعين. ويتم اعتماد اختصارات الدوريات حسب نظام Wordlist of Scientific Reviewers.

الجدول: تعطى الجداول أرقاماً متسلسلة يشار إليها في النص. ويجب طباعة كل جدول على صفحة منفصلة مع عنوان فوق الجدول. أما الحواشي التفسيرية، التي يشار إليها بحرف فوقي، فتكتب أسفل الجدول.

الرسوم التوضيحية: يتم ترقيم الأشكال والرسومات والرسومات البيانية (المخططات) والصور، بصورة متسلسلة كما وردت في النص.

تقبل الرسوم التوضيحية المستخرجة من الحاسوب والصور الرقمية ذات النوعية الجيدة بالأبيض والأسود، على أن تكون أصيلة وليست نسخة عنها، وكل منها على ورقة منفصلة ومعرفة برقمها بالمقابل. ويجب تزويد المجلة بالرسومات بحجمها الأصلي بحيث لا تحتاج إلى معالجة لاحقة، وألا تقل الحروف عن الحجم 8 من نوع Times New Roman، وألا تقل سماكة الخطوط عن 0.5 وكتافة متجانسة. ويجب إزالة جميع الألوان من الرسومات ما عدا تلك التي ستنشر ملونة. وفي حالة إرسال الرسومات بصورة رقمية، يجب أن تتوافق مع متطلبات الحد الأدنى من التمايز (1200 dpi Resolution) لرسومات الأبيض والأسود الخطية، و 600 dpi للرسومات باللون الرمادي، و 300 dpi للرسومات الملونة. ويجب تخزين جميع ملفات الرسومات على شكل (jpg)، وأن ترسل الرسوم التوضيحية بالحجم الفعلي الذي سيظهر في المجلة. وسواء أرسل المخطوط بالبريد أو عن طريق الشبكة (Online)، يجب إرسال نسخة ورقية أصلية ذات نوعية جيدة للرسومات التوضيحية.

مواد إضافية: تشجع المجلة الباحثين على إرفاق جميع المواد الإضافية التي يمكن أن تسهل عملية التحكيم. وتشمل المواد الإضافية أي اشتقاقات رياضية مفصلة لا تظهر في المخطوط.

المخطوط المنقح (المعدل) والأقراص المدمجة: بعد قبول البحث للنشر وإجراء جميع التعديلات المطلوبة، فعلى الباحثين تقديم نسخة أصلية ونسخة أخرى مطابقة للأصلية مطبوعة بأسطر مزدوجة، وكذلك تقديم نسخة إلكترونية تحتوي على المخطوط كاملاً مكتوباً على Microsoft Word for Windows 2000 أو ما هو استجد منه. ويجب إرفاق الأشكال الأصلية مع المخطوط النهائي المعدل حتى لو تم تقديم الأشكال إلكترونياً. وتخزن جميع ملفات الرسومات على شكل (jpg)، وتقدم جميع الرسومات التوضيحية بالحجم الحقيقي الذي ستظهر به في المجلة. ويجب إرفاق قائمة ببرامج الحاسوب التي استعملت في كتابة النص، وأسماء الملفات على قرص مدمج، حيث يعلم القرص بالاسم الأخير للباحث، وبالرقم المرجعي للمخطوط للمراسلة، وعنوان المقالة، والتاريخ. ويحفظ في مغلف واقٍ.

حقوق الطبع

يُشكّل تقديم مخطوط البحث للمجلة اعترافاً صريحاً من الباحثين بأن مخطوط البحث لم يُنشر ولم يُقدّم للنشر لدى أي جهة أخرى كانت وبأي صيغة ورقية أو إلكترونية أو غيرها. ويشترط على الباحثين ملء نموذج ينصّ على نقل حقوق الطبع لتصبح ملكاً لجامعة اليرموك قبل الموافقة على نشر المخطوط. ويقوم رئيس التحرير بتزويد الباحثين بإنموذج نقل حقوق الطبع مع النسخة المُرسلة للتتقيح. كما ويُمنع إعادة إنتاج أيّ جزء من الأعمال المنشورة في المجلة من دون إذن خطّي مُسبق من رئيس التحرير.

إخلاء المسؤولية

إن ما ورد في هذه المجلة يعبر عن آراء المؤلفين، ولا يعكس بالضرورة آراء هيئة التحرير أو الجامعة أو سياسة اللجنة العليا للبحث العلمي أو وزارة التعليم العالي والبحث العلمي. ولا يتحمل ناشر المجلة أي تبعات مادية أو معنوية أو مسؤوليات عن استعمال المعلومات المنشورة في المجلة أو سوء استعمالها.

الفهرسة: المجلة مفهرسة في:

	Emerging Sources Citation Index (ESCI)	
---	---	---

المجلة الأردنية للفيزياء هي مجلة بحوث علمية عالمية متخصصة مُحكمة تصدر بدعم من صندوق دعم البحث العلمي، وزارة التعليم العالي والبحث العلمي، عمان، الأردن. وتقوم بنشر المجلة عمادة البحث العلمي والدراسات العليا في جامعة اليرموك، إربد، الأردن. وتنتشر البحوث العلمية الأصيلة، إضافة إلى المراسلات القصيرة Short Communications، والملاحظات الفنية Technical Notes، والمقالات الخاصة Feature Articles، ومقالات المراجعة Review Articles، في مجالات الفيزياء النظرية والتجريبية، باللغتين العربية والإنجليزية.

تقديم مخطوط البحث

تقدم البحوث عن طريق إرسالها إلى البريد الإلكتروني : jjp@yu.edu.jo

تقديم المخطوطات إلكترونياً: اتبع التعليمات في موقع المجلة على الشبكة العنكبوتية.

ويجري تحكيم البحوث الأصيلة والمراسلات القصيرة والملاحظات الفنية من جانب مُحكمين اثنين في الأقل من ذوي الاختصاص والخبرة. وتُشجّع المجلة الباحثين على اقتراح أسماء المحكمين. أما نشر المقالات الخاصة في المجالات الفيزيائية النشطة، فيتم بدعوة من هيئة التحرير، ويُشار إليها كذلك عند النشر. ويُطلب من كاتب المقال الخاص تقديم تقرير واضح يتسم بالدقة والإيجاز عن مجال البحث تمهيداً للمقال. وتنتشر المجلة أيضاً مقالات المراجعة في الحقول الفيزيائية النشطة سريعة التغير، وتشجّع كاتبي مقالات المراجعة أو مُسكّتيها على إرسال مقترح من صفحتين إلى رئيس التحرير. ويرفّق مع البحث المكتوب باللغة العربية ملخص (Abstract) وكلمات دالة (Keywords) باللغة الإنجليزية.

ترتيب مخطوط البحث

يجب أن تتم طباعة مخطوط البحث ببنت 12 نوعه Times New Roman، وبسطر مزدوج، على وجه واحد من ورق A4 (21.6 × 27.9 سم) مع حواشي 3.71 سم، باستخدام معالج كلمات ميكروسوفت وورد 2000 أو ما استُجد منه. ويجري تنظيم أجزاء المخطوط وفق الترتيب التالي: صفحة العنوان، الملخص، رموز التصنيف (PACS)، المقدمة، طرق البحث، النتائج، المناقشة، الخلاصة، الشكر والعرفان، المراجع، الجداول، قائمة بدليل الأشكال والصور والإيضاحات، ثمّ الأشكال والصور والإيضاحات. وتُكتب العناوين الرئيسية بخط غامق، بينما تُكتب العناوين الفرعية بخط مائل.

صفحة العنوان: وتشمل عنوان المقالة، أسماء الباحثين الكاملة وعناوين العمل كاملة. ويكتب الباحث المسؤول عن المراسلات اسمه مشاراً إليه بنجمة، والبريد الإلكتروني الخاص به. ويجب أن يكون عنوان المقالة موجزاً وواضحاً ومعبراً عن فحوى (محتوى) المخطوط، وذلك لأهمية هذا العنوان لأغراض استرجاع المعلومات.

الملخص: المطلوب كتابة فقرة واحدة لا تزيد على مائتي كلمة، موضحة هدف البحث، والمنهج المتبع فيه والنتائج وأهم ما توصل إليه الباحثون.

الكلمات الدالة: يجب أن يلي الملخص قائمة من 4-6 كلمات دالة تعبر عن المحتوى الدقيق للمخطوط لأغراض الفهرسة.

PACS: يجب إرفاق الرموز التصنيفية، وهي متوافرة في الموقع <http://www.aip.org/pacs/pacs06/pacs06-toc.html>.

المقدمة: يجب أن توضّح الهدف من الدراسة وعلاقتها بالأعمال السابقة في المجال، لا أن تكون مراجعة مكثفة لما نشر (لا تزيد المقدمة عن صفحة ونصف الصفحة مطبوعة).

طرائق البحث (التجريبية / النظرية): يجب أن تكون هذه الطرائق موضحة بتفصيل كاف لإتاحة إعادة إجرائها بكفاءة، ولكن باختصار مناسب، حتى لا تكون تكراراً للطرائق المنشورة سابقاً.

النتائج: يستحسن عرض النتائج على صورة جداول وأشكال حيثما أمكن، مع شرح قليل في النص ومن دون مناقشة تفصيلية.

المناقشة: يجب أن تكون موجزة وتركز على تفسير النتائج.

الاستنتاج: يجب أن يكون وصفاً موجزاً لأهم ما توصلت إليه الدراسة ولا يزيد عن صفحة مطبوعة واحدة.

الشكر والعرفان: الشكر والإشارة إلى مصدر المنح والدعم المالي يكتبان في فقرة واحدة تسبق المراجع مباشرة.

Jordan Journal of

PHYSICSAn International Peer-Reviewed Research Journal issued by the
Support of the Scientific Research Support Fund

Published by the Deanship of Research & Graduate Studies, Yarmouk University, Irbid, Jordan

Name: الأسم:
 Specialty: التخصص:
 Address: العنوان:
 P.O. Box: صندوق البريد:
 City & Postal Code: المدينة/الرمز البريدي:
 Country: الدولة:
 Phone: رقم الهاتف:
 Fax No: رقم الفاكس:
 E-mail: البريد الإلكتروني:
 No. of Subscription: عدد الاشتراكات:
 Method of Payment: طريقة الدفع:
 Amount Enclosed: المبلغ المرفق:
 Signature: التوقيع:

Cheques should be paid to Deanship of Research and Graduate Studies - Yarmouk University.

I would like to subscribe to the Journal
For

- One Year
 Two Years
 Three Years

One Year Subscription Rates

	Inside Jordan	Outside Jordan
Individuals	JD 8	€ 40
Students	JD 4	€ 20
Institutions	JD 12	€ 60

Correspondence**Subscriptions and Sales:**

Prof. Ibrahim O. Abu Al-Jarayesh
 Deanship of Research and Graduate Studies
 Yarmouk University
 Irbid – Jordan
Telephone: 00 962 2 711111 Ext. 2075
Fax No.: 00 962 2 7211121



جامعة اليرموك



المملكة الأردنية الهاشمية

المجلة الأردنية

للفيزياء

مجلة بحوث علمية عالية متخصصة محكمة
تصدر بدعم من صندوق دعم البحث العلمي

المجلة الأردنية
للفيزياء
مجلة بحوث علمية عالمية محكمة

المجلد (12)، العدد (2)، آب 2019م / محرم 1441هـ

المجلة الأردنية للفيزياء: مجلة علمية عالمية متخصصة محكمة تصدر بدعم من صندوق دعم البحث العلمي، عمان، الأردن، وتصدر عن عمادة البحث العلمي والدراسات العليا، جامعة اليرموك، إربد، الأردن.

رئيس التحرير:

ابراهيم عثمان أبو الجرايش

قسم الفيزياء، جامعة اليرموك، إربد، الأردن.

ijaraysh@yu.edu.jo

هيئة التحرير:

نبيل يوسف أيوب

رئيس الجامعة الأمريكية في مادبا، مادبا، الأردن.

nabil.ayoub@gju.edu.jo

جميل محمود خليفة

قسم الفيزياء، الجامعة الأردنية، عمان، الأردن.

jkalifa@ju.edu.jo

سامي حسين محمود

قسم الفيزياء، الجامعة الأردنية، عمان، الأردن.

s.mahmood@ju.edu.jo

مروان سليمان موسى

قسم الفيزياء، جامعة مؤتة، الكرك، الأردن.

mmousa@mutah.edu.jo

محمد خالد الصغير

قسم الفيزياء، الجامعة الهاشمية، الزرقاء، الأردن.

msugh@hu.edu.jo

عبد المجيد الياسين

قسم الفيزياء، جامعة اليرموك، إربد، الأردن.

alyassin@yu.edu.jo

محمد العمري

قسم الفيزياء، جامعة العلوم والتكنولوجيا، إربد، الأردن.

alakmoh@just.edu.jo

إبراهيم البصول

قسم الفيزياء، جامعة آل البيت، المفرق، الأردن.

Ibrahimbsoul@yahoo.com

سكرتير التحرير: مجدي الشناق

ترسل البحوث إلى العنوان التالي:

الأستاذ الدكتور إبراهيم عثمان أبو الجرايش
رئيس تحرير المجلة الأردنية للفيزياء
عمادة البحث العلمي والدراسات العليا، جامعة اليرموك
إربد، الأردن

هاتف 00 962 2 7211111 فرعي 2075

E-mail: jjp@yu.edu.jo Website: <http://Journals.yu.edu.jo/jjp>